Some Rock Mechanics Problems with Application for Hydraulic Fracturing

by

Saied Mighani

B.S., Amir Kabir University of Technology (2011)
M.S., University of Oklahoma (2014)

Submitted to the Department of Earth, Atmospheric and Planetary Sciences
in partial fulfillment of the requirements for the degree of
Doctor of Philosophy in Geophysics
at the
MASSACHUSETTS INSTITUTE OF TECHNOLOGY
May 2019

Signature redacted
Author...

Department of Earth, Atmospheric and Planetary Sciences
Massachusetts Institute of Technology
May, 10, 2019

Signature redacted
Certified by...
Brian J. Evans
Professor of Geophysics, Massachusetts Institute of Technology
Thesis Supervisor

Signature redacted
Accepted by...
Robert D. van der Hilst
Schlumberger Professor of Earth and Planetary Sciences
Head, Department of Earth, Atmospheric and Planetary Sciences

Some Rock Mechanics Problems with Application for Hydraulic Fracturing

by

Saied Mighani

Submitted to the Department of Earth, Atmospheric and Planetary Sciences
on May 10th, 2019, in partial fulfillment of the requirements for the degree of
Doctor of Philosophy in Geophysics

Abstract (350 words)

Hydraulic fracturing is an essential tool used to enhance connectivity in shale gas reservoirs by maximizing the intersection between the hydraulic fracture (HF) and pre-existing natural fractures (NF) or faults. The technique is most effective when the hydraulic fracture crosses natural fractures rather than arresting on them. Experiments conducted to examine the interaction between HF and artificial pre-existing faults suggest that the coupling of diffusivity and fault slip is an important element of the HF-fault interaction problem. Fault slip, once activated is associated with an apparent increase in diffusivity. Whether the hydrofracture crosses or arrests on the pre-existing fault is also affected by surface roughness, differential stresses, and fault slip mode (i.e., stable or stick-slip sliding). Calibrated piezoelectric transducers were used to measure acoustic emissions (AE) generated during HF and fault slip. Moment tensor analysis of these events was used to distinguish pure tensile, shear, and possibly closure events during the experiments. Seismic moment magnitudes were approximately -7 for events during the initiation of the HF and about -5 for events during fault slip. Such a low ratio of seismic moments for tensile and slip events may explain the small numbers of tensile events recorded during reservoir stimulations. I also studied the time-dependent behavior in shales to gain insight into the post-stimulation efficiency of exploitations. Shale experiences strain hardening and compaction during loading by both isostatic (pressure-driven) and differential stress (shear-driven). Transient creep strain increased linearly with log(time), possibly transitioning to constant rate in timescale of several days. Motivated by the multi-scale nature of heterogeneities in shales, I examined the micromechanics of deformation using the nano-indentation technique. Elastic and creep moduli found in nano-indentation and triaxial tests agreed within a factor of 2, but within that factor, the creep strength may depend on spatial scale.

Thesis Supervisor: Brian J. Evans
Title: Professor of Geophysics

Acknowledgments

> "Beyond the earth,
> beyond the farthest skies
> I try to find Heaven and Hell.
> Then I hear a solemn voice that says:
> "Heaven and hell are inside."
> — Omar Khayyám,

My Ph.D. studies at MIT has been a journey, as besides moving from laid back Oklahoma's environment to Boston's lifestyle, I had to transfer my knowledge as a petroleum engineer practitioner to an Earth, and at some periods Planetary, Scientist. In this journey, I learned many lessons from tremendous people I was surrounded by at MIT, whom I will always do remember. Some were advisors and some my fellow students.

Especially, I would like to acknowledge my Ph.D. advisor Brian Evans, whose office door was always open to me. I will carry his wise advice in experimental techniques, as well as life, with me a long way. Having a kind advisor makes Ph.D. life way more pleasant. Yves Bernabe, whose love of science sometimes even led to sessions of non-stop hours-long discussion. David Lockner, with a broad sight, taught me patiently how to design experiments as a hands-on experimentalist. Ben Weiss, whose enthusiasm took me to look beyond Earth. Thanks to him, I feel special to have worked with lunar rocks. Matej Pec, who taught me academic lessons as fresh blood. And, Bradford Hager, who always has questions in his pocket to spot you. Brian Kilgore, who taught me how to get an instrument going by a single touch; I hope I grasped some. Alan Schwartzman, who taught me the nuts and bolts of Hysitron nanoindenter. Specifically, I would like to acknowledge my M.Sc. advisor, Carl Sondergeld who introduced me to the fascinating world of rock mechanics. I learned from these people to be a scientific skeptical, critical thinker, courageous, big-picture thinker, concise, and yet a modest person. I feel blessed to have been a pupil of such great scientists. I am also indebted to the United States Geological Survey (USGS).

I would like to thank Farrokh Sheibani and Hamed O. Ghaffari who gave me wise advice throughout my Ph.D. as my buddies. I would also like to thank Uli Mok, Jahan Ramezani, Abdel

Boulenouar, Carolyn Morrow, Diane Moore, Jianhua Gong, Chen Gu, Yuval Tal, Shujuan Mao, Clara Maurel, Caue Borlina, Rona Oran, and others whom are not mentioned due to my forgetful memory. The kind administrations at EAPS, most especially Brenda Carbone, is also thanked who always ensured my academic well-being.

Mom, dad, this thesis was not possible without you…

]

Contents

List of Figures

List of Tables

Chapter 1: Introduction

1.1 Problem statement

Natural earthquakes may redistribute and raise the local pore pressure, either mechanically or thermally. This excessive pore-fluid pressure could then trigger new earthquakes by lubricating the fault (Nur and Booker, 1972; Sibson, 1973; Lee and Delaney, 1987). Human activities could also cause earthquakes; studies show a causal connection between anthropogenic subsurface fluid injection and local seismicity (Healy *et al.*, 1968; Ellsworth, 2013). These activities, driven by continuing energy demands, have resulted in ongoing concern over induced and triggered earthquakes. Some of these activities include hydraulic fracture (Holland, 2013), waste-water disposal (Keranen *et al.*, 2014; McGarr *et al.*, 2015; Weingarten *et al.*, 2015; Schoenball *et al.*, 2018), geothermal energy (Majer *et al.*, 2007), CO_2 sequestration (Zoback and Gorelick, 2012), enhanced oil recovery (Gan and Frohlich, 2013), or even fluid withdrawal (Davies *et al.*, 2013; Willacy *et al.*, 2018), all of which may increase the risk for larger earthquakes.

In some cases, an effective stress change of smaller than 0.5 MPa was enough to cause seismic moment magnitude $M > 1$ earthquake, tens of kilometers away from the injector (Keranen *et al.*, 2014). Seismometers, however, cannot always detect the fault sliding as it sometimes proceeds aseismically (Guglielmi *et al.*, 2015), which will complicate the mitigation of potential risks. This necessitates the hydro-mechanical analysis of fault response to injections and fault stability conditions. In this report, I focus on hydraulic fracture effects; in particular, the mechanics of fluid-driven tensile hydraulic fracture and the dynamics of interaction between hydraulic fracture (HF) and pre-existing faults. The published HF-related seismic activities mainly focused on the delayed seismicity due to pore pressure raises upon diffusion of pressurized fracturing fluid [e.g., see Holland (2013)]; while, the dynamics, hence the concurrent propagation of hydraulic fracture and slip, during this intersection remain unknown. Understanding the dynamics may lead to a better understanding of this interaction. For example, the elastic coupling in addition to poroelasticity may lead to far-reaching induced seismic events (Goebel and Brodsky, 2018).

The HF-fault interaction is also crucial for the stimulation of unconventional resources; where the interaction between hydraulic fracture and local preexisting natural fractures (NF) are believed to determine the efficiency of the stimulation process by creating a connected fracture network (Maxwell *et al.*, 2002; Rutledge and Phillips, 2003; Gale *et al.*, 2007). Microseismics, in particular, has been essential in providing a better image of hydraulic fracture growth (Warpinski *et al.*, 2001). Moreover, the activation of poorly oriented (Zoback *et al.*, 2012) or gouge-filled (Mighani *et al.*, 2018b) natural fractures may also proceed a/subseismically. This again necessitates the study of underlying mechanics of this interaction, in addition to the seismic signatures. To maximize the productivity of a well, it is desirable to have the hydraulic fracture *cross* the natural fractures deep into the formation; otherwise, the fluid-driven tensile fracture would be blunted after short-circuiting the fluid by the permeable fault and be *arrested.* Numerous field scale numerical analyses have studied the influencing operational, *in-situ* and mechanical parameters on this interaction [e.g., see Dahi-Taleghani and Olson (2011); Weng *et al.* (2011); Sheibani (2013); Wang *et al.* (2019)], and the volumetric extent of stimulation [so-called stimulated reservoir volume (SRV)], during the propagation of a hydraulic fracture.

Laboratory experiments, in addition, provide the opportunity to isolate and study the mechanical, operational, and *in-situ* parameters on this interaction. Among the extensive literature in this subject are the studies on natural fracture cementation (Wang and Li, 2017; Fu *et al.*, 2018), material's tensile strength (Hanson *et al.*, 1980), fault's friction coefficient (Bunger *et al.*, 2015), differential stress and injection rate (Lockner and Byerlee, 1977), and stress regime (Zhou *et al.*, 2008). Hydraulic fracture experiments in rock/cement specimens with discontinuities also reveal the role of discontinuities on the complexity and tortuosity of the generated fracture network (Beugelsdijk *et al.*, 2000; Sharma *et al.*, 2013; Hou *et al.*, 2015; Damani *et al.*, 2018). Understanding the necessary conditions for activation of the natural fracture, the expected magnitude of slip and enhanced fluid transmissivity, and the impact of this slip on the hydraulic fracture path is a key to understanding the hydraulic fracture process.

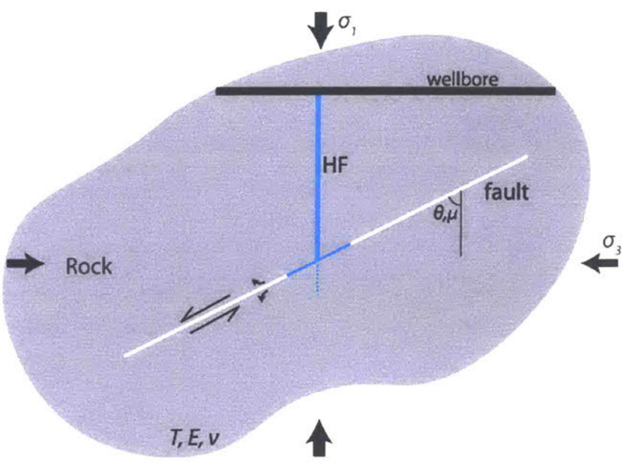

Figure 1-1. 2D geometry of a hydraulic fracture (HF) emanating from a borehole and approaching a pre-existing fault. The maximum and minimum far-field stresses are σ_1 and σ_2, respectively. Fault has an angle of θ from σ_1 and friction coefficient, μ. Depending on the conditions, the HF may cross, arrest on and/or activate the fault, resulting in shear/volumetric displacements. The pertinent rock properties are Young's modulus, *E,* Poisson's ratio, *v*, and tensile strength, *T*.

After the hydraulic fracture operations, the production rate in the formation usually declines (Patzek *et al.*, 2013), suggesting that there are time-dependent changes in the structure, mechanical, and transport properties of the rocks (Polak *et al.*, 2003; Kassis and Sondergeld, 2010). As production declines, subsidence may also occur (Chang *et al.*, 2014), and wellbore stability may be affected (Schoenball *et al.*, 2014). In some cases, the altered effective stresses may trigger induced seismicity (Davies *et al.*, 2013; Ellsworth, 2013). Poroelastic deformation is a possible source of time-dependent behavior, as shown for reservoir subsidence (Altmann *et al.*, 2010), wellbore stability (Ghassemi and Zhang, 2004), or induced seismicity (Segall and Lu, 2015); but inelastic creep within shales may also be important. For example, creep properties have been used to determine the evolution of *in-situ* stresses (Sone and Zoback, 2014; Yang *et al.*, 2015). Unfortunately, details concerning the physical mechanisms of creep and their controlling parameters are poorly constrained to make predictions of the mentioned phenomena.

Creep strain in rocks, when measured under a constant load, has often been described as consisting of three sequential regimes: transient (decelerating rate), secondary (constant rate), and tertiary (accelerating rate, leading to failure) (Scholz, 1968). This description is a generalization that depends on the active mechanisms and their kinetics, which vary for different rock types and for different conditions of differential stress (Kemeny, 1991; Geng *et al.*, 2018), pore-fluid chemistry (Chester *et al.*, 2007), confining stresses, temperature (Brantut *et al.*, 2013; Geng *et al.*, 2018), and test duration. Thus, all three regimes may not be observed in a given set of tests. A range of mechanisms may drive creep in rocks such as subcritical crack growth (Kemeny, 1991; Chester *et al.*, 2007; Brantut *et al.*, 2012a; Brantut *et al.*, 2013; Brantut *et al.*, 2014a; Heap *et al.*, 2015), pressure solution (Brantut *et al.*, 2012a; Geng *et al.*, 2018), and particle rearrangement (Hartley and Behringer, 2003; Vandamme and Ulm, 2009).

The creep stress levels are generally compared with the ultimate failure stress (differential stress peak), *FS*, typically determined at fast constant strain rates of $\dot{\varepsilon}>10^{-6}$ (Kirby, 1980; Lockner, 1995; Paterson and Wong, 2005; Sarout *et al.*, 2014; Dewhurst *et al.*, 2015). During low-pressure, low-temperature creep tests on hard rocks like granite, transient dilational creep is generally observed at differential stresses exceeding 70% of the rock's *FS* (Scholz and Kranz, 1974; Sano *et al.*, 1982; Kemeny, 1991; Lockner, 1993b; Heap *et al.*, 2009b) and sometimes leads to tertiary creep and failure. For these rocks, creep strains are generally small when the stress is lower than 50% of the *FS* (Parsons and Hedley, 1966). For such rock types, the transient phase is usually followed by secondary creep, although primary creep was sometimes immediately succeeded by accelerating dilatant (tertiary) behavior (Heap *et al.*, 2009b). Some creep tests on sandstones (Heap *et al.*, 2009b; Brantut *et al.*, 2013), shales (Rybacki *et al.*, 2017), and clayey rocks (Fabre and Pellet, 2006) show secondary creep regime (~60 minutes, ~30 minutes, and ~200 days, respectively); secondary creep rates are better observed in soils and unconsolidated sands [see e.g., Enomoto *et al.* (2015)]. Yet, it could be argued that secondary creep simply represents a transition from primary to tertiary regimes (Lockner, 1993b; Heap *et al.*, 2009b). For example, primary creep in dense rocks has been attributed to subcritical crack growth, a mechanism that does not lead to a significant stage of secondary creep (Kemeny, 1991). However, the applicability of such brittle descriptions during compactional creep is still subject to question.

Unlike stiff, well-indurated rocks, shales show measurable creep strains, even at low fractions of the *FS* (Parsons and Hedley, 1966). Among the parameters influencing creep response in shales are confining pressure (Rybacki *et al.*, 2017), differential stress (Ghassemi and Suarez-Rivera, 2012; Li and Ghassemi, 2012; Sone and Zoback, 2013b), temperature (Geng *et al.*, 2017, 2018), rock anisotropy (Sone and Zoback, 2013b), and shale composition (Sone and Zoback, 2013b). Transient creep under triaxial loading may involve compaction (Villamor Lora and Ghazanfari, 2015), but, in some cases, high differential stresses can also activate dilational processes (Heap *et al.*, 2015), which may lead to tertiary creep (Ghassemi and Suarez-Rivera, 2012; Geng *et al.*, 2017; Nicolas *et al.*, 2017; Rybacki *et al.*, 2017).

Shales are usually both heterogeneous and anisotropic. Heterogeneities at the grain scale originate from mineral inclusions (Boulenouar *et al.*, 2017), soft organic matter (Kumar *et al.*, 2012; Shukla *et al.*, 2013; Zargari *et al.*, 2013; Mighani *et al.*, 2015b; Wilkinson *et al.*, 2015; Abedi *et al.*, 2016b; Slim, 2016), and pores and other defects (Sarout and Guéguen, 2008; Sondergeld *et al.*, 2010); heterogeneities also exist at larger spatial scales (Abedi *et al.*, 2016a). Nanoindentation, coupled with chemical analyses of the indented spots, provides a detailed image of such heterogeneities and give insight into the length-scale of the mechanical anisotropy and a potential representative elementary volume (REV). In addition, the averaged parameters from nanoindentation measurements might be used to constrain macro-scale mechanical properties; some studies suggest that Young's moduli measured during nanoindentation are comparable to those obtained in inch-sized shale samples (Kumar *et al.*, 2012).

1.2 Thesis outline

During the five chapters of this thesis, I touch on some of the complexities involved in HF mechanics and address these issues from a laboratory perspective. The thesis chapters are self-standing, and, hence, each chapter contains sections with the detailed background of the problem, the background literature, conclusions and remarks, and future directions.

Chapter 2 discusses the dynamics when an HF intersects a saw-cut fault. It examines the AE events that are generated, as well as the evolution of fault slip and pore pressure response. Chapter 2 originally had a much larger extent, as the work on HF experiments has been further extended to consider scaling of HF experiments to field operations and the fracturing fluid properties. However, those analyses are incomplete and need more development before being published.

Chapter 3 describes the creep behavior of shale rocks at the nanoindentation scale. I provide a framework to obtain upscaled mechanical properties from the nanoindentation to triaxial creep properties. The discussion revolves around the fact that the primary creep strains in both nanoindentation and triaxial scales increase with the logarithm of time.

Chapter 4 describes the rock-fluid interactions at the nanoindentation scale. It describes how the fluid might chemically and physically interact with rock and manifest in the elastic, creep, and strength properties of rocks.

Chapter 5 provides a summary of the results and suggests further work.

Chapter 2: Interaction between hydraulic fracture and saw-cut fault

David Lockner, Brian Kilgore, Carolyn Morrow, Farrokh Sheibani, and Brian Evans contributed to this chapter.

Abstract

In this chapter, I have studied the interaction between a hydraulic fracture and a polished saw-cut fault. During the experiments, a hydraulic fracture initiated from a pressurized axial borehole (using water and approached a dry fault that was inclined at an angle θ with respect to the borehole axis. Samples were prepared from Poly(methyl) Meta Acrylate (PMMA) and Solnhofen limestone, a finely grained (<5 μm grain), low permeability (<10 nD) carbonate. The confining pressure in all experiments was 5 MPa, while the differential stress (1-80 MPa) and approach angle, θ (30, 45, 60, 90°) were experimental variables. During the hydraulic fracture, acoustic emissions (AE), slip velocity, slip magnitude, stress drop and pore pressure were recorded at a 5 MHz sampling rate. I measured piston velocity using a Doppler laser vibrometer mounted outside the pressure vessel. From these measurements, I inferred fault slip duration. A strain gauge adjacent to the saw-cut provided a near-field measure of axial stress. Below, I discuss three different topics: 1.) the interaction on a stably sliding fault (Solnhofen limestone) vs. a fault with stick-slip characteristics (PMMA); 2.) The role of fault gouge on the interaction; and 3.) the role of fault surface roughness on the frictional and flow characteristics of faults and the impact on the fracture/ fault interaction.

2.1 Interaction in Solnhofen limestone vs. PMMA

2.1.1 Background

Several experimental works have been performed to approach this problem. Hanson *et al.* (1980) conducted HF experiments on bonded faults (using Chloroform) in cubic blocks of Nugget sandstone, Indiana limestone, and PMMA. The HF never crossed PMMA interface even at 13.8 MPa normal stress, while it could cross the bonded fault for Indiana limestone and Nugget sandstone. For un-bonded faults in Indiana limestone, the HF could cross the smooth interface at normal stresses higher than 9.2 MPa (the experiments were in an unconfined condition). The required normal stress for HF to cross the Nugget sandstone fault was 6.9 MPa. In an additional experiment on the sandstone, by roughening the fault surface, the HF could cross the interface at 4.6 MPa. The authors did not report the surface roughness or the fault surface's coefficient of friction. They also bonded blocks with different materials. The HF could cross from PMMA to limestone and from Nugget sandstone to limestone but not the other way around. In a later study on Indiana limestone blocks and similar experimental configuration, Thorpe *et al.* (1982) studied the so-called "step-cracks". By inserting a strip of lubricant 0.75 inches wide, they observed the HF to pass along this reduced friction section and then cross the interface with an offset. Step cracks have been observed in mine-back experiments by Warpinski *et al.* (1982) in tuff at Nevada Test Site and observed in experiments on limestone and gypsum in which a wedged tensile fracture approached an inclined fault (Goldstein and Osipenko, 2015). Hydraulic fracture on blocks of Wondabyne sandstone also revealed a step-crack of 10-15 mm at an approach angle of 30^0 (Bunger *et al.*, 2015).

Using continuum mechanics, several analytical cross/arrest criteria have also been developed. Blanton (1986) analyzed the interaction problem by considering the competition between the material's tensile strength and sliding of a Coulomb-type frictional interface. He compared his proposed criterion to results from experiments on blocks of Devonian shale and hydrostone at various fault orientation angles of 30, 45, 60, and 90 degrees. The main outcome of this analysis was that an asymptotic fault angle exists below which the hydraulic fracture does not cross the fault. This angle depends on static coefficient of friction, μ, along the fault. Renshaw and Pollard (1995) presented a theoretical criterion for the crossing of a tensile fracture through an orthogonal frictional interface. They considered the competition between the stress intensity singularity at the tensile fracture tip and shear stresses along the interface. Similar to the Blanton model, the interface in their model followed a simple linear friction law, i.e., $\tau = \mu\sigma_n$. The Renshaw and Pollard (1995) criterion has further been extended to consider the non-orthogonal interfaces (Gu *et al.*, 2012) and the cohesive strength of the interface (Sarmadivaleh and Rasouli, 2014). This problem has also been approached numerically by various authors; see Wang *et al.* (2017), Taheri-Shakib *et al.* (2016), Chen *et al.* (2017) for reviews of some of the recent numerical works.

However, some experimental observations contradict these model criteria. One example is seen in the experiments of Bunger *et al.* (2015) where HF crossed a fault with 15^0 orientations. It seems likely that fault failure during fluid injection cannot be modeled by a simple linear friction law over the entire interface. Instead, the pore fluid diffusion inside the fault during post-slip sliding might play a crucial role, which is yet to be understood. The fault constitutive behavior, i.e., its stable/unstable sliding mode, could also be quite important. In addition, fault slip before HF intersection could change the direction of HF propagation. In this report, I investigated the interaction between an approaching HF and an inclined fault in triaxial stress conditions. First, I measured the coefficient of friction by sliding experiments and then performed hydraulic fracture experiments on samples containing both a borehole and an inclined fault. Data on acoustic emissions, pore pressure, and stresses were acquired at high rates in order to study dynamic processes during interactions of the HF and fault. Finally, the observations are compared to existing crossing criteria and the limitations and contradictions are discussed.

2.1.2 Experimental procedure

The heterogeneous nature of shale gas rocks is well known to the rock mechanics experimentalists. Therefore, having a multitude of shale samples with identical properties for parametric lab studies is quite impossible, even withstanding the difficulties in obtaining a set of solid shale sample with specific dimensions needed for lab tests. As an alternative, I selected a homogenous rock that would represent a reasonable analog for shale rocks. An analog rock needs a low Young's modulus, i.e., 20-40 GPa (Mighani *et al.*, 2015b), should have a grain size <10 μm, and permeability < 100 nD (Tinni *et al.*, 2012). Solnhofen limestone is fine-grained (<5 μm), has low permeability (<10 nD) carbonate, and has Young's modulus = 41 GPa and Poisson's ratio = 0.28. Thus, this rock was a natural candidate. PMMA is not an analog for nature shales, but it provides homogeneity at very small scales; also, the transparency of PMMA allows observations the HF geometry.

Cylindrical samples of PMMA and Solnhofen limestone were prepared and the end surfaces were ground parallel. The cylinders have a diameter of 1.5 inches and a length between 2.7 and 2.9 inches. Faults with specified orientations were then saw cut and the fault surfaces were finely polished with P1000 sandpaper. This resulted in measured root mean square (rms) surface roughness of ~1 μm (see Appendix S1). The fault orientations include 30, 45, 60, and 90 degrees with respect to the vertical axis (see Figure 2-1). A blind borehole with a diameter of 2.92 mm was then drilled into the top sample half. The bottom of the borehole in all samples was 6 mm vertical distance from the fault surface as shown schematically in Figure 2-1 along with other sample dimensions. Four piezoelectric transducers were mounted on the sample. Two transducers were mounted (attached using conductive epoxy) inside the top and bottom spacers. The two radial transducers were mounted (using conductive epoxy) on bronze posts diametrically opposite to each other; one face of the bronze piece is machined to a radius of curvature of 0.75 inches in order to conform to the sample surface. The bronze posts are epoxied in holes in the polyurethane jacket. Therefore, confining pressure forces the posts directly against the sample surface, providing mechanical coupling between the transducer and sample. The piezoelectric ceramics are p-wave type transducers with resonant frequency of 1.5 MHz. The AE transducers are calibrated with respect to the moment magnitude of ball drop AE events. The procedure is explained in details in Appendix S4. One vertical strain gauge is also mounted on the surface of the bottom half of sample (foot-wall) below the fault surface to record the temporal vertical strain variations. A pore pressure transducer outside of the pressure vessel records the pressure in the borehole. The frequency response of the pore pressure transducer, evaluated in Appendix S5, acts as a low-pass filter at 1.4 kHz. A Doppler laser vibrometer that is focused on the load point records the vertical motions of the system's piston and captures the displacement/velocity. The vibrometer is calibrated by the manufacturer (Polytec Inc.) with a signal output in mm/s/V. The experimental data is recorded independently on two different systems. The mechanical data including the confining pressure, axial stress, pore volume, and vertical displacement is recorded with a sampling rate of 1 Hz. The piezoelectric sensors, strain gauge, pore pressure transducer, and laser vibrometer response is recorded using a TraNET EPC-32 acquisition system (Elsys Inc.) with trigger-based sampling rate of 5 MHz. The acquisitions are conducted in a specific mode developed by Elsys Inc., referred to as ECR mode. In this mode, the data are acquired and streamed to disk with no dead-time which is a major drawback in typical trigger-based acquisition systems. Therefore, it ensures no data loss at the 5 MHz sampling rate. The acoustic emission (AE) response is preamplified by either 30 or 54 dB preamplifiers; the strain gauge and pressure transducer response were input into a signal conditioner (gain×100 and excitation voltage 2V) before the acquisition.

The pore pressure transducer records the pore pressure 17 inches away from the borehole. The laser vibrometer also records the load point motion velocity outside of the vessel, 16 inches away from the sample. In order to synchronize these measurements with acoustic emission and axial stresses from strain gauge, the pore pressure and vibrometer velocity readings were time-shifted considering the travel time for compressional wave in water line and steel parts by 288 and 71 μsec, respectively.

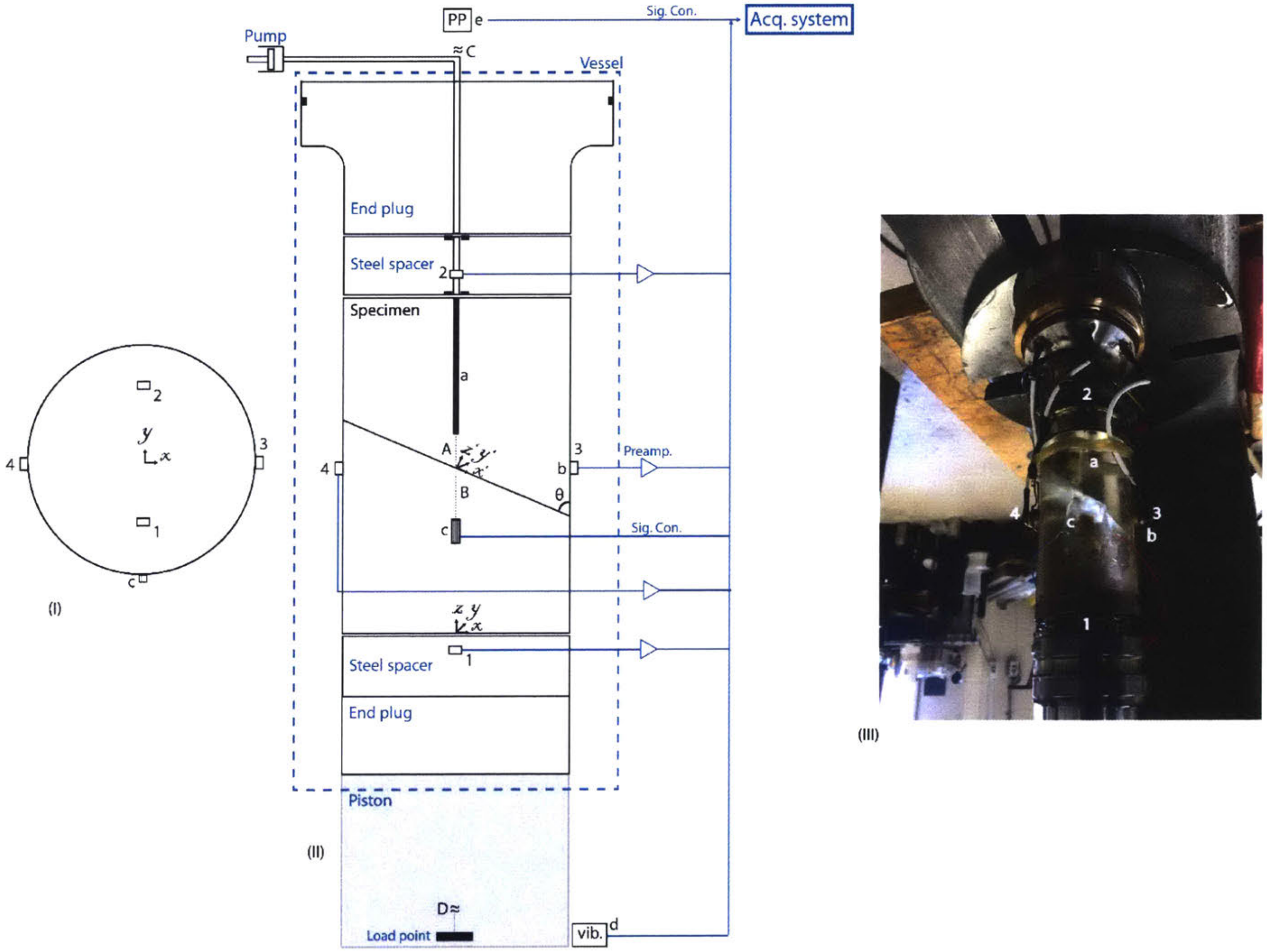

Figure 2-1. Schematic (I and II) and real picture (III) for the geometry of sample and sensors during the experiments. Note that the schematic is not drawn in scale. (a) is a blind borehole drilled in the top half of sample close to a fault with orientation of θ. Two coordinate systems are shown with their origins as xyz and x'y'z'; x'y'z' is obtained by clockwise rotation of xyx wrt to y axis by 90-θ. (b) is the AE transducer and numbers correspond to the transducer number. (c) is the strain gauge mounted on the sample surface and measuring the vertical stress. (d) is the Doppler laser vibrometer measuring piston's vertical velocity at the load point. (e) is the pore pressure transducer measuring the borehole pressure. (A) is the vertical distance between borehole bottom

and fault which is always 6 mm. (B) is the vertical distance between strain gauge center and fault which is always 0.6 inches. (C) is the distance between pore pressure transducer and borehole bottom which is 17 inches. (D) is the distance between load point and sample which is 16 inches. The AE signal is fed to a preamplifier, the pore pressure and strain gauge are fed to a signal conditioner. The vibrometer which is calibrated by provider company has a signal output of mm/s/V. The whole dynamic data is then acquired by the acquisition system.

The confining pressure in all experiments is maintained at a constant value of 5 MPa. I conducted two separate types of experiments. In ***sliding experiments***, a constant axial shortening rate of 2 µm/sec was applied. This led to relative sliding on the fault surface in the sample. The axial stress during the experiment was corrected for the contact area losses during the fault sliding (Tembe *et al.*, 2010). For the triaxial stress conditions with σ_1 and σ_3 as the maximum and minimum *in-situ* stresses, the resolved shear (τ) and normal (σ_n) stresses on a fault plane with orientation of θ with respect to the maximum stress are obtained as:

$$\tau = 0.5\,(\sigma_1 - \sigma_3) sin(2\theta) \tag{1}$$

$$\sigma_n = \sigma_3 + 0.5\,(\sigma_1 - \sigma_3)(1 - cos(2\theta)) \tag{2}$$

The resolved shear and normal stresses on the fault plane can then be calculated and the apparent coefficient of friction (or $\mu^{apparent}$, in the measurements referred to as μ) is obtained as the ratio of maximum shear stress over normal stress for a certain fault angle (Lockner *et al.*, 2017). The vibrometer velocity reading is useful in inferring the fault slip velocity and the duration of the stick-slip events. The total fault parallel slip can be estimated using two independent ways: 1- integrating the area under the load point velocity record for the slip event duration time ($d=\int v.dt$). 2- provided that the fault slip is large enough to be detected by DCDT, we estimate the fault parallel slip based on the load point axial displacement reading, x_{lp}, (DCDT transducer) and correct for the shortening of the load column (Lockner *et al.*, 2017):

$$d = \frac{x_{lp} - \tau/k_{lp}}{cos(\theta)} \tag{3}$$

with τ being the shear stress resolved on the fault plane with orientation θ relative to the vertical axis (see Figure 2-1). k_{lp} is the system stiffness which is measured to be 49 MPa/mm for the bare surface fault in Solnhofen limestone. For more explanation on the system stiffness refer to Lockner *et al.* (2017). I determined the system stiffness only for the bare surface fault.

In the second type, ***hydraulic fracture***, the axial stress was increased by advancing the piston and then locking it in place when the desired stress was achieved. Throughout this report, I use the "differential stress" term which refers to the difference between the maximum (σ_1) and minimum (σ_3) *in-situ* stresses. The pore pressure (resulting in local changes in σ_3) inside the borehole was then raised by injecting deionized water under constant injection rate of 2.6 cm^3/min. After a critical pore pressure, i.e. breakdown pressure (*BP*), the hydraulic fracture initiated and propagated towards the fault.

2.1.3 Results

2.1.3.1 Sliding Experiments

During the sliding of fault surfaces under constant axial shortening rate, either stable or unstable sliding (stick-slip) can occur. The stable/unstable sliding between bare fault surfaces is governed by the rock type and its saturation state, strain rate, normal stress, and the loading machine stiffness which contributes to this instability (Byerlee and Brace, 1968). Prior to HF experiments, the oriented fault surfaces ($\theta < 90$) were briefly slid (less than 1 mm slip along the fault) and the sliding was recorded as explained in the previous section. The maximum slip velocity and total slip were estimated from load point velocity and slip duration ($d = \int v.dt$). The moment magnitude of the event was estimated from AE signals. The stress drop after sliding is derived from strain gauge stress readings. Table 2-1 shows the experimental conditions for the sliding experiments. As a standard in reporting the coefficient of friction, I adapted the following procedure: for stable sliding, the coefficient of friction, μ, is reported at the axial shortening displacement of 0.2 mm. For stick-slip sliding, μ is obtained by averaging the first three peaks for stick-slip events. Again, all these experiments were conducted under a constant axial shortening rate of 2 μm/sec.

Table 2-1. The experimental conditions and obtained parameters for sliding experiments. The μ for PMMA experiments with stick-slip behavior is reported by averaging 3 events. The μ for Solnhofen limestone with stable sliding is reported by its value at 0.2 mm axial shortening. For experiment names, PM stands for PMMA. SH stands for Solnhofen limestone. The number corresponds to the fault orientation. Note that the confining pressure was constant and equal to 5 MPa for these experiments. The axial shortening rate was also 2 μm/sec. SD stands for stress drop.

Experiment name	μ	Maximum slip velocity, mm/s	Slip duration, μs	Inferred slip, μm	SD, MPa	M
PM30	0.30±0.03	84.0	123	5.39	2.2	-5.69
PM45	0.30±0.02	72.6	114	4.69	2.1	-
PM60	0.24±0.02	-	-	-	2.2	-
SH30	0.12	NA	NA	NA	NA	NA
SH45	0.21	NA	NA	NA	NA	NA
SH60	0.11	NA	NA	NA	NA	NA

The sliding in PMMA was associated with stick-slip events. The slip velocity during stick-slip events in PMMA reached values of ~0.1 m/s for a duration of ~0.1 msec (see Table 2-1). The slip velocity and total slip decreased at increased fault orientation angles. The stress drop also reached values of ~2 MPa, which is more than 60% of axial pre-peak differential stress. During the sliding in Solnhofen limestone no slip velocity or stress drop was registered and sliding was stable. Figure 2-2 shows the evolution of μ during a sliding experiment in PMMA and limestone samples for a 30^0 fault orientation. The variation of (measured apparent) μ with respect to the fault orientation is also summarized in Figure 2-2. The apparent coefficient of friction for both PMMA and Solnhofen limestone tends to slightly reduce as the fault angle approaches 60^0 and becomes less steep. The reduction in μ at less steep fault angles has also been previously observed by Savage *et al.* (1996) in granite samples. The saw-cut faults in granite samples showed a maximum μ at about $20\text{-}30^0$ and a reduction from 0.78 to 0.62 for their largest tested fault angle, i.e., 50^0. The coefficient of friction values in Slate by Donath *et al.* (1972) also showed a slight reduction (0.03) by changing the fault orientation from 30^0 to 45^0. It is also worth mentioning that the PMMA μ values in the experiments are significantly lower than the values reported by Dieterich and Kilgore (1994). The PMMA fault surfaces in Dieterich and Kilgore (1994) with μ=0.75 with normal stress of 2.5 MPa had a surface finish of #60 grit size (3.89 μm roughness in Appendix S1) compared to the finely-polished and smooth fault surfaces (The fault surfaces are shiny with a surface roughness of ~1 μ in Appendix S1). The PMMA fault in (McLaskey, 2011) with a surface finish of #600 grit size measured μ=0.57. The measured coefficient of friction for limestone in this report is also much lower compared with Donath *et al.* (1972) reported values of 0.72. The limestone fault with an inclination of 26^0 in Donath *et al.* (1972) was created after triaxial failure of the intact material in which higher surface roughness is expected compared to the finely polished surfaces in this report. One possible explanation is that the coefficient of friction is sensitive to the surface roughness and is much less for these polished surfaces.

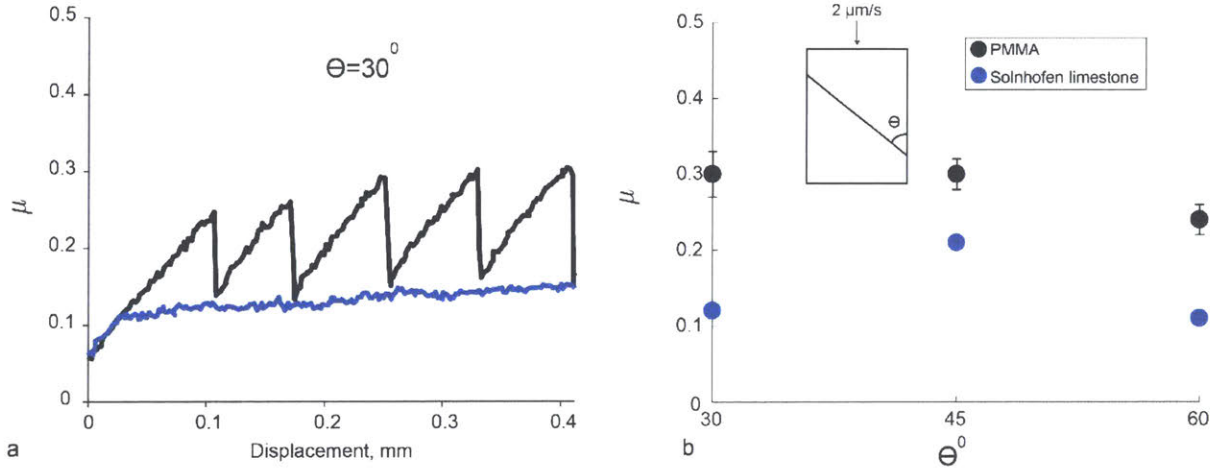

Figure 2-2. (a) Two examples of sliding experiments in Solnhofen limestone and PMMA with a 30^0 fault angle. The fault surfaces are finely polished (rms roughness=1.07 μm). The fault in Solnhofen slides stably, while in PMMA it slides with stick-slip events. (b) variation of the apparent coefficient of friction (for a definition, see the text) with respect to the fault orientation. The 60^0 fault has the lowest μ.

Figure 2-3 shows an example for AEs during a stick-slip event for a 30^0 PMMA fault. The stick-slip event generates AE signals and is associated with a partial post-slip stress drop. The moment magnitude of the AE event was estimated using calibration from a ball drop experiment (see Appendix S4). In this experiment, the AE signal was preamplified by 30 dB, unlike all other experiments and ball drop tests in the Appendix (which had a preamplification of 54 dB). So, the entire slip event could be captured by AE transducers; while the slip event in other experiments was clipped (went off-scale).

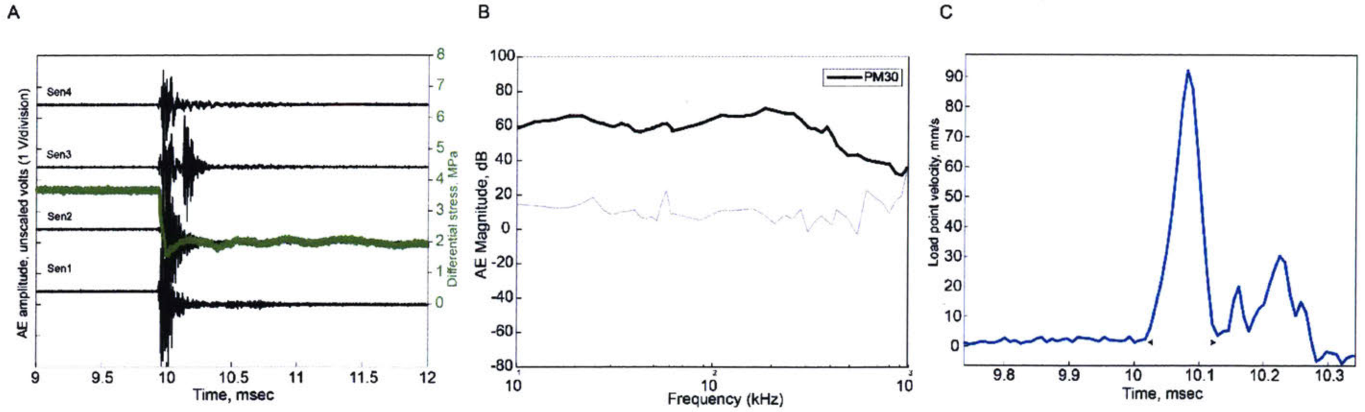

Figure 2-3. (a) The AE events and stress drops from piezoelectric transducers and strain gauge readings during a stick-slip event in PMMA sample with 30^0 fault orientation (PM30). The position of AE sensors and strain gauge is described in Figure 2-1. (b) The AE event spectrum averaged over 4 sensors. I use a ball-drop experiment (see Appendix S4) to estimate the moment magnitude, M, of the stick-slip event. Note that the pre-amplification for this event (30 dB) is different from ball drop and all other experiments, which had pre-amplification of 54 dB. Therefore, the AE signals do not go off-scale like the slip events in Figure 2-4. The gray line also shows the background noise spectrum. Notice the good signal-to-noise ratio for a wide frequency band. Local peaks observed in the signal spectrum coincide with the noise spectrum (c) Doppler laser vibrometer velocity response for a PM30, but a different event than (a). The slip event duration is 116 μs as shown by the double-sided arrow. The total slip along the fault is considered as the area under this curve for the slip duration divided by cos(θ).

The time window for deriving the signal spectrum is selected so that the entire event is captured. Based on trial in these stick-slip experiments, a 2 ms time window is long enough to represent the event with the middle of the time window at the signal peak amplitude. The laser vibrometer velocity recording is also shown for a stick-slip event. Once again, the vibrometer reads the vertical motion of the piston at the load point outside the pressure vessel, far from the sample. However, it is useful to derive the slip duration [similar to Lockner *et al.* (2017)] and total slip along the fault.

2.1.3.2 Hydraulic fracture experiments

The pressurized fluid inside the borehole results in initiation of a hydraulic fracture at the borehole wall. It is generally thought that the hydraulic fracture initiates as a tensile mode fracture (Haimson and Fairhurst, 1969; Detournay and Cheng, 1992). Further propagation of HF under either Mode

I or mixed I and II modes depends on the local stresses and discontinuities in the rock (Hanson *et al.*, 1980). The experiments in this section evaluate the propagation of the HF and its approach to a neighboring fault. Figure 2-4 illustrates an example for the recorded events during a hydraulic fracture experiment in PMMA with a 30^0 fault. Water was injected at a constant rate of 2.6 cm^3/min. The slip on the fault was detected independently by vibrometer, strain gauge, and acoustic emission signals. Slip resulted in an abrupt change in vibrometer velocity, significant acoustic signals that go off-scale and are clipped, and a partial stress drop. The abrupt drop in pore pressure is associated in time with the slip on the fault. The pore pressure then drops to the confining pressure possibly indicating that the pore fluid has reached the sample jacket. The AE transducers also record a series of events some 100's μsec before the major slip (Figure 2-4b). These are HF initiation and propagation events detected as AEs before the HF intersects the fault. To obtain the moment magnitude of HF events, I consider only the initiation events; I select a time-window equal to twice that of the rise time of the initiation. The center of this window is at the peak amplitude (see green arrow in Figure 2-4 which shows the time of HF initiation). Therefore, in PMMA the hydraulic fracture created a significant slip event after intersecting the fault.

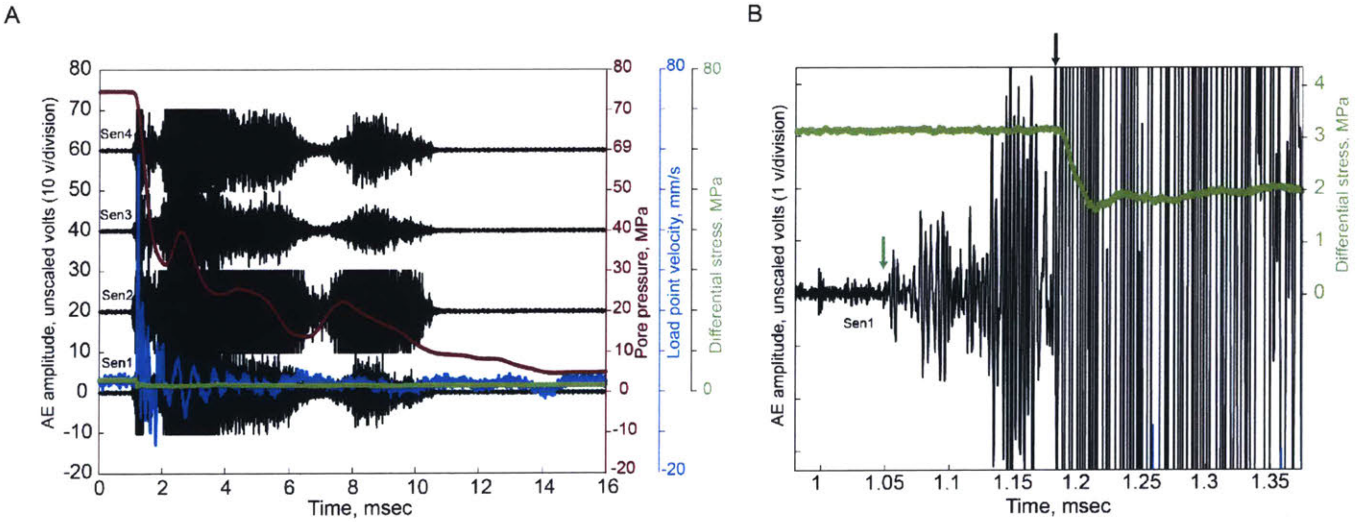

Figure 2-4. High acquisition rate recordings during a hydraulic fracture experiment in a PMMA sample with a 30^0 fault (PM30-3 in Table 2-2). (a) the AE, stress, and pore pressure readings. The fault slip event after HF intersection is expressed as a burst in AE signals, stress drop, and abrupt decrease in pore pressure. Note that the pore pressure and vibrometer readings are time-shifted

based on the time delay for a stress wave to travel from the sample to the detection point on the piston (for piston motion) and for a pressure change at the HF to register at the transducer (for pore pressure). (b) magnified view of AE signal in one of the transducers (Sen1) and differential stress drop. AE sensors detect HF initiation signals (green arrow) about 130 μsec prior to the slip event (black arrow).

The hydraulic fracture was also arrested at fault orientations of 45^0 and 60^0 and 90^0 and resulted in either sliding or opening of the fault. The AE transducers can, in fact, detect HF events prior to the fault slip. With certain assumptions, I can estimate the HF propagation velocity before intersecting the fault: HF initiates at the borehole bottom which, in all cases, is 6 mm away from the fault surface along the vertical axis. The HF travels vertically towards the fault; this hypothesis is supported by the fact that the breakdown pressure is significantly influenced by the differential stress. Therefore, the axial stress is the direction of HF propagation (Haimson and Fairhurst, 1969). The average propagation velocity of HF in the PMMA experiment is 44 m/sec.

Figure 2-5 shows an example for a hydraulic fracture experiment in Solnhofen limestone. Similar to PMMA experiments, the intersection of HF and fault here is also associated with AE signal burst, pore pressure drop, slip velocity increase, and stress drop. The AE burst during the fault slip, on the other hand, is not as noisy as in the case of PMMA. Also, the post-slip stress drop is not as significant as for PMMA. The HF was able to cross the fault with subtle fault sliding with a slip velocity of 0.5 mm/sec. The HF propagation velocity based on AE events was 12.6 m/sec.

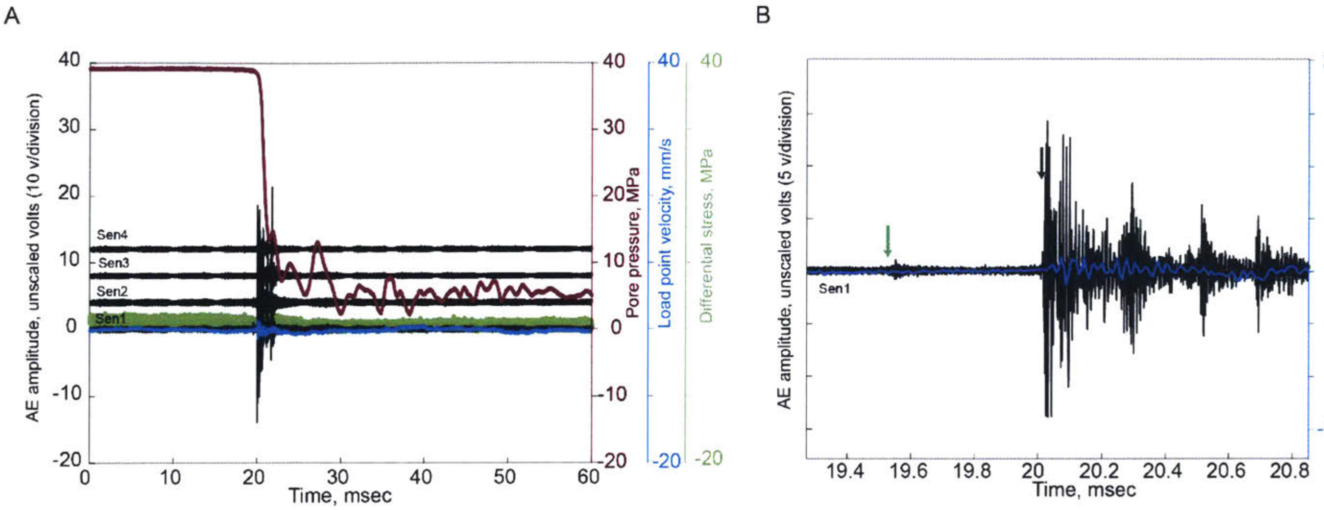

Figure 2-5. Hydraulic fracture experiment in a Solnhofen limestone sample with a 30^0 fault (SH30-1 in Table 2-2). For explanation of sensor responses refer to Figure 2-4 caption. The fault slip is associated with a burst in AE (black arrow) and a small jump in slip velocity. Again, here we observe a small HF event (green arrow) initiating prior to the slip indicated by the large burst in AE activity (black arrow). We use the time difference between these two markers to estimate the HF average propagation velocity before intersecting the fault, in this case, 12.6 m/s. Note the less noisy AE, smaller slip velocity, shorter slip duration, and smaller stress drop compared to Figure 2-4.

The HF was able to propagate across the fault at orientations of 30^0, 45^0, and 90^0, with an exception at 60^0. The experiments are summarized in Table 2-2. The variation of breakdown pressure and HF crossing/arrest is also plotted in Figure 2-6. The HF in PMMA was arrested by the fault at all orientations and differential stresses. The experimental studies by (Hanson *et al.*, 1980) on PMMA-PMMA interface blocks with differential stresses of 14 MPa have resulted in the same conclusion. These observations have important constraints for models of hydraulic fracture/fault interactions: the crossed Mode I fracture is not a simple continuation of the initial HF, but needs to be re-initiated at the other side of the interface.

For the triaxial stress conditions with the maximum vertical stress, in the absence of a fault, the hydraulic fracture preferentially initiates along the borehole axis, with no preference in azimuth. In these experiments, the presence of the fault seems to impose a preferred azimuth for HF, i.e., normal to the fault strike or parallel to dip (see Figure 2-6). The breakdown pressure value for both

PMMA and Solnhofen limestone has a peak at 30^0. In contrast to PMMA, HF was able to cross the fault at almost all fault orientations and differential stresses. The Brazilian test measurements and hydraulic fracturing experiments give a tensile strength of 16 MPa for Solnhofen limestone (Mighani *et al.*, 2015a), a value consistent with results from a HF experiment in a sample with only a borehole. A tensile strength of 58 MPa for PMMA is inferred from the breakdown pressure in the hydraulic fracture experiment.

The HFs in the experiments have propagation velocities on the order of 10's of m/s (see Table 2-2), much faster than the velocities measured in some other tests. For example, (Lockner and Byerlee, 1977) measured velocities of 0.5 mm/sec in Weber sandstone for slow injection rates of 0.02 cm^3/min. The very low permeability in Solnhofen and PMMA can explain this difference. Depending on the relative magnitude of rock matrix diffusivity and the fluid injection rate, diffusion of the fluid into the region surrounding a fracture can decrease the local effective stress, aid the tensile fracture, reduce the breakdown pressure and increase the speed of the mode I fracture (Detournay and Cheng, 1992)

Table 2-2. Experimental conditions for hydraulic fracture experiments. The experiment's name is adapted as material (PM for PMMA and SH for Solnhofen)-fault angle (degrees)-differential stress (MPa). DS: Differential stress prior to HF. BP: Breakdown pressure. SD, Stress drop. All tests were run at a constant confining pressure of 5 MPa.

Experiment Name	DS, MPa	BP, MPa	HF velocity, m/s	Slip velocity, mm/s	Slip Duration, μs	Slip, μm	SD, MPa	Interaction
PM30-3	3	76	44.1	59.0	121	3.51	1.4	Arrest
PM45-3	3	69	36.8	39.1	165	2.56	1.2	Arrest
PM45-5	5	71	35.3	48.7	116	2.98	1.4	Arrest
PM60-3	3	81	14.9	8.1	112	1.09	1.2	Arrest
PM90-3	3	66	59.9	-	-	-	0.2	Arrest
PM90-70	70	43	10.5	-	-	-	0	Arrest
SH30-1	1	39	12.6	0.5	29.9	0.01	0.5	Cross
SH45-1	1	27	8.8	0.5	34.4	0.02	0	Cross
SH60-1	1	28	39.1	0.3	37.4	0.02	0	Arrest
SH90-1	1	27	10.7	-	-	-	0	Cross

SH90-30	30	29	7.4	-	-	-	0	Cross

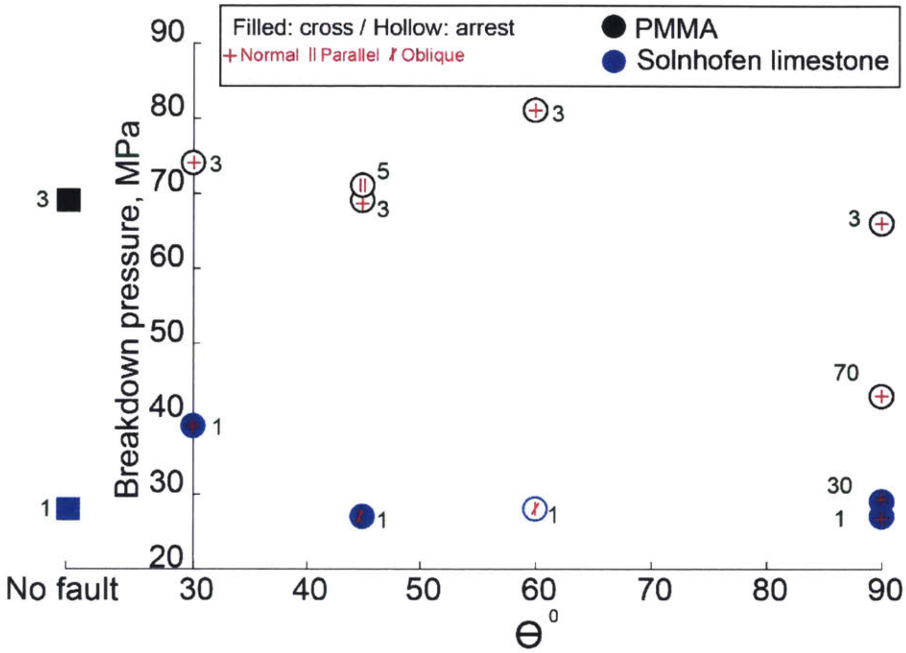

Figure 2-6. Variation of breakdown pressure as a function of fault orientation for PMMA and Solnhofen limestone. The breakdown pressure value for an intact sample with no fault is also shown for comparison. In addition to breakdown pressures, the crossing/arrest and HF azimuth wrt fault azimuth are also shown. The breakdown pressure for both PMMA and Solnhofen shows a peak at 30^0. However, this peak could be within the experimental variations in breakdown pressure values.

The ability of HF to cross the fault in Solnhofen with $\mu=0.12$, but to be arrested by the fault in PMMA where $\mu=0.3$ might be unexpected. I will discuss this in the remainder of this section. Figure 2-2 showed the differences in the sliding behavior of faults in Solnhofen limestone compared with PMMA. The fault sliding in PMMA was associated with stick-slip events with significant slip velocity (from vibrometer). In addition to significant stress drop, there was a transient weakening, about 40 μsec, before reaching a steady post-slip stress level (see Figure 2-4 and Figure 2-5). This is observed in both dry sliding and HF experiments in PMMA. The slip in Solnhofen, on the other hand, is stable during sliding experiments. During HF, a subtle fault sliding occurred with 120 times slower slip velocity. No transient weakening was observed during Solnhofen sliding. I analyze the pore pressure drop to study its decline after the slip occurrence.

The pore pressure decline was associated with the fault slip and not the initiation of HF (see Figure 2-4). The analysis of the HF propagation regime also confirms this observation (Bunger *et al.*, 2015). Based on the experimental parameters, the HF propagates in the toughness-dominated regime where the fluid front and the fracture tip coincide; therefore, we do not expect pressure drops during the HF propagation (Toughness-dominated regime). Figure 2-7 compares the pore pressure drops in all experiments. The pore pressure uniformly declines until the fluid front reaches the jacket. After reaching the jacket, it is associated with a back-pressure which results in a jump in pressure response. we can then determine the fluid travel time to reach the fault boundary from this pressure spike (see Figure 2-7 and Table 2-3).

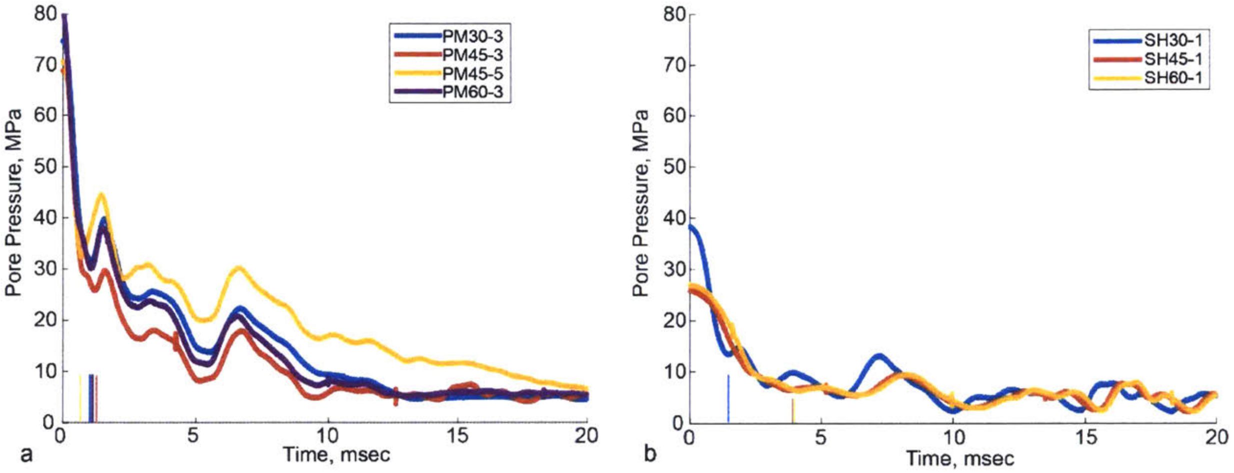

Figure 2-7. Pore pressure decline in the fault after its intersection with HF in PMMA (a) and Solnhofen limestone (b). The timing of fluid front reaching the fault boundary (diffusion time) is determined on the x axis from the pressure spikes. The diffusion time for limestone fault is generally slower than the PMMA fault.

The transient diffusion of fluid inside the fault is analogous to the linear heat flow inside an infinite solid bounded by two parallel plates (Carslaw and Jaeger, 1959). (Martin, 1968) and following him, Bernabe and Brace (1990) use this analogy for fluid diffusion inside a porous rock. I use similar derivation for fluid flow inside a fault with a constant hydraulic aperture. The flow inside the fracture follows Poiseuille's law (Kranzz *et al.*, 1979). The derivation is explained in Mighani et al. (2018). Therefore, we can write the following differential form of fluid flow. The left boundary ($x' = 0$ in Figure 2-1) or fault inlet (intersection of HF and fault) is insulated with zero pressure gradient. The right boundary or the fault end near the jacket is at constant pressure equal to confining pressure. Notice that P in the following equation is the fluid net pressure, i.e. $P_f - P_c$.

$$\frac{\partial^2 P}{\partial x^2} - \frac{\mu}{K}\frac{\partial P}{\partial t} = 0 \qquad (4)$$

$$\frac{\partial P}{\partial x} = 0 \; when \; x = 0$$

$$P = 0 \; when \; x = L$$

$$P = P_0 \; when \; x = 0 \; and \; t = 0$$

with K being the fault transmissivity. In the above formulation, an incompressible fluid is assumed to flow in laminar conditions. The fault transmissivity is a cubic function of hydraulic aperture (h) and function of fracture width (w), i.e. $K = h^3.w/12$ (Zimmerman and Bodvarsson, 1996). For more description of the derivation procedure refer to Mighani *et al.* (2018c), which involves the full solution for compressible fluids. The fluid inside the fault is water with a viscosity of μ =1 cp (10^{-3} Pa.s) and is assumed to be incompressible. The inlet pressure decline curve is then fit to the observed pore pressure decline. Table 2-3 shows the derived diffusion times from the pressure decline curve.

Table 2-3. Derived diffusion times from the observed pore pressure declines in Figure 2-7. The diffusion time for Solnhofen limestone fault is consistently greater than the PMMA fault.

Experiment Name	PM30-3	PM45-3	PM45-5	PM60-3	SH30-1	SH45-1	SH60-1
ΔP	71	64	66	76	34	22	23
Diffusion time (msec)	1.04	1.21	0.73	1.10	1.42	3.73	4.09

The diffusion time values derived for Solnhofen limestone are greater than those for PMMA, and, thus, the inferred fault transmissivity and hydraulic aperture are expectedly smaller for Solnhofen. Notice that these parameters are transient, and may change during fault slip. It is possible that unstable sliding in PMMA was associated with a significant dilation, allowing increased fluid diffusion along the fault. This interpretation is consistent with the results from Ottawa sand fault gouge sliding experiments Marone *et al.* (1990) between the steel plates, where step increases in sliding velocity were accompanied with increased porosity (dilation). Compaction occurred as the velocity was reduced.

2.1.3.3 AE source analysis

The hydraulic fracture and stick-slip events generated acoustic emission signals on piezoelectric transducers. Both Solnhofen limestone and PMMA did not generate any detectable precursory AE events, unlike stick-slip events in granite which had a measurable number of AEs (McLaskey and Lockner, 2014). Figure 2-8 shows the spectrum of HF events in both Solnhofen limestone and PMMA. The stick-slip event during PMMA sliding experiment is also inserted in this figure for comparison. The HF event spectrum in PMMA lies above limestone spectrum and has a lower corner frequency. The slip event in PMMA has a much larger magnitude and lower corner frequency than the HF events in PMMA and Solnhofen. The obtained moment magnitude, *M*, for slip event is -5.69. The *M* for HF events in PMMA and limestone is -6.95 and -6.8, respectively. Therefore, the hydraulic fracture initiation event is 1.4 *M* scale lower than slip event, so 125 times less strong.

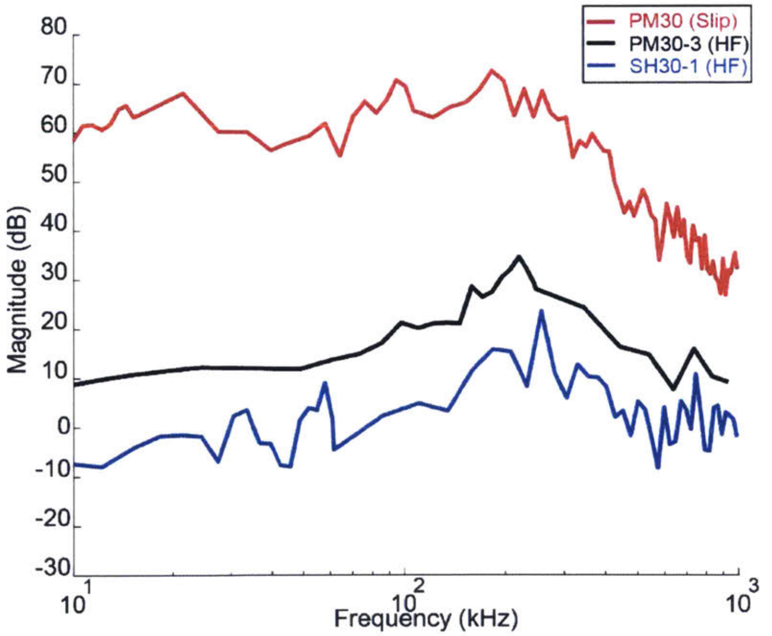

Figure 2-8. The spectrum of AE events in HF, and sliding experiments. Using the spectrum and derived instrument response and the procedure in Appendix S4 I can obtain the moment magnitude

of events. Stick-slip event in PMMA has a moment magnitude of -5.69. The HF events in PMMA and limestone have moment magnitudes of -6.95 and -6.80, respectively.

2.1.4 Comparison with cross/arrest criteria

The shear activation of a preexisting fault under tectonic stresses is governed by the resolved shear (τ) and normal (σ_n) stresses on to the fault plane. The necessary condition for the activation of this fault follows the Amonton's law:

$$\tau = \mu(\sigma_n - p_f) \tag{5}$$

with μ being the material's static coefficient of friction and p_f the *in-situ* pore fluid pressure. For a 2D geometry with σ_1 and σ_3 as the maximum and minimum far-field stresses, the resolved shear and normal stresses on a fault plane with orientation of θ with respect to the maximum stress are obtained using equations (1) and (2). By rearranging equation (5) using equations (1) and (2), we can obtain the required stress ratio (R) for the fault activation (Sibson, 1985):

$$R = (\sigma_1 - p_f)/(\sigma_3 - p_f) = \frac{(1+\mu cot\theta)}{(1-\mu tan\theta)} \tag{6}$$

Using equation (6) one can obtain the optimal orientation for fault reactivation, $\theta^* = (0.5)\text{atan}\,(1/\mu)$. By forcing the denominator in equation (6) to zero, R approaches infinity. This orientation is the fault lock-up angle and equals $\theta^r = \text{atan}\,(1/\mu)$. For orientations larger than $\theta^r$the fault does not slip, unless $(\sigma_3 - p_f)$ becomes negative, i.e., pore fluid over-pressure. The lock-up angle for coefficient of friction values of 0.12, 0.3, 0.6, 0.8 is 83^0, 73^0, 60^0, and 51^0, respectively. Based on the observations during the previous sections, the HF in Solnhofen limestone could cross the fault with μ=0.12 and orientation of 30^0, much steeper than the fault lock-up angle. This means that the fault slip under transient pore fluid diffusion does not simply follow equation (5) which assumes constant pore fluid pressure inside fault.

Now we consider the special geometry of an approaching hydraulic fracture to a fault interface. The material properties on both sides of the interface are similar. The hydraulic fracture which has exceeded the material's tensile strength, T, at the borehole creates a stress field ahead of its tip (Broek, 2012). The re-initiation of the hydraulic fracture on the other side of the frictional interface is an appealing assumption to describe the HF crossing after reaching the interface (Lam and Cleary, 1984). The re-initiation occurs at a critically-stressed Griffith type flaw due to the stress singularity ahead of the tip of the approaching HF. The necessary condition for the propagation of the hydraulic fracture is:

$$P_{HF} > T + \sigma_3 \tag{7}$$

Two scenarios could be considered for the interaction:

1- The hydraulic fracture reaches the fault and the fluid pressure propagates inside the entire finite length of the fault; therefore, the fluid over-pressurizes the fault and the fault fails either by opening or sliding. In other words, the fault "arrests" the hydraulic fracture.

2- The hydraulic fracture reaches the fault; however, the hydraulic fracture tip singularity is enough to result in the tensile failure of the material on the opposite side of the fault surface. Therefore, the hydraulic fracture re-initiates on the opposite side of the fault and not necessarily on the same plane as its original plane with some offset. In other words, the hydraulic fractures "crosses" the fault.

(Blanton, 1986) approached the problem by considering the competition between material's tensile strength and sliding of a Coulomb type frictional interface. (Renshaw and Pollard, 1995) and its further extension for non-orthogonal faults by (Gu *et al.*, 2012) and (Sarmadivaleh and Rasouli, 2014) considered the competition between the stress intensity singularity at the HF tip and shear stresses along the interface. Figure 2-9 shows the cross/arrest predictions based on these criteria including our experimental observations. The extensions of (Renshaw and Pollard, 1995) for non-orthogonal faults obey similar treatment of the problem. Therefore, here I review only (Renshaw and Pollard, 1995) criterion. The criteria predict the required differential stress for the crossing of the hydraulic fracture.

Equation (8) shows the Renshaw and Pollard criterion:

$$\frac{\sigma_1}{-T+\sigma_3} > \frac{0.35+0.35/\mu}{1.06} \tag{8}$$

Blanton criterion is as follows:

$$\sigma_1 - \sigma_3 > \frac{-T}{cos(2\theta)-b.sin(2\theta)} \tag{9}$$

with b having an asymptotic value of:

$$b = \frac{1}{2\pi} ln\left[\frac{1+\left(1+e^{\pi/2\mu}\right)^{0.5}}{1-\left(1+e^{\pi/2\mu}\right)^{0.5}}\right]^2 \tag{10}$$

Therefore, the obvious dependency on the material's tensile strength and interface's coefficient of friction are an outcome of these criteria.

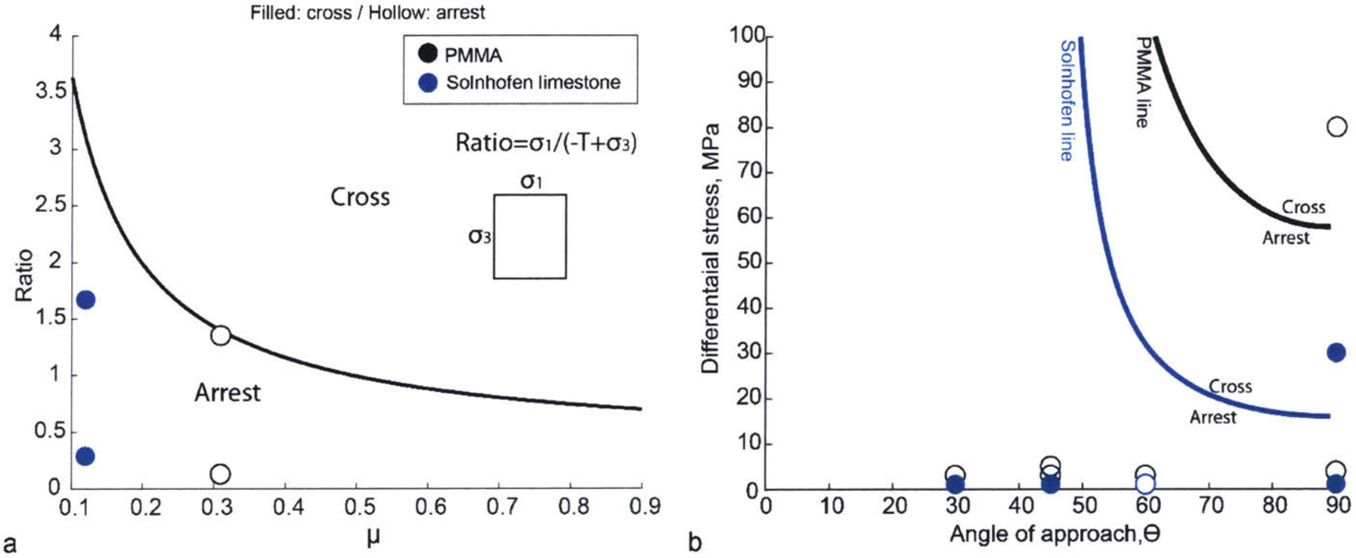

Figure 2-9. Existing cross/arrest criteria including our experimental observations. (a) shows Renshaw and Pollard (1995) criterion for an orthogonal fault. The Solnhofen limestone observations apparently contradict the crossing criterion. (b) shows Blanton (1986) cross/arrest criterion for a non-orthogonal fault. There is an asymptotic fault angle below which the HF does not cross the fault. Our observations again contradict the criterion.

It is shown in Figure 2-9 that the criteria fail to predict the observations of cross/arrest in the experiments. They could not predict the crossed HF in Solnhofen experiments; they could not also predict the HF arrest by PMMA for a 90^0 fault and high differential stress. I summarize the hydraulic fracture experiments in the literature in the presence of a fault in Table 2-4.

Table 2-4. Compilation of literature hydraulic fracture experiments with interaction with a fault. The crossing approach angle for fault orientations of less than 90^0 is also reported.

	Tensile strength, MPa	Young's modulus, GPa	Poisson's ratio	μ	Fluid viscosity, cp	Θ,^{0} (cross Θ)	Cross DS
Smooth Nugget SS[a]	5.6	30	0.07	0.55	300	90	4.5
Rough Nugget SS[a]	5.6	30	0.07	0.6	300	90	4.5
Smooth Indiana LS[a]	5.3	26	0.12	0.5	300	90	5.5
PMMA[f]	62	2.5	0.33	-	-	90	Not up to 13.8
Rough Indiana LS[a]	5.3	26	0.12	0.62	300	90	3.4
Coconino SS[b,e]	6.4	34.5	0.24	0.68	-	30-90 (≥60)	10.3 (60^0) 6.9 (90^0)
Hydrostone[c]	3.1	10	0.22	0.7	-	30-90 (≥60)	15 (60^0) 9 (90^0)
Wondabyne SS[d]	3.2	15	0.31	0.76	20,000	15-90 (≥15)	9.8 (15^0), 23 (30^0) 7 (90^0)
ABG Gabrro[d]	10.9	102	0.27	0.17	30	90	6.8

[a]Anderson (1981) [b]Warpinksi and Teufel (1987) [c]Blanton (1986) [d]Bunger et al. (2015) [e]Teufel and Clark (1981) [f]Hanson et al. (1980)

The properties and conditions present in the current experiments differ from earlier work in several important aspects. Many earlier studies conducted on cubic samples were under true triaxial stress conditions, i.e., stress states more comparable to the field operations. Sample dimensions were tens of centimeters (Hanson *et al.*, 1980) to meter (Gu *et al.*, 2012), thus providing much larger fault surfaces during the interaction. Often, earlier studies were performed on sandstone samples with permeabilities larger than a micro-darcy (Warpinski and Teufel, 1987; Bunger *et al.*, 2015) and low tensile strength values, i.e., 3-10 MPa (Blanton, 1986). The matrix permeability may affect the cross conditions by influencing the effective stresses; HF will be easier to re-initiate (Detournay and Cheng, 1992), while fault will be easier to activate. Crossing will also be favored by the high values of coefficient of friction (0.6-0.7) (Blanton, 1982) and the low tensile strengths. In the experiments reported here, the matrix permeability is of the order of a nano-darcy and the matrix can be treated as impermeable for the experimental time scales. The coefficient of frictions are quite low and the fault dimensions are small, whereas the tensile strength in both Solnhofen and especially PMMA are quite large by comparison (Table 2-4). We notice that HF's in recent experiments by (Bunger *et al.*, 2015) crossed faults even at orientations of 15^0, also contradicting the model criteria.

2.1.5 Impact of fault on HF azimuth

In 8 of 11 experiments, the hydraulic fractures intersected the fault at an azimuth roughly orthogonal to the fault strike, or parallel to dip. In only 1 in 11 experiments was the HF parallel to strike. We have conducted finite element calculations in order to compute the stresses near the borehole. The geometry of the model is shown in Figure 2-10 which includes a blinded borehole and a fault. The finite element calculations are conducted using PyLith finite element code. For a hollow cylindrical geometry, the tangential and radial stresses inside the solid are independent from the azimuth and only dependent on the radial distance from the internal boundary (Timoshenko *et al.*, 1970). Figure 2-10 shows the distribution of σ_{yy} near the borehole for both PMMA and Solnhofen limestone. The boundary and loading conditions are similar to PM30-3 and SH30-1 experiments in Table 2-2. This figure shows that due to the presence of fault, the symmetry of stress near the borehole breaks down. Therefore, there is a preferential azimuth for initiation of the hydraulic fracture; it initiates at the maximum tensile region, i.e. perpendicular to the fault strike. Therefore, the presence of fault results in perturbation of local stresses which gives the tensile (hydraulic) fracture preference to propagate normal to its azimuth. Fault-normal joints have also been observed in geological scales in Rough and Rocky Mesa in Utah (Kattenhorn *et al.*, 2000). Displacement Discontinuity modeling (DDM) of an approaching joint to a normal fault also suggests the influence of stressed fault on local stress orientations which affects the joint propagation path (Sheibani, 2013).

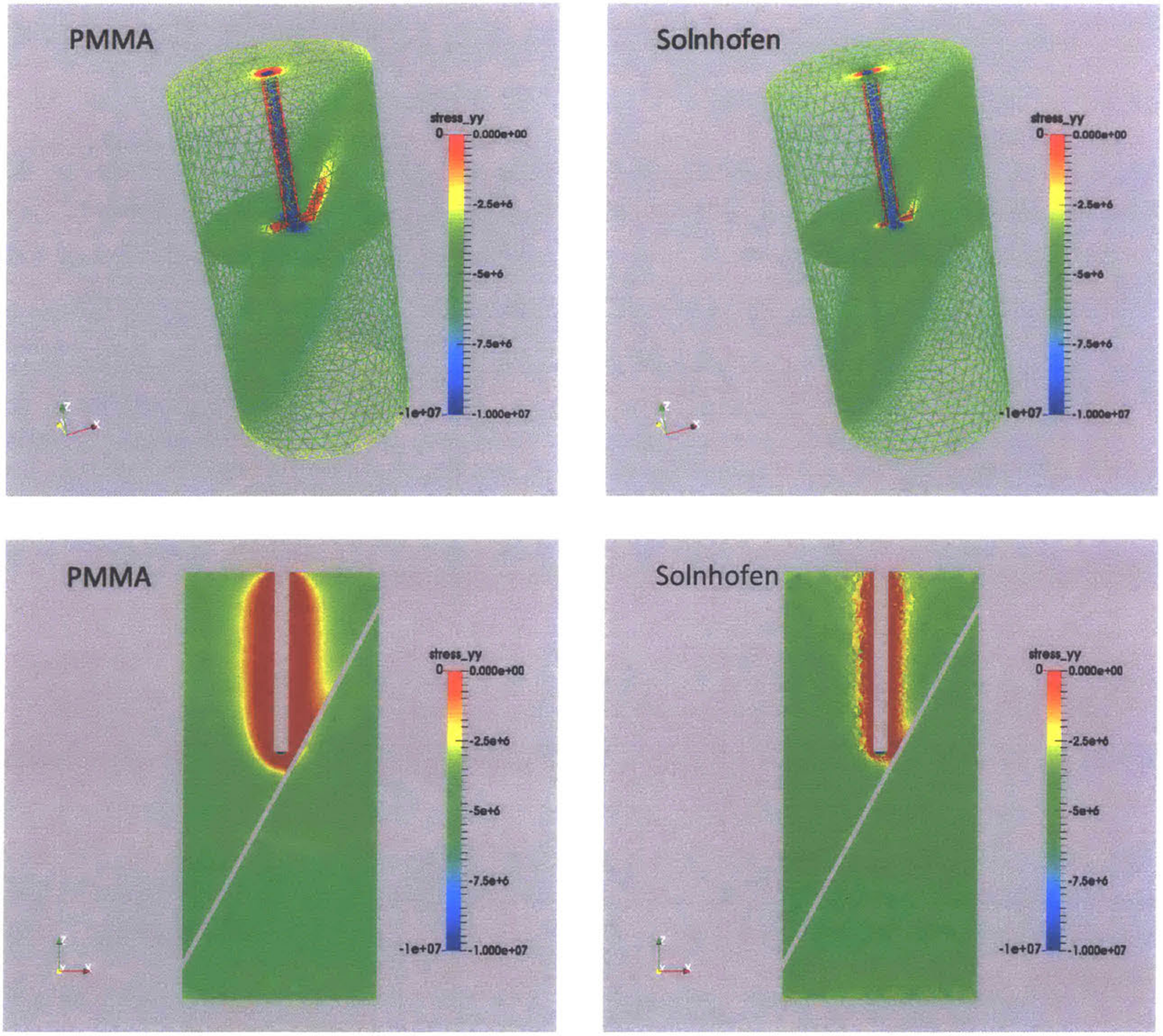

Figure 2-10. The distribution of $\boldsymbol{\sigma_{yy}}$ in 3D Finite Element (FE) models of our experimental geometry. Left and right show results for conditions similar to PM30-3 and SH30-1, respectively. The stresses are shown on a cross section intersecting the bottom of the borehole and the inclined fault (top) and an axial plane crossing perpendicular to fault azimuth (bottom). The fault in this figure has an inclination of 30^0 with its strike in y direction. The radial stress is equal to confining pressure, 5 MPa. The borehole is under constant pressure. Tensile stresses are shown by hot, while compressional stresses are shown by cold colors. The fault breaks the azimuthal symmetry of stresses making the $\boldsymbol{\sigma_{yy}}$ more tensile in x direction, i.e. perpendicular to the fault azimuth.

2.1.6 Conclusions

The sliding experiments showed low μ values and different sliding schemes for the limestone (stable) and PMMA (stick-slip). The values of apparent coefficient of friction in this report are low compared to commonly reported values of ~0.6. The measured surface roughness of 1.07 μm for our finely polished fault surface may explain this anomalously low value for both PMMA and limestone. Hydraulic fracture was arrested by the fault in PMMA, and was accompanied by a significant stress drop and slip rate in inclined faults. In contrast, in Solnhofen limestone, the HF usually crossed the fault. The hydraulic fracture initiated normal to the strike of the fault. The propagation velocity of HF in the experiments could easily reach 10's of m/s. The stick-slip event in PMMA had a moment magnitude of -5.69. The HF event had a moment magnitude of -6.8 (Solnhofen) and -6.95 (PMMA).

The observations cannot be explained based on the existing cross/arrest criteria of (Blanton, 1986) and (Renshaw and Pollard, 1995). The criteria underpredict the differential stress required for crossing in PMMA and overpredict this value for Solnhofen. The pore pressure decline after the HF intersection was used to estimate the fluid transmissivity of the fault based on the observed pore pressure decline. The main observations were:

1- In PMMA, the HF was arrested after the intersection with fault at all fault orientations and differential stresses. The fault slid with a slip velocity of ~60 mm/s and a significant drop in differential stress (~ 45%). The pore pressure dropped to a much lower value within 1 mseconds after the stick-slip event.

2- The HF in Solnhofen limestone behaved differently. After HF intersection, the fault slid with a slow slip velocity of 0.5 mm/s and a subtle stress drop. The HF was able to cross the fault at almost all fault orientations. The pore pressure decline was longer than PMMA experiments.

The experiments suggest that in order to fully describe the interaction phenomenon, the slip-induced fluid diffusivity needs to be considered. Therefore, the reciprocal behavior of fault sliding and the fluid diffusion as a result of this sliding needs to be considered in order to modify the existing criteria.

2.2 Role of fault gouge in Solnhofen limestone

Observations of downhole core samples suggest that these natural fractures are in fact veins filled with minerals such as calcite (Mighani *et al.*, 2016). I study this interaction during the approach of a hydraulic fracture to a smooth saw-cut fracture under triaxial stress conditions. The specimen is Solnhofen limestone, a fine-grained (<5 μm grain), low permeability (<10 nD) carbonate. The differential stress (1-20 MPa) and inclination of the fault which determines the approach angle, θ (30, 60°) are the experimental variables. I conduct the experiments on both bare surface and gouge-filled fault surfaces. The gouge is a 1 mm thick crushed powder of Solnhofen limestone with <106 μm grain size. During the hydraulic fracture, acoustic emissions (AE), inferred slip velocity, axial stress and pore pressure are recorded at a 5 MHz sampling rate.

2.2.1 Background

The hydraulic fracture experiments in the literature were generally conducted on frictional interfaces with the bare surface as a proxy to natural fracture. However, the in-situ natural fractures in shale formations are apparently not bare surface and contain inclusions (Gale *et al.*, 2007; Mighani *et al.*, 2016). They are present as discontinuities filled with minerals such as calcite (Figure 2-11) precipitated during the formation's depositional history. The main scientific objective in this report is to answer the following question: "How is our current lab understanding of the interaction problem modified by inserting fault inclusions, i.e., fault gouge?".

The coefficient of friction is first measured in sliding experiments and followed by a set of hydraulic fracture experiments. Using high acquisition rate recordings of acoustic emissions (AE), pore pressure, and stresses, the dynamic processes during this interaction are studied. The influence of fault gouge and the relation between the lab and field HF operations are discussed.

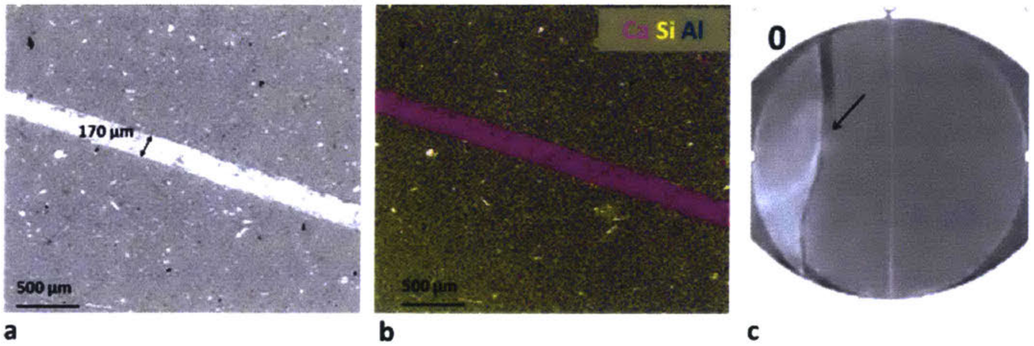

Figure 2-11. a) Backscattered SEM image of a calcite-filled vein in Wolfcamp shale formation, b) a superposed energy-dispersive x-ray spectroscopy (EDX) map with color-coded elemental abundances; the vein filling mineral is mostly calcite. c) Snapshot of a failed vein in Wolfcamp shale during the Brazilian test. Notice the generated debris (black arrow) as a result of the vein failure. For more description, refer to (Mighani *et al.*, 2016).

2.2.2 Experimental procedure

Cylindrical samples of Solnhofen limestone were prepared and the end surfaces were ground parallel. The cylinders have a diameter of 38.1 mm and a length between 65.6 and 73.7 mm. Artificial faults with orientations of $\theta = 30$ and 60^0 (with respect to the sample axis) were then saw-cut and the fault surfaces were finely polished (rms surface roughness=1.07 μm). A gouge mixture was prepared by crushing and sieving the same limestone starting material so that the sample and gouge layer have the same composition. Also, the gouge layer composition is similar to the natural calcite veins such as in Figure 2-11. The crushed gouge was passed through a 106 μm sieve. Gouge paste was prepared by adding deionized water and was applied as a 1 mm thick gouge layer was placed on the fault surface. A blind borehole with a diameter of 2.92 mm was drilled into the top half of the cylinder. The bottom of borehole in all samples has a constant vertical distance of 6 mm from the fault surface as shown schematically in Figure 2-12 along with other sample dimensions. The sample was assembled in a polyurethane jacket as depicted in Figure 2-12. For a complete description of the experimental procedure refer to section 2.1. I followed similar loading history and procedure as in section 2.1.

2.2.3 Results

2.2.3.1 Sliding experiments

The fault surfaces were sheared briefly with an axial shortening rate of 2 μm/sec before each hydraulic fracture experiment. The bare fault surfaces were slid for less than 0.2 mm axial shortening to maintain the original polished surface and avoid formation of surface wear grooves.

Table 2-5. Frictional properties of the faults during sliding experiments. μ in bare and gouge-filled surfaces is reported at 0.2 mm and 1 mm fault parallel slip, respectively. SH and number in names stand for Solnhofen and fault orientation, respectively.

Experiment Name	μ
SH30-Bare	0.12
SH60-Bare	0.11
SH30-Gouge	0.65
SH60-Gouge	0.42

The gouge-filled faults were sheared for 1 mm axial shortening to pre-condition the gouge and fault surface. The reported coefficient of friction is summarized in Table 2-5. Figure 2-13 shows the evolution of μ during the sliding experiments. The 1mm thick gouge layer is significantly stronger ($\mu \geq 0.42$). For the gouge-filled surfaces, μ is notably lower for the 60^0 fault than for the 30^0 fault. It also runs at a slightly lower μ in 60^0 fault compared to the 30^0 fault in the bare surface sliding tests. Lower μ at less oblique fault angles has been previously observed in granite (Savage *et al.*, 1996) and in Solnhofen limestone (Donath *et al.*, 1972). The unstable (stick-slip) sliding experiments in PMMA by (Mighani *et al.*, 2018c) also showed lower μ for a 60^0 fault compared with a 30^0 fault. One more notable difference between the two surfaces is the strain-hardening behavior; the gouge-filled surface still experiences strain-hardening after 1 mm displacement, while the bare surface has a comparatively flat frictional behavior at 0.2 mm displacement. During this initial stage in both bare and gouge-filled faults, only stable sliding was observed.

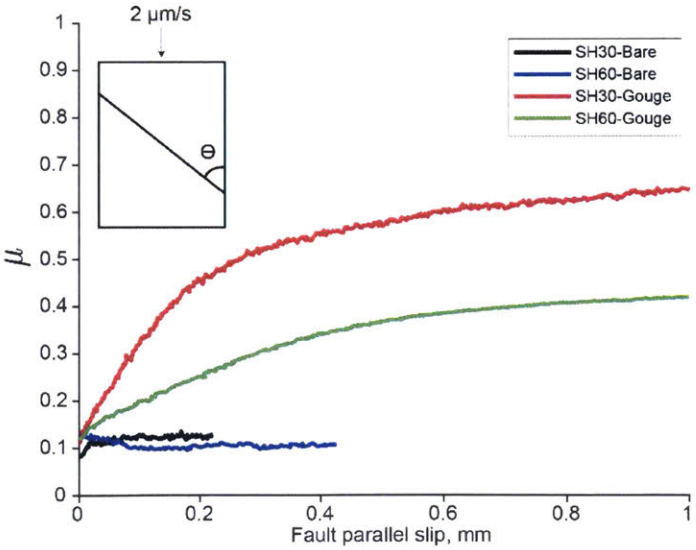

Figure 2-12. The evolution of the coefficient of friction, μ, during sliding experiments in bare and gouge-filled Solnhofen limestone fault surfaces. The x axis is the fault parallel slip derived by subtracting the piston elastic shortening from the axial displacement (see main text). The gouge is

a 1 mm thick layer of Solnhofen powder with < 106 μm grain size. Notice the increased μ value in gouge-filled surfaces. SH60-Gouge shows a strong strain-hardening which might reach closer to the SH30-Gouge curve at longer slip displacements; however, for the reasons explained in the text we did not slip the faults further to explore this.

2.2.3.2 Hydraulic fracture experiments

The hydraulic fracture was generated after pressurization of the borehole fluid. In this section, I present results for four HF experiments conducted on samples with bare surface and gouge-filled faults. The experimental conditions and the results are summarized in Table 2-6. The differential stress for the bare surface tests is 1 MPa. Due to low frictional strength, higher differential stresses were not possible for HF tests with bare surface fault. The differential stress value for gouge tests was the value at the end of 1 mm axial shortening.

In order to avoid disturbance of the evolved sheared gouge, I chose not to modify this value by adjusting the piston prior to HF tests. Therefore, the differential stress in gouge-filled 30^0 and 60^0 faults was 12 and 20 MPa, respectively, after 1 mm sliding and prior to HF experiments. Although it would have been better to keep the differential stresses the same in all HF experiments, but it was not possible due to the mentioned constraints for both bare and gouge-filled faults. Figure 2-14 shows the HF results for the bare surface.

Table 2-6. Experimental conditions for hydraulic fracture experiments. The experiment's name is adapted as material (SH for Solnhofen)-fault angle (degrees)-B as bare surface or G as gouge-differential stress (MPa). DS: Differential stress prior to HF. BP: Breakdown pressure. SD, Stress drop. Inferred slip is estimated from the vibrometer velocity readings. DCDT slip is estimated by correcting the DCDT data for piston elastic shortening. Fluid diffusion time is discussed in the following section and Figure 2-15.

Experiment Name	DS, MPa	BP, MPa	Inferred maximum slip velocity, mm/s	Slip duration, μs	Inferred slip, μm	DCDT Slip, μm	Fluid Diffusion time, msec	SD, MPa	SD, %	Interaction
SH30-B-1	1	39	0.5	29.9	0.01	-	1.42	0.5	50	Cross
SH60-B-1	1	28	0.3	37.4	0.02	-	4.09	0	0	Arrest
SH30-G-12	12	23	2.9	2533.8	2.48	59	4.18	6.4	53	Arrest

SH60-G-20	20	24	8.2	3406.5	19.04	331	4.31	18.8	94	Arrest

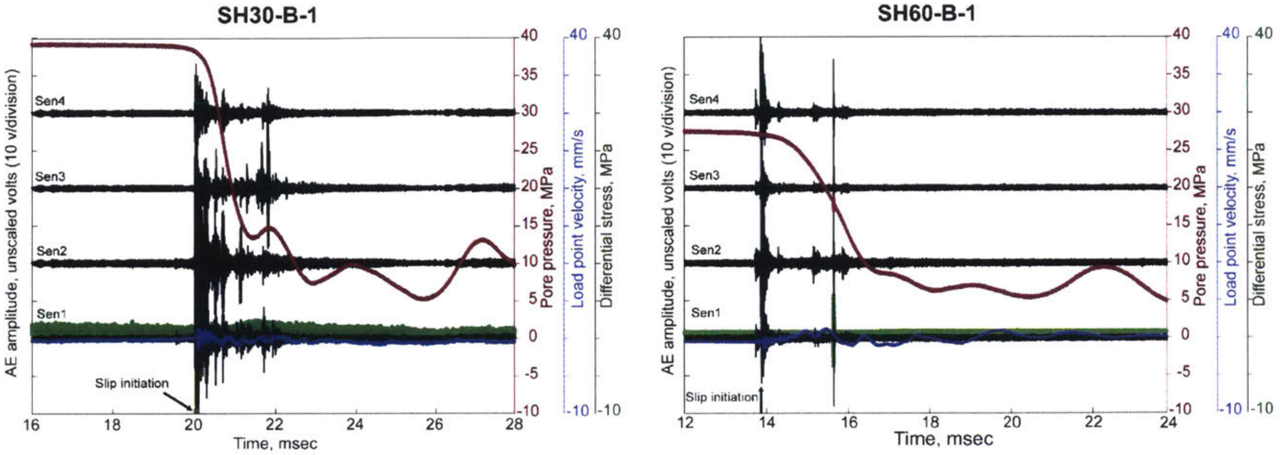

Figure 2-13. The recording of hydraulic fracture experiments for bare surface fault tests in Solnhofen limestone with 30^0 (left) and 60^0 (right) orientations. The hydraulic fracture was able to cross the fault at 30^0 orientation. Notice the short fault slip durations in vibrometer readings compared to Figure 2-13. The signal burst at ~ 15.8 msec in SH60-B-1 test is due to an unknown electrical noise (~120 Hz) source. The unscaled AE amplitudes have been calibrated based on ball drop experiments and the calibrated AE moment of the slip events are shown in Figure 2-16. The time of slip initiation is indicated based on the burst in AE signals.

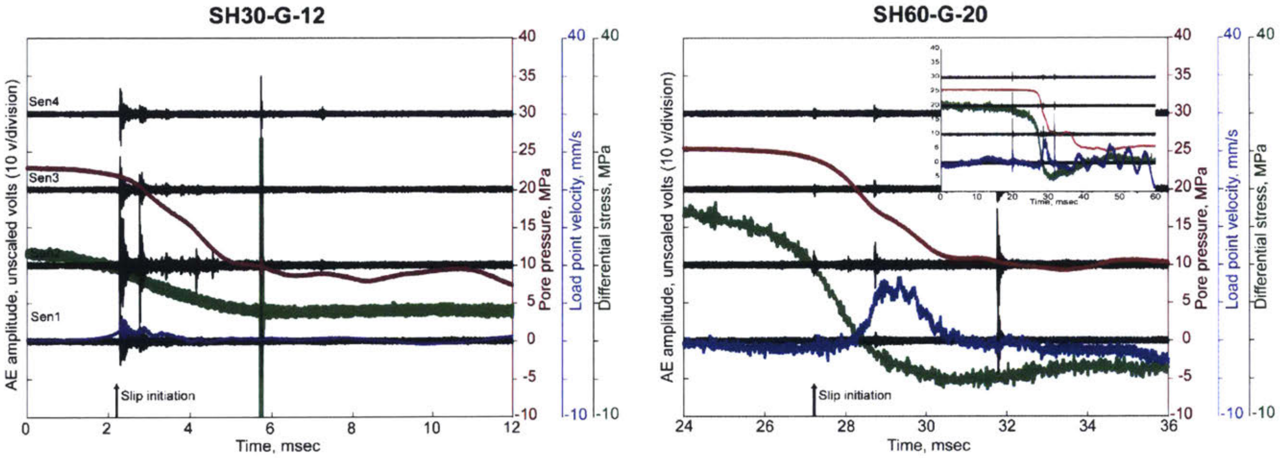

Figure 2-14. The recording of hydraulic fracture experiments for gouge-filled fault tests in Solnhofen limestone with 30^0 (left) and 60^0 (right) orientations. There is a large stress drop in both experiments, while the AE signals are less noisy compared with bare surface fault tests (Figure 2-13). The vibrometer also records a long duration slip event. I also show the entire recording in the

right figure which shows the recovered stress level after a transient weakening. The signal burst at ~ 5.8 msec in SH30-G-12 test is due to an unknown electrical noise (~120 Hz) source. The unscaled AE amplitudes have been calibrated based on ball drop experiments and the calibrated AE moment of the slip events are shown in Figure 2-16. The time of slip initiation is indicated based on the burst in AE signals.

Based on the high rate recorded response (Figure 2-13 and Figure 2-14), there are some notable characteristics during the HF intersection. The slip on the fault can be detected independently by vibrometer, strain gauge, and acoustic emission signals. It results in an abrupt change in the vibrometer velocity, significant generated acoustic signal, and a partial stress drop. The abrupt pore pressure drop is associated with the slip on the fault. The pore pressure then drops to the confining pressure value as the pore fluid reaches the sample jacket. I determined the time of slip initiation based on the burst in AE signals. The AE-based slip initiation coincides with the vibrometer velocity increase. The strain gauge readings, especially in the gouge experiments with high differential stress tend to decrease before the slip starts. This decrease could be related to the Poisson's effect during the fluid injection into the borehole. As the fluid is injected into the borehole, the sample expands radially and because of the Poisson's effect, it becomes shorter. Since the piston is locked, the vertical stress tends to decrease which can be seen in Figure 2-14. The HF was able to cross the bare surface fault to the other side of the fault at orientations of 30^0, and 45^0 (see (Mighani *et al.*, 2018c) for 45^0 fault results), but not at 60^0. The intersection of the HF and fault is associated with an AE signal burst, pore pressure drop, slip velocity increase, and stress drop (see Figure 2-13). The stress drop was less than 0.5 MPa and the slip duration was short, on the order of ~30 μsec. The maximum inferred slip velocity did not exceed 0.5 mm/sec. The HF was arrested by the gouge-filled fault for fault orientations of 30^0 and 60^0. In contrast to the bare surface fault, the slip was associated with a large stress drop and the AE bursts during the fault slip were less noisy (see Figure 2-14). The slip duration was ~2.5-3.5 msec and the maximum inferred slip velocity reached ~3-8 mm/sec (see Table 2-6). The slip values in Table 2-6 were estimated using two independent methods (see procedure section). Note that the slip values obtained from DCDT are much larger than the inferred slip by the vibrometer. This might be due to the fact that the inferred slip velocity considers only the slip duration time window; while, DCDT measures an accumulated displacement over 1 second (DCDT sampling rate is 1 Hz). Nevertheless, the relative total slip between 30 and 60^0 gouge-filled fault remains roughly the same. In the following section, I examine the distinctions between the bare surface and the gouge-filled fault behavior during the HF intersection.

2.2.4 Slow slip on the gouge-filled fault

In order to better compare the inferred slip velocity and pore pressure response during these tests, they are shown separately in Figure 2-15. As we interpreted and discussed the pore pressure decline in previous sections, we could infer the following scenario for the pore pressure decline: After the HF intersects the fault, the pore pressure declines until the fluid front reaches the jacket. After reaching the jacket, it is associated with a back-pressure which results in a jump in the pressure response. we can then determine the fluid travel time to reach the fault boundary from this pressure spike. The pore pressure finally declines to the confining pressure value. Comparing the slip duration time with fluid diffusion time (Table 2-6) in bare surface fault tests suggests that the fluid front traveled with much slower rates than the slip pulse (2 orders of magnitude difference in the two time constants). On the other hand, the fluid diffusion time and the slip duration for the gouge-filled tests are roughly equal, within the same order of magnitude. Although it is possible for the pressure spikes to be related to the pore fluid system's (pore pressure transducer + pore fluid lines + borehole fluid...) ringing during the pressure drop, we have evaluated the pore pressure response to a step-wise pressure drop during a burst disk failure. Appendix S5 describes these tests. The rise time in the pore pressure response to this step function was 603-705 μs, equivalent to 1.4-1.7 kHz frequency response. Therefore, any rise time longer than this value, i.e., the case of all our HF experiments, seems physically meaningful.

The AE and stress drops can easily be evaluated by comparing Figure 2-13 and Figure 2-14. The large fault displacements and stress drops after the HF intersection were not reflected in the radiated stress waves or AE response. In other words, in contrast to the bare surface fault, the slip on the gouge-filled fault occurred with significantly fewer radiated AE events. This suggests that relying merely on the high frequency AE events to interpret the sliding behavior may be misleading, especially when deformation involves fault gouge.

The presence of gouge along the fault changes both the mechanical interaction of the fault surfaces and the accessible volume for fluid flow. The sliding experiments in the presence of glass beads or angular quartz grains (Mair *et al.*, 2002) and their numerical simulations (Morgan and Boettcher, 1999) (Morgan, 2004) suggest the dominant role of "Particle rolling" in the case of spherical grains and “inter-particle sliding” and “dilation” in the case of angular grains during the sliding of a gouge-filled fault. However, at higher normal stresses, gouge grain crushing may be involved, changing the nature or magnitude of these effects. The role of fault gouge in stabilizing sliding has often been observed experimentally. Granite sliding experiments (Byerlee and Summers, 1976) suggest that the presence of fault gouge increased the normal stresses at which sliding transitioned from stable to unstable. This effect was enhanced by increasing the gouge thickness. In experiments by (Engelder *et al.*, 1975), stick-slip sliding along bare surfaces of Tennessee sandstone became stable when fault gouge was inserted. The dilatancy hardening which modifies the local effective stress on the fracture tip may also explain some of the observations. Triaxial experiments by (French and Zhu, 2017) suggest that under similar nominal effective stresses, at elevated fluid pressures, dilatancy hardening results in a lengthened duration of failure. So, the failure rate is limited by the ability of the fluid to fill the void volume and reach the newly formed fracture tip. This may explain why in gouge-filled fault tests, the fluid and slip front coincided (fluid diffusion time roughly equal to slip duration).

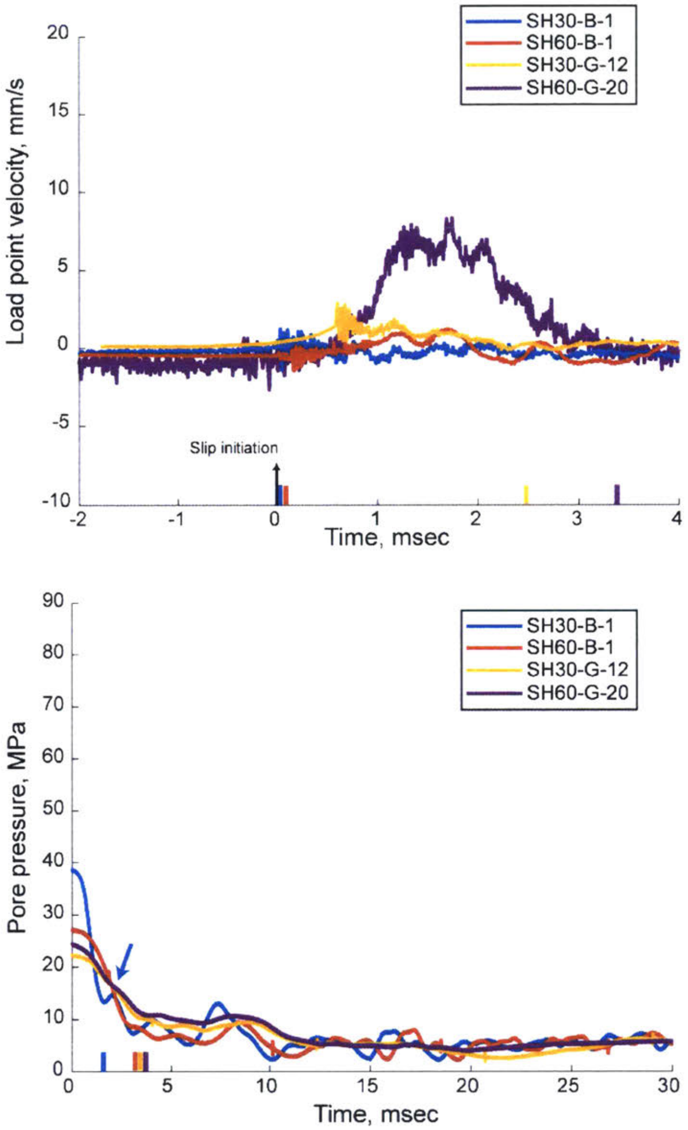

Figure 2-15. Slip velocity response (top) and pore pressure (bottom) comparison for bare surface and gouge-filled fault surfaces. In the top figure, the slip duration is indicated on the x-axis using vertical lines. In the bottom figure, the timing of the fluid front reaching the fault boundary (fluid diffusion time) is determined on the x-axis from the pressure spikes (e.g., blue arrow in the bottom figure for SH30-B-1). Notice the long duration of slip and smeared pore pressure decline in the gouge-filled tests. For a description of test names, refer to Table 2-6. Note that compared to Figure 2-13 and Figure 2-14, the sensor response in this figure are time-shifted so that slip (top) and pore pressure decline (bottom) initiate at time zero.

In total, the presence of the fault gouge resulted in a distinctly different activation of the fault when compared to the bare surface fault. Characteristics were manifested as: 1- The slip velocity readings from the vibrometer recorded longer duration slip events for the gouge-filled faults (see Figure 2-15). 2- The piezoelectric transducers recorded AE events with lower amplitude for the gouge-filled fault (see Figure 2-13 and Figure 2-14). 3- The stress drop was greater in the gouge-filled fault with a long weakening time and greater weakening (see Figure 2-13 and Figure 2-14). 4- The transient pore pressure decline response was longer in the gouge-filled fault with lower back-pressure spikes (smeared fluid diffusion) (see Figure 2-15). These observations suggest that the fault gouge promotes longer duration slower slip events.

2.2.5 Slip source analysis

The time window for deriving the signal spectrum is selected so that the entire seismic event is captured. I determined that a 400 μsec time window is long enough to represent the event with the middle of the time window at the signal peak amplitude. Notice that the time window does contain a cluster of AE events, not just a single event. So, the seismic spectrums and estimated moments are for the cluster of AE events during the slip. Figure 2-16 shows the spectrum of the slip events in different tests after removing the instrument response from the raw signal recordings. The seismic moment and the equivalent moment magnitude of the AE events shown in Figure 2-16 were estimated using ball drop experiments. The slip events in these experiments are similar to stick-slip events in the sense that the slip ruptures the entire fault surface. Since the slip event is not contained within the rock, the source dimension analysis becomes more complicated (Thompson *et al.*, 2009). Therefore, the formulations for contained events such as the Brune type shear event (Brune, 1970) were not relevant to these events. Consequently, we were not able to invert for source dimension in these events.

The released quasi-static moment during the fault's sliding can be estimated by using the following equation (McGarr, 2012):

$$M_{QS}=G.A.D \tag{11}$$

with G being the medium shear modulus, A, the rupture area, and D the fault-parallel displacement. In these experiments, Solnhofen limestone's shear modulus is ~16 GPa. The rupture area for these slips events, A, is the entire fault surface as discussed. D is the fault-parallel displacement shown in Table 2-6. As the fault sliding occurs under a compliant frame, the frame compliance also has to be considered for moment release calculations; it could either be included in the G or D term;

here we considered it in the D term by inserting the stiffness-calibrated displacements. When the DCDT slip displacements were below the resolution, I used the vibrometer inferred slip values. The vibrometer inferred slip tends to be on the lower end as the comparison between the two slip values in the gouge experiments indicate. Therefore, the vibrometer inferred slip gives a lower bound on the released moment. Notice that in this form of equation, the unloading stiffness which is a lumped function of the sample and loading frame stiffness contribute to D; the higher the stiffness, the lower D and as a result, the lower M_{QS} will be [(McGarr, 2012): equations 5 and 7]. The seismic and quasi-static moments are summarized in Table 2-7.

Table 2-7. Results of source analysis during the faults slip after hydraulic fracture intersection. The second and third columns are the estimated seismic source moment and moment magnitude, respectively. The fourth column is the estimated released quasi-static moment.

Experiment Name	M_0, N.m	M	M_{QS}, N.m
SH30-B-1	22	-5.17	> 4*
SH60-B-1	20	-5.20	> 4*
SH30-G-12	12	-5.33	2077
SH60-G-20	1	-5.97	6884

*Based on the vibrometer inferred slip

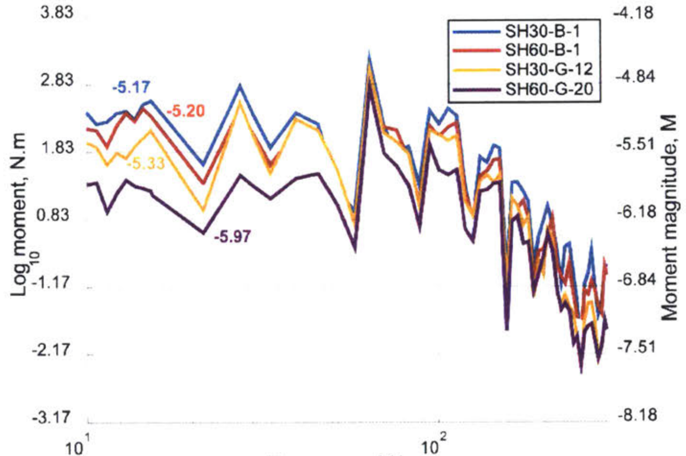

Figure 2-16. Spectrum of AE events during slip events after HF intersection with the fault. The instrument response is removed from the raw signals and the response is calibrated based on ball drop experiments. The numbers on the curves correspond to the equivalent moment magnitude of the AE events (see Table 2-7).

Table 2-7 suggests that even though the released moment during the fault gouge sliding is three orders of magnitude higher than the bare surface tests, the released seismic moment in the gouge experiments is lower. This suggests that the seismic efficiency in the gouge-filled experiments is orders of magnitude lower than the bare surface experiments. It reaffirms the slow slip failure mechanism for gouge experiments.

2.2.6 Similarity to LPLD events

During the microseismic recordings of hydraulic fracture operations in clay-rich Barnett shale, (Zoback *et al.*, 2012) (Das and Zoback, 2013) observed some Long Period Long Duration (LPLD) events in association with the microseismic events. The LPLD events had a duration of 10-100 sec in contrast to the usual ~0.1 s long microseisms. These events were in the 10-80 Hz frequency band compared with ~1 kHz microseisms. (Zoback *et al.*, 2012) suggested that the LPLDs occur as a result of the sliding on the natural fractures which do not have a favorable orientation for sliding under in-situ stresses. Therefore, under high fluid pressure, they can activate, but the slip does not go unstable (due to the fault orientation). Therefore, the rupture front does not exceed the fluid front. The experiments in this report suggested an additional mechanism for the generated slow slip events during the sliding of the natural faults. As described in previous sections, the fault gouge has developed small AEs, long duration slip events compared with a bare surface fault. The relative sliding of the fault surfaces can be accommodated by relative displacement and rotation of the fault gouge grains. Figure 2-17 shows a schematic of this sliding in the presence of the fault gouge grains. Therefore, sliding occurs under slow slip resulting in a significant displacement (slip) on the fault (see Table 2-6). So, the presence of gouge grains can stabilize the fault more towards a slower slip with less generated acoustic waves or AEs, similar to the low frequency LPLD events.

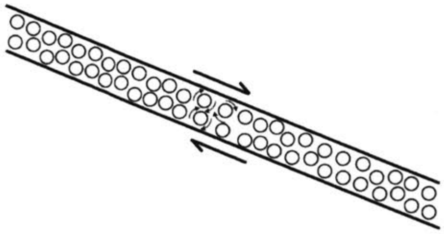

Figure 2-17. The schematic for the slip on a gouge-filled fault. The grains during the sliding can rotate and displace to facilitate the displacement along the fault.

2.2.7 Conclusions

I conducted hydraulic fracture experiments in Solnhofen limestone and in the presence of a pre-loaded fault. The fault was either bare or contained 1 mm thick fault gouge layer. The hydraulic fracture was not able to cross the gouge-filled fault. Instead, it generated a significant stress drop due to the induced fault slip. A characteristic slip event was detected by the laser vibrometer for the gouge-filled fault tests; the slip had a longer duration but with similar slip velocity as the bare surface fault. Therefore, the total fault slip increased. The increased total slip and stress drop in the gouge-filled fault occurred while the AE slip events were lower magnitude in the gouge-filled fault. In other words, the released quasi-static moment was larger for gouge-filled faults, while the seismic efficiency was lower. The slip duration for the bare surface fault tests is 2 orders of magnitude faster than the fluid diffusion time; so the fluid front lags behind the slip front. While, for gouge-filled fault tests, these two values are within the same order, i.e. the slip front does not exceed the fluid front. The observed gouge events are similar to the stable LPLD events observed by (Zoback *et al.*, 2012) during the activation of stimulated natural fractures in Barnett shale. The resulting slow slip could be effective in generating a connected fracture network which may not be detected as acoustic emissions/seismic signals. It has to also be mentioned that the specific observed behavior for calcite gouge does not necessarily generalize to other gouge compositions; for example, the glass gouge grains have been found noisy producing a large number of AEs during sliding (Rouet- Leduc *et al.*, 2018).

2.3 Fault transmissivity controls on the interactions

Extensive theoretical and experimental developments have been put forward to analyze the quasi-static aspects of this interaction. I designed and performed triaxial experiments (P_{conf}=5 MPa) in Solnhofen limestone, to study the dynamics of this interaction. In particular, by varying the fault surface roughness and fluid viscosity, I studied the role of fault's fluid diffusivity (fault transmissivity/fluid viscosity). In the experiments, a fluid-driven tensile fracture initiates from a pressurized borehole, traveling towards a saw-cut fault (used to mimic a frictional fault). Acoustic emissions (AE), fault slip, stress drop, and pore pressure were recorded at a 5 MHz sampling rate. A threshold value for fluid diffusivity was observed, below which the HF was able to cross the fault. Otherwise, the fluid-infiltrated fault activated; resulting in a finite fault-parallel slip, ~<1-90% stress drop, and a burst in AE signals. Moreover, the slip induced an enhanced fluid diffusivity of ~>4 orders of magnitude on the fault. The calibrated AE sensors recorded seismic moment magnitudes of ~-5 for slip events vs. ~-7 magnitudes for HF initiation events. The experiments imply that the diffusion of fluid, driven by the fault slip, majorly controls the cross/arrest conditions. Hence, considering the dynamics of this variable, coupled with fault slip, would be a necessity for full considerations of the interaction problem. Also, the low tensile/slip events' seismic moment ratios might explain the paucity of tensile events during microseismic recordings of reservoir stimulations.

2.3.1 Background

Here, I recap the developed theoretical understanding of interaction problem, which helps put the experimental framework into a context. Specifically, three well-recognized cross/arrest criteria (in 2D stress space; Figure 1-1) have been experimentally verified and derived: by comparing the required pressure to reinitiate the tensile fracture on the opposite side vs. the required pressure to reactivate the pressurized fault, Blanton (1986) proposed a crossing criterion; this criterion suggests an asymptotic angle below which the HF cannot cross the fault. By estimating the resolved shear and normal stresses on an oblique fault surface, Warpinski and Teufel (1987) presented the conditions for fault's slippage/dilation. Using a first-order stress analysis near a Mode I fracture tip, Renshaw and Pollard (1995), herein referred to as *RP* criterion, presents the required friction coefficient, material tensile strength, and differential stress for the propagation of a dry tensile fracture across an orthogonal frictional interface. Since then, this criterion has received attention and been extended to include non-orthogonal faults (Gu *et al.*, 2012), cohesion (Sarmadivaleh and Rasouli, 2014), fault cementation strength (Fu *et al.*, 2018). Collectively, these criteria emphasize the importance of fault's friction coefficient and angle and material's tensile strength and *in-situ* stresses. More importantly, they predict a minimum asymptotic required angle (>30°) for crossing. Hence, they neglect the dynamic variation of fault condition upon fluid infiltration and its impact on the crossing conditions. While, recent studies have shown that the fault's transmissivity and its evolution may entirely dominate the processes (Mighani *et al.*, 2018c). In particular, these experiments showed that HF is able to cross a fault in Solnhofen limestone with low friction coefficient (μ~0.1), even at steep angles of 30°. While, HF was arrested by a fault in PMMA, even under abnormally high differential stresses of ~70 MPa although the criteria predicted cross for these conditions. Cross at anomalously steep angles has also been observed in sandstones, where HF was able to cross even at 15° fault angles (Bunger *et al.*, 2015).

To better understand the role of fault transmissivity, I designed a set of triaxial experiments, where a hydraulic fracture approached a sawcut fault as a proxy for a natural fracture. I varied the fault's transmissivity by modifying the fault surface roughness using different surface polishes. Doing so, I was able to investigate transmissivity variations of four orders of magnitude. I also studied the effect of fluid viscosity, which would also control the ability of fluid infiltration onto the fault surface. Dynamic measurements of stresses, displacements, acoustic emissions and pore pressure, allows us to observe the evolution of processes occurring during the interaction.

2.3.2 Procedure

2.3.2.1 Hydraulic fracture experiments

I prepared cylindrical samples of Solnhofen limestone and ground the end surfaces parallel. The cylinders have a diameter of 38.1 mm and lengths between 76-84 mm. Faults with specified orientations of 30, 45, and 60° [with respect to the vertical axis (Figure 2-18)] were then saw-cut using a circular saw blade. The fault surfaces were then polished to three different roughness levels; the smoothest fault surface was obtained using a fine sandpaper level of P1000. For the medium and rough surfaces, I hand-lapped the fault surfaces against each other in the presence of wet #400 and #80 Al_2O_3 grits. The surface roughness profile for these three polish levels are summarized in Figure S2-1; the root mean square (rms) roughness varies from 0.91, 1.06, and 2.47 μm, respectively (see text S1). A blind borehole with a diameter of 2.92 mm was then drilled into the top half of the cylinder. The bottom of the borehole in all samples always has a constant axial distance of 6 mm from the fault surface as shown schematically in Figure 2-18. The bare fault surfaces were then put together, and the two sample halves were sandwiched inside a polyurethane jacket, which isolates the specimen from confining medium.

The assembly used here is similar to the sub-chapters 2.1 and 2.2, with a difference that the number of AE sensors have been enhanced to 10 piezoelectric ceramic transducers (PZT-5A) to record acoustic emissions (AE) events during the experiments. The PZTs are p-wave type with a resonant frequency of 1.5 MHz (1.04 mm thick) and a diameter of 6.4 mm. The jacket was instrumented with 8 PZT transducers, i.e., Sen1-8, through holes, which housed 6.4 mm cylindrical bronze couplants. The transducers were mounted (epoxied using conductive epoxy) on the outer face of couplants. The inner face of the couplants, with sample interface, is machined to a surradius of curvature of 19.05 mm to conform to the sample surface. The holes in the jacket were permanently sealed using a two-component, shear-resistive epoxy. Two transcoders were mounted (epoxied using conductive epoxy) on the top (Sen9) and bottom (Sen10) steel spacers (Figure 2-18). Therefore, confining and axial stresses provide the coupling between the transducer and sample.

The pore fluid pressure for hydraulic fracture experiments was provided using a gear pump, which operated under a constant injection rate. To isolate the pore fluid from confining medium, an o-ring groove was inserted in the steel top spacer which houses an o-ring (Figure 2-18). Axial stress provides the required o-ring seal between the sample and steel spacer to prevent the pore fluid from leaking past the end of the sample to the jacket. Two fluids with different viscosities were used during hydraulic fracture experiments, i.e, deionized water (1 cp) and oil-based silicone emulsion (350 cp) (Clearco Inc.). Prior to the HF tests, pore pressure lines were de-gassed using a vacuum pump. For the HF tests conducted using silicone fluid, I also mounted a free-sliding piston separator to prevent pump contamination by the silicone fluid. A pore pressure transducer (Honeywell Inc.) outside the triaxial vessel records the pressure variations inside the borehole. The frequency response of the pore pressure transducer is evaluated in Appendix S5 of Mighani *et al.* (2018c) as 1.4 kHz. This means the pore pressure transducer records the response as a low-pass 1.4 kHz filter. The experimental data are recorded independently on two different systems. The mechanical data including the confining pressure, axial stress, pore pressure, pore volume, and vertical displacement are recorded with a sampling rate of 1 Hz (averaging 10 values sampled at 10 sample/s). The high rate acquisition data were recorded at a 5 MHz rate as explained below.

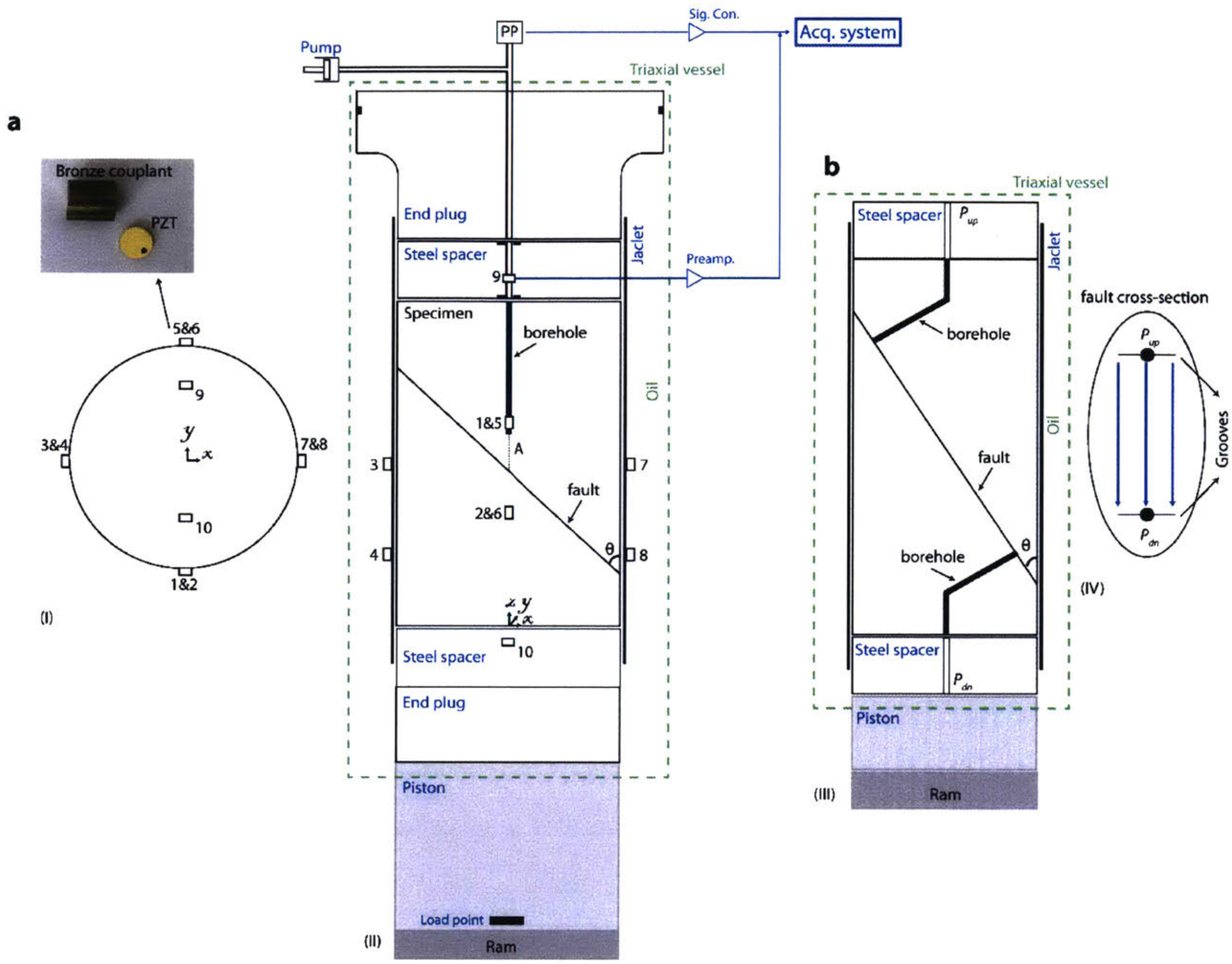

Figure 2-18. Schematics for triaxial assembly and transducers. (a) the hydraulic fracture and sliding test assembly. (I) the plan view for AE sensor locations (inset shows a PZT and a couplant). (II) shows the side of the sample assembly and triaxial apparatus (not scaled). In (II), (PP) is the pore pressure transducer measuring the borehole pressure outside the vessel. (A) is the vertical distance between borehole bottom and fault, which is always 6 mm. (b) fault permeability measurement experiments. (III) the geometry of fault transmissivity measurements, where two angled boreholes are connected to upstream (P_{up}) and downstream (P_{dn}) reservoirs. The downstream side is connected to the open atmosphere. (IV) fault cross-section with two parallel grooves cut on the fault surface to register better parallel fluid flow (blue lines).

To infer fault-parallel slip, I corrected the DCDT displacement readings for the load column elastic shortening, using system stiffness. The system stiffness at the load point was estimated as the slope of resolved shear stress onto the fault over the load point displacement ($k_{lp}=\tau/x_{lp}$; see Appendix S3). The system stiffness including the Solnhofen specimen at a confining pressure of 5 MPa is 73

MPa/mm. Notice that this system shows a stiffer behavior compared to the previous experiments on in chapters 2.1 and 2.2, where the stiffness was 49 MPa/mm, so that sliding should tend to occur more stably in these tests.

2.3.2.1.1 AE acquisition, location, and moments

The AE signals, along with pore pressure, were recorded using a TraNET EPC-32 acquisition system (Elsys Inc.) with a sampling rate of 5 MHz and 14-bit resolution. The full-range of acquisitions was ±10 Volts. The AE signals were preamplified via a multi-channel preamplifier (digital wave Inc.), with a 20 kHz high-pass filter. Some high-energy signals, such as energetic slips, would be clipped. To increase the dynamic range of AE waveforms, the amplified signals of four transducers (Sen3,7,9,10) were split and passed through 28 dB (× ~1/26) attenuators. The background noise level in the whole acquisition system was ~16 mV (Figure S2-6a), which is chiefly injected by the preamplifier circuit into the system. The acquisitions were conducted in a trigger-based (so-called ECR) dual mode. In this mode, the data are continuously recorded and streamed to disk at a lower acquisition rate of 50 kHz. Once an event triggers an AE sensor (trigger level of 0.3 V), a time window of data is recorded at a 5 MHz sampling rate with no dead-time, which is a major drawback in other typical trigger-based acquisition systems. This system ensures no data loss within a certain acquisition bandwidth. The triggered time windows were ~40 msec after triggering on one of the AE transducers, recording 20 msec before and after the trigger time.

To locate the AE sources, I used a standard grid search technique assuming an isotropic compressional velocity for Solnhofen limestone and straight ray paths. I manually picked the first P-wave arrivals. The arrivals times were corrected for the time delays of sensor couplants made from bronze ($V_P \sim$ 3530 m/s) for radial transducers and steel ($V_P \sim$ 5930 m/s) spacers for the axial (top and bottom) transducers. I followed the following procedure for source location: if the error between the calculated and observed arrival time for a sensor was more than 2 μs, that sensor was eliminated; we accepted only the locations calculated from at least 6 sensors. The location accuracy was estimated from the root mean square of the misfit between the predicted and observed arrival times on each sensor; on average the location error was ±~3 mm. Considering the wave velocity in Solnhofen, the theoretical limit on the location accuracy for a 5 MHz acquisition rate is ±0.8 m. However, the sensor's aperture size, as well as difficulties in picking the first arrivals would limit the located event's accuracy. I found this location scheme quite robust; as, after considering the acceptable sensors for each source (< 2μm error), random removal of sensors did not result in source location migrations. However, due to high dynamics of experiments, the entire AE activity occurred in less than a second during intersection of HF with saw-cut. This obscured the first arrivals on some events, as the sensors were still resonating from the previous events. Hence, during each experiment only a handful of events (10's at best) were locatable.

The absolute moment magnitudes of the AE events were obtained by comparing the spectrum of signals to a ball drop event, with a known released momentum. For the ball drop events, it was assumed that the recorded seismic signal by transducers was equivalent to the released momentum due to the Hertzian ball drop impact, where the fact that the bounced ball could rise more than half of the initial drop height suggests the impact was primarily elastic, so the released energy did not part into inelastic frictional heating [(McLaskey *et al.*, 2015); see Appendix S4]. By comparing the measured and theoretical ball drop spectrums, I also estimated the instrument response spectrum.

I also estimated the full seismic moment tensors of selected AE events. In past studies, the polarity of the first motions were often used as a relative discriminating indicator for the source type (Tensile +, Compressional -, Shear +&-) (Sondergeld and Estey, 1982; Lockner, 1993a) [although in (Zang *et al.*, 1998), the signs are reverse due to possibly a mistake]. Also, by prescribing the event as a double-couple (DC) type, a rough estimate of fault-plane solutions have been obtained (Sondergeld and Estey, 1982). However, exact details of the source, specifically point force directionality and volumetric vs. non-volumetric components at the source location, could be extracted from the inverted full tensor components (force couples). Moreover, the controlled conditions, as well as the decent focal sphere coverage, during laboratory experiments provide an unprecedented opportunity to assess the moment tensor method for analysis of natural and induced Earthquakes.

One challenge in seismic moment tensor inversions, specifically for AE events, is to assess whether the received waveforms are far-field (decaying as $1/r$), or they are superposed on near-field (decaying as $1/r^3$), components. The pure far-field waveforms allow the seismic event to be considered as a point source. The condition for the waveform with frequency f being far-field is: $r_o^2 \leq (V_p.r)/(2.f)$, where r_o is the source dimension (Sondergeld and Estey, 1982). We take a source size of ~3 mm (largest stick-slip events reported by McLaskey *et al.* (2014) are ~5 mm).

Therefore, for traveling distances larger than 1.5 mm, the entire AE spectrum is far-field, which is generally the case for our sample dimensions. The amplified events for repeat ball drop tests had consistent first motion polarities and amplitudes (Figure S2-3); however, full-waveforms may have been distorted during preamplification (see Figure S2-3), making full waveform moment tensor inversions less reliable. Hence, I used the first P-wave motion amplitudes. In addition to the propagation effects, AE sensors may also dampen the amplitudes; by considering the amplitude dependence on the incidence angle and spherical radiation, I estimated the sensor coupling transfer functions for each sensor (station corrections) [see Appendix S4 and Kwiatek *et al.* (2014)]; hence, the amplitudes used for inversion were first corrected for the sensor coupling.

Moment tensor, a symmetric 2nd rank tensor which is used ubiquitously to represent seismic point forces, requires six independent components. Making certain assumptions about the source (such as DC, CLVD, ISO, …) could further simplify the tensor; however, here we are interested in the general representation of moment tensor, *m*, with six independent force couples:

$$m = \begin{bmatrix} M_{11} & M_{12} & M_{13} \\ M_{12} & M_{22} & M_{23} \\ M_{13} & M_{23} & M_{33} \end{bmatrix} = \qquad (12)$$

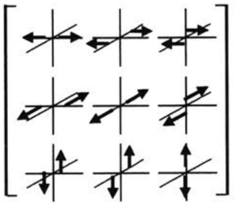

For the AE frequency ranges, the first P-wave motions in volts are taken to represent the displacements (McLaskey *et al.*, 2014). The displacement felt by the receiver *j* from the source *i* could be reconstructed by convolving the moment tensor and medium's Green's function from source to receiver (here, I only consider P-wave components, as the sensors are P-wave type):

$$u_{ij}^{P} = G^{p}{}_{ij} \times M_{ij} \qquad (13)$$

To invert for the moment tensors, first the coordinate system is transformed, so that the source is at the origin. The Green's function for a P-wave in the local source coordinates is single-component and parallel to the P-wave direction. The local Green's function is then rotated twice considering the take-off (clockwise angle from *x* direction), θ, and azimuth (0 if source direction is in negative *z* direction), φ, angles, to be in the global coordinate system. Considering the medium as homogenous and isotropic and spherical P radiation, the recorded displacements at the *i*th AE receiver, u_{ij}^{P}, would be (Aki and Richards, 2002):

$$u_{ij}^{P} = \left[\frac{\dot{w}}{4\pi\rho V_p^3}\right] \gamma_i \gamma_j \gamma_k \frac{1}{r_{ij}} M_{jk} \tag{14}$$

where γ's and $\dot{w}$ represent the direction cosines and source displacement rate function, respectively. As I used a separate method to determine the seismic moment magnitudes, seismic moment tensors were used to provide a relative sense of volumetric vs. non-volumetric motions. Considering the tensor rotations, the simplified form of the Green's function is then (Dahm, 1996): As the P-wave AE transducers are sensitive to 1D particle motion, the amplitudes are

$$u_{ij}^{P} = I_j \sum_{k=1}^{6} m_{ki} a_{jk} \tag{15}$$

with

$$a_{j1} = -sin^2\theta . cos2\varphi, a_{j2} = sin^2\theta . sin2\varphi, a_{j3} = -sin\, 2\theta . cos\varphi, a_{j4} = -sin\, 2\theta . sin\varphi, a_{j5} = sin^2\theta - 2cos^2\theta, a_{j6} = 1$$

and

$$M_{11} = -m_{1i} + m_{5i} + m_{6i}, M_{22} = m_{1i} + m_{5i} + m_{6i},\ \ M_{33} = m_{6i} - 2m_{5i},\ \ M_{12} = m_{2i},\ \ M_{13} = m_{3i},\ \ M_{23} = m_{4i} \tag{16}$$

where we take $m = [M_{11}, M_{22}, M_{33}, M_{12}, M_{13}, M_{23}]$, as a vector form of the components of moment tensor matrix. If we take vector d as the multiplication of the first P-motions by distance on n sensors, and A as the matrix of coefficients, the observed first motions would relate to moment tensor components through:

$$d = u^{p}{}_{n\times 1} . r_{ij} = A_{n\times 6} m_{6\times 1} \tag{17}$$

Then, m would be obtained through the following least squares ($n \geq 7$) solution (Eaton and Forouhideh, 2011; Menke, 2018):

$$m = (A^T A)^{-1} A^T d \tag{18}$$

If the normalized error between predictions and observations were more than 0.3 on a single station, I discarded that sensor for inversion. I reported the inversions on at least 7 sensors, where the RMSE would still be meaningful ($n \geq 7$). The average RMSE's over the sensors were generally less than ~0.3. The moment tensor solutions (equations 15-17) were verified by comparing with the solutions of the HybridMT benchmark code (Kwiatek *et al.*, 2016).

Using the eigenvalues of the moment tensor matrix ($\overline{M}_1 > \overline{M}_2 > \overline{M}_3$), I could obtain the contribution of non-volumetric (deviatoric) and volumetric components. The eigenvectors could also be used to obtain the orthogonal T (tension) < N (neutral/intermediate) < P (pressure) axes (Vavryčuk, 2015). Such analyses have been found to consistently reproduce the in-situ principal stresses in both laboratory (McLaskey and Lockner, 2018) and field (Baig and Urbancic, 2010) deformations. In this report, I focus only on the eigenvalues. Using the three eigenvalues I have (Vavryčuk, 2015):

$$M_{ISO} = \frac{1}{3}(M_1 + M_2 + M_3)$$

$$M_{CLVD} = \frac{2}{3}(M_1 + M_3 - 2M_2)$$

$$M_{DC} = \frac{1}{2}(M_1 - M_3 - |M_1 + M_3 - 2M_2|) \tag{19}$$

where, I report the normalized fractions of above terms by the scalar seismic moment, $M = |M_{ISO}| + |M_{CLVD}| + M_{DC}$. The three respective fractions would be C_{ISO}, C_{CLVD}, C_{DC}. The moment tensors are graphically represented on Hudson's skewed *u*-*v* diamond source-type plots (Hudson *et al.*, 1989) using the three eigenvalues, $u = -\frac{2}{3}(\overline{M}_1 + \overline{M}_3 - 2\overline{M}_2), v = \frac{1}{3}(\overline{M}_1 + \overline{M}_2 + \overline{M}_3)$. Bars on eigenvalues represent the normalized values by the maximum $\overline{M}_i$. In addition to finding the best solution of the moment tensor, I also conducted a limited uncertainty assessment of the inverted solutions, shown on the source-type plots. I assessed the uncertainties in location (±3 mm), as well as amplitude readings (±20% random amplitude error on each sensor). Due to the limited number of sensors, I did not attempt to assess the solution uncertainty with respect to local station biases by randomly removing the sensors for inversions. Such detailed uncertainty analyses of moment tensors are beyond this work. Note that at the end, here I report the normalized moment tensors; so, the relative magnitude of components does not depend on their absolute values.

2.3.2.2 Fault transmissivity measurements

Besides sliding and hydraulic fracture experiments, I also measured the fault transmissivity for different surface roughness and observed its evolution during fault slip. To do so, I designed a separate set of experiments on 25.4-mm Solnhofen cylinders in a separate triaxial apparatus. During these experiments, I only recorded the mechanical data. After preparing the faults with different roughness using a procedure similar to that described in the previous section, I drilled angled boreholes, normal to the fault and cylinder's end surfaces, in each sample half (Figure 2-18b). Two parallel notches were then cut on the fault surface (0.8 mm deep with extending wings of 10-13 mm from the boreholes). In this way, nearly parallel flow was achieved rather than the divergent flow that would occur around circular injection and sink holes (Figure 2-18b). Two fault orientations of 30 and 60° were prepared with the upstream/downstream notches spaced 25.4 and 12.7 mm from each other in these orientations, respectively.

The top and bottom boreholes were connected to the upstream and downstream pore pressures. The upstream reservoir was connected to a hydraulic pump, and the downstream was connected to the open atmosphere. The pore fluid was deionized water. I used two pumps with different reservoir capacities. Depending on the flow rate required, I connected each to the pore fluid system (a minimum flow rate of 4.2×10^{-10} cm^3/s was registered on a closed pore pressure system. This is equivalent to a minimum attainable permeability of ~0.02 nD on a 25.4 by 25.4 mm cylinder). To assess the contribution of matrix permeability to the fault transmissivity measurements, I also measured the matrix permeability on a solid 25.4 ×25.4 mm Solnhofen cylinder (see Appendix S2).

To calculate fault permeability, I used the steady-state flow method, where a constant pressure head was held between the upstream/downstream (P_{up}/P_{dn}) reservoirs using a computer-control feedback system. I then recorded the registered flow rate. The upstream reservoir pressure was held at 1 MPa, and the downstream pressure was atmospheric. If we assume the pore pressure gradient was linear, the average pore pressure was 0.5 MPa. I applied a computer-controlled confining pressure of 5.5 MPa, so that the effective pressure is kept at 5 MPa, similar to the confining stress conditions during sliding and hydraulic fracture experiments. To reduce the effects of storativity during transmissivity measurements, I pre-saturated the samples by driving a 1 MPa upstream pore pressure and closing the downstream and waited for the flow rate to reach practically negligible values. Hence, for the smooth fault, we had to wait for about a day before measurements due to Solnhofen's tight permeability. The equivalent permeability could be estimated using a steady-state, laminar generic form of:

$$q = \frac{kA}{\eta}\frac{\Delta P}{L} \tag{20}$$

where q, ΔP, and η are flow rate, pore pressure difference ($\Delta P = P_{up} - P_{dn}$), and fluid viscosity, respectively; L and A are length and cross-section area, parallel and normal to fluid flow, respectively. For a porous medium, according to Darcy's law, k is matrix permeability. By viewing the fluid flow along the fault as a one-dimensional parallel-plate flow model, we take the cross-section area normal to fluid flow as $A=h.w$, with h and w being the plates separation and effective width, respectively. Since I do not have a direct measure of fault separation (h), I report $K = k.A$ where K is transmissivity (Zimmerman and Bodvarsson, 1996). Hence, in accordance with the cubic law, $K=h^3.w/12$ (equivalent Darcy permeability is $k=h^2/12$). By reporting K, we also avoid the prescription of effective width (w), which altogether facilitates direct comparisons in these experiments. In SI units, k and K have units of m^2 and m^4, respectively. K is a function of geometry and our reported K's here are specific to our geometry.

2.3.3 Results

2.3.3.1 Fault transmissivity measurements

During the transmissivity measurements we made three important observations: 1- during every test, after fault sliding by 0.3 mm, I consistently observed a decline in the fault transmissivity by at least an order of magnitude (Figure S2-2). This change was more pronounced for the rougher fault. 2- for the same conditions, I observed that fault surface roughness results in 4 orders of magnitude variations in transmissivity, with the lowest value for the smooth fault (Figure 2-19). 3- I also observed a time-dependent decline in transmissivity during the first four hours, which is more pronounced for the rougher faults. I do not report the time dependencies here and only report the transmissivities after the initial decline. The time-dependent decline is most probably related to the fault aperture reduction due to creep of rough contacting asperities. Indentation tests, which mimic the single asperity contact, show significant weakening and increased creep rates in limestone in the presence of water (Mighani *et al.*, 2018a). In the following sections, I discuss some of these observations. Solnhofen limestone had a matrix permeability of 16.6 nD at an effective pressure of 5 MPa (Figure S2-1). Hence, compared to the fault transmissivities (equivalent permeability for a fault with transmissivity of 10^{-17} m^4, and opening and width of 20 μm and 0.0254 m, is ~10 D), we would expect a negligible contribution from the matrix flow.

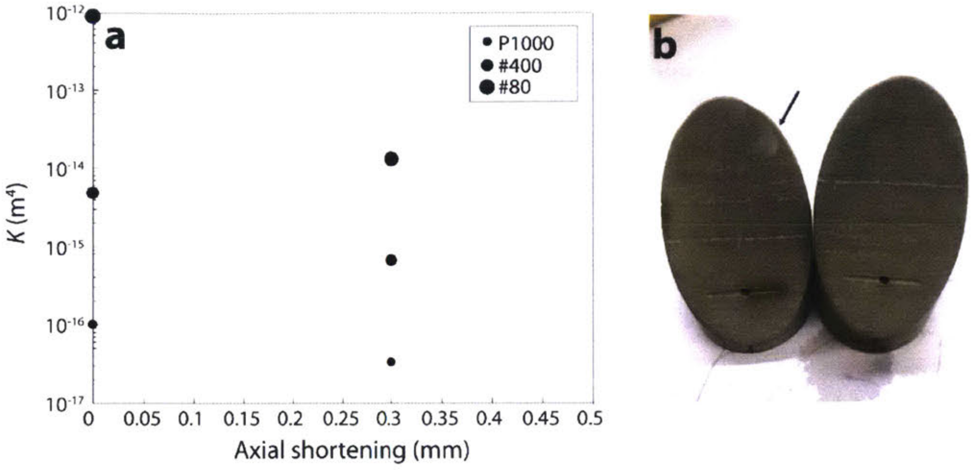

Figure 2-19. (a) Fault transmissivity evolution on a 30° Solnhofen fault for different surface roughnesses. Two things are noticeable: a) by changing the surface roughness only from 1 to 4 μm, the transmissivity varies by 4 orders b) after sliding by 0.3 mm, the transmissivity decreases by ~1 order of magnitude. (b) production of fine gouge grains during fault sliding as shown by black arrow (refer to Figure 2-18b for experimental geometry). Picture shows #400, 30^0 fault surfaces opened up after a transmissivity test and sliding for 0.3 mm. The gouge grains may be produced during the indentation of fault surface asperities (Engelder and Scholz, 1976).

The observations of higher transmissivities for rougher faults is consistent with the observations for tensile (Mighani *et al.*, 2016) and axially failed (Kassis and Sondergeld, 2010) fractures, where rougher fractures showed enhanced transmissivity by sometimes 3 orders. The drastic transmissivity variations of four orders with rms increases of only 0.9 to 2.5 μm is conceivable by relating to the previous analytical/numerical studies of flow properties in rough fractures. (Brown, 1987) suggests the tortuous flow around asperities would make the hydraulic aperture less effective than the mechanical aperture, especially when mechanical aperture approaches the roughness surface roughness at smaller apertures. Hence, it would add to the cubic law. The surface profile spectrum (Figure S2-1) shows ~6 μm distinct heights for the roughest faults compared to the 0.9 μm for the smooth fault. Hence, two orders, according to the cubic law, is the lowest expected bound on the transmissivity difference.

The reduced transmissivity upon sliding has been observed by previous studies. The sheared fault gouges under rotary shear experiments (Zhang *et al.*, 1999) also showed reduced fault permeability in association with gouge compaction, though the normal stresses of 100 MPa and shear displacements of 150 mm were significantly different from our conditions. The triaxial gouge experiments by Morrow *et al.* (1984) also showed reduced permeability upon sliding under high confining pressures up to at least 4 mm slip. The permeability reduction was more pronounced for coarse grains, similar to the rough faults here. One way of viewing the transmissivity reduction after sliding is the wear on the asperities and the subsequent aperture reduction which is shown experimentally and theoretically to directly influence flow properties (Walsh, 1981; Brown, 1987). The wear on the asperities would also produce fine gouge grains (Figure 2-19b) which could clog the flow path for the pore fluid (Vogler *et al.*, 2016).

2.3.3.2 Fault frictional properties

Dry sliding experiments, prior to HF experiments, occurred under stable sliding mode for all surface roughnesses. The boundary conditions for all these sliding tests were constant sliding velocity rate of 2 μm/s. Figure 2-20 shows the variation of the friction coefficient with surface roughness. μ is found to strongly depend on the surface roughness; it increases from 0.1 for the smoothest fault to 0.8 for the roughest fault. It is also dependent on the fault orientation and reduces at less steep fault angles.

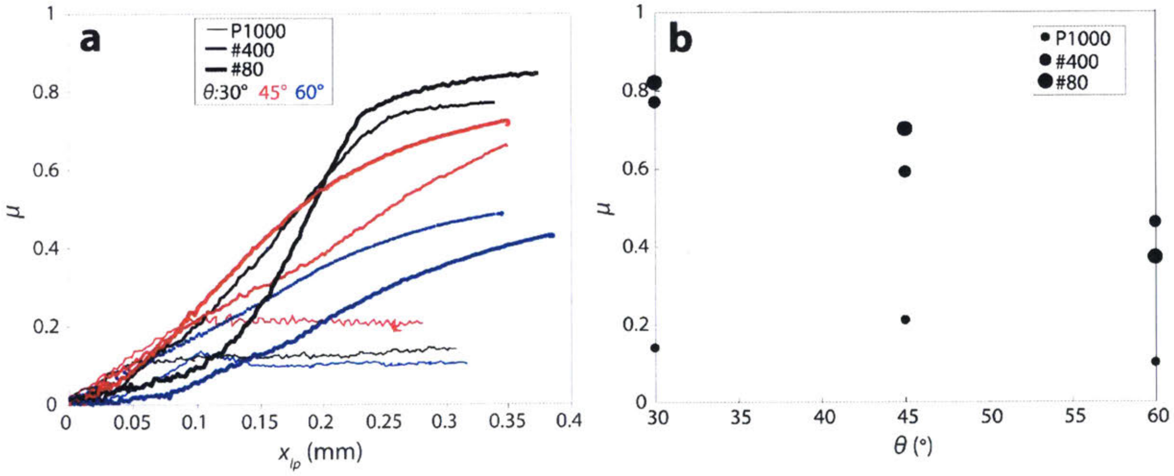

Figure 2-20. Coefficient of friction during the sliding of Solnhofen faults with different roughnesses. (Left) shows the evolution of μ as a function of axial shortening. Thin, medium, and thick lines are smooth, medium roughness, and rough faults. Black, red, and blue colors are 30, 45, and 60° fault orientations. (Right) shows μ as a function of fault orientation for the axial shortening of ~0.3 mm. μ is heavily dependent on surface roughness, as well as fault orientation.

The strong dependence of μ on surface roughness has been observed as well for the low-normal stress friction tests on PMMA; by increasing the surface roughness from P1000 to #600 to #60, μ has been found to increase from 0.3 to 0.57 to 0.75, respectively (Dieterich and Kilgore, 1994; McLaskey, 2011; Mighani *et al.*, 2018c). I also found a dependence of μ on the fault angle, as it decreased for higher fault orientation angles. Lower μ at less steep fault angles has been previously observed in PMMA (Mighani *et al.*, 2018c), Solnhofen limestone (Mighani *et al.*, 2018b), and granite (Savage *et al.*, 1996). The compilation of rock friction data in Figure 3 of (Chen *et al.*, 2013) also shows a direct relation between μ and rms, where μ increases with log(rms).

2.3.3.3 Hydraulic fracture experiments

As we observed in the previous two sections, modifying the surface roughness provided a wide parameter space to explore the influence of fault's friction coefficient and transmissivity. I also modified the fracturing fluid viscosity to investigate how the fluid viscosity would impact the HF-fault interaction. Table 2-8 summarizes the experimental conditions and the name convention for the HF tests.

Table 2-8. The experimental conditions and parameters for hydraulic fracture tests.

Experiment[a]	σ_d **(MPa)**	BP **(MPa)**	**Slip,** d **(μm)**	$\Delta\sigma$ **(MPa)**	**Interaction**
SH-#400-30°-1-watl	1.0	22	9	1.0	Arrest
SH-#80-30°-2-watl	1.8	21	9	1.8	Arrest
SH-#400-45°-1-watl	1.4	20	13	1.4	Arrest
SH-#80-45°-1-watl	1.1	22	12	1.1	Arrest
SH-#400-60°-1-watl	1.4	23	<3	0.3	Arrest
SH-#80-60°-20-watl	19.8	21	5	0.3	Arrest
SH-P1000-60°-2-watl	1.9	24	2	0.4	Arrest
SH-#400-45°-26-SF350	26.3	21	204	11.2	Cross
SH-#80-45°--17-SF350	16.9	20	324	16.9	Arrest
SH-#80-60°-12-SF350	12.0	20	<1	0	Cross

The major motivation was to assess whether the hydraulic fracture was able to cross the fault. For all the rough faults, when using water, the HF was arrested by the fault and was never able to cross the fault. While, during earlier observations (Mighani *et al.*, 2018c), I observed the HF to cross the smooth (P1000) faults. For the viscous fluid cases, the HF was able to cross the fault in some cases. Therefore, it seems that the fault diffusivity controls the cross/arrest conditions. Also, the HF initiated at the borehole bottom and propagated hydraulic fracture was generally sub-normal to the fault strike. This observation is again consistent with earlier observations (Mighani *et al.*, 2018c), where the analysis of elastic stresses showed that the presence fault resulted the minimum principal stress around the borehole to rotate in the direction of perpendicular to the fault azimuth.

2.3.3.3.1 Mechanical results

During the borehole pressurization, after the maximum (breakdown) pressure, the pore pressure declined very fast (faster than the 1 second time resolution of the low-rate pressure transducer) to the value of confining pressure, indicating a fast propagation of hydraulic fracture. The created hydraulic fracture initiated sub-parallel to the axis of cylinder. AE locations confirmed that HF initiated from the bottom of borehole. The axial plane of initiated HF is expected as the confining pressure is the minimum stress and axial stress is always maximum. HF's were always bi-wing, but the two wings were not always co-planar and in some cases were even perpendicular. The propagating HF upon approaching fault created a complex geometry. However, the HF azimuth in most cases was perpendicular to the azimuth of saw-cut fault. The elastic analysis of stresses in our geometry (Mighani *et al.*, 2018c) suggested that the presence of fault results in the rotation of principal stresses close to borehole; so the minimum stress would be perpendicular to the fault azimuth. Future attempts in modeling the propagation of a mode I fracture as it approaches a fault would certainly be intriguing.

The generated HF Upon the intersection of the initiated hydraulic fracture with the fault, fault experienced a stress drop associated with a slip on the fault (Figure 2-21). Provided that the fault slip is large enough to be detected by DCDT, I estimated the fault-parallel slip (equation 3) and report them in Table 2-8. The breakdown pressure values between different experiments were also quite consistent. The average breakdown pressure for all these tests was 21.4 ± 1.3 MPa. This indicates that the prepared boreholes using our drill bits had consistently smooth finishes at the bottom, where HF initiated. Also, the predicted tensile strength from these tests would be 11.4 ±

0.1 MPa according to this equation: $T = BP\text{-}2.p_c$ (Thiercelin and Roegiers, 2000). Using this formulation, to simplify, I assume that the initiated tensile fracture is only dependent on the confining pressure, against which it opens. The viscous silicon fluid showed a more compressible behavior, which might be well due to the compressibility of the silicon fluid and more importantly the large fluid volume in the separator which did not exist during HF tests with water.

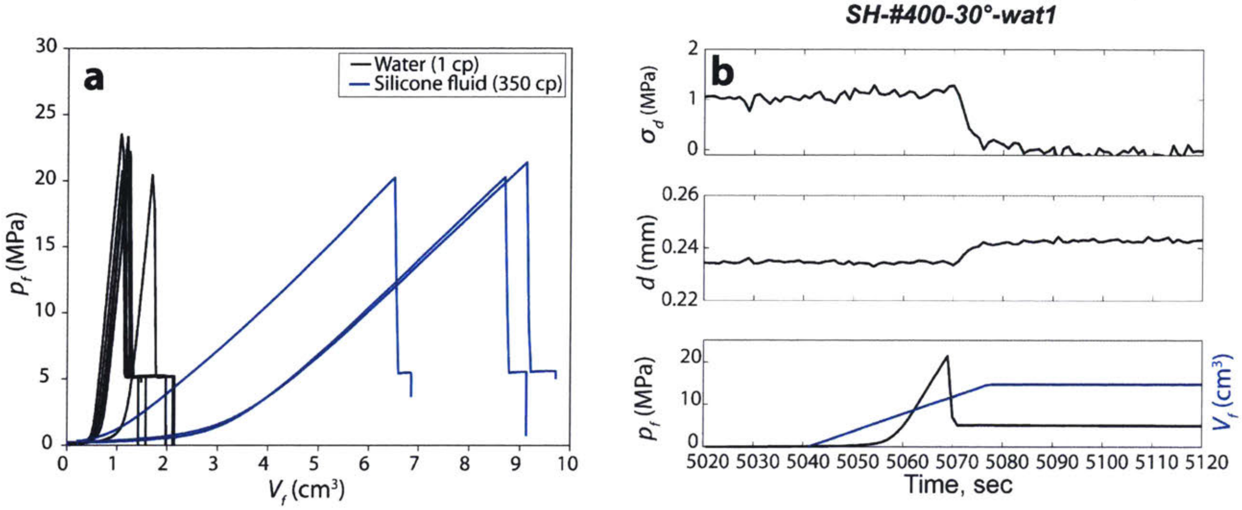

Figure 2-21. Mechanical response during hydraulic fracture experiments. (a) Borehole (pore) pressure vs. pore fluid volume for hydraulic fracture tests. After the maximum (breakdown pressure) pressure, the pore pressure declines to the confining pressure value very fast (5 MPa). The Fast declines indicate fast propagation speeds for hydraulic fractures. Further declines occur after the experiment when pore pressure line is opened to atmosphere. The average of all breakdown pressures is 21.4±1.3 MPa, indicating consistency between all experiments. Fast pressure rises for water indicate lower system compressibility during pressurization, while the silicone fluid was more compliant. (b) Mechanical response during hydraulic fracture experiments. After the HF initiation and intersection with fault a shear stress drop (τ) and fault-parallel slip (d) is observed. This specific case shows the results for "SH-#400-30°-wat1" test (see Table 2-8).

2.3.3.3.2 AE results

During the fluid pressurization, I did not observe many pre-breakdown events. It could be due to either less brittle nature of Solnhofen limestone, or the low sensitivity of AE transducers, or high recording triggering thresholds (0.1 V ~ M-8). Also, the relatively high injection rates compared to low matrix permeability would not allow enough time for the fluid to diffuse into the near-borehole region, to result in local shear or tensile failures. Hence, the chance for local activities decreased. Figure 2-22 shows the generated AEs on 10 acoustic emission transducers along with the record of high-rate pore pressure transducer.

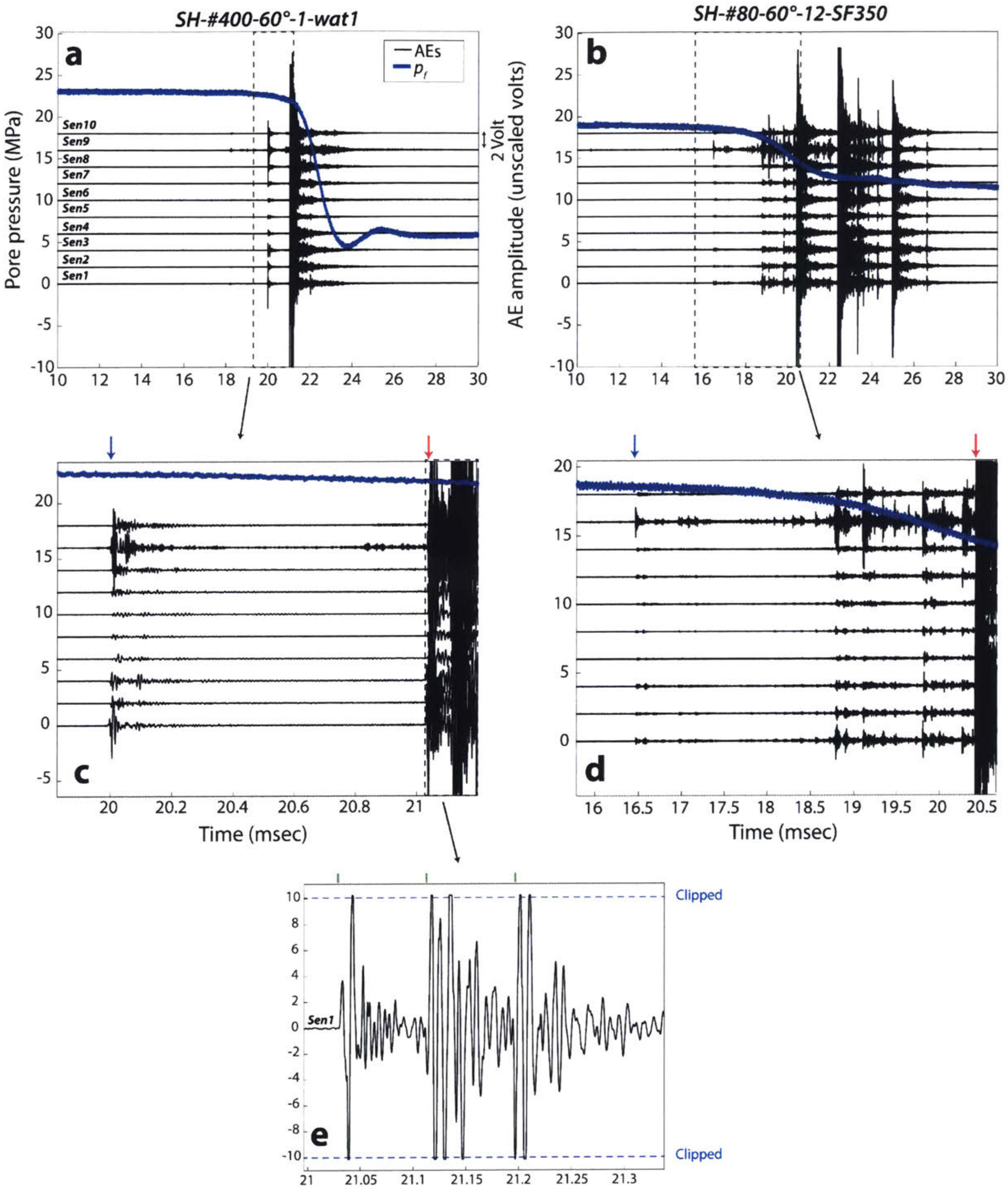

Figure 2-22. High rate acquisition of AEs and pore pressure during two hydraulic fracture tests. c and d show the magnified view of dashed black windows in a and b. Blue and red arrows in c and d correspond to the inferred HF initiation and slip on the fault, respectively. e shows the magnified

view of sensor 1 response from black dashed window in c. The response is clipped beyond ±10 V. Green vertical lines in e show the initiation of consecutive events, where the arrivals of only first event is identifiable.

Note that the transducer response is time-shifted considering the p-wave velocity of water (see procedure section) to synchronize with AE data. Not all the experiments recorded the tensile fracture initiation events. In Figure 2-22, I show the experiments, where we also observed tensile fracture events (blue arrows in Figure 2-22). Upon the intersection of HF with fault, a high energy burst in energy is observed due to the slip of the activated fault (red arrow in Figure 2-22). Separate suites of tests (Mighani *et al.*, 2018c) have shown that this burst is associated with a drop in local stresses and registration of slip on a laser vibrometer focused on load point, confirming the slip.

The intersection of HF with fault is also associated with a drop in pore pressure. A steep decline in pore pressure is associated with the fault slip; although during HF initiation, pore pressure shows a slow decline, which might be due to the opening of HF. However, the opened volume is much lower compared with the lost fluid on fault surface. The pore pressure decline for the viscous case seems also slower compared to the test with water. Also, the viscous case shows more activities during fault slip, as well as during the HF propagation. Below, I will compare the characteristics of these generated AEs and the pore pressure time series.

For each experiment, I created a catalog of about 10's of discrete events from the 5 MHz continuous recordings. The single events generally had durations of <~400 μs, with slip events having longest durations with endured low-frequency tremor-type ringing of AE transducers. The ringing made the first arrival pickings of the sequential slips difficult (see Figure 2-22c). Out of these, I was able to locate a handful of AE events during each experiment. The HF initiation events.

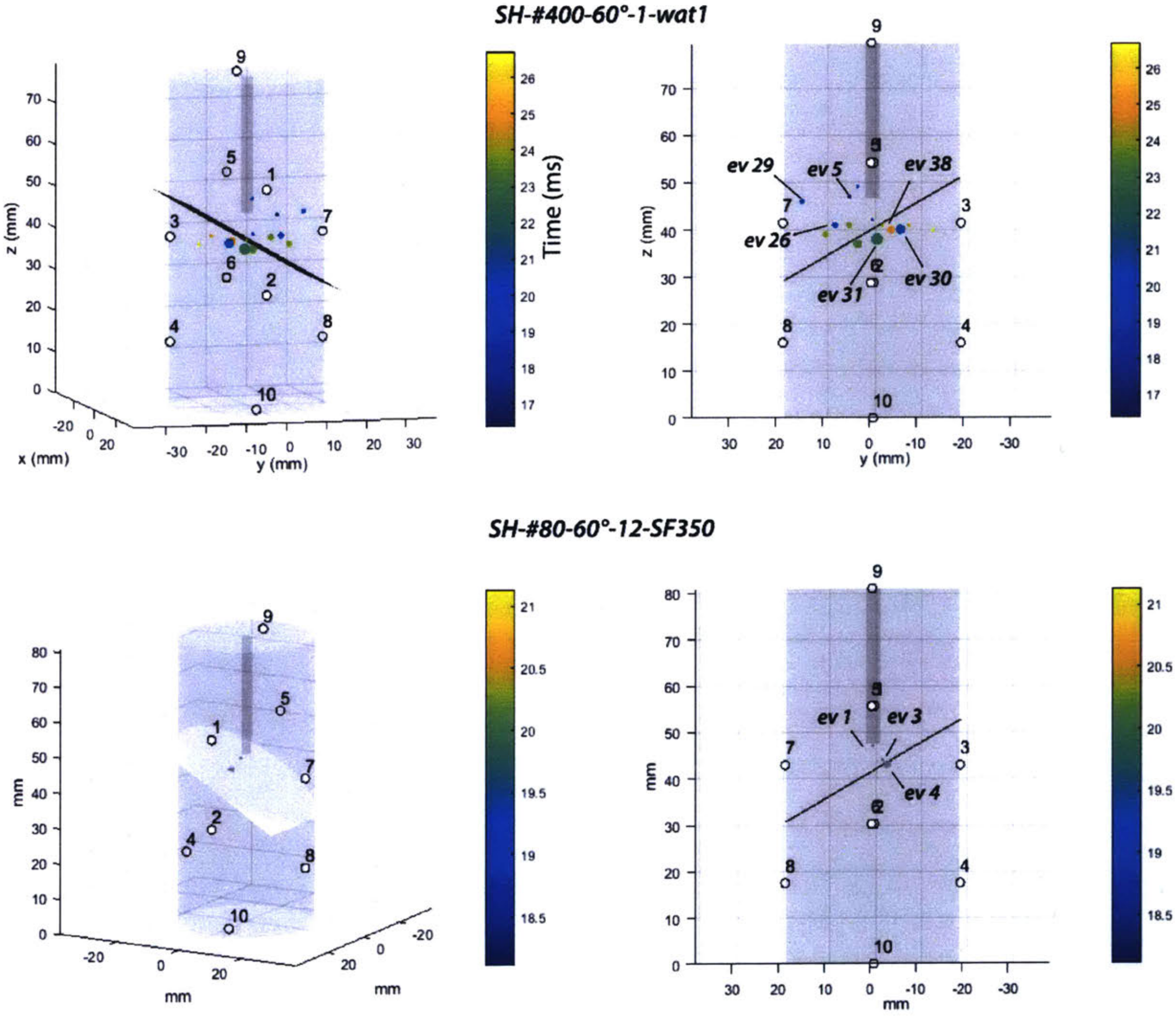

Figure 2-23. The located AE events for two hydraulic fracture experiments shown in Figure 2-22. The size and color of the events correspond with the moment magnitude (see Figure 2-24 and Moment magnitudes section) and timing of the events. Although the fault orientations are similar, the viscous fluid (top case) results in much more generated AE events.

One opportunity in our experiment was the ability to physically distinguish between the pure hydraulic fracture vs. HF-fault interaction events. This allows us to evaluate distinct features of both event types; while, generally during HF tests the AEs are mixed. As the event locations indicated, the AEs initiated from the borehole and travelled towards the fault as expected. I compare the absolute moment magnitudes obtained using ball drop calibrations. Figure 2-24 shows the spectrums for four selected events, two located at the borehole during HF initiation, and two at the fault intersection. Both raw recorded spectrums and the corrected and calibrated spectrums (see Appendix S4) are shown in this figure.

Characterizing the source dimensions from these sensors is ambiguous due to sensor transfer function which may mask source events; however, the first 3 μs shown as red segments suggest that the first P-motion rise time, i.e., source duration, is 3-5 μs. This suggests a corner frequency of 200-350 kHz for these events. Since the source characteristics in tensile, shear, or even ball drop are different, I did not fit any theoretical spectrums onto our calibrated signals to get more information such as corner frequency or frequency-dependent moment drops. Such details are beyond the scope of current report. Also, note that these differences have not been taken into account during moment calibrations as all AE sources have been taken as internal sources compared to external ball drop sources. To report the moment magnitude of events I take a flat response between 20-50 kHz frequency band for our events, as it is well below the corner frequency (also see Figure 2-24a).

The workable frequency range for AEs was 20-300 kHz, above which the signal was overridden by noise [see low signal-to-noise ratios (SNR) in Figures S5 and S6]. Such frequencies are well resolved in the recorded events considering our 5 MHZ acquisition rate. Frequencies below 20 kHz were filtered by the preamplifier's high-pass filter; frequencies above 300 kHz are expected to attenuate by cm's [frequency-attenuation relation: $f = 2(A/\Delta A)(V_p Q/r)$]; taking Q factor (1/attenuation) of 103 for Solnhofen (Kern *et al.*, 1997), for $f >$ 360 kHz, the amplitude drops to below 10% after only a 2 cm traveling distance]; so they may not reach to all transducers.

One caveat in obtaining the moments for AEs from the ball drop event is the fact that they are not collocated, and events might be affected by propagation effects, such as geometrical spreading, or the medium's attenuations. Moreover, the sensitivity limitations, such as finite aperture, sensor-sample coupling, and uni-directional sensitivity of sensors also result in amplitude dampening. To take into account the geometrical (spherical) spreading, while assuming negligible attenuation (as our Solnhofen sample is low-porosity, free of stress-induced damage, and in dry state; Q factor (1/attenuation) for Solnhofen is 103 (Kern *et al.*, 1997), 5 times higher than granite values (Wulff *et al.*, 1999)) and neglecting incidence angle effects, some studies report the estimated average of amplitudes, normalized at a sensor-event distance sphere of 10 mm (Zang *et al.*, 1998; McLaskey and Lockner, 2014). But, since our reported moment magnitudes rely on averaging the entire event spectrum over all sensors, I simply do not consider the propagation or station effects. Also, most of our events are within the virtual sphere enclosed by the sensors. This means that the closeness of an event to one sensor would be traded off by its farness from the opposite sensor. So, by averaging over all sensors, the geometrical effects would be alleviated. Nevertheless, since the occurred surface ball drop events are farther than any internal AEs, the reported absolute moment magnitudes would then be upper limits. If the same ball drop event had occurred at the sample center rather than its top, the ball drop amplitudes would be ~3 times higher (considering only spherical spreading, $1/r$). So, the moment magnitude of the calibrated events would be shifting by at most -0.3 [$2/3.\log_{10}(1/3)$] for our sample. One more interesting observation is the subtle resonance of events at ~200 kHz (see blue line in Figure S2-6d); the radial resonance mode of 1.5 MHz PZTs are expected to be slower by their diameter/thickness ratio of ~6.2, i.e, 240 kHz, matching the observed resonances. Bi-modal spectrum are also observed during active ultrasonic acquisitions via p-wave PZTs by Stanchits *et al.* (2003).

The released seismic moment during HF initiation is ~0.04 N.m (for M~-7). The released mechanical work during the HF propagation is the released Griffith-type fracture energy, $2G.c$, and the work exerted for opening the HF against confinement before HF reaching the Comparing the released during hydraulic fracture experiment.

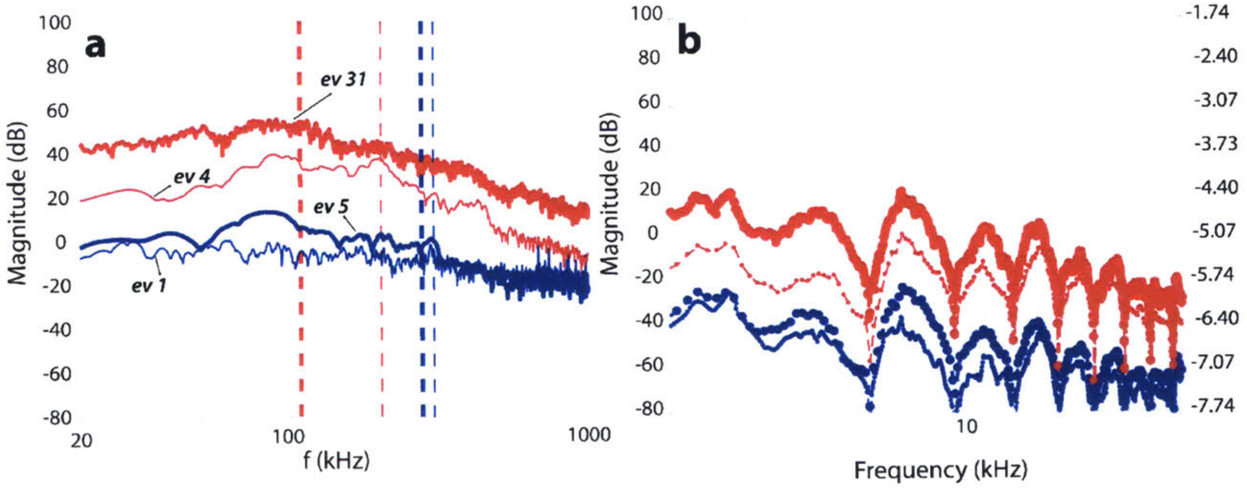

Figure 2-24. Moment magnitude of generated AE events. a and b show the raw and corrected amplitudes, respectively, for two HF (blue) and two fault interaction (red) events. Event numbers

are consistent with Figure 2-23. Dashed lines in a show the corner frequency limit for reach event, above which the amplitude declines. Notice the right y axis in b showing the moment magnitudes. Troughs in b are due to the calibration with respect to ball drop tests (see ball drop troughs in Figure S2-6).

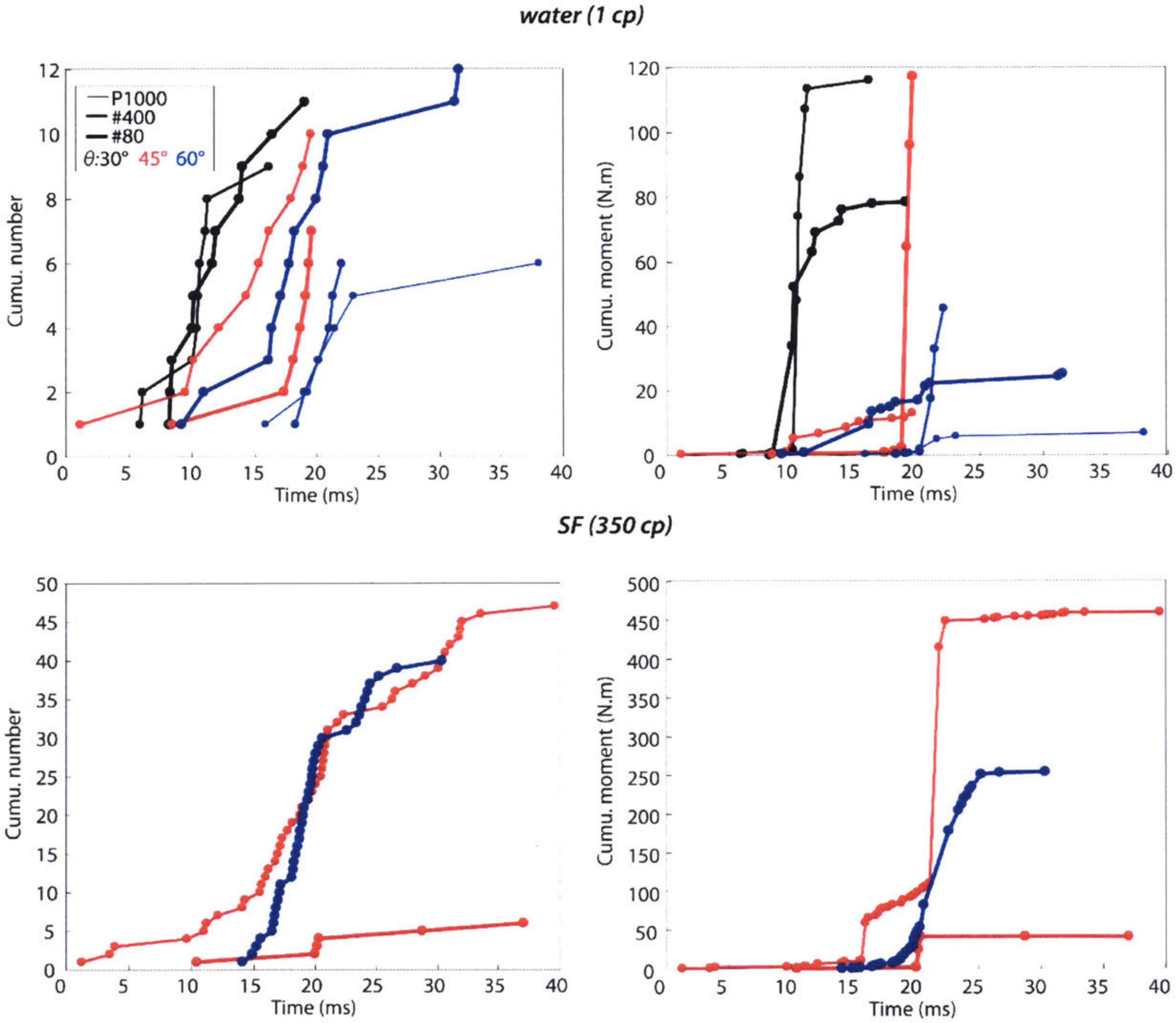

Figure 2-25. AE hit numbers and released seismic moments during entire experiments.

2.3.3.3.2.2 Moment tensor

The full (unconstrained) moment tensor inversion has the benefit of deriving the volumetric components, in addition to the generally described zero-volume DC components. The AE events showed complex sources, where a contribution from the three ISO, CLVD, and DC components were observed. Figure 2-26 shows the source-type plot for selected located AE events during "SH-#80-60°-12-SF350" experiment. Only few events on each experiment resulted in acceptable moment tensor solutions (misfit less than 0.3 on all sensors, and RMSE<0.3 in Figure 2-26c). Some high energy events were clipped; whenever possible, I used the split attenuated signals on sensors 3, 7, 9, and 10. The events seem to initiate as tensile events during HF initiation; they then migrate towards the center of the source-type plot by losing isotopic component. And, finally the DC events, as well as fracture closure events are observed. The uncertainties due to location and first amplitudes uncertainty seem to result in scatter, especially for events near DC corner. However, they mechanisms are still distinct. Table 2-9 also summaries the decomposed components. HF initiation events show 0.42 ISO component (thought as an explosive point source), 0.35 CLVD (thought as Mode I fracture opening, though more difficult to picture), and 0.23 DC (zero-volume fault-parallel slip); while the events on the fault have more DC components as expected, with contribution from CLVD. The CLVD during the intersection might be due to normal displacement modes on the fault. The pressurized fluid may well help this normal mode.

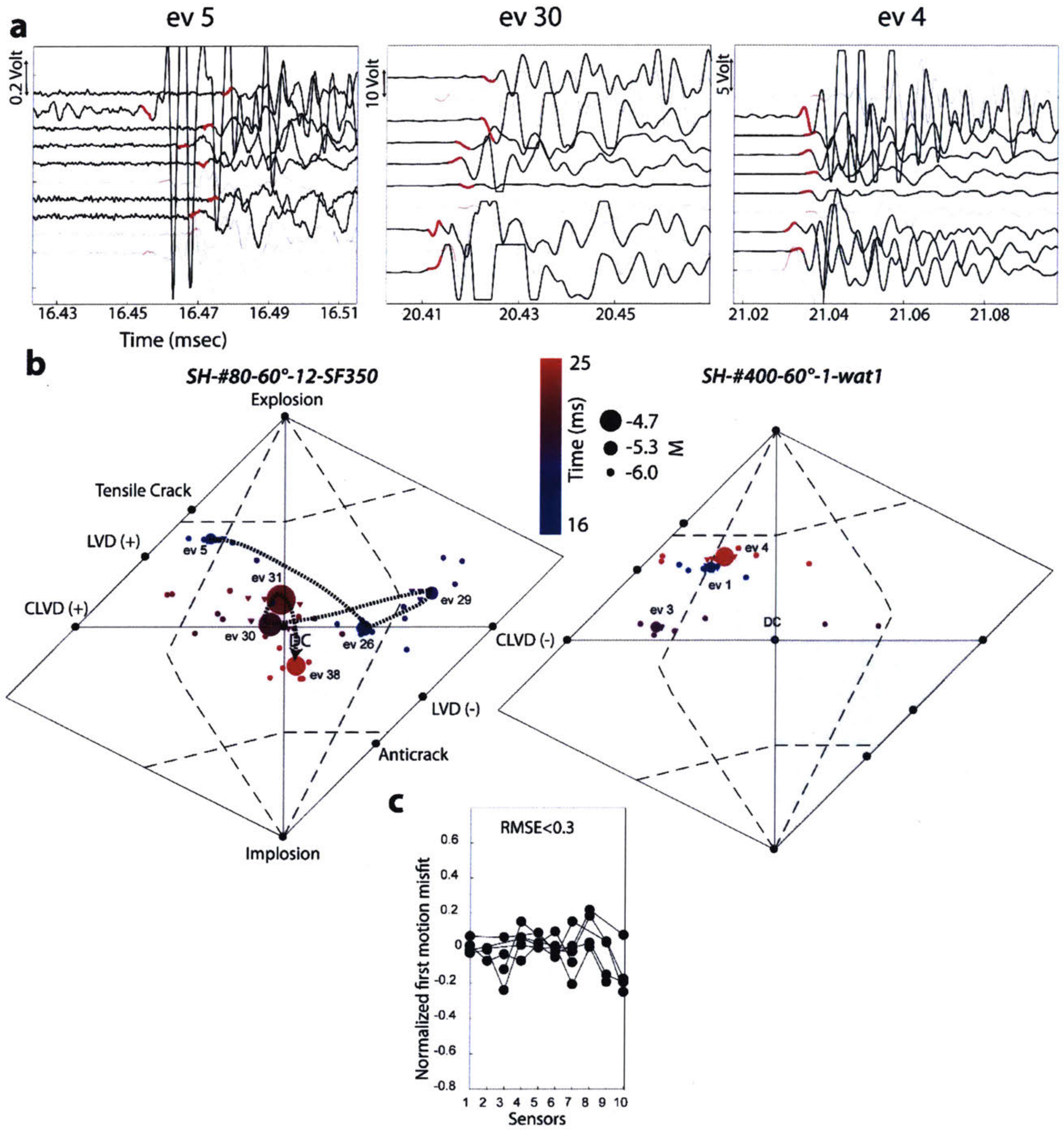

Figure 2-26. Moment tensor results of AE events. a shows the waveforms sensors for three typical HF initiation and crossing/arresting by the fault. Waveforms with misfits>0.3, shown as gray lines, were neglected for inversions. The first 3 μs of P arrivals are shown as red segments. b shows the Hudson plot for events (marker size and color represent scalar moment magnitude and event time, respectively). Small circles and triangles show the solution uncertainty with respect to the location

(±3 mm) and amplitudes (±20%), respectively. c shows the inversion misfits on sensors for all the events.

Table 2-9. The component decomposition of moment tensors.

	ev5	**ev30**	**ev4**
Focal mechanism			
ISO	0.42	0.01	0.39
CLVD	0.35	0.06	0.24
DC	0.23	0.93	0.36
Volumetric (ISO)	0.42	0.00	0.39
Non-volumetric (CLVD+DC)	0.58	0.99	0.60

I decomposed the moment tensors into DC components [fault plane solutions; (Conder and Arciniegas, 2017)]. The isotopic components are also represented as rectangles whose dimensions are the diagonals of the normalized tensors, considering the signs (see Figure 2-27). The HF initiation event (ev 5) shows no DC solution, while all diagonal terms are positive (compressional on sensors and dilational inside medium). The maximum direction (11) is consistent with the visual direction of opened tensile fracture. The latest event (ev 38) also shows negative diagonals, with maximum in (11) direction; it is probably the HF closure event, which showed consistent directionality. Also, the volumetric components during intersection may indicate fault opening, although the directionality of the event is less conclusive.

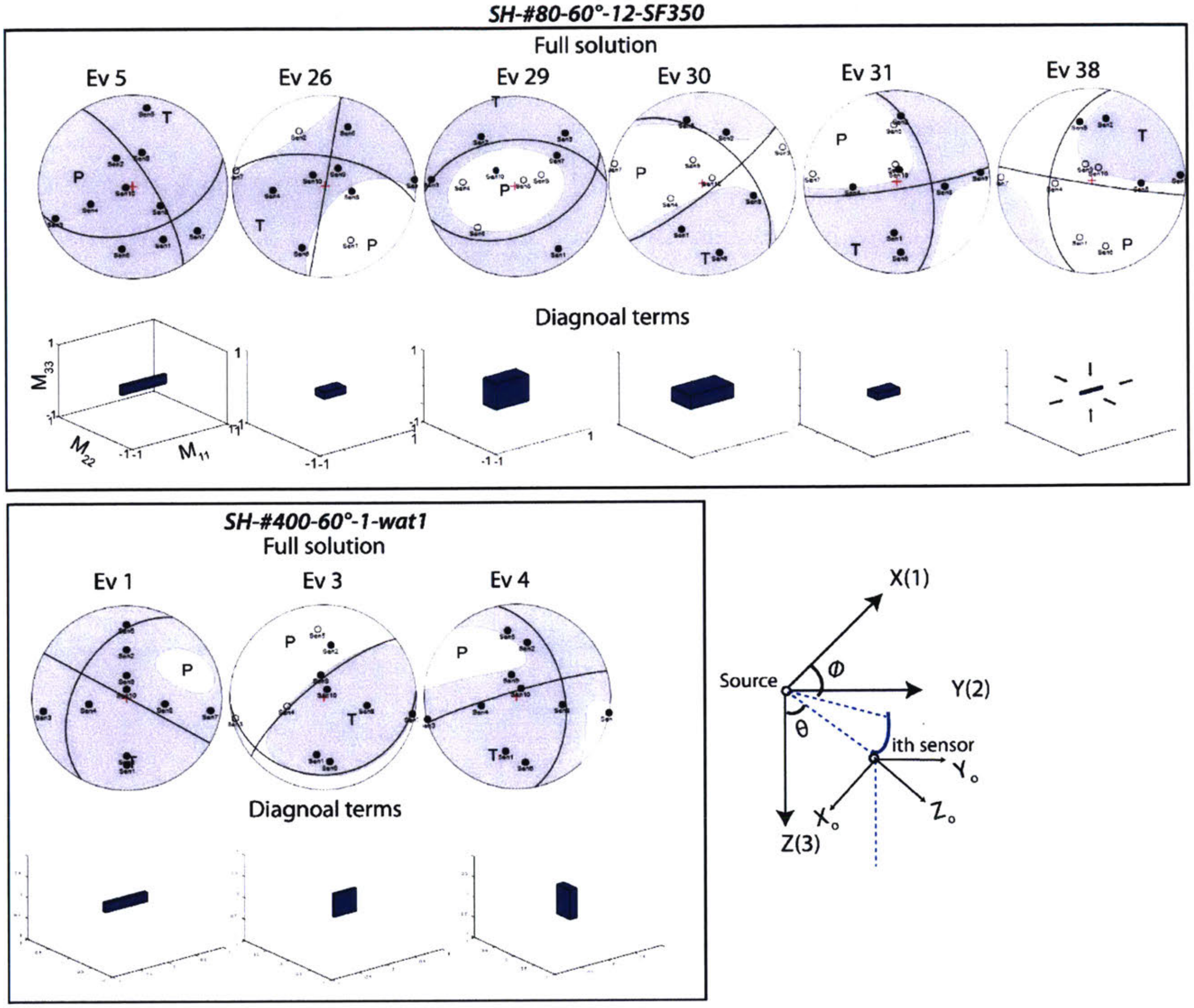

Figure 2-27. The full moment tensor and diagonal terms of the normalized moment tensors. b shows the beach ball solution for both DC and ISO components. e shows the global coordinates (XYZ), source coordinates ($X_0Y_0Z_0$), and the take-off and azimuth angles.

The hydraulic fracturing tests showed source mechanism changes during the propagation of hydraulic fractures; the source initiated as +isotropic-dominant components during HF initiation; then, they migrated more toward DC components as the HF intersected with the fault. At this point, the source mechanism of cross vs. arrest events were not discernible; however, the crossed event on the other side of frictional interface were more +isotopic, meaning tensile events. The fault solutions for the DC components were consistent with the fault orientation. And, the ISO component shows the direction of opening. Hydraulic fracture experiments by (Li *et al.*, 2019) in two-dimensional geometry show a DC component contribution of 60% during the experiments, where DC components concentrated near the sheared regions.

2.3.3.4 High rate pore pressures

The pore pressure recordings are summarized in Figure 2-28. I also insert a modeled decline of pore pressure for a fault with transmissivity of 10^{-8} m^4 [see (Mighani *et al.*, 2018c)]. The pore pressure declines suggest that the dynamic fluid diffusivity of the fault enhanced by at least 4 orders of magnitude upon slip, compared to the quasi-static transmissivity values that were reported.

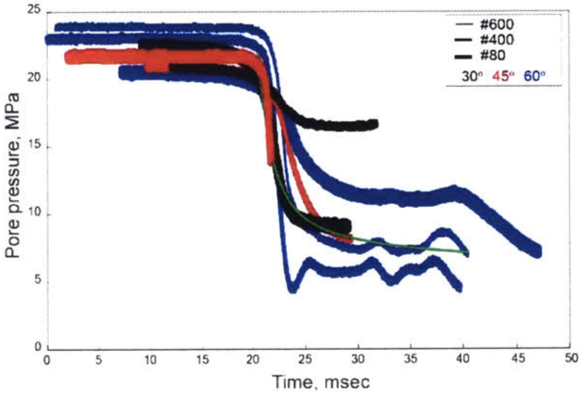

Figure 2-28. This figure shows all pore pressure declines during HF tests (using water). Green line shows the numerically modelled transient pore pressure decline [see (Mighani *et al.*, 2018c) for details] with $K \sim 10^{-8}$ m^4. Therefore, the transmissivity during fault slip was at least 4 orders of magnitude higher than its quasi-static measured values.

2.3.4 Cross vs. arrest

Similar to the discussion of arrest vs. cross in section 2.1, I plotted the data points onto the existing criterion of Blanton (1986). Again, this analysis suggests that the criteria are not consistent with the experiments as discussed in section 2.1.

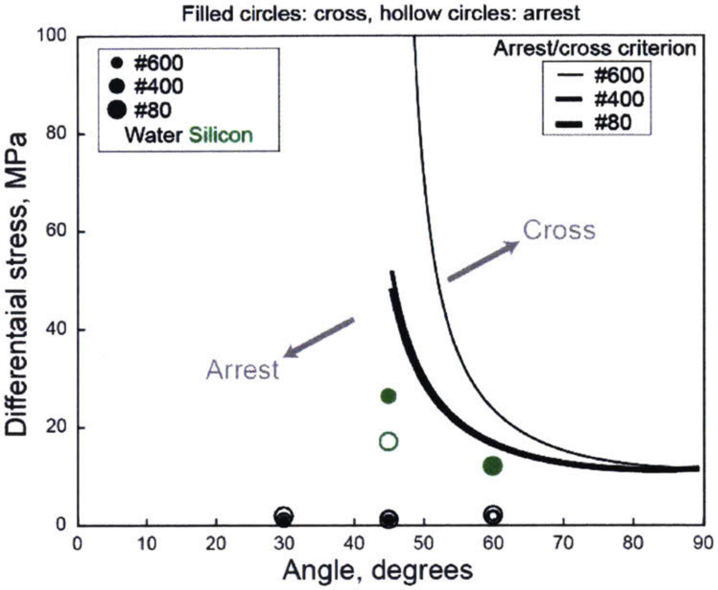

Figure 2-29. Experimental data points of section 2.3 compared to (Blanton, 1986) criteria. The experiments always lie below the required cross conditions of (Blanton, 1986), yet in some, the HF was able to cross the fault.

However, as the transmissivity and the fluid viscosities were known, I tried to compare the cross vs. arrest in term of fluid diffusivity (*K*/*η*) of the fault. I sorted the experiments in terms of their quasi-static diffusivity in Table 2-10. There seems to be a threshold below which the HF is able to cross. However, at this point, it is not clear whether the fault has slid before the HF intersection; thus, the exact roles of quasi-static and dynamic transmissivities are subject to question.

Table 2-10. The experiments sorted with respect to their fluid diffusivity. The gray and white rows show the crossed and arrested experiments, respectively.

Fault finish (#)	Fault angle (°)	Fluid η (Pa.s)	Fault K (m^4)	**K/η (m^4/Pa/s)**	HF interaction
600	30	0.001	3.3×10^{-17}	**3.3×10^{-16}**	Cross
400	45	0.35	6.6×10^{-16}	**1.9×10^{-15}**	Cross
80	60	0.35	9.8×10^{-15}	**2.8×10^{-14}**	Cross
80	45	0.35	1.3×10^{-14}	**3.7×10^{-14}**	Arrest
400	30	0.001	6.6×10^{-16}	**6.6×10^{-13}**	Arrest
80	30	0.001	1.3×10^{-14}	**1.3×10^{-11}**	Arrest

2.3.5 Conclusions

We observed how the fault diffusivity influences the interaction of HF and fault. Although at this point it is not clear whether the quasi-static or dynamic transmissivities are relevant to assess the cross vs. arrest conditions, the quasi-static transmissivity values seem to correlated with the ability of the HF to cross the fault. The dynamic transmissivity of the fault, measured by the high-rate pore pressure transducers, is found to increase by more than 4 orders of magnitude.

The detailed acoustic emission analysis in this chapter showed the location of the initiated event and how the HF propagates towards the fault. The AE magnitudes, from HF initiation ~-7 grew larger as the HF intersected the fault, i.e., ~-5. The location of events and the event types, tensile, shear, and closure, determined from moment tensor analysis were logically consistent with measurements of slip and pore-fluid changes. The diagonal terms of moment tensor, also seem to be an indicator for volumetric deformations at the source and the directionality of this volume.

Supplementary information

Text S1-surface roughness measurements

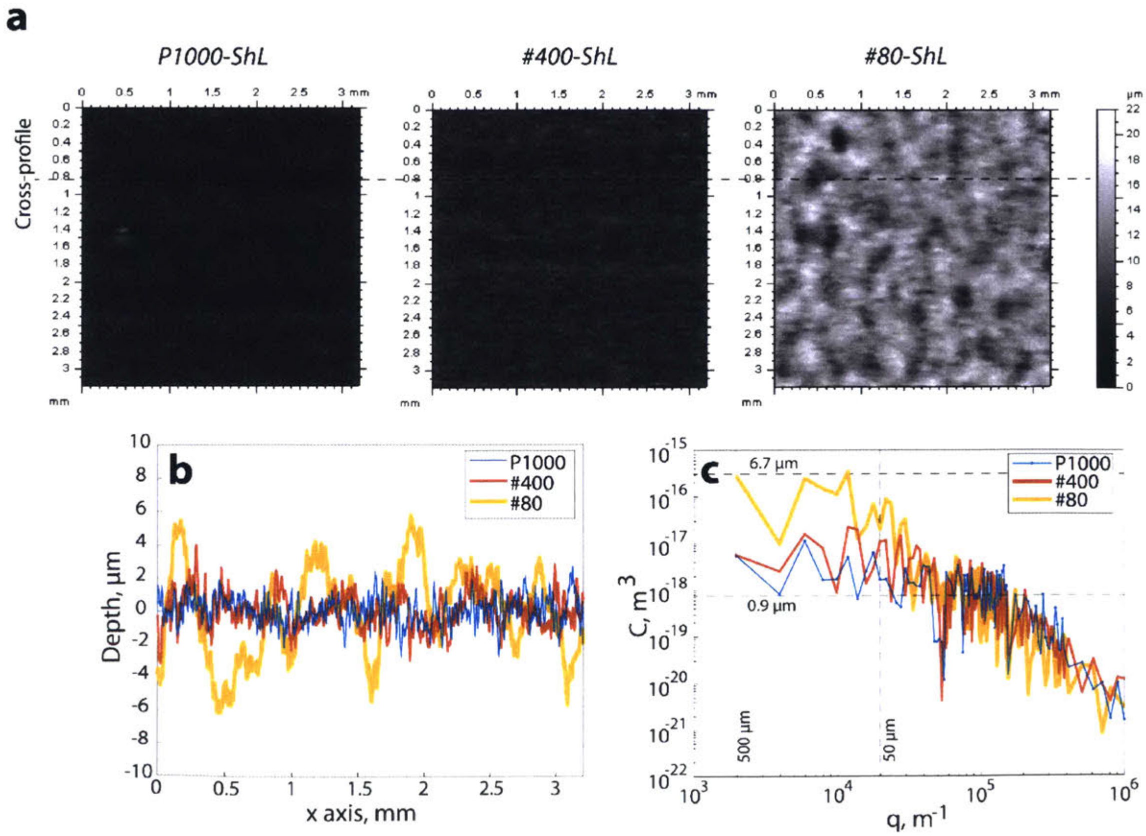

Figure S2-1. Surface roughness measurements of faults with different surface finishes in Solnhofen limestone (ShL). (a) measurements are conducted using a Talyscan 150 (Taylor Hubson Ltd.) laser profilometer. Surface heights are scanned in 1 μm (x, y) steps over a 3.3 mm × 3.3 mm surface area. Bottom profile in b shows the cross-profile along the dashed line in the top figures. The nominal height resolution is 20 nm, though the laser spot itself has a practical resolution of ~1 μm. The surface roughness data have been processed to remove rigid-body tilt, and an 800 μm Gaussian filter has been applied to remove the long-wavelength waviness. The surface finishes of P1000, #400, and #80 show rms roughness values of 0.91, 1.06, and 2.47 μm, respectively. c shows the extracted spectrum of 1D profile shown in b (Kanafi, 2016).

Text S2. Permeability measurements

In this section, I describe the pore fluid pressure and flow rate during permeability measurements tests. During the permeability measurements, I used two pumps, depending on how low of a flow rate we were trying to measure. All reported permeability tests used deionized water. We were able to measure a minimum flow rate of 4.2×10^{-10} cm^3/s on a closed pore pressure system. This is equivalent to a minimum obtainable permeability of ~0.02 nD on a 25.4 by 25.4 mm cylinder using the pore fluid system.

Figure S2-1 shows the results for matrix permeability measurements on a 25.4 by 25.4 mm cylinder of Solnhofen limestone. Prior to measuring the matrix permeability, the cylinder was vacuum-saturated and was left under saturation inside the triaxial vessel under closed pore pressure system until an insignificant flow rate was obtained ($<10^{-9} cm^3/s$ in Figure S2-1). The downstream was then opened to the atmosphere for permeability measurements. The measured matrix permeability was 16.6 nD. In a different test at differential stress of 14 MPa, similar to the maximum exerted stress levels on the fault during sliding tests, the matrix permeability remained in the same range value, i.e., 14.3 nD.

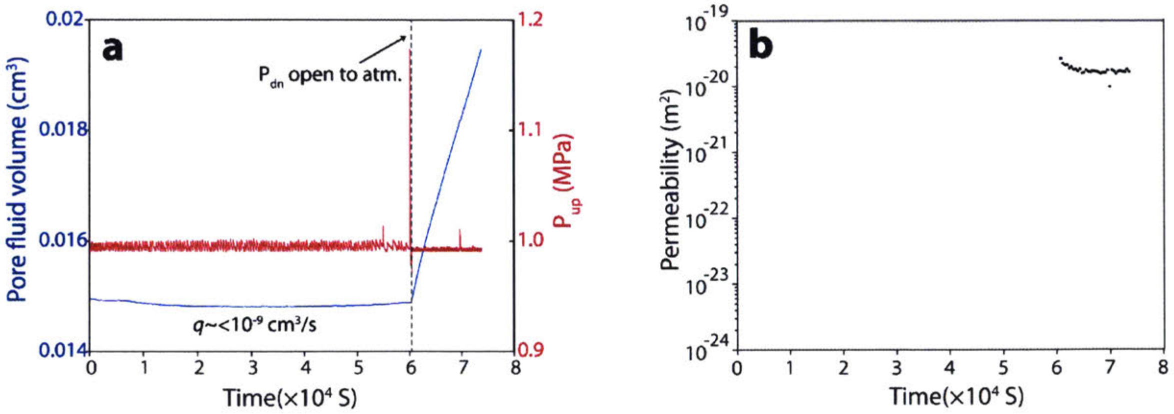

Figure S2-2. Solnhofen matrix permeability measurements. (**a**) shows the pore fluid volume (blue line) and upstream pore pressure (red line). After ensuring the full saturation ($q<10^{-9}$cm^3/s), the downstream was opened to the atmosphere. (**b**) shows the matrix permeability after opening the downstream to the atmosphere. Notice the linear fluid volume slope (steady state flow rate) in **a**.

Following are the results of the fault permeability measurements for a P1000 30^0 fault, which were run under similar confining and pore pressures as in Figure S2-1; the faults were slid and the fault transmissivity was tracked.

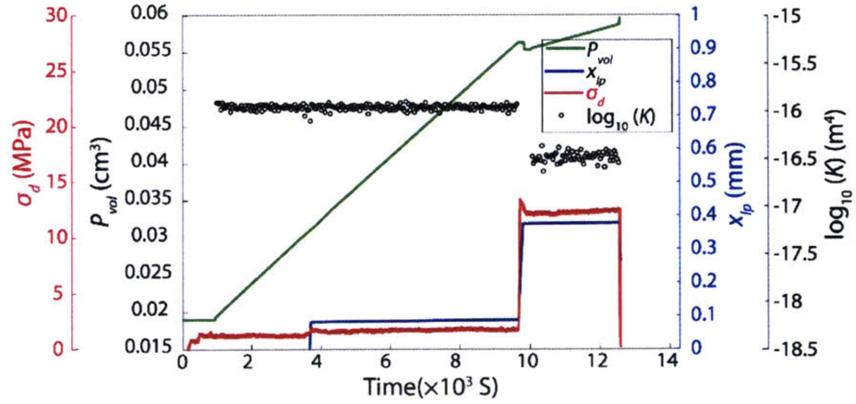

Figure S2-3. The evolution of fault transmissivity during sliding of a 30° smooth fault in Solnhofen limestone. The effective pressure during the entire experiment was 5 MPa. The fault transmissivity prior and after sliding was 1.0 e-16 and 3.3 e-17 m^4, respectively. Transmissivities are reported every 40 seconds.

Text S3. Mechanical results

Figure S2-4 shows the shear stress vs. displacement for sliding on a 60° smooth fault with a constant displacement rate of 2 μm/s. Only in this anomalous test, I observed subtle stick-slip, unless all other stable sliding observations Figure 2-20. Possible reasons for the stick-slip observations is the fault surface modifications and consequent mating; this could occur via vaporizing the polishing fluid moisture and vacuum production on the fault surface or having the fault remained under confining pressure for an extended period of time. I show the shear stress and friction coefficient evolution during sliding in Figure S2-4. I used this test to derive the system stiffness ($k_{lp}=\tau/x_{lp}$), as the fault remained locked between stick-slips (see Figure S2-4). The system stiffness was 73 MPa/mm. For PMMA, the system stiffness was 20 MPa/mm.

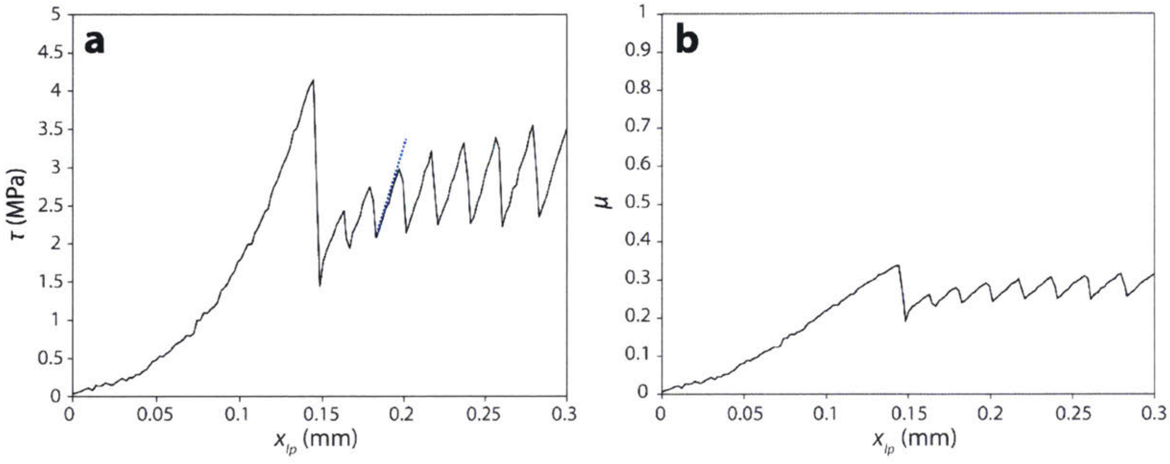

Figure S2-4. Shear stress evolution during sliding of a 60° smooth fault at 2 μm/s. This fault showed anomalous subtle stick-slip (unlike all other tests in Figure 2-20). I used the loading slope between stick-slip events (blue line) to infer system stiffness. An essential condition for deriving the stiffness is having the fault locked up. Similar loading slopes between stick-slips supports this.

Text S4. AE signals

In order to estimate the moment magnitude of the AE events and, as well as study possible distortions of the preamplifier+acquisition system on AE response, I recorded the AE events from free-fall ball drop events on top of the sample, for which I knew the theoretical released moment (McLaskey *et al.*, 2015). The ball drop experiments were conducted on the bench-top, where a steel ball with a diameter of 6.3 mm and mass of $m = 1.02\ g$ dropped from a height of 7 inches onto the center of sample's top surface (Figure S2-5). To ensure a good sample/sensor coupling, I pulled vacuum on the jacket (equivalent to 0.1 MPa confinement). I infer the first impact velocity from $v_1 = \sqrt{2h/g}$ with h and g being the free-fall drop height and Earth's gravitational acceleration, respectively. The time difference between the first and the second impact, Δt, is used to compute the rebound velocity as $v_2 = \sqrt{g.\Delta t/2}$. The change of momentum is then calculated as $\Delta P = m(v_2 - v_1)$ where v_i is a vector. The theoretical impact source spectrum is then obtained from the spectrum of the theoretical force-time function normalized by the change of momentum. The instrument-apparatus response spectrum, Ψ_{ext}, was then derived by dividing the measured signal by the theoretical spectrums (see Figure S2-6d).

The corner frequency in the ball drop experiment for limestone is 34 kHz. The change of momentum (ΔP) in the ball drop experiments in limestone is 0.0035 N.s. For internal AE sources, the instrument response, Ψ_{int}, is obtained from the observed AE signal, i.e. S_{int} (McLaskey *et al.*, 2015):

$$\Psi_{ext} = C_{F\dot{M}} \cdot \Psi_{int} \tag{S1}$$

$C_{F\dot{M}}$ is the force-moment-rate constant which is equal to $(V_p + V_s)$ with V_p and V_s being the material's compressional and shear velocity, respectively. $C_{F\dot{M}}$ for limestone is 8.9 km/sec. And, for an AE source:

$$S_{int} = M_0 . \Psi_{int} \tag{S2}$$

Now, combining equations A1 and A2 I can obtain the moment of the internal AE events as:

$$M_0 = \Delta P \times C_{F\dot{M}} / (\Psi_{ext}/S_{int}) \tag{S3}$$

And the equivalent moment magnitude is (Hanks and Kanamori, 1979):

$$M = 2/3 \times log_{10}(M_0) - 6.067 \tag{S4}$$

The equivalent moment magnitude for ball drop experiments in PMMA and limestone is -5.31 and -5.04, respectively.

Figure S2-5 shows the ball drop trials on Tennessee sandstone with and without preamplifier. For each case, I repeated the ball drop for three times. To make the amplified/unamplified first motions consistent, I mirrored the signal for one particular channel. The consistency of first motions after this treatment in repeat experiments suggests this phase reversal was probably due to internal electronic circuits in preamplifier. The first P-wave motions for both un-amplified and amplified signals have positive polarities which is expected from the explosive-type ball drop event. The polarity consistencies are also reconfirmed by observing a hammer strike event on the piston top outside the pressure vessel. The nice thing is the sample is under experimental stress condition; however, this is just a sign check and by no means provides quantitative amplitudes (see Figure S2-6e). The first motions on all sensors are positive for this explosive-type hammer strike. The theoretical ball drop event duration was ~36 μs, while the observed ball drop event duration was ~500-700 μs. The long observed event duration might well be due to sensor ringing, or the coda waves due to superposition with the reflections from the sample surfaces. Comparing the spectrum of ball drop events (Figure S2-5b) suggests that the signal-noise-ratio (SNR) for amplified events is acceptable for 20-250 Hz (background noise for amplified events was ~150 mv; see Figure S2-5b). However, the unamplified events extend up to 350 kHz.

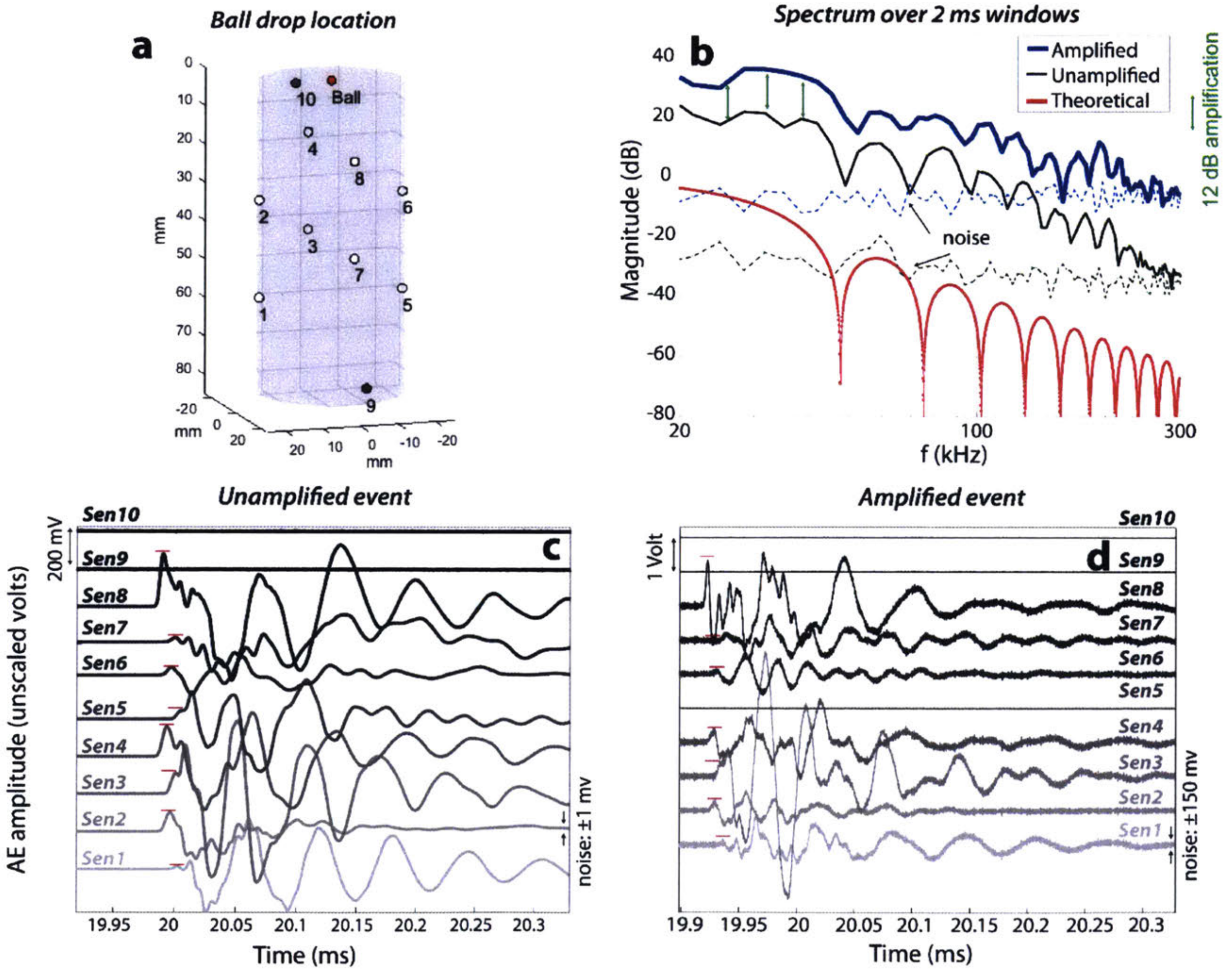

Figure S2-5. Ball drop AE events on Tennessee sandstone. **a** shows the ball drop location (red mark at [0, 0, 0] coordinates), where sensors 1-8 (gray marks) were active and 9-10 (black marks) were inactive. **b** shows the spectrum of theoretical and average of observed ball drop events in **c** and **d**. dashed lines in b are the noise spectrum. Red horizontal bars in **c**, **d** show the first motions.

I then repeated ball drop experiments on Solnhofen limestone. By the time emitted stress waves from the source arrive to the receivers, the first motion amplitude has been dampened due to several propagation effects such as geometrical spreading, or the medium's attenuations. Moreover, the sensitivity limitations, such as finite aperture, sensor-sample coupling, and uni-directional sensitivity of sensors also result in amplitude dampening. To take into account the geometrical (spherical) spreading, while assuming negligible attenuation (as Solnhofen sample is low-porosity, free of stress-induced damage, and in dry state; *Q* factor (1/attenuation) for Solnhofen is 103 (Kern *et al.*, 1997), 5 times higher than for granite (Wulff *et al.*, 1999)) and neglecting incidence angle effects, some studies report the estimated average of amplitudes, normalized at a sensor-event distance sphere of 10 mm (Zang *et al.*, 1998; McLaskey and Lockner, 2014). But, since the reported moment magnitudes rely on averaging the entire event spectrum over all sensors, I simply do not consider spherical spreading. Also, most of the events are within the virtual sphere enclosed by the sensors. This means that the closeness of an event to one sensor would be traded off by its farness from the opposite sensor. So, by averaging over all sensors, the geometrical effects would be alleviated. Nevertheless, since the occurred surface ball drop events are farther than any internal AEs, the reported absolute moment magnitudes would then be upper limits. If the same ball drop event had occurred at the sample center rather than its top, the ball drop amplitudes would be ~3 times higher (considering only spherical spreading, $1/r$). So, the moment magnitude of the calibrated events would be shifting by -0.3 ($2/3.\log_{10}(1/3)$) for tis sample. One more interesting observation is the subtle resonance of events at ~200 kHz (blue line in Figure S2-6d); the radial resonance mode of 1.5 MHz PZTs are expected to be slower by their diameter/thickness ratio of ~6.2, i.e, 240 kHz. Bi-modal spectrum are also observed during active ultrasonic acquisitions via p-wave PZTs by Stanchits *et al.* (2003).

The reported moment tensor components, on the other hand, rely solely on first motion amplitudes. By comparing the first motions on different sensors during ball drop test, where we know the source magnitude and exact location, I estimated the coupling factor on each sensor, i.e., site correction (Kwiatek *et al.*, 2014). I take the observed amplitude at sensor *i* as A_i, assume spherical spreading between source-sensor at a distance r_i and negligible attenuation. The amplitude dependence on incidence angle would intuitively be cosine-type (as of a dot product between raypath and sensitivity direction); however, Manthei (2005) suggested a deviation from cosine function at large incidence angles and presented a bell-shape function of ~exp ($-a.\theta^b$) on incidence angle (angle between ray path and sensitivity direction of the P-wave transducers), θ; linear local site effects, S_i, can then be determined by minimizing the misfit in following equation and local first motion observations (Manthei, 2005; Kwiatek *et al.*, 2014):

$$A_i(r, \theta) = \frac{A_o}{r_i}[exp(-a.\theta^b)]S_i \tag{S5}$$

with a, b, and S_i as unknown variables. Figure S2-6 shows four ball drop attempts, along with first amplitude and spectrum analysis.

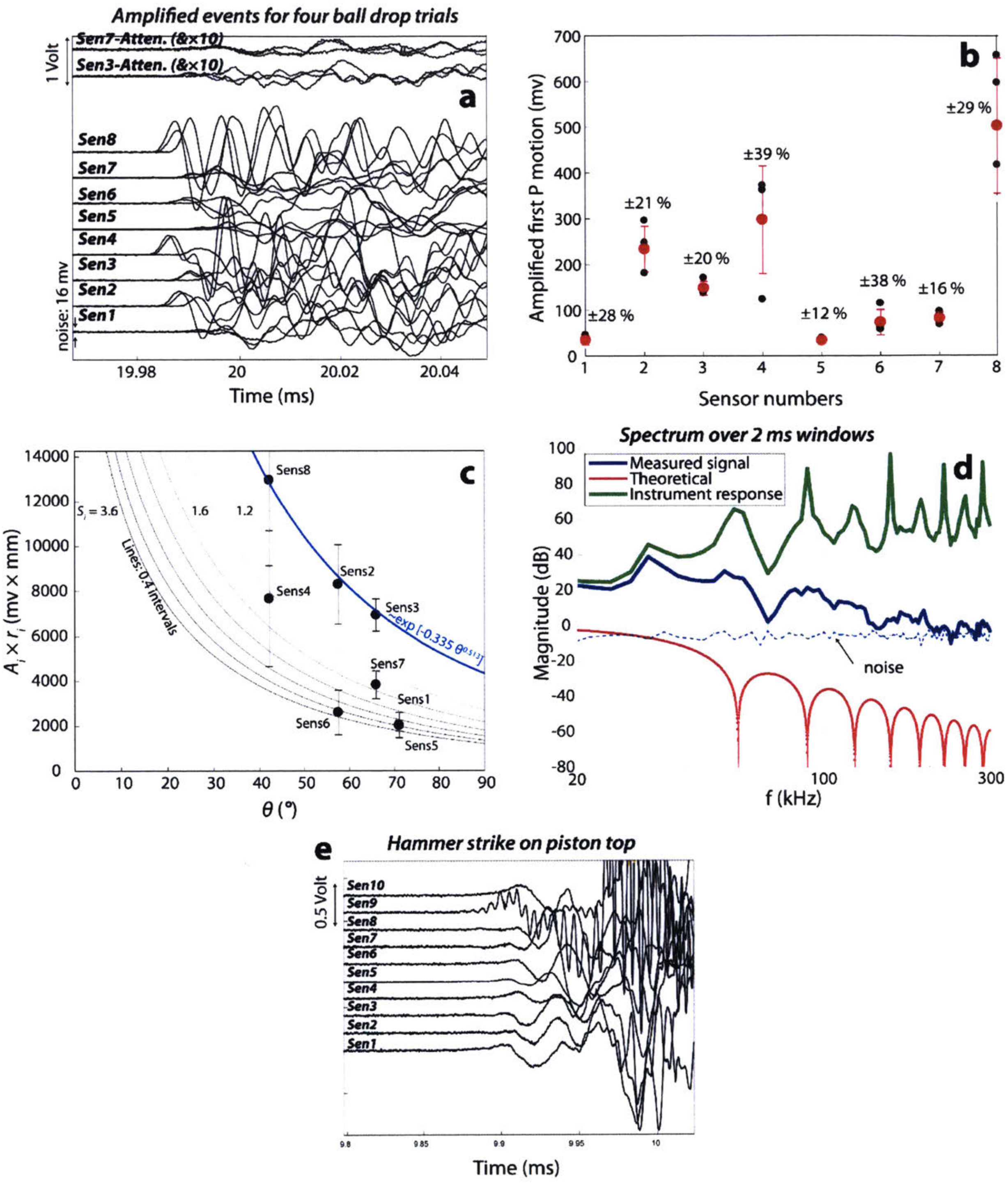

Figure S2-6. Ball drop results on Solnhofen limestone. **a** shows the AE signals for four ball drop events on Solnhofen limestone (ball impact location and sensors shown in Figure S2-5a). Notice the similarity of signals in each sensor and first motions. **b** shows the first motions as black and their mean and uncertainty (standard deviation) as red marks/lines. I observe an uncertainty of 10-40 % on each sensor. **c** shows the correction of sensors coupling, S_i, as a set of parallel lines. **d**

shows the spectrum of the event and the derived instrument response, based on sensors 1-8. **e** shows the response of a hammer strike, notice the positive polarities on all transducers.

Table S2-1 shows the coupling factors for the sensors 1-8. The correction factors have a maximum value of ~3.3. Admittedly, these correction factors are for vacuumed bench-top events; however, the comparison of ball drop tests in bench-top vs. confined conditions (McLaskey *et al.*, 2015) suggested that the bench-top amplitudes are adequately similar to the confined conditions.

Table S2-1. The sensor coupling factors for sensors 1-8.

Sensors	**Sen1**	**Sen2**	**Sen3**	**Sen4**	**Sen5**	**Sen6**	**Sen7**	**Sen8**
S_i	3.15	1.04	1.03	1.68	3.21	3.31	1.86	1.00

All polarities show consistently positive first motions. However, the repeat experiments reveal an uncertainty factor of 10-40 % for first motion amplitudes. The uncertainty could stem from the manual handing of drop of ball on the top of sample, which is hard to imagine to be repeatable. Also, since it is a surface event, during the internal AE events, I would expect much less uncertainties. I also estimated the instrument response (McLaskey *et al.*, 2015) from the difference between theoretical and measured signal spectrums [see Figure S2-6d and Appendix S4].

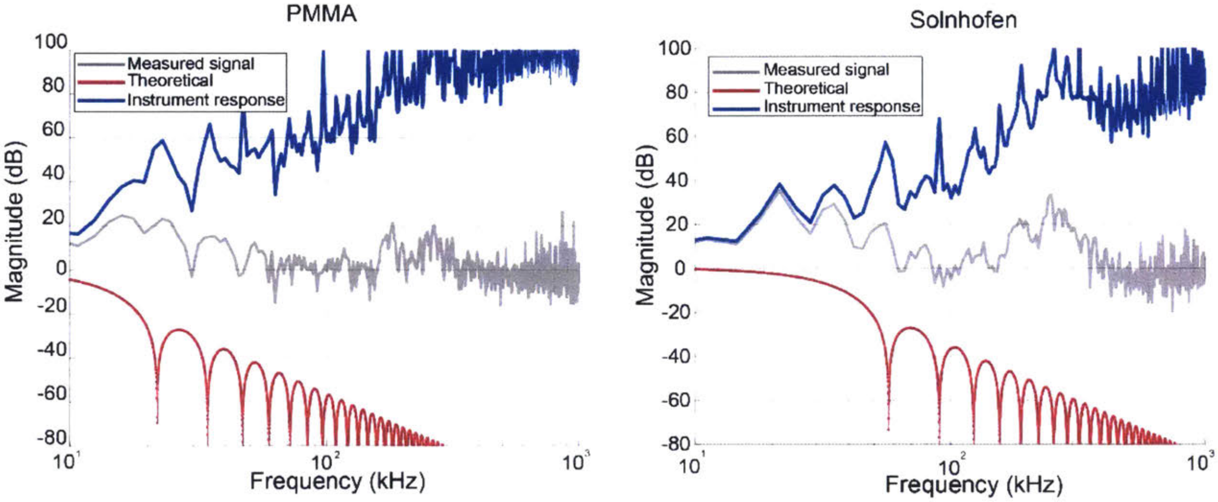

Figure S2-7. Calibration of AE sensors response for their magnitude based on ball drop experiments on four sensors used for sections 2.1 and 2.2. (left) shows the calibration for PMMA, while (right) shows the calibration for limestone. The red line is the spectrum of the theoretical ball drop response, the gray is the measured AE signal in the lab. The AE signal spectrum is obtained from a time window of ~2 ms including the event. The blue line is the Instrument response obtained by dividing the Measured signal by the theoretical spectrums. Note that the y axis is in dB units (logarithmic) and dividing between the two responses is simply done by subtracting the two responses.

Text S5. Pore pressure transducer

The pore pressure transducer is a Honeywell Inc. Ultra Precision Super TJE model. The nominal frequency response is 2 kHz. In order to evaluate the frequency response of the pore fluid pressurizing system, instead of the sample assembly, a burst disk valve was added to the pressurizing system. The burst disk fails instantaneously at 15 MPa (±0.6 MPa) pressure. I recorded this burst-type event using the same recording system and procedure as the HF events at an acquisition rate of 5 MHz. Figure S2-8 shows the recording of the transducer for this event. I conducted this experiment for three times. For the first experiment, a long pipe was attached before the disk. The pipe had the same length as the sample assembly line. Water was added behind the disk, so it bursts into a small fluid reservoir, somehow similar to a real HF experiment. For the second experiment, the small fluid reservoir was removed and the disk bursts into air. For the third time, the long pipeline was removed and the disk was still open to air. As can be observed in Figure S2-8, the instantaneous burst event was recorded at a certain time constant or rise time. This rise time is related to the transducer's frequency response. For instance, the rise time of 705 μsec in Figure S2-8 corresponds to a frequency response of 1.4 kHz. Therefore, the transducer acts as a low-pass filter and the recorded signal is physically meaningful for frequencies up to 1.4 kHz. The frequency spectrum analysis of the response also shows a flat response up to a corner frequency of 1.4 kHz. The response rolls off abruptly after this corner frequency. It is also noteworthy to mention that the short-pipe system (see Figure S2-8) has the lowest rise time, i.e. highest frequency response. In other words, by increasing the pipe length and the fluid system volume, the system becomes more compliant which directly affects the system response.

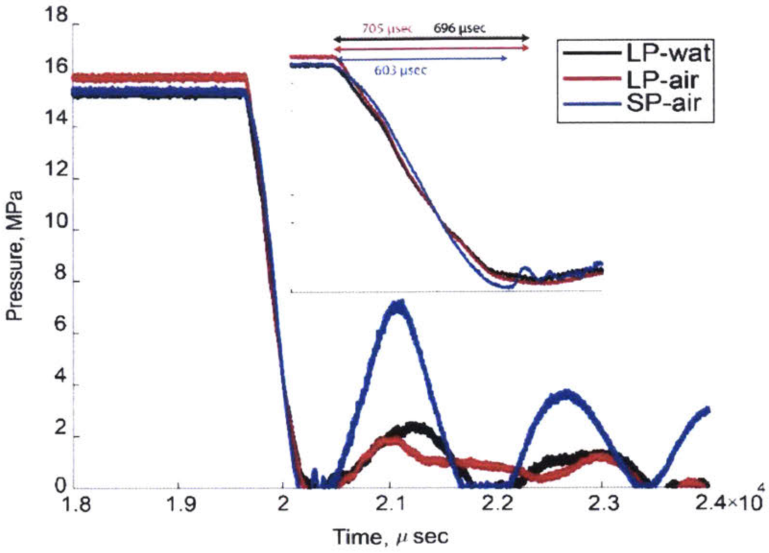

Figure S2-8. The pore pressure response for three burst disk tests as explained in the text. The transducer records this instantaneous pressure drop with a rise time between 603-705 μsec, equivalent to frequency response of ~1.4 kHz. SP and LP stand for short pipe and long pipe. Wat stands for water. For explanation of these three experiments refer to the text in A1.

Chapter 3: Creep deformation in shale from nanoindentation to triaxial experiments

Yves Bernabé, Abdelhamid Boulenouar, Ulrich Mok, and Brian Evans contributed to this chapter.

Abstract

We performed nanoindentation (2-minute) and triaxial (12-hour) creep experiments in samples cored from the Vaca Muerta shale reservoir. In all cases, we observed transient creep wherein strain increased as the logarithm of time. Creep was always compactional, led to increased moduli, could be triggered by changes in both hydrostatic and deviatoric stresses, and occurred under stresses well below the failure stress of Vaca Muerta shale. Our results are consistent with yield cap models previously proposed for the description of shear-enhanced compaction of sandstones and carbonates, provided that the yield surface is assumed to depend on strain rate. We also compared our results to earlier studies that observed the transition of creep from transient to approximately constant strain rate behavior. Short-term creep before the inferred transition time, t_c, is quantified by a creep modulus, C, while long-term creep is characterized by viscosity, η; the two are related: $\eta = Ct_c$. Owing to the extreme heterogeneity of shale, the Young's and creep moduli, E and C, measured during individual nanoindentation tests varied by several orders of magnitude. A simple technique, used to upscale the indentation results, slightly overestimated the values for E and C compared to their triaxial counterparts. Log-time creep is seen in different materials and under a variety of loading circumstances; the kinetics can be represented by a simple conceptual model that describes the interplay of viscoelastic elements with widely distributed characteristic times. Thus, we argue that log-time creep is an emerging phenomenon, independent of the identities of the underlying physical mechanisms.

3.1 Introduction

Transient creep strain in shales has been described in some studies as increasing with the logarithm of time (Chang and Zoback, 2008; Ghassemi and Suarez-Rivera, 2012), while, in others, the combined transient and secondary creep regimes were modeled as a single power-law in time (with power $n < 0.1$) (Sone and Zoback, 2011; 2014; Rassouli and Zoback, 2016; Rybacki *et al.*, 2017; Hasbani and Hryb, 2018; Rassouli and Zoback, 2018). Transient creep can also be interpreted using the Burgers (Ghassemi and Suarez-Rivera, 2012; Li and Ghassemi, 2012) or modified standard linear (Almasoodi *et al.*, 2014) viscoelastic models. But, Sone and Zoback (2014) argued that such simplified models only worked for short experiments (a few hours) and could not account for the sustainably-decelerating creep strain rates observed in their long-term creep steps. All these models provide approximate and empirical descriptions for creep strain occurring over times of a few hours to several weeks, but often there is no compelling reason to prefer one description over another.

A number of questions still remain open. For instance, conflicting observations have been reported concerning the pressure-dependence of creep; some experiments report weak dependence of creep on hydrostatic stresses (Sone and Zoback, 2014), while others indicate direct dependence (Chang and Zoback, 2008; Ghassemi and Suarez-Rivera, 2012; Villamor Lora and Ghazanfari, 2015; Rybacki *et al.*, 2017). Other unanswered questions include: Why and how does creep occur in shales, even at low stresses? How do the creep rates evolve? What are the exact physical deformation mechanisms, e.g., subcritical crack growth, frictional slip, pressure solution, internal grain deformation, grain sliding, basal slip along internal planes of weakness, or the collapse of clay floccules?

The yield of porous rocks under compressive triaxial loading is often modeled using an elliptical yield surface in p (mean stress) vs. q (deviatoric stress) space [for a review, see Wong and Baud (2012)]. Below the yield surface, deformation is sometimes modeled as elastic; but some studies [see section 5 and Choens and Chester (2018)] suggest that the yield surface, in fact, depends on strain rate.

Here, we studied the creep behavior of full-core samples of Vaca Muerta shale using both triaxial and nanoindentation tests. Our main goals are to describe the primary creep, its kinetics, its relation with elastic parameters, and the relationship between the macro-scale creep and local material properties (heterogeneities at the nanoindentation scale). Hence, we concentrated on observations of primary creep, and restricted triaxial stresses to below ~20% of the shale's *FS*. The two methods spanned four orders of magnitude in length scale (from ~1 μm to ~8 cm), two orders in time (from 2 minutes to 12 hours), and six orders in force (from ~12 mN to ~40 kN). We found that the Vaca Muerta shale rocks yielded at slow strain rates ($<10^{-7}$ s^{-1}), even when the stresses were a small fraction of the *FS*. Creep was driven both by differential stresses (shear-enhanced compaction) and mean isostatic stress (hydrostatic compaction). Although our experiments were short-term, we infer a few long-term implications based on published creep results on other shales and discuss the possibility of the emergence of secondary creep at long times.

3.2 Materials

The Vaca Muerta shale formation is located in the Neuquina basin in Argentina. The clay and organic matter contents vary from 10 to 30 and 1 to 8 wt%, respectively (Garcia *et al.*, 2013). The Vaca Muerta shale has a moderately laminated texture associated with a significant anisotropy (Ambrose, 2014). Typical values of Young's modulus measured parallel (P orientation) and normal (N orientation) to the bedding are 27 ± 11 and 18 ± 7 GPa, respectively (Ambrose, 2014). Like many other shale formations, the Vaca Muerta formation is extremely heterogeneous over a wide range of scales. The samples were retrieved from bottom hole full-cores within the oil-window and were consequently preserved in a vacuum-sealed container. It has been shown by Sarout *et al.* (2014) that the properties of shale samples depend on fluid saturation. During our sample preparation, indentation experiments, and triaxial tests, no water was added to the system as discussed below, and no attempt was made to control the humidity. The experiments were conducted less than two days after breaking the preservation seals, and we took extreme care to avoid overheating the samples during preparation. Hence, it is expected that the water content of the samples during tests are comparable to their retrieved conditions from underground.

Given its high clay content, Vaca Muerta shale is largely fine-grained (<5 μm), with dispersed hard mineral inclusions (<100 μm in diameter; see Figure 3-1). Porosity, density, and matrix permeability were measured in a sample of the VMSX2 full-core, adjoining ours, yielding values of ~7%, ~2.6 g/cm^3, and ~0.3 μD, respectively. The organic and clay contents are 3.2 and 13.0 wt%, respectively. Calcite, dolomite, and quartz are other major constituents each reaching ~20 wt%, with traces of albite, pyrite, apatite, and gypsum (order in decreasing abundance). The *in-*

situ stress regime at the full-core depth is dominantly strike-slip (Garcia *et al.*, 2013; Su *et al.*, 2014). Based on stress gradients reported by Garcia *et al.* (2013), effective *in-situ* stresses are estimated to be 5.3-5.5 MPa for σ_h, 13.5-14.0 MPa for σ_v, and 18.2-18.9 MPa for σ_H. Note that these values are lower limits as they are based on an effective pressure law coefficient of $\alpha \sim 1$ and also ignore the effect of stress concentrators such as fractures or the wellbore itself.

As part of a separate study of indentation behavior (Boulenouar *et al.* (2017), I cut samples from 3 core fragments, one full-core (VMSX1), and two mature and immature outcrop blocks. These samples differed in coloration, mineralogy, and orientation with respect to bedding. More information can be found in that reference. Here, I focus on the indentation experiments on the "dark-P" subsample of the VMSX1 full-core. A back-scattered electron (BSEM) image (using a Zeiss Merlin High-resolution SEM microscope) of the indented face (with an indentation array shown as orange dots) is shown in Figure 3-1. The indentation axis was parallel to the bedding plane.

For the triaxial tests, a precisely machined cylindrical sample with ~38 mm diameter and ~83 mm length was prepared from a full-core (VMSX2) similar to that used for the nanoindentation experiments (Figure 3-1). The cylinder axis was normal to the bedding plane.

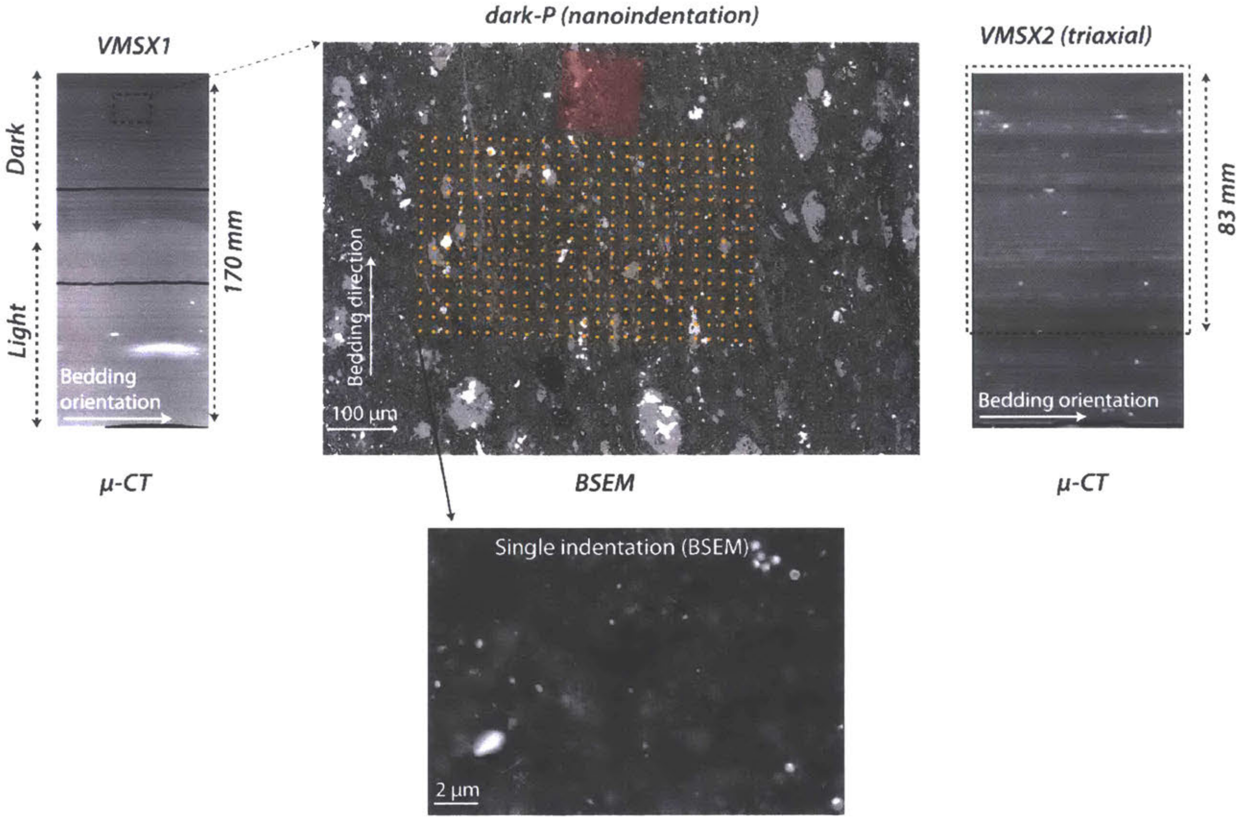

Figure 3-1. Typical microstructures for Vaca Muerta shale. Bedding plane orientations are shown by white arrows. Left: micro-computed tomography (μ-CT) image of VMSX1 (provided by Total Inc.); Center: BSEM image (15 kv, 3 nA beam) of the dark-P sample where I created an indentation array. Note that the bedding plane is vertical. The tiny orange circles and red square indicate the locations of the nanoindentation array and the microindentation, respectively. A magnified view of a single indentation in BSEM mode is shown. Right: μ-CT image of VMSX2. Dotted rectangle shows the location of the triaxial deformation sample.

3.3 Experimental procedures

3.3.1 Nanoindentations

Tests were performed using a Hysitron nanoindenter capable of continuously monitoring loads and displacements. This apparatus allows the material hardness and elastic modulus to be calculated directly without having to image the indentation imprint [for a review see Oliver and Pharr (2004)]. One particularly key capability of the Hysitron nanoindenter is that it can be operated using dynamic mechanical analysis (DMA), a technique developed for the study of the glass-rubber transition in polymers (Menard, 2008). In nanoDMA mode, the indenter load is modulated with small monochromatic oscillations. The amplitude and phase of the displacement response at the same frequency can then be used to calculate continuous variations of complex contact stiffness [i.e., the complex-valued load-to-displacement ratio (Asif *et al.*, 1999; Asif *et al.*, 2001; Cohen and Kalfon-Cohen, 2013; Hangen *et al.*, 2014)]. The storage and loss moduli can then be obtained from the real and imaginary parts of the contact stiffness [see also Appendix A in Mighani *et al.* (2018a)]. The nanoDMA technique allows for more accurate identification of the instant of the first contact, enables better calibration of the indenter-area function and load-frame compliance, and, most importantly, provides a method to correct for thermal drift of the displacement readings during creep tests (Hysitron Inc., 2011).As discussed below, the out-of-phase (loss) modulus is fairly small for this rock.

For our tests, rectangular arrays of nanoindentations were made on the polished sample faces using a 3-sided, pyramidal Berkovich indenter and the nanoDMA mode (calibrated using standard Fused Quartz). I polished the sample faces using sandpapers with the finest level of P2500 [rms roughness of ~0.3 μm (Kinnari *et al.*, 2010)], mounted on a glass plate. Polishing was done under room humidity, and no water was added. The indentations were made at room temperature, with no attempt to control the humidity during the tests. On the dark-P sample, I made an array of 15 × 25 indentations, spaced 20 μm apart (>3 times the radius of the surface imprint for the largest single indentation to prevent interference between single indentations) next to a previous Vickers microindentation made with a load of 4.9 N. The Vickers indentation imprint helped locate the indentation array under the SEM after indentation experiments. I used loading procedures that included alternating sequences of rapid loading and unloading (rate of 1.25 mN/seconds), separated by hold steps of 120 seconds. On the dark-P sample, I used a two-step procedure (Figure 3-2a). The first hold step followed initial loading to a maximum indentation force of 12.5 mN and the second was implemented after partial unloading to 6.25 mN. The maximum depth of penetration for single indentations ranged between ~0.4 to ~5 μm.

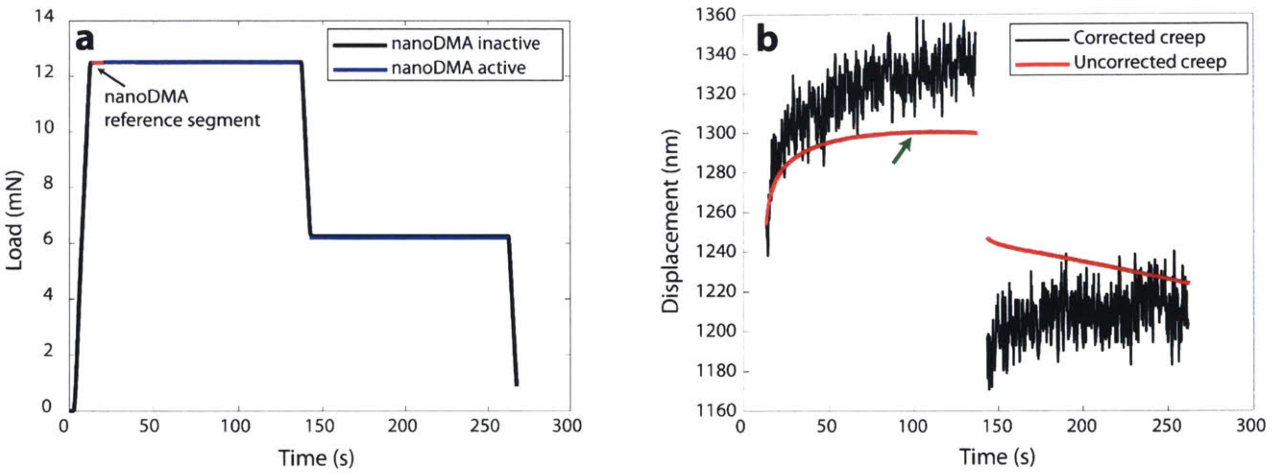

Figure 3-2. (a) The nanoindentation loading procedure used for the dark-P sample. NanoDMA load oscillations are implemented during the hold steps (blue line). The 5-second reference segment used for drift correction is indicated in red. (b) An example of uncorrected (red lines) and drift-corrected (black lines) creep curves in the dark-P sample. The green arrow indicates the point where the uncorrected creep curve shows a physically impossible reversal of the indenter motion. Note also that, after partial unloading, the corrected creep curve does not display recovery. The Young's modulus for this single nanoindentation was 23 GPa.

To correct for the thermal drift during the hold steps, the constant load was modulated with a small load oscillation (220 Hz in frequency and 100-200 μN in amplitude), which produced a 1-2 nm oscillatory displacement response. In these conditions, the phase shift between the load and displacement tends to be very small, implying that the storage modulus (i.e., the real part of the complex modulus) can, in principle, be interpreted as a measure of the elastic Young's modulus, *E* (Asif *et al.*, 1999). Since thermal drift is negligible at very early times, an accurate reference value for *E* can be measured during the 5-second segment at the beginning of the first hold (Figure 3-2a). If I assume that the subsequent variations of *E* are artifacts, the reference modulus can be used to correct the measured displacements for thermal drift (Asif *et al.*, 1999). The assumption of a constant material modulus, *E*, may not be fully valid in porous materials that compact under load. However, variations in the uncorrected creep curves were generally quite large, and the curves changed erratically from one nanoindentation to the next, suggesting that artifacts from thermal drift were much larger than any real changes owing to the material compaction. The material modulus, *E*, can also be estimated from the final unloading curves, but the long duration 2-minute hold steps tend to render the unloading-derived moduli less reliable than nanoDMA (Goodall and Clyne, 2006). To illustrate the importance of drift correction, corrected and uncorrected creep curves are shown in Figure 3-2b. The uncorrected creep curves even sometimes display apparent reverse creep (see green arrow in Figure 3-2b), which is almost certainly an experimental artifact. The hardness value (*H*) during the creep time gradually decreased, consistent with rate-dependent plastic materials under indentation (Gomez and Basaran, 2006); to report hardness, I averaged its value over the creep time.

Nanoindentations and triaxial tests differ in loading geometry as well as scale, and it is useful, for comparison purposes, to estimate the stress magnitudes achieved in the indented solid under the tip. Based on plasticity theory and the "cavity" model (Johnson, 1985), the mean pressure acting on the indenter surface is given by the hardness (*H*) and is proportional to the yield stress (σ_Y). For conical indenters, the mean stress immediately underneath the indenter is approximately equal to $3\sigma_Y$, reduces to σ_Y at the elastic-plastic boundary, and finally vanishes at distal points (Tabor, 1951; Johnson, 1970). Although this model may be inaccurate for compacting porous materials such as shales, it provides an order of magnitude estimate of up to 320 and 160 MPa, respectively, for the mean and differential stresses present under the indenter. Also, the strain around the indentation is very high [i.e., 0.07 or 70 millistrain (Tabor, 1951)].

3.3.2 Triaxial creep experiments

I conducted the triaxial creep experiments in an NER AutoLab 3000 triaxial cell using hydraulic oil as the confining medium. Both axial stress, σ_1, and confining pressure, p_c, which are measured internally, were servo-controlled within about ±0.09 and ±0.05 MPa, respectively. In this report, compressive stresses and strains are taken to be positive. A thermocouple mounted inside the vessel, near the internal load cell, recorded the temperature variations during the experiments (Appendix S1). The data were recorded with an acquisition rate of 10 samples per second. As mentioned in the Materials section, the shale sample's diameter and length were ~38 mm and ~83 mm, respectively. A neoprene jacket isolates the sample from confining oil. Axial and radial strains (me) were measured using strain gauges (resistance 120 Ω, grid length 1.5 mm); two axial gauges were mounted in the middle of the sample with a 90° azimuthal separation and a radial gauge was positioned next to one of the axial gauges. All were directly glued on the sample surface. The electrical leads passed through small perforations in the neoprene jacket and were sealed with epoxy. In addition to the strain gauges, I measured the total column (sample + piston + spacers) displacement using an external linear variable differential transformer (LVDT) outside the pressure vessel. I corrected for the shortening of the load column using two control experiments on aluminum and titanium dummy samples.

The creep tests were implemented using loading procedures similar to those of nanoindentation tests, namely, sequences of rapid loading/unloading stages separated by hold steps, although the holds were much longer (6 and 12 hours). Before the first hold step, p_c was raised to the target value while the differential stress, $\sigma_d = \sigma_1 - p_c$, remained very low. After a few minutes, σ_d was then raised to the target value. Unloading/reloading cycles were systematically used to move to the next loading conditions after each hold. I proceeded by first unloading σ_d to 6 MPa (to obtain unloading elastic parameters), then changed p_c when necessary to the appropriate value at constant σ_d; and, finally reloaded σ_d to the next target value. In all cases, the loading/unloading rate was automatically controlled at ~ 3 MPa/min. The equivalent strain rate during these loading/unloading steps was $\sim 3\times10^{-6}$ s^{-1}.

During the loading/unloading cycles, we assume that the time-dependent strains were negligible. Also, since the stresses were well below the Vaca Muerta shale yield surface [see the fast loading rate tests of Ambrose (2014) in Appendix S2], the inelastic strains ($\varepsilon_j{}^{in}$) occurring during loading/unloading steps were insignificant. Therefore, we assume that only elastic strains ($\varepsilon_j{}^{el}$) occurred during the loading/unloading cycles. During the hold steps, as the stresses were held constant, only time-dependent (inelastic) creep strain, $\varepsilon_j{}^{c}$, occurred so that it could be derived by simply subtracting the elastic strain from the total strain ($\varepsilon_j{}^{tot}$) (Figure 3-3c).

We used the early portions of the unloading cycles to obtain the elastic properties of the sample at current values of σ_d and p_c. Vaca Muerta shale is a transversely isotropic (TI) material with the isotropic planes parallel to bedding (Ambrose, 2014). Therefore, the elastic properties obtained during σ_d unloading are Young's modulus, E_N, and Poisson's ratio, ν_N, normal to the plane of isotropy. Using the strain readings during p_c unloading at constant σ_d (steps 1-7 and 2-4 in Figure 3-3), we were also able to determine the Poisson's ratio, ν_P, parallel to the bedding (Appendix S3). The values of Young's modulus reported here are based on averaging the strain readings of the two axial strain gauges and LVDT. To determine Poisson's ratio, we used the neighboring axial/radial strain gauges.

The uncertainties on the measured elastic constants arise from: 1) the experimental errors linked to the precision of sensors and small fluctuations of the experimental conditions, in particular temperature, and, 2) the heterogeneity of the sample as demonstrated by the differences in the readings of the two axial gauges (± 20% with respect to the mean value). I estimate that the relative variations of the local elastic constants were measured with a precision of about ± 1%. Nevertheless, owing to the limited probe size (strain gauge grids of 1.5 ×1.5 mm squares) and the material heterogeneity, the strain gauge measurements may not be representative of the elastic properties measured at the sample scale. Hence, in addition to the strain gauges, I also report the LVDT values, which supposedly represent the global sample deformation. However, LVDTs are also subject to uncertainties, especially stemming from the column corrections. For example, the method used to estimate the column correction is exclusively based on the elastic properties of the standards and does not include the displacements associated with variation of stiffness at the sample/piston interfaces (Pyrak-Nolte and Morris, 2000). These displacements are probably larger for shale samples than for the precisely machined, homogenous metallic standards used for the column corrections.

I performed two successive creep experiments (experiments 1 and 2) on the VMSX2 sample, between which the sample remained in the pressure vessel for about 19 hours, almost completely unloaded (Figure 3-3). The stress conditions were within the range of the *in-situ* stresses at the depth where the full-core was retrieved (see Materials section). The first experiment included six 12-hour hold steps (labeled 1-1 to 1-6) and one 19-hour step (1-7) and the second, four 6-hour holds (2-1 to 2-4). Hold steps 1-2, 1-5, 2-2, and 2-4 followed differential stress loading steps (i.e., increasing the axial stress σ_1 while maintaining p_c constant), while steps 1-3 and 1-6 were after σ_d unloading steps and step 1-4 after an isostatic loading stage (i.e., raising p_c while maintaining σ_d constant). Hold steps 1-1, 2-1, and 2-3 were associated with mixed loading stages, wherein both p_c and σ_d were successively changed (Figure 3-3a). Note that σ_d loading does not correspond to a pure increase of the deviatoric stress, $q = \sigma_1 - p_c$, since the mean stress, $p = (2p_c + \sigma_1)/3$, also increases with σ_1. The maximum axial stress applied in the triaxial experiments ($\sigma_1 = 75$ MPa at $p_c = 39$ MPa) was about 20% of the compressive differential strength measured under similar confining pressures and constant strain rate of 10^{-5} s^{-1} (Ambrose, 2014). The strength is usually assumed strain rate-independent (Kirby, 1980) as mentioned in Introduction.

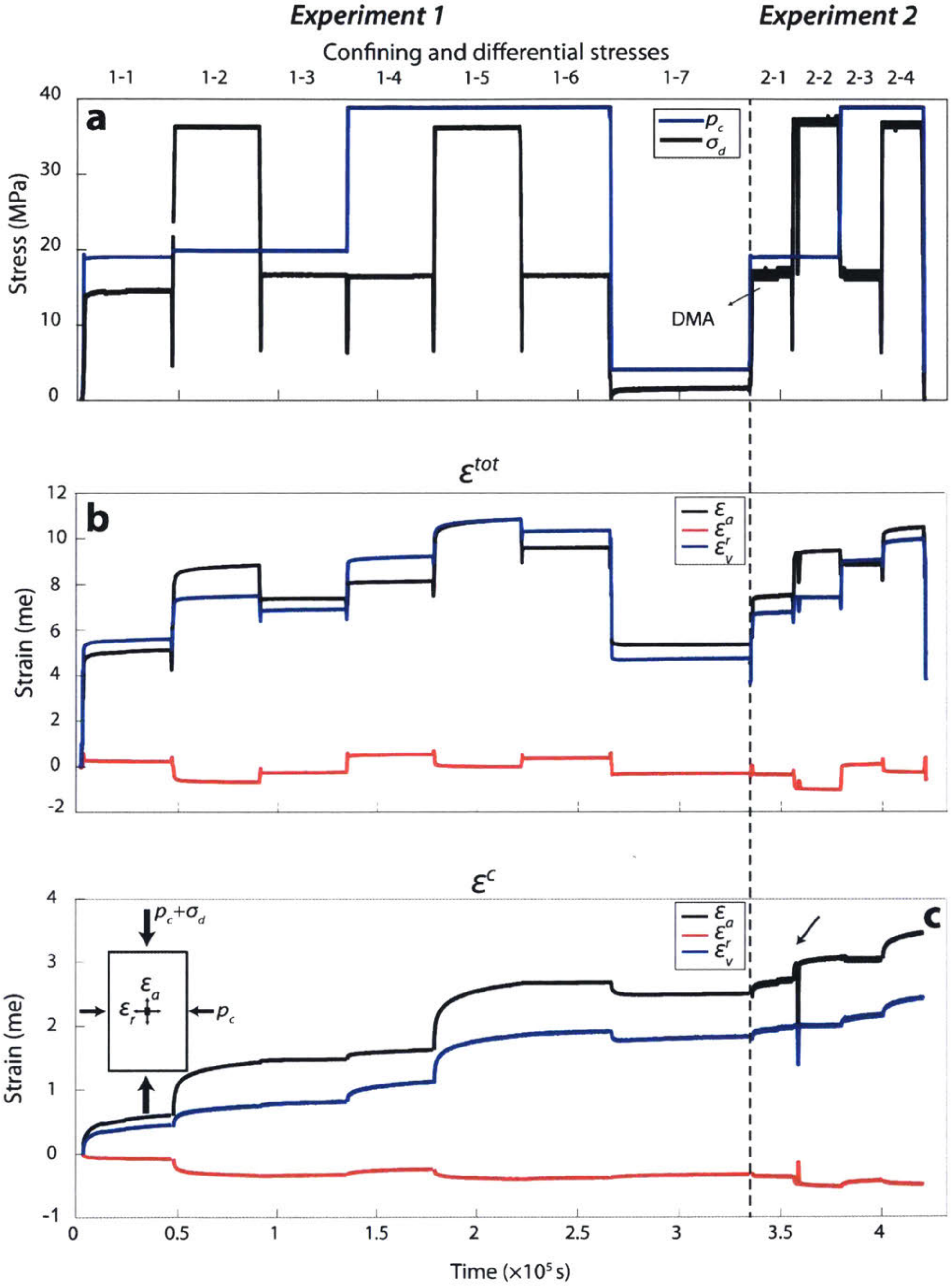

Figure 3-3. Stress and strain history during triaxial experiments. (a) Stress history (p_c, blue; σ_d, black). (b) Total axial, radial, and volumetric strains (black, red, and blue, respectively). (c) Creep strains recorded during the hold steps. An accidental drop in σ_d occurred during step 2-2 (black

arrow) owing to a glitch of the control system. See results section for detailed commentary. Inset in c shows the triaxial stresses, bedding planes (gray horizontal lines), and measured strains.

In the second creep experiment, I used a DMA-inspired technique to track time variations of E_N and v_N. A small triangular load oscillation was superposed on the constant σ_1 during the hold steps (Figure 3-4). I segmented the DMA data into 100-second windows and corrected the oscillating strains of the long-term creep trend (detrending) to isolate the purely elastic strains for derivation of the elastic parameters. Because the period of the load oscillation is short (10 s) and the amplitude small (0.8 MPa), I expect the detrended strain response during DMA to be predominantly elastic, rather than inelastic (see the phase coherence of the stress and strains in Figure 3-4b). The elastic parameters, E_N and v_N, in each window were calculated by comparing the stress oscillations to the de-trended axial and radial strains. Due to the accidental stoppage of the high-gain load cell recordings, no accurate oscillatory stress data are available to report DMA moduli for hold step 2-2.

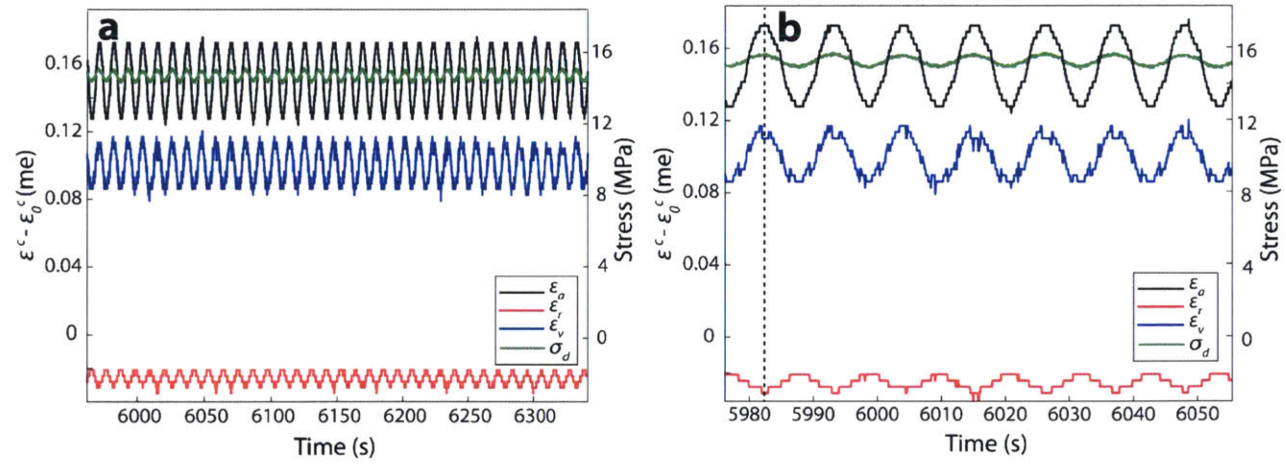

Figure 3-4. (a) Stress oscillations and the strain response during DMA hold steps. I show a time window at the end of hold step 2-1, when the creep rate was slow, to facilitate the visual comparison of stress and strain oscillations. (b) The enlarged view of the diagram, which demonstrates the in-phase oscillation of strains and stress (see dashed line). $\boldsymbol{\varepsilon_0}^{\boldsymbol{c}}$ is the creep strain at the beginning of the hold step.

3.4 Results

3.4.1 General observations

The stresses during our triaxial experiments were always less than the failure envelopes determined at fast loading rates using Ambrose (2014) data (see Appendix S2). Except for step 1-7, inelastic creep strains measured during the hold steps were compactional, ($\varepsilon_v{}^c > 0$); so, dilatancy and strain-softening did not occur. The only time we observed a dilational creep strain reading was during step 1-7. Thermocouple temperature readings revealed a sudden temperature drop of 4°C upon vessel depressurization, from 39 to 4 MPa, during step 1-7 (Appendix S1). The coincidence of temperature and creep strain transients (Figure S1 in Appendix S1) suggests that the dilation observed was most probably due to the adiabatic decompression of the confining fluid.

Changes in $\varepsilon_v{}^c$ were greater in response to when σ_d was increased compared to those when p_c alone was increased. The summation of axial creep strains measured from the strain gauges during the entire experiment was ~3.50 me (Figure 3-3c). This value is comparable to the unrecovered total axial strains at the end of the experiments (Figure 3-3b), suggesting that the creep strain is in fact inelastic and accumulates as a permanent strain. Neither the nanoindentations nor the triaxial creep tests showed any evidence of creep recovery after unloading [consistent with Sone and Zoback (2014) and Hasbani and Hryb (2018) unloading creep tests on shale], as might be expected if the material obeyed the viscoelastic Kelvin-Voigt model. Instead, creep resumed at a slower rate (see the second indentation hold in Figure 3-2b and triaxial hold periods 1-3, 1-6, and 2-3 in Figure 3-3c).

3.4.2 Log-time creep

In both nanoindentation and triaxial creep tests, we found that displacements and strains approximately depended on the logarithm of time (Figure 3-5). This log-time creep was generally preceded by a very short transient (5 to 10 seconds for the nanoindentations and about 500 seconds for the triaxial tests), likely related to the fact that, in practice, the prescribed stresses and forces were not exact step-functions of time. As a consequence, the beginning of a hold step is not well-defined, and it is difficult to separate time-independent strains generated during the final moments of the loading cycles from the time-dependent strain that started to accumulate at the same time.

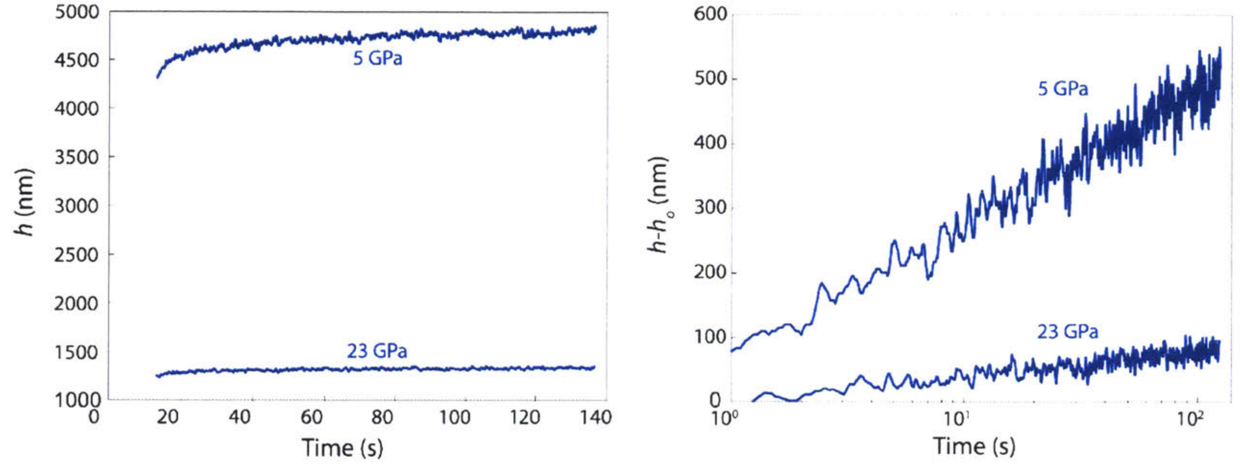

a
Nanoindentation creep (dark-P)

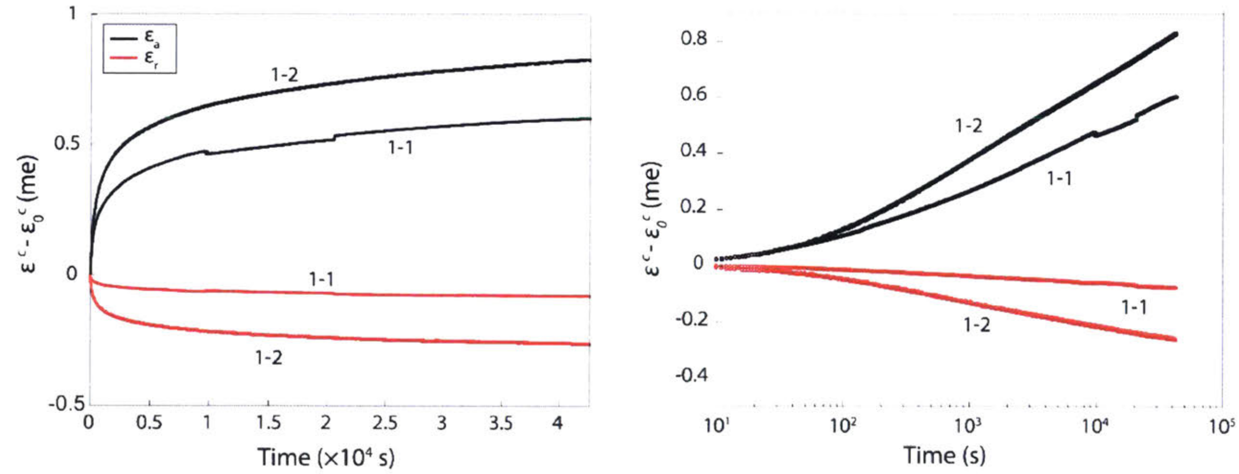

b
Triaxial creep (VMS-X2)

Figure 3-5. Examples of creep curves for (a) Drift-corrected nanoindentations and (b) Triaxial experiments. The displacements and strains are shown in linear (left) and logarithmic (right) time spaces. Notice that, the creep strains become proportional to the logarithm of time after ~5-10 seconds for the indentations and after ~500 seconds for the triaxial creep experiments. The numerical values indicated in (a) are Young's moduli of single indentations. The scatter in log-time plot of nanoindentations results in 2-6% uncertainty (95% confidence interval) in slopes.

In nanoindentations, log-time creep has been expressed as (Vandamme and Ulm, 2013; Slim, 2016):

$$h(t) - h_0 \approx x_1 ln(t - t_0 + 1) \tag{21}$$

where h is the indenter depth, x_1 a fitting constant, and t_0 and h_0 the time and depth at the beginning of the hold. The rate of change of the creep compliance, $\dot{L}(t)$, is related to the rate of change of $h(t)$, effective contact radius, $a(t)$, and the constant load, P, by

$$\dot{L}(t) = \frac{2a(t)\dot{h}(t)}{P} \approx \frac{2a_U\dot{h}(t)}{P} \tag{22}$$

Because the increase in contact radius during the 120-second hold steps was less than 10%, $a(t)$ in equation (22) is replaced by the contact radius, a_U, measured at a fixed time, $t = 100$ s (Vandamme and Ulm, 2013). Equations (21) and (22) then yield:

$$\dot{L}(t) \approx \frac{1}{Ct} \tag{23}$$

where the contact creep modulus, C (in units of GPa), characterizes the nanoindentation creep behavior.

For the triaxial creep tests, the counterparts of equations (21) and (22) are:

$$\varepsilon_j{}^c(t) - \varepsilon_{j0}{}^c \approx x_1 ln(t - t_0 + 1) \tag{24}$$

where $\varepsilon_{j0}{}^c$ is the creep strain at the beginning of the hold step. Then, the rate of change of the creep compliance during the triaxial tests is

$$\dot{L}_j(t) = \frac{\dot{\varepsilon}_j{}^c(t)}{\sigma} \approx \frac{1}{C_j t} \tag{25}$$

where the subscript j identifies axial, radial, or volumetric strain, and σ is the conjugate loading parameter, i.e., either confining pressure, p_c (1-4 in Figure 3-3), or differential stress, σ_d (1-2, 1-3, 1-5, 1-6, 2-2, and 2-4). The creep modulus can also be expressed as:

$$C_j = \frac{\sigma}{x_1} \tag{26}$$

Note that hold steps 1-1, 2-1, and 2-3 had changes in both p_c and σ_d. Because the creep response to isostatic stress is less than 20% of that occurring under similar differential stress loads (see Figure 3-3), these hold steps were treated as following a simple σ_d change.

As mentioned in the introduction, creep in shales has also been represented using a power-law function ($\sim B.t^n$). We tested this representation and found that power-laws with $n<0.07$ provided a satisfactory fit to our data and were consistent with the exponent values of $n<0.04$ obtained by Hasbani and Hryb (2018) for Vaca Muerta shale samples in the oil window. Power-law exponents lower than 0.1 have generally been reported for a wide range of shales (Sone and Zoback, 2014; Rassouli and Zoback, 2016; Rybacki *et al.*, 2017; Hasbani and Hryb, 2018; Rassouli and Zoback, 2018), suggesting that these creep data could also be satisfactorily fitted using the log-time model (indeed, logarithmic and power-law models yield nearly identical strain rate decays, $1/t$ and $1/t^{1-n}$, respectively, if and only if the exponent n is very small). Here, we found the log-time description more convenient than power-law because it allowed us to use the creep modulus concept developed for nanoindentation creep experiments (Vandamme and Ulm, 2013). One particularly important property of C is that nanoindentation measurements can be upscaled and compared to triaxial values.

3.4.3 Elastic moduli, hardness, and creep modulus

3.4.3.1 Nanoindentations

Nanoindentations yielded strikingly large spatial variations in E, H, and C: 4-100 GPa, 0.02-6.5 GPa, and 10-10^7 GPa, respectively. In the dark-P sample, these variations correlated with local mineralogical composition as determined from energy dispersive spectroscopy (EDX) elemental maps [Figure 3-6, and (Boulenouar *et al.*, 2017)]. In general, the highest values were obtained when inclusions of pyrite, dolomite, calcite, and quartz were indented, while moderate and low values corresponded to the clayish matrix forming the bulk of the rock. The correlation between nanoindentation moduli and local mineralogical composition has also been established in previous studies (Vandamme, 2008; Abedi *et al.*, 2016a; Slim, 2016). The compilation of moduli and hardness values exhibited relatively well-defined power-law relations, $H \propto E^{1.8\pm0.2}$, $C \propto E^{2.9\pm0.8}$ and $C \propto H^{1.6\pm08}$ (uncertainties are 95% confidence interval) (Figure 3-7).

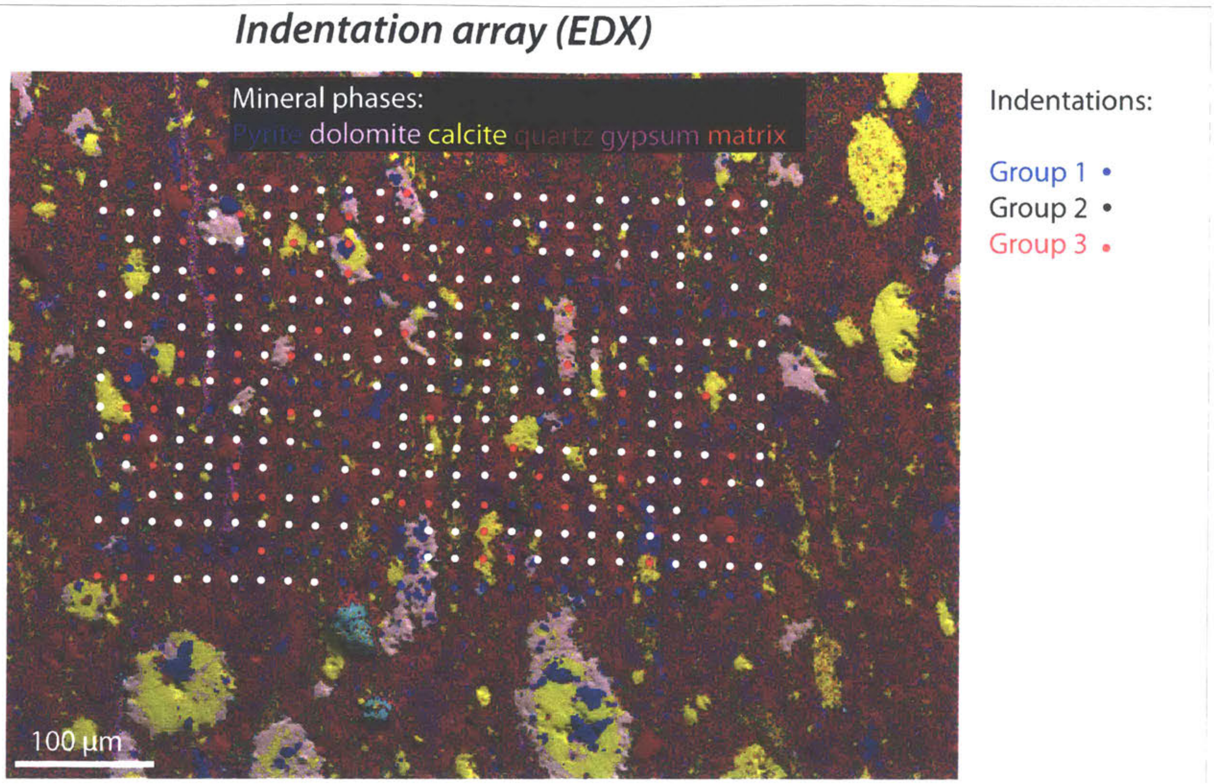

Figure 3-6. Scanning electron microscope (SEM) images of the 15 × 25 array of Berkovich nanoindentations in the dark-P sample. The nanoindentations are highlighted with tiny circles. The mineral phases were identified based on EDX elemental maps (Boulenouar *et al.*, 2017). The following elements were mapped: Al, C, Ca, Fe, K, Mg, Na, O, S, and Si. The indentations were classified into three groups that are color-coded in the image. Groups 1, 2, and 3 were distinguished by their mechanical properties as discussed in the text (see Boulenouar *et al.* (2017) for additional details).

The statistics of E, H, and C measured in the horizontal and vertical directions of the indentation array in Figure 3-6 did not show any significant differences. Similarly, nanoindentations in samples orientated normal and parallel to bedding produced undistinguishable statistics. One explanation is that the indentation arrays were smaller than the thickness of a single bed and the anisotropic structure of the rock was not sampled.

I identified three nanoindentation groups based on the clustering of data-points in E-H-C space (Figure 3-7). The softest indentations (approximately bounded by $E < 10$ GPa, $H < 0.1$ GPa and $C < 100$ GPa) were mainly located in the background clayish matrix (Figure 3-6) and formed a clearly separate, compact group (G1) (lower-left cluster in Figure 3-7). The hardest group (G3) contains the indentations with highest *E-H-C* values (approximately bounded by $E > 30$ GPa, $H > 1$ GPa and $C > 7000$ GPa). Most of the G3 indentations fell within or very near hard pyrite, dolomite, calcite, or quartz inclusions (compare inclusion features in Figure 3-6 and Figure 3-1). The remaining nanoindentations define the intermediate group (G2). They were located within the clayish matrix and had intermediate values of *E*, *H*, and *C*. The intermediate group G2 was the most abundant (~70% of indentations) component, while the other two had roughly equal abundances (15%).

Similar groups of nanoindentations have been identified in North American shale samples using chemo-mechanical clustering methods (Slim, 2016). These groups commonly overlap with our G2 and G3, but almost none with G1, which appears to be a distinct feature of Vaca Muerta shale (at least in the oil window). Young's moduli lower than 10 GPa have been observed for single indentations of organic material in shales (Shukla *et al.*, 2013; Khatibi *et al.*, 2018), organic pyrobitumen, shungite, and highly porous synthetic clay aggregates (Slim, 2016), suggesting that the group G1 may be associated with a relatively high organic matter content within the porous clay matrix [see also Zargari *et al.* (2013) and Wilkinson *et al.* (2015)].

The grouping described above was used to upscale the elastic and creep moduli, *E* and *C*, using Hashin-Shtrikman (HS) bounds [Appendix S4; (Boulenouar *et al.*, 2017)]. Characteristic values of *E* and *C* were assigned to each group ($E = 6$, 25 and 60 GPa, and, $C = 50$, 1000 and 20000 GPa for G1, G2, and G3, respectively). The method consisted of homogenizing G1 and G2 into a composite phase G*, and then G* and G3 into the effective upscaled phase G^{ups}. The upper Hashin-Shtrikman (HS) bound was used in the first binary homogenization because the stiffest phase was percolating; the lower HS bound was used for the second homogenization step since the stiffest phase was the disconnected inclusions [see Boulenouar *et al.* (2017) for more details]. The ternary homogenization method yielded aggregate average moduli of $E^{ups} = 22$ GPa and $C^{ups} = 750$ GPa.

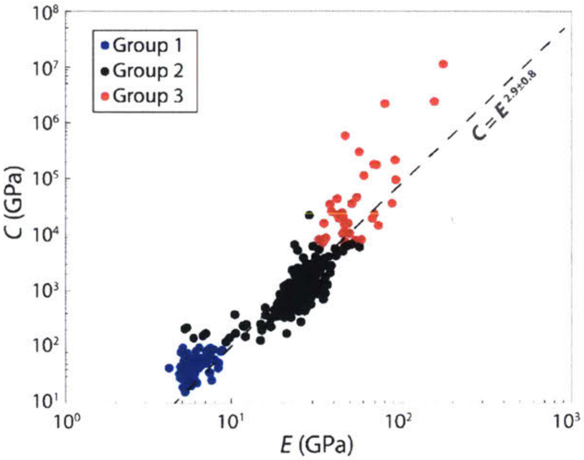

Figure 3-7. Contact creep modulus, C, measured in nanoindentation creep tests versus Young's modulus, E, for the Vaca Muerta dark-P sample. The blue, black and red marks indicate the grouping of the indentations. Data from the entire ensemble roughly follows a trend of $\boldsymbol{C} \propto \boldsymbol{E}^{\mathbf{2.9\pm0.8}}$. However, it is clear that the values within each group vary substantially, and so the relation between the two moduli will also vary from one group to another.

3.4.3.2 Triaxial tests

In the triaxial tests, the elastic properties (E_N and v_N) were measured discretely in each σ_d unloading cycle, as well as continuously during the DMA hold periods. The two independent measurements were quite consistent (Table 3-1). Young's moduli obtained by the two axial strain gauges, $E_{N,1}$ and $E_{N,2}$, differed by about 40%. Raising p_c and σ_d tended to reduce the discrepancy ($E_{N,1}/E_{N,2}$ dropped from 1.4 to 1.3 at high stresses). Compared with strain gauges, the external LVDT modulus, $E_{N,LVDT}$, yielded lower values. At low stresses, $E_{N,LVDT}$ was approximately half the average value of $E_{N,1}$ and $E_{N,2}$, but a better agreement was obtained at higher stresses (Table 3-1). Lower $E_{N,LVDT}$ may be partially due to the underestimation of the column corrections, which was found more pronounced at low stresses, as well as low-stiffness shale sample/piston interfaces, as previously discussed. One other possibility for lower LVDT moduli, besides displacement correction underestimations, would be the sampling volume for measurements; LVDT which samples a much larger volume (entire sample) compared to finite strain gauges would sample more compliant defects and cracks. Nevertheless, all three sensors showed consistent relative variations during the experiment.

All E_N measurements (strain gauges, LVDT, or DMA) consistently showed a strong increase when σ_d was raised at constant p_c (hold steps 1-2, 1-5, 2-2, and 2-4) and much smaller increments after p_c was raised at constant σ_d (hold period 1-4). Comparing the elastic properties at the same stress conditions, after unloading stages (hold periods 1-6 and 2-3) showed moderate rock stiffening, possibly owing to the inelastic strains accumulated during hold steps. Similarly, DMA measurements showed a brief transitory increase of E_N during the hold steps following the σ_d steps (2-1 and 2-4) (Figure 3-8) but no changes after unloading (2-3). E_N appeared to drop back to its initial value almost entirely during the 19-hour rest period separating the two experiments. Poisson's ratio, ν_N, remained close to 0.2 and experienced lower relative changes compared to E_N; ν_N increased from 0.2 to 0.27 during experiment 1 and from 0.22 to 0.24 during experiment 2. Poisson's ratios measured during DMA tended to be lower than the unloading ones and showed significant fluctuations. I also measured the ratio of radial over axial elastic strains, $\varepsilon_r{}^{el}/\varepsilon_a{}^{el}$, in the beginning of p_c unloading cycles (hold periods 1-7 and 2-4), obtaining 0.29 and 0.31, respectively.

Table 3-1. Evolution of elastic properties during creep steps from the strain gauges and external LVDT measurements.

Creep step	p_c, **MPa**	σ_d, ***MPa***	$E_{N,1}$, **GPa**[a]	$E_{N,2}$, **GPa**[a]	$\nu_{N,1}$	$E_{N,LVDT}$, **GPa**	$E_{N,1}{}^{DMA}$, **GPa**[b]	$E_{N,2}{}^{DMA}$, **GPa**[b]	$\nu_{N,1}{}^{DMA}$
1-1	19	16	14.2	9.6	0.21	6.1			
1-2	19	36	22.4	17.2	0.22	16.8			
1-3	19	16	16.0	11.5	0.20	7.0			
1-4	39	16	16.5	11.9	0.25	7.4			
1-5	39	36	22.2	17.0	0.23	13.9			
1-6	39	16	17.8	13.2	0.27	8.2			
1-7	4	1	-	-	-	-			
2-1	19	16	14.9	10.6	0.23	7.0	14.3:15.1	9.7:10.4	0.19
2-2	19	36	21.5	15.5	0.24	12.7	-	-	0.19
2-3	39	16	16.7	12.2	0.23	8.6	17.2:17.4	12.2:12.3	0.22
2-4	39	36	21.2	16.1	0.24	14.5	20.8:21.4	15.0:16.3	0.19

Notes: [a]The subscripts *1*, *2*, and *LVDT* indicate that the values were obtained with the axial strain gauges 1, 2, and LVDT. [b]The superscript DMA refers to the elastic properties obtained by DMA oscillation method. Note that the DMA moduli are the values at the beginning and end of a step, separated by ":". For Poisson's ratios, the long-term DMA values are listed here.

Using the logarithmic slope of the creep strains [equations (24) and (25)] during hold steps, I obtained the axial (C_{ax}) and volumetric (C_{vol}) creep moduli (C_{ax}: steps 1-1, 1-2, 1-5, 2-1, 2-2, and 2-4; C_{vol}: 1-4). Similar to Young's modulus, I obtained three sets of axial creep moduli depending on whether the strain gauges or external LVDT were used (see Table 3-2). Just like their elastic counterparts, $C_{ax,1}$, $C_{ax,2}$ and $C_{ax,LVDT}$ were different in magnitude but followed identical relative evolutions during the experiments. I obtained a global estimate, $C_{ax,avg}$, by averaging over these three values. $C_{vol,avg}$ was estimated from the neighboring radial/axial strain gauge pair.

Table 3-2. Evolution of the axial and volumetric creep moduli during creep steps from the strain gauges and external LVDT measurements.

Creep step	p_c, **MPa**	σ_d, ***MPa***	$C_{ax,1}$, **GPa**[a]	$C_{ax,2}$, **GPa**	$C_{ax,LVDT}$, **GPa**	$C_{ax,avg}$, **GPa**	$C_{vol,avg}$, **GPa**[b]
1-1	19	16	181	71	42	98	
1-2	19	36	300	141	115	185	
1-3	19	16					
1-4	39	16					604
1-5	39	36	233	139	96	156	
1-6	39	16					
1-7	4	1					
2-1	19	16	401	212	116	243	
2-2	19	36	580	323	183	362	
2-3	39	16					
2-4	39	36	485	310	199	331	

Notes: [a]The subscripts *1*, *2*, and *LVDT* indicate that the values were obtained with the axial strain gauges 1, 2, and LVDT. [b]Note that the volumetric creep moduli were only relevant for step 1-4, which followed a pure incremental isostatic stress step.

Figure 3-8 shows the triaxial elastic vs. creep moduli, and their relationship with the accumulated creep strain. The elastic and creep moduli increased with accumulated creep strain (Figure 3-8). Strain hardening was more pronounced for *C* than for *E*. Likewise, Young's modulus showed a slight increase with creep strain accumulation during the DMA steps (~1 GPa stiffening during step 2-1 in Figure 3-8c). The creep moduli obtained in experiments 2 are larger than those determined in experiment 1 in equivalent stress conditions by a factor of 2 to 3 (offset in Figure 3-8a). In each experiment, C_{ax} tended to scale linearly with E_N, as opposed to the power-law relation during nanoindentations ($C \propto E^{2.9\pm0.8}$ in Figure 3-7). The volumetric creep modulus C_{vol} was about 5 times higher than C_{ax}, showing that steps in isostatic stress produced much smaller creep deformation than σ_d loading steps. I also measured C_{ax} for hold steps 1-3, 1-6, and 2-3 and found very large values (>2000 GPa), reflecting the fact that there was almost no creep deformation observed after σ_d unloading.

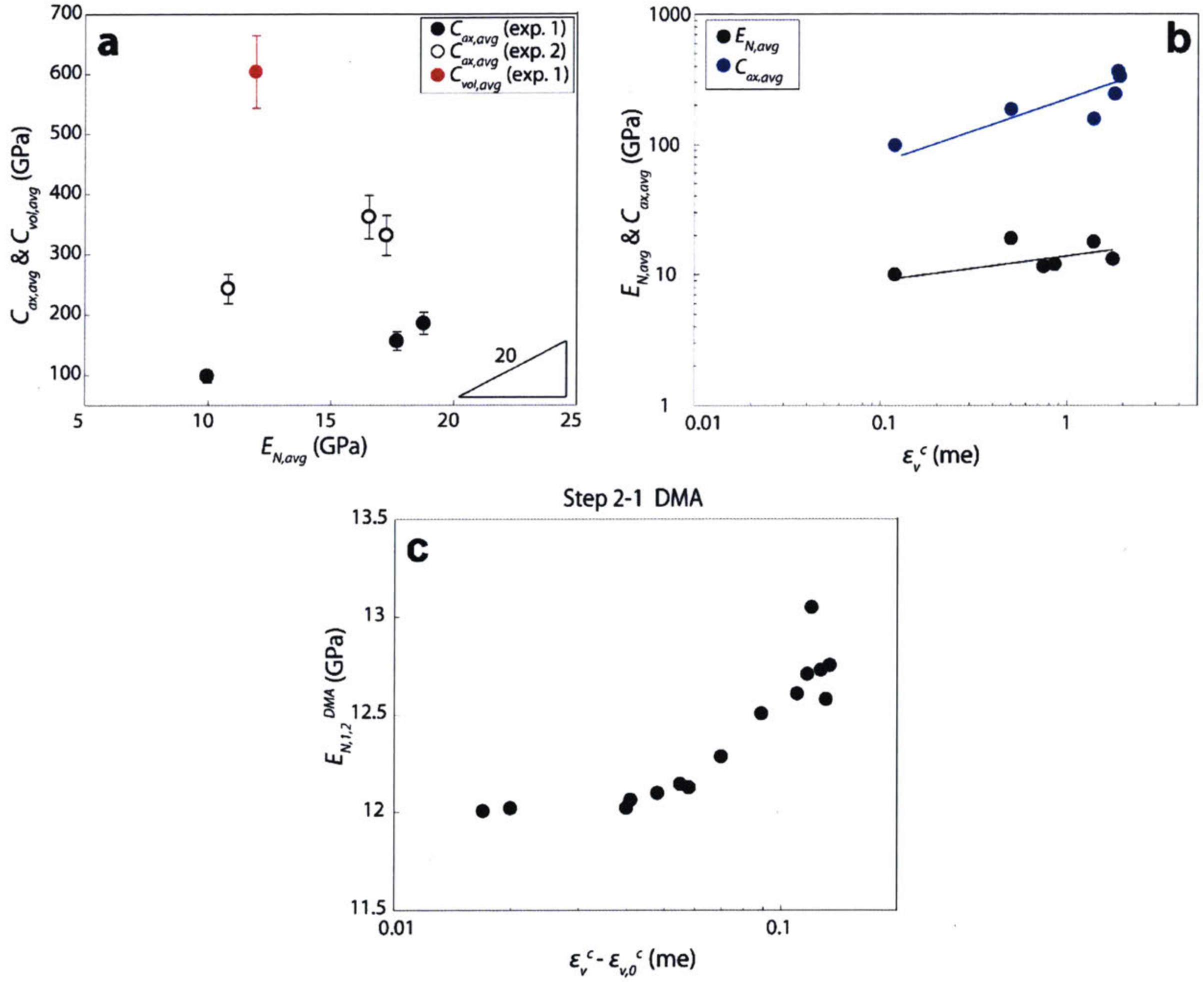

Figure 3-8. (a) Triaxial measurements of the axial and volumetric creep moduli vs. Young's modulus estimated in the same pressure/stress conditions. The vertical error bars indicate the experimental uncertainty (about ±10%) on C. To consider error bars on E, I considered only the sensors precision (about ±1%) as the three separate strain gauges 1, 2, and LVDT sensors showed

similar modulus evolution during experiments. (b) Elastic and creep moduli as functions of accumulated creep strain. E_{avg} and $C_{ax,avg}$ denote the averages of $E_{N,1}$, $E_{N,2}$, and $E_{N,LVDT}$, and, $C_{ax,1}$, $C_{ax,2}$ and $C_{ax,LVDT}$, respectively. (c) An example for the evolution of E during a single DMA step.

3.4.3.3 Nanoindentation vs. triaxial moduli

The triaxial Young's moduli for U.S. shales seem to have a lower bound of ~15 GPa [Sone and Zoback (2013a); Yang and Zoback (2016)], so the Vaca Muerta (**Error! Reference source not found.**) moduli lie at the lower end of this range, and within the range of immature Kimmeridge shale (Kumar *et al.*, 2012). European shales such as Alum, Posidonia, and Bowland shale also show softer Young's moduli of ~10 GPa (Rybacki *et al.*, 2015; Herrmann *et al.*, 2018). The presence of soft indentation group G1 in **Error! Reference source not found.**, specific to Vaca Muerta shale, might explain the low stiffness of Vaca Muerta. On the other hand, the nanoindentation average modulus obtained using Hashin-Shtrikman (HS) bounds had a relatively high value, E^{ups} ~ 22 GPa. Our HS homogenization method implicitly assumes an isotropic distribution of the local moduli, which is not consistent with the layered structure of Vaca Muerta shale, and therefore is expected to produce values intermediate between E_N and E_P. Using the E_P/E_N ~ 1.5 (Ambrose, 2014), the expected higher end for the triaxial E_P is 22.5 GPa, close to indentation E^{ups}. The overestimation of indentation E^{ups} with respect to the observed triaxial values may also indicate the presence of highly deformable features in Vaca Muerta shale such as cracks that were not sampled by the nanoindentations. Yet, the indentation-derived E^{ups} for Vaca Muerta still lies on the softer side compared with the nanoindentation moduli of other U.S. shales (Kumar *et al.*, 2012; Slim, 2016).

Similar to Young's modulus, the creep modulus for Vaca Muerta shale was also lower than the set of values estimated from triaxial creep experiments on U.S. shales (Sone and Zoback, 2011; Sone and Zoback, 2013b; Boulenouar *et al.*, 2017). I note that the indentation C^{ups} ~750 GPa was similar to indentation values of >600 GPa for mature shales (Slim, 2016). Similar to the elastic moduli, the upscaled C^{ups} is higher than the triaxial values of C following a σ_d step. Unlike Young's modulus, the creep modulus data are not sufficient to estimate the effect of rock anisotropy on C.

The Voigt (iso-stress, upper bound) and Reuss (iso-strain, lower bound) averages (Mavko *et al.*, 2009) also provide elastic bounds of our ternary G1-3 groups, albeit looser than the HS bounds

(Vanorio *et al.*, 2003; Kumar *et al.*, 2012; Sone and Zoback, 2013a; Herrmann *et al.*, 2018). These bounds have been found useful to estimate shale anisotropy (Sone and Zoback, 2013a). I found that the Voigt-Reuss (VR) bounds for E and C were 18.0-27.4 and 269-3708 GPa, respectively, while the Voigt-Reuss-Hill (VRH) average yielded 22.7 and 1988 GPa. The VRH value for E seems closer to the HS bounds than for C. A detailed comparison between such averaging methods is beyond the scope of this report; however, I notice that our triaxial values are closer to the Reuss bound (the case for a vertical sample), consistent with published experiments (Sone and Zoback, 2013a; Herrmann *et al.*, 2018). The VR bounds of Young's modulus are also broadly consistent with the Vaca Muerta triaxial moduli obtained by Ambrose (2014), 27 ± 11 and 18 ± 7 GPa in horizontal and vertical samples, respectively.

Both elastic and creep moduli increased significantly with increasing differential stress and only slightly with increasing confining pressure. The dominant effect of σ_d over p_c is probably due to the nature of deviatoric vs. isostatic loading, as well as the alignment of the maximum principal stress and the weakest principal direction of anisotropy (i.e., normal to bedding). Incremental C after inelastic strain accumulation under triaxial tests is also consistent with the C values for indentations measured after partial unloading, which were generally much higher than those measured after initial loading. In the next section, we will discuss the strain hardening during creep experiments.

3.5 Discussion

Three aspects of the creep behavior were evident in the shale experiments: shear-enhanced compaction, strain hardening, and time-dependent creep. The first owes to the competition between processes that result in non-dilational shear or compaction. As inelastic strain accrues, the elastic and creep compliances change, probably because of changes in the rock structure. It is plausible to suppose that compaction contributes to strain hardening. The third aspect reflects the rate-kinetics of the physical processes responsible for the inelastic strain. We wish to discuss these three aspects in a qualitative way. Quantitative treatment will require detailed knowledge of the exact physical mechanisms responsible for dilation and compaction and of their kinetics.

3.5.1 Shear-enhanced compaction during creep

Yield-cap models, first developed in soil mechanics, are often used to describe the time-independent compaction in porous sandstones and limestones (Wong *et al.*, 1997; Baud *et al.*, 2006; Wong and Baud, 2012). Depending on the loading path, when compaction dominates, inelastic yield may be characterized by the onset of shear-enhanced compaction as measured by deviation from the hydrostat, C^*, or by the critical effective pressure measured by the deviation point of the hydrostat from linearity under fully isotropic loads, P^* (Baud *et al.*, 2006; Wong and Baud, 2012). In sandstones and limestones, the yield curve is usually expressed as an elliptical function of the mean and differential stresses, p and q:

$$\frac{(p-C')^2}{A'^2}+\frac{q^2}{B'^2}=0 \qquad (27)$$

where A' and B' are the semi-axes of the elliptical cap, and C' is the p-coordinate of the center. The elliptical yield curve may not accurately represent behavior under low confinement, when dilational processes dominate. A more general viewpoint, the double yield cap, can be obtained by considering separate criteria for dilational yield and shear-enhanced compaction (e.g., see (Rudnicki, 2004; Wong and Baud, 2012). In the following, I do not consider the dilation regime because our experiments were done exclusively under stress conditions that caused compaction.

Strain hardening implies that the yield cap expands as inelastic strain accumulates. It is usually assumed that the elliptical shape is retained, and specific rules have been proposed to describe the evolution of the ellipse (Wong and Baud, 1999; 2012). For example, the initial parameters, A_0, B_0, and C_0, in the Carroll's model might change to A, B, and C in response to an increment of inelastic strain, with the following conditions: $A = A_0$ (i.e., constant length of the p semi-axis) and $B = B_0 + m(C-C_0)$. Thus, the peak of the yield cap, i.e., the point (C, B) in a p-q plot moves along a "critical state line" with a constant slope m. In a second model, the aspect ratio of the elliptical yield cap, $B/A = B_0/A_0$ is held constant (Wong and Baud, 2012). Both models are empirical. They strictly apply only to isotropic materials because yield is a function of the first two stress invariants only. As a first-order approximation, I assume that these models can be applied to anisotropic materials deformed under co-axial loading, i.e., when principal directions of the material and those of the imposed stresses coincide, as was the case in our experiments and some of Ambrose (2014) triaxial tests. Using triaxial tests on Vaca Muerta samples oriented normal to the bedding (Ambrose, 2014), I plotted the evolution of the yield curves for a strain rate of 10^{-5} s^{-1} (Figure 3-9). In addition to differing in strain rates, these tests covered a wider range of confining pressures (0 - 69 MPa) than our experiments. Carroll's model produced an acceptable fit to the data (Figure 3-9). The details of the yield curve analysis are given in Appendix S2. The constant strain rate experiments show evidence of strain hardening during shear-enhanced compaction, culminated by dilatant failure (Figure S2).

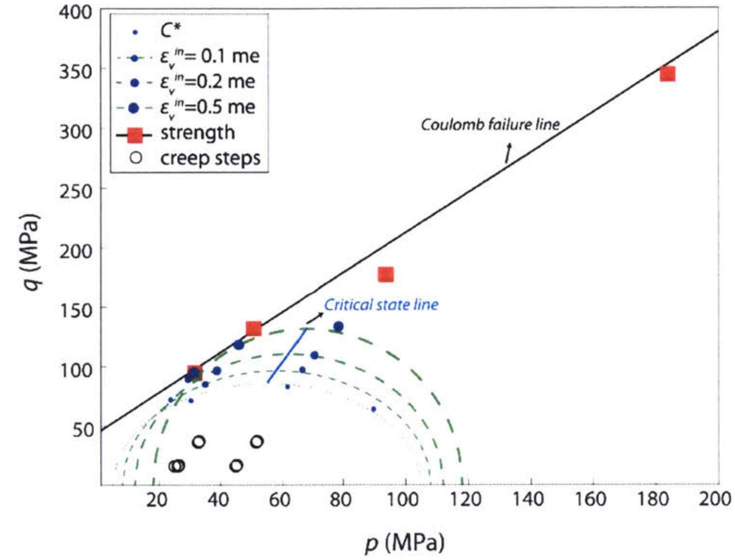

Figure 3-9. Yield curves (dashed green curves using Carroll's cap model) for Vaca Muerta shale during triaxial experiments at a strain rate of 10^{-5} s^{-1} (Ambrose, 2014). See Appendix S2 and Figure S2. For comparison, loading conditions for creep steps in this paper (strain rates: $\sim 10^{-10}$-10^{-7} s^{-1}) are shown with black open circles. The creep conditions are well below the yield curves of the fast-rate triaxial experiments, shown by the green ellipses, and below the limiting fast-rate differential strength, shown by the red squares. Blue and black solid lines show the critical state line [Carroll's critical state model in Appendix S2; (Carroll, 1991; Baud et al., 2006)] and Coulomb failure line.

In our experiments, the stresses were always completely enclosed within Ambrose's yield curves, i.e., creep stresses were below 50% of C^* and 40% of P^* (Table 3-3 and Figure 3-9), and still creep occurred. Initial creep strain rates were much slower than 10^{-5} s^{-1} in Ambrose's experiments and declined steadily from 2×10^{-7} to 10^{-10} s^{-1} as the sample deformed (Table 3-3). Yield-cap models can be generalized to creeping materials by assuming that, in addition to depending on the inelastic strain, the yield curve is also a function of strain rate. Experimental observations support this model. Yield surfaces that depend on strain rate have been observed in granular geomaterials such as soils and clays at both dynamic (Tong and Tuan, 2007) and slow (10^{-6}-10^{-8} s^{-1}) (Boudali, 1995; Augustesen *et al.*, 2004) loading rates, as well as in quartz sands (Choens and Chester, 2018). Dependence of yield stresses upon strain rate is also established during both brittle dilation and compaction of sandstones and limestones at low temperatures (Heap *et al.*, 2009a; Brantut *et al.*, 2012a; 2013; 2014a). Typically, in tests with loading at a constant displacement rate, the yield stress increases with strain rate (Rutter, 1974; Kirby, 1980).

Yielding occurs at very low stresses in Vaca Muerta shale, provided that the creep strain rate is sufficiently low. Furthermore, I expect the strain rates in constant-stress tests to decrease with time if the hardening caused by accumulating inelastic strain is compensated by decreasing strain rate. Unfortunately, I do not have sufficient experimental data to model the details of the strain rate dependence of the yield curve. The only information available is that, during a creep test in constant stress conditions, the point (p_0, q_0) must lie on the elliptical yield cap, i.e., the yield function must verify $(p_0-C)^2/A^2+q_0^2/B^2=1$.

Table 3-3. Mechanical parameters during the creep steps compared to those for constant loading rate.

Creep step	σ_d/C^* (%)[a]	σ_d/FS (%)[a]	Pc/P^* (%)[b]	$\dot{\varepsilon}_a{}^c$ @ 5 h (s^{-1})[c]	$\dot{\varepsilon}_v{}^c$@ 5 h (s^{-1})[c]	$\varepsilon_v{}^c$@ 10^{-7},$^{-8}$,$^{-9}$ s^{-1} (me)[c]
1-1	20	8	19	4.5×10^{-9}	4.4×10^{-9}	0.12, 0.33, 0.45
1-2	49	20	20	11.4×10^{-9}	10.1×10^{-9}	0.50, 0.65, 0.68
1-3	21	9	20	-6.8×10^{-11}	-9.9×10^{-10}	N, 0.75, 0.77
1-4	21	9	38	7.0×10^{-10}	4.1×10^{-9}	0.86, 0.93, 1.01
1-5	49	20	38	1.4×10^{-8}	1.4×10^{-8}	1.40, 1.63, 1.77
1-6	21	9	38	-1.8×10^{-9}	-8.4×10^{-10}	N, 1.85, 1.85
1-7	1	<1	4	1.4×10^{-10}	3.4×10^{-10}	-
2-1	21	9	20	-	-	1.81, 1.84, 1.85[c]
2-2	49	20	20	9.3×10^{-10}	7.8×10^{-9}	1.88, 1.89, 1.91
2-3	21	9	38	-	-	1.92, 1.93, 1.95
2-4	49	20	38	4.0×10^{-9}	7.3×10^{-10}	2.06, 2.14, N

Note: [a]The loading conditions during creep steps are normalized by C^*= 74 MPa and compressive differential strength (*FS*)= 177 MPa that were observed during experiments of Ambrose (2014) at p_c=34 MPa and constant loading rate of 10^{-5} s^{-1}. [b]The value for P^*, 106 MPa, was calculated from that data for an elliptical yield cap (see Appendix S2). [C]This column summarizes the corresponding inelastic volumetric strains at the mentioned strain rates. The strain rates are based on average slopes in intervals of 300 seconds. The normalized 95% confidence interval uncertainty on strain rate reached a maximum of ~25% at slow rates.

3.5.2 Transient creep and the transition to linear viscoelasticity

3.5.2.1 Log-time creep systematics

Log-time creep occurred in Vaca Muerta shale during nanoindentation and triaxial tests, at time scales from 2 min to 12 hours (Figure 3-5), consistent with various North American shale data summarized in Table 3-4 and Figure 3-10 and Figure 3-11. Our results are similar to the published shale studies in several aspects: compaction commonly occurs during creep in shale under both isostatic and triaxial loading, the transient creep is log-linear (see Figure 3-11), the mechanical behavior depends on the orientation of loading with respect to bedding, and creep strain rates loaded with triaxial stresses are typically larger than those in isostatic compression (Ghassemi and Suarez-Rivera, 2012; Sone and Zoback, 2014; Villamor Lora and Ghazanfari, 2015).

Log-time creep has also been observed in soils; where the short-term consolidation creep is generally followed by longer lasting, secondary compression obeying log-time kinetics (Lambe and Whitman, 1969; Whittle, 1993; Pestana and Whittle, 1999). The log-time kinetics are not restricted to porous materials; for example, Vickers indentation creep on quartz and olivine crystals (Scholz and Engelder, 1976) and creep of asperities during closure of normally stressed fractures (Dieterich, 1978) also obey log-time kinetics. The presence of log-time behavior in such wide ranges of materials and conditions suggests that these kinetics do not arise in response to specific physical mechanisms.

Several physical deformation processes might be active during creep, either singly or concurrently. These processes might include intra-granular (Den Brok and Spiers, 1991; Bernabe *et al.*, 1994) or inter-grain (Baud *et al.*, 2000) cracking and slip, which may activate via subcritical crack growth (Kemeny, 1991; Chester *et al.*, 2007; Heap *et al.*, 2009a; Brantut *et al.*, 2012a; 2013; 2014a; Heap *et al.*, 2015) or pressure solution at intergranular contacts (Rutter, 1983; Spiers *et al.*, 2003; Geng *et al.*, 2018). The clayey nature of shale may also house active creep processes, such as granular and particle sliding (Kuhn and Mitchell, 1993; Kwok and Bolton, 2010), overcoming interparticle forces (Santamarina, 2003), and particle rearrangement (Hartley and Behringer, 2003; Vandamme and Ulm, 2009). In porous rocks, poroelasticity (Mahyari and Selvadurai, 1998) may also play a role in time-dependent deformation. The partitioning of strain amongst these processes will depend on mineralogy, thermodynamic conditions, loading geometry and magnitudes, rock lithification, pore-fluid conditions, and many other factors. Without a rather detailed set of experiments and observations, it is difficult to isolate the set of processes that control the deformation.

Although we are not able to speculate on its causal mechanisms, log-time creep in Vaca Muerta shale can be adequately quantified by means of the creep modulus C. This creep measure is specific to the log-time kinetics and has been used in oedometric (Lambe and Whitman, 1969; Whittle, 1993; Pestana and Whittle, 1999), triaxial (Chang and Zoback, 2008) and indentation tests (Vandamme and Ulm, 2013; Slim, 2016). Consistent with Vaca Muerta results presented in previous section, the creep moduli of other shales tend to correlate with other mechanical parameters such as Young's modulus (Figure 3-10). Figure 3-10 also shows that Vaca Muerta is a very soft shale rock, comparable only to Haynesville: SZ13.

Table 3-4. Transient and linear viscoelastic creep parameters for published triaxial creep tests on different shales.

Shale	t (hrs)	ε^a, O^b	p_c (MPa)	σ_d (MPa)	$\dot{\varepsilon}^c$ @ 5 h (s^{-1})	C (GPa)	E (GPa)	t_c $(s)^c$	η $(GPa.s)^c$	Reference
Haynesville: SZ11	336	*a*,-	20	30	3.3×10^{-10}	1424	64	8.0×10^4	11.4×10^7	(Sone and Zoback, 2011)
Haynesville: SZ13	3	*a, N*	30	32	-	199	18	-	-	(Sone and Zoback, 2013b)
Barnett: SZ13	3	*a, N*	20	46	-	830	25	-	-	(Sone and Zoback, 2013b)
Barnett: GS12	18	*a, N*	16	45	7.1×10^{-10}	1184	32	-	-	(Ghassemi and Suarez-Rivera, 2012)
Mancos: GS12	77	*a*, -	0	37	8.0×10^{-10}	1250	-	4.3×10^4	5.4×10^7	(Ghassemi and Suarez-Rivera, 2012)
Haynesville: LG12	47	*a, N*	16	63	2.9×10^{-9}	774	18	2.9×10^4	2.2×10^7	(Li and Ghassemi, 2012)
ulf of Mexico: CZ08	120	*v*, -	30	0	7.2×10^{-8}	15	-	8.9×10^4	0.1×10^7	(Chang and Zoback, 2008)
Marcellus: VG15	3	*a, N*	30	30	-	582	22	-	-	(Villamor Lora and Ghazanfari, 2015)

Notes: ^{a} *a* and *v* refer to the recorded strains as axial and volumetric strain, respectively. ^{b} *N* and *P* refer to normal and parallel orientations to bedding, respectively. ^{c} transition time, t_c(s), and linear viscosity, η, were determined during long-term experiments.

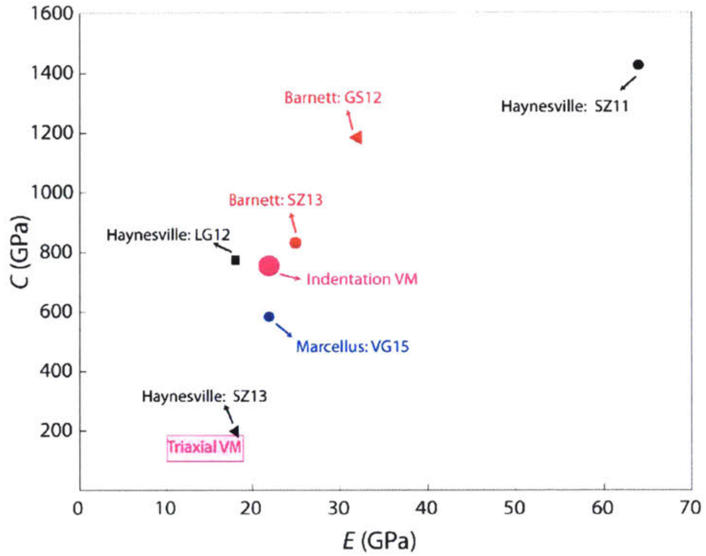

Figure 3-10. The relation between C (creep moduli here are axial moduli) and E for published triaxial creep tests along with data from this study. I included the averaged nanoindentation moduli for Vaca Muerta (large purple circle mark). The purple rectangle for triaxial data shows the bounds on moduli for fresh (experiment 1 cycles) Vaca Muerta shale. In general, the two moduli are directly related. The references indicated by the data point labels are given in Table 3-4.

3.5.2.2 Transition to linear viscoelastic creep

Nanoindentation tests necessarily represent short-term creep. Even with the nanoDMA technique, thermal drift correction is unreliable for times longer than a few minutes. Thus, it is striking that contact creep moduli measured during indentation agree with creep moduli measured in triaxial tests lasting up to 12 hours. But, even triaxial experiments may often be too short to make definitive long-term predictions. One exception was the two-week creep test on a Haynesville shale sample (here labeled SZ11) reported by Sone and Zoback (2011). Plots of the "Haynesville: SZ11" creep deformation data in linear and log time scales show a transition from log-time creep at times before ~10^5 s to creep at constant strain rate at longer times (Figure 3-11a,b). Hints of similar transitions were also observed in other shale experiments (Figure 3-11c,d). The long-term creep rates appear to be consistent with linear viscoelasticity, as suggested by the nearly linear dependence of creep strain rates on stress seen in some tests (Fabre and Pellet, 2006; Ghassemi and Suarez-Rivera, 2012; Li and Ghassemi, 2012; Sone and Zoback, 2013b). Thus, at least in some cases, long-term creep of shales might be characterized by a single viscosity η:

$$\varepsilon_j{}^c - \varepsilon_{j,0}{}^c \approx \frac{\sigma}{\eta} t \tag{28}$$

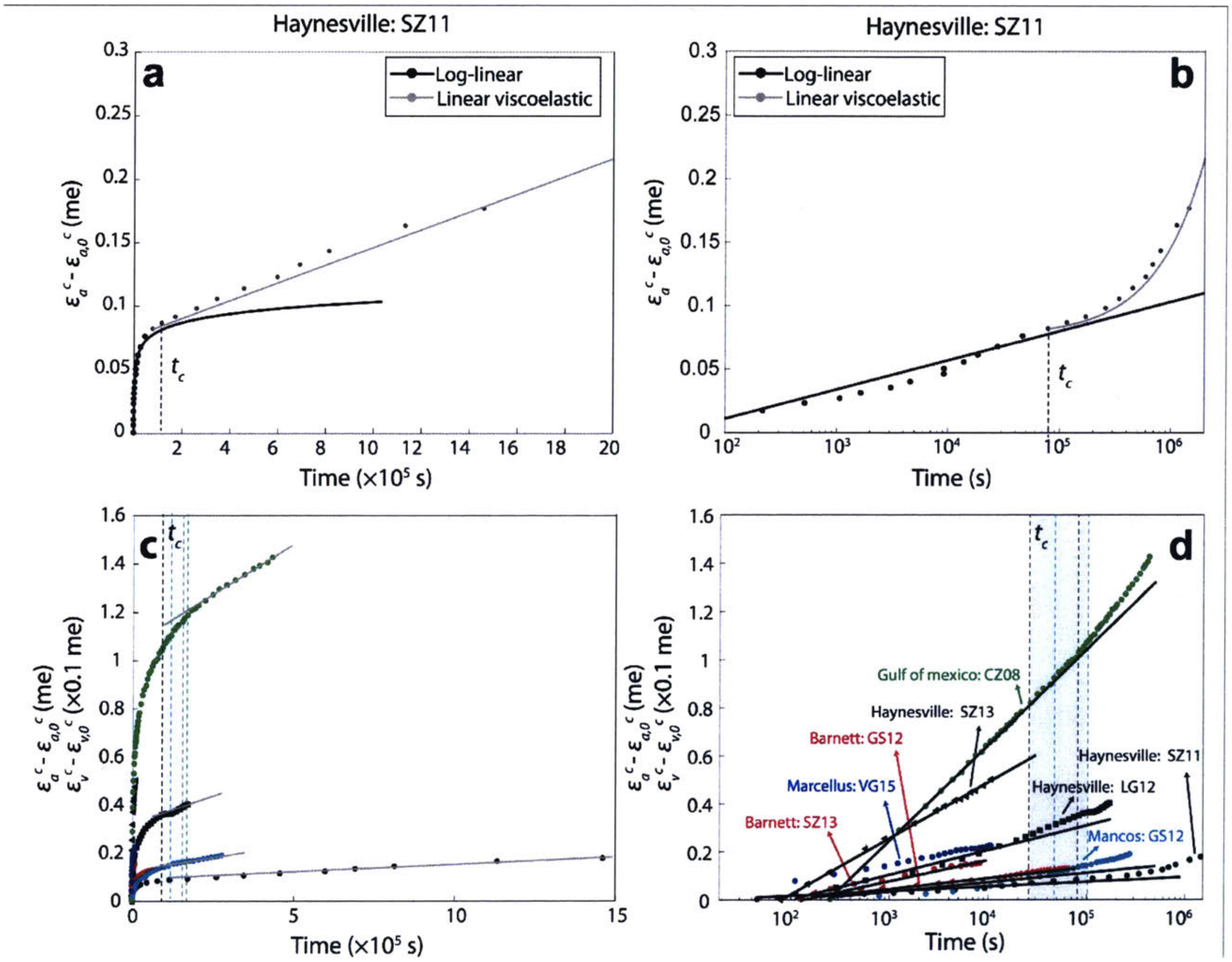

Figure 3-11. Long-term creep response of shales shown in linear (**a**, **c**) and logarithmic time scales (**b**, **d**). References to labels are listed in Table 3-4. Color codes are similar to that of Figure 3-10. Gray lines in a and c, and black lines in b and d are best-fits for viscous creep and transient, respectively. The approximate time of transition from log(t) to linearly viscous behavior is given by vertical dashed lines in a, b, and gray areas in c, d.

The transition time, t_c, is the approximate time when the creep response changes from log(t) to linearly viscous behavior. This change occurred rather suddenly for the Haynesville: SZ11 sample, but was more gradual in the other cases. In general, 0.3×10^5 s< t_c<10^5 s. The continuity of the creep function at t_c then gives:

$$\dot{\varepsilon}_j{}^c\,(t_c) = \frac{\sigma}{\eta} \quad \text{for } t \geq t_c, \qquad \dot{\varepsilon}_j{}^c\,(t_c) = \frac{\sigma}{Ct_c} \quad \text{for } t \leq t_c, \quad \text{so} \qquad \eta = C.t_c \tag{29}$$

Thus, the long-term viscosity, η, can be obtained from the short-term creep modulus, *C*, provided t_c is known. In the experiments shown in Figure 3-11, long-term viscosity values varied between 0.1 and 11×10^7 GPa.s and transition times had a relatively limited range of ~ 9 to 30 hours (Table 3-4). Based on a value of ~200 GPa for *C*, the long-term viscosity of Vaca Muerta shale should lie between 0.6 and 2×10^7 GPa.s. I emphasize here that such creep descriptions, including log(t), linear viscoelastic, and power-law kinetics are empirical and approximate fits to the data. In addition to extending the long-time data, further studies should be done to constrain the exact physical mechanisms responsible for creep and to obtain information on the effects of changing stress conditions, thermodynamic states, or rock type on the creep kinetics.

Observations of a transition from transient decelerating creep to linear viscoelasticity are not incompatible with the yield-cap model. During creep under constant loads, the yield surface evolves by a combination of expansion owing to strain hardening and contraction as strain rates decrease (Figure 3-12b). By analogy with critical state soil mechanics theory (Wood, 1990), the deformation of the yield curve (contraction/expansion and translation along the *p* axis) is assumed to cause convergence of the creep stress point (p_0, q_0) and the peak of the yield cap. For example, the behaviors expected in triaxial, constant strain rate and constant stress, creep tests are illustrated in Figure 3-12a, b, respectively. During creep tests, both strain hardening and strain rate decrease become insignificant at the critical point. Creep can then proceed at nearly constant strain rate for an extended period of time. In soil mechanics, unconsolidated granular aggregates can indefinitely remain critically stressed (i.e., at the peak of the yield cap) because their internal state only depends on packing density. Consolidated rocks, including very soft shales, do not share this property and the yield curve evolution of critically stressed rock samples should not stop entirely. The stress point may eventually fall on the dilatational portion of the yield curve (left side of the cap peak), leading to tertiary creep under constant-stress conditions or dilatant failure at constant strain rate (note that in double yield-cap models the dilatational yield curve segment does not necessarily have the elliptical shape represented in Figure 3-12). The amount of time spent near the critical state should depend, among other things, on the current strain rate, implying that, once reached, linear viscoelastic creep may persist a long time in rocks such as Haynesville shale under specific stress conditions (Sone and Zoback, 2011). Alternately, the rocks might fail quickly after the onset of dilatancy as was the case in the fast-rate Vaca Muerta shale tests of Ambrose (2014) (Figure S2).

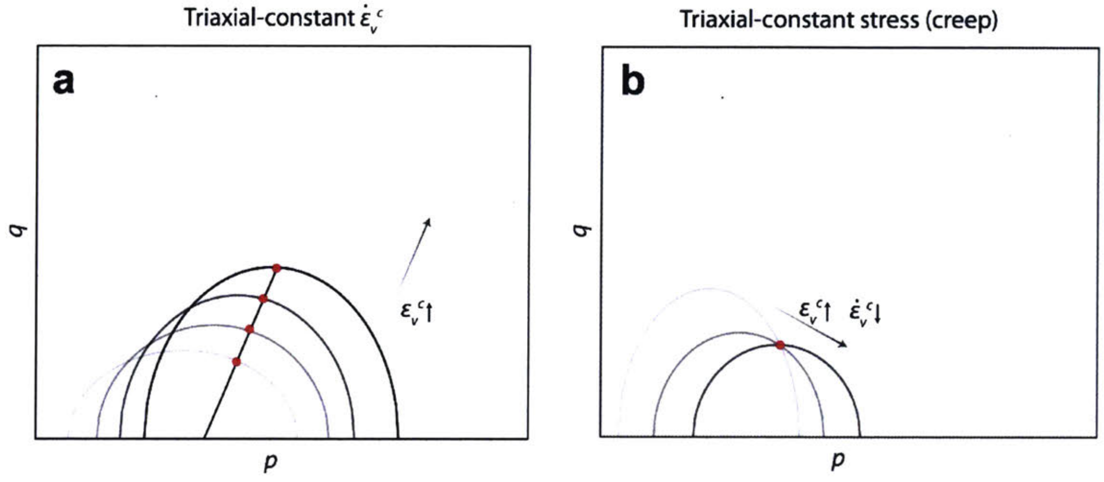

Figure 3-12. Schematic representation in p - q space of the evolution of the yield curve during **a**) a triaxial, constant strain rate test and **b**) a constant stress creep test. The red dots show the stress conditions experienced by the material at different times during the tests. The blue arrows indicate the evolution at increasing times.

3.5.2.3 Origin of log-time kinetics

Although the yield cap model qualitatively rationalizes the observations of decelerating, transient creep in shales, it does not specifically predict log-time kinetics. The frequent occurrence of log-time relaxation and creep in a very broad range of materials under very different stress and temperature conditions suggests that it is a statistically emerging behavior. Snieder *et al.* (2016) proposed a conceptual model stating that log-time kinetics stem from the combination of mechanisms associated with a large number of different relaxation times. A similar idea has been used to model the log-time relaxation characteristic of the so-called slow dynamics observed in many materials including rocks (Gibbs *et al.*, 1983; TenCate *et al.*, 2000; Zaitsev *et al.*, 2003; Zaitsev *et al.*, 2014). To illustrate the concept, Snieder *et al.* (2016) showed that summing individual relaxation functions with exponential Maxwell kinetics, $fi(t)=\exp(-t/\tau i)/\tau i$, where τi is the relaxation time, gives an aggregate relaxation function characterized by a long log(t) behavior at intermediate times. One important feature of this model is that the duration of the log(t) segment can be arbitrarily extended by increasing the range of relaxation times, i.e., [τmin, τmax]. In the same paper, Snieder *et al.* (2016) presented another illustrative model with no variations in relaxation time, but which, nevertheless, produced approximate log(t) kinetics. This model considers the time-dependent closure of a rough fracture contained in a linear viscoelastic Kelvin material (dashpot and spring *in-parallel*). For the sake of simplicity, the fracture asperities are idealized as *in-parallel* Kelvin elements with identical spring constants and viscosities, but with different heights, so that only a few asperities come into immediate contact upon loading. At early times, the local contact stresses are very high and the fracture closes very rapidly. As time evolves new contacts are formed, and stresses are transferred to the new contacts, causing fracture closure to decelerate. Snieder *et al.* (2016) observed approximate log-time fracture closure at intermediate times when the distribution of asperity heights (i.e., the distribution of times of contact) was sufficiently broad.

Similarly, log(t) creep in a porous rock undergoing shear-enhanced compaction could be produced by delayed activation of viscoelastic elements. To demonstrate the concept, we considered yet another conceptual model consisting of N *in-parallel* Maxwell elements (each with a stiffness k_i and viscosity η_i connected in series) with a broad distribution of activation displacements, $\delta_i \geq 0$ (see inset in Figure 3-13). To reduce the degrees of freedom of the model, we deterministically related the corresponding values of the stiffness, k_i, and viscosities, η_i, to δ_i through some simple monotonic functions. Thus, the more creeping elements with the lowest viscosity had the lowest stiffness and activated early during the creep period. Applying a force step (S) at $t = 0$ initially triggered $n_0 < N$ elements. As displacement accumulated, the number of triggered elements $n(t)$ grew and stress was transferred from the initially activated elements to the new ones according to the following equation (derived from the creep response of a Maxwell element):

$$\delta(t) - \delta_i = \frac{s_i(t)}{k_i} + t\frac{s_i(t)}{\eta_i} \qquad (10)$$

and the distribution of local forces:

$$S = \sum\nolimits_{n(t)} s_i(t) \qquad (11)$$

where $\delta(t)$ is the global displacement and s_i the local force ($s_i = 0$ when the element is not yet activated). We ran a small numerical version of this model ($N = 20$). By plotting the simulated creep curve in linear and semi-log time space (Figure 3-13), we can indeed see a log(t) segment at intermediate times and a transition to linear viscoelasticity when all the elements have finally been triggered. In this specific implementation, the activation displacements were exponentially distributed and related to k_i and η_i through linear and exponential functions, respectively. These particular functions are probably not necessary for the production of a log(t) segment. The essential features of the model are the presence of a large number of displacement-activated sites in the rock and a very broad distribution of activation displacements. Such distributions might arise from variations of microstructural parameters, including pore size and shape, surface roughness and geometry, or grain-grain contact dimensions, and heterogeneities in many other microstructural features might also contribute. The specific nature of the activated sites (here, viscoelasticity) is not important however. In consequence, observation of log-time kinetics does not provide any information on the identity of the local creep mechanisms acting in particular materials under specified stress and temperature conditions.

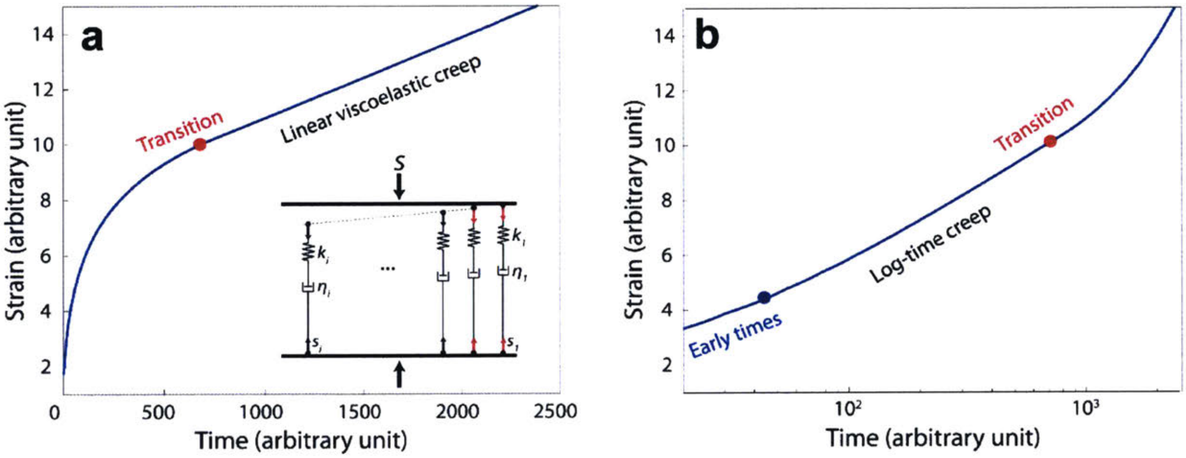

Figure 3-13. Example of a simulated creep curve using the viscoelastic model in (a) linear and (b) semi-log time space. The log-time and linear viscoelastic segments are easily visible in the right and left diagrams, respectively. Approximate limits of the log-time segments are indicated by colored marks. The inset shows an *in-parallel* arrangement of Maxwell elements with contact gaps (i.e., activation displacements) decreasing from left to right (see dashed gray line; red arrows highlight the elements in actual contact); note that this schematic representation does not reflect the physical location of single elements.

3.6 Conclusions

I performed nanoindentation and triaxial creep experiments on the Vaca Muerta shale. These methods shed light on complementary aspects of the creep behavior of shale. Nanoindentations provide the elastic, creep, and strength properties of the rock matrix at the micrometer-scale, giving insight into the mechanical properties and spatial distribution of the individual mineral constituents. However, the influence of the differential stress and confining pressure cannot be separated using this technique. Also, the volumetric strain and its evolution during creep cannot be directly derived from the indentation displacements. In contrast, the triaxial experiments allow independent control the differential stress and confining pressure as well as separate monitoring of axial, radial and volumetric strains. Also, the less complex stress states generated in triaxial geometry facilitate direct comparison with *in-situ* stresses. Combining nanoindentation and triaxial tests on samples of Vaca Muerta shale yielded useful conclusions:

- We observed log-time creep behavior at time-scales varying from 2-minutes (indentations) to 12-hour (triaxial tests). Indentation tests and EDX observations showed that hard minerals such as pyrite, dolomite, calcite, and quartz occurred as disconnected inclusions dispersed throughout the clay/organic matrix. We also found unusually soft areas ($E<$ 10 GPa), likely associated to organic matter and clays (group G1). The HS averaging method yielded values of the elastic and creep moduli, E^{ups} and C^{ups}, of 22 GPa and 750 GPa, respectively. In the triaxial tests, Young's modulus normal to bedding (E_N) and the axial creep modulus (C_{ax}) strongly increased with increasing σ_d. Smaller increases of E_N and C_{ax} resulted from confining pressure increases and, more generally, from creep strain accumulation. The triaxial elastic and creep moduli were lower than E^{ups} and C^{ups}, with the smallest values obtained from LVDT readings. These observations suggest a possible scale dependence of the elastic and creep moduli, since the nanoindentations, strain gauges and LVDT's probe increasing volumes of material (Figure 3-14). It is also possible that the nanoindentations did not provide a complete statistical description (due to statistical biases in sampling small volumes) of the material's micro-scale properties or that our upscaling technique was not optimal for Vaca Muerta shale.
- All triaxial creep tests produced volumetric compaction. Creep compaction was driven by both σ_d and p_c, and occurred at stress levels well below the yield surfaces measured at faster strain rates. Creep strains accumulated (after 12 hours) during σ_d loading steps were as large

as seven times higher than those caused by similar increases in p_c (compare steps 1-2 vs. 1-4). Similarly, C_{vol} was 4 times higher than C_{ax}. Both the elastic and creep moduli increased with increasing inelastic strain. Inelastic strain did not recover upon removal of the load.

- Our observations are consistent with a yield cap model positing strain rate-dependent yielding; during a creep step, the yield surface is assumed to contract more owing to decreasing strain rates rather than expanding due to strain hardening. This model does not exclude a transition from decelerating to constant strain rate creep, as was indeed observed in previous experiments on shales.
- The log-time kinetics observed here correspond to transient (or primary) creep and can be characterized using the creep modulus C. Previous creep tests in shales revealed that a transition to constant strain rate creep may occur at longer times. Accordingly, the long-term creep can be characterized by a single parameter, viscosity, $\eta \sim C\, t_c$. Several previous studies suggest that the transition time in various shales is between 0.4 and 1.2 days. Using this range of t_c, the creep moduli observed in Vaca Muerta yield a long-term viscosity term of 0.6 to 2×10^7 GPa.s.
- Finally, I devised a conceptual model containing viscoelastic elements that remain inactive until certain activation strains (represented as displacements in the model) are reached. When there are many different elements with widely distributed activation strains, the model produces time-dependent global deformation approximately proportional to log(t), and the response eventually becomes asymptotically linear in time when all the elements are activated. According to this model, log-time kinetics emerge from the interaction of widely different elements. The viscoelastic nature of the elements is convenient for numerical implementation but is not conceptually essential, suggesting that log-time kinetics may not be specific to a particular class of physical mechanisms.

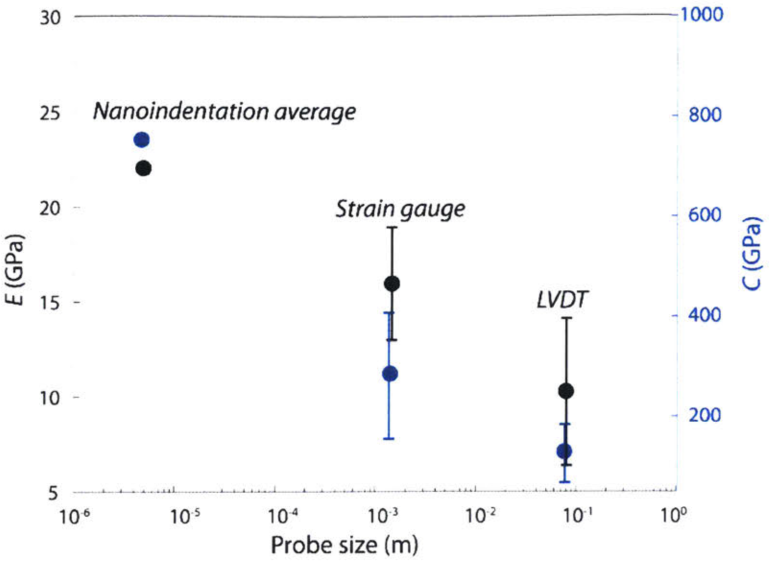

Figure 3-14. The elastic and creep moduli for Vaca Muerta shale obtained in this study. As the measurement length scale increases, the shale rock shows softer behavior. To compare the detailed probe sizes see inset in Figure 3-1 and results section. The strain gauge values are the mean between the two gauge measurements (±20% difference). The indentation values are the averages. The triaxial values are averaged from Table 3-1 and Table 3-2. Whether the spatial scaling extends to larger sizes at the same rate depends entirely on the heterogeneity of the formation.

Supplementary information

The supplementary materials provide auxiliary information about the temperature variations in the pressure vessel following adiabatic decompression of the confining liquid (S1), the determination of the high strain rate yield surfaces for Vaca Muerta shale (S2), the elastic response of a transverse isotropic (TI) solid to a hydrostatic compression (S3), and the averaging procedure used to upscale the indentation elastic and creep moduli (S4).

Text S1. Temperature variations in the pressure vessel during the triaxial experiments

Temperature inside the pressure vessel was continuously recorded during the experiments by a thermocouple mounted near the load cell. The temperature variations generally reflected temperature fluctuations in the laboratory with two notable exceptions, the sudden positive and negative temperature jumps at the start of the hold periods 1-4 and 1-7 (Figure S1). These sharp temperature variations were synchronous with the adiabatic compression/decompression of confining oil corresponding to the confining pressure steps; however, the return to thermal equilibrium lasted ~2 hours due to the large mass of the apparatus and oil. This suggests that the simultaneous ~2 hours dilational creep episode observed in hold step 1-7 is likely an artifact (Figure S1c). I are therefore confident that dilational creep cannot occur in Vaca Muerta shale in the stress conditions considered in this study.

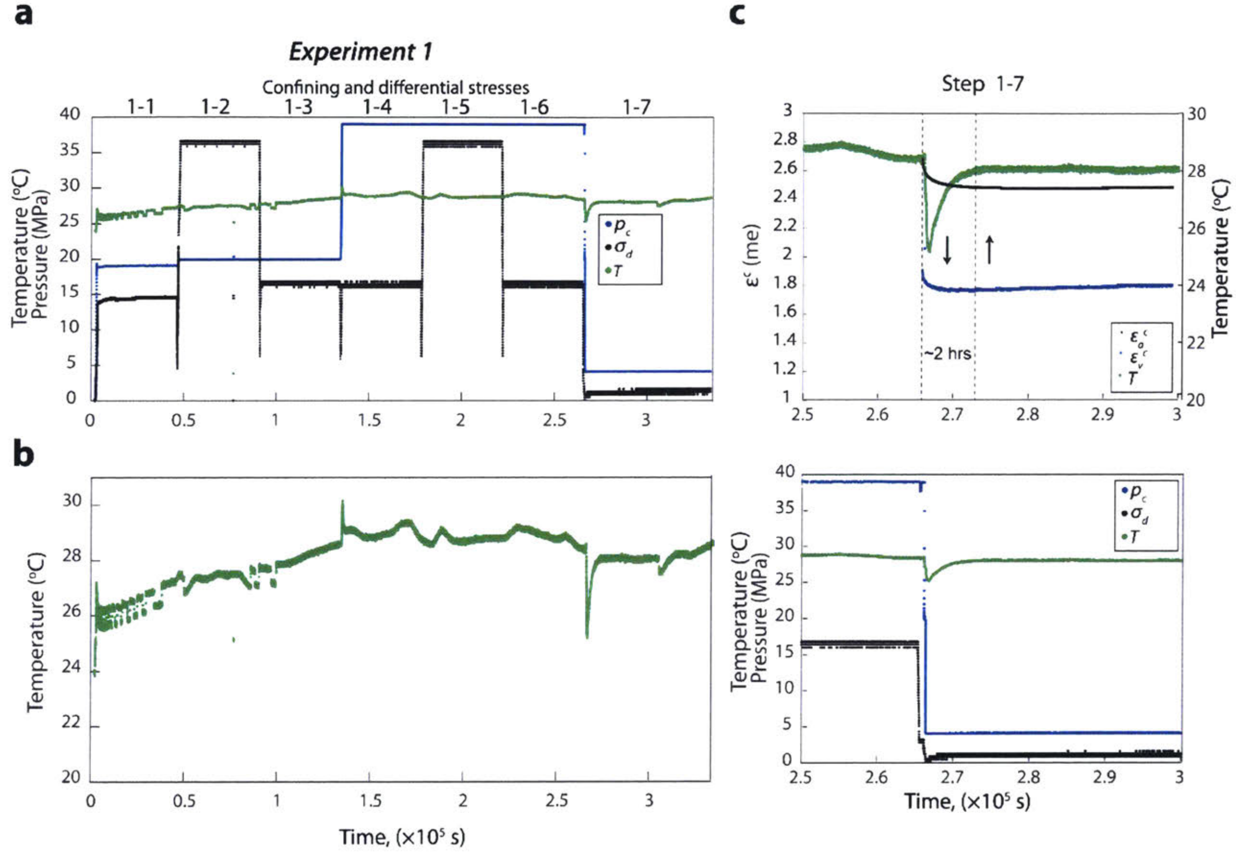

Figure S1. Temperature variations in the pressure vessel during triaxial creep experiment 1 (**b** shows a magnified view of the temperature variations in **a**). The vessel temperature remained approximately constant during differential stress steps but sudden temperature jumps coincided with the confining pressure steps preceding holds 1-4 and 1-7. (c) shows a sharp ~ - 4 °C temperature spike at the start of hold 1-7 and the subsequent ~ 2 hours return to thermal equilibrium. An apparent, probably artificial, dilational creep strain transient and a small differential stress excursion coincided with the temperature transient, after which creep strain resumed compression at a slow rate.

Text S2. Yield surfaces for Vaca Muerta shale

The triaxial experiments conducted by Ambrose (2014) on vertical (i.e., normal to bedding) Vaca Muerta samples yielded a sufficiently large dataset to determine the yield curve in p-q space at 4 different values of the inelastic strain. In these experiments, the confining pressure ranged between 0 and 69 MPa. The mechanical tests were conducted at a constant strain rate of 10^{-5} s^{-1}. The initial yield point, C^*, was determined as the mean stress level, p, at which the total volumetric strain, ε_v^{tot}, starts to deviate from linearity (Baud *et al.*, 2006) (Figure S2); the subsequent yield curves were constructed by determining the stress level corresponding to fixed values of the inelastic strain. The inelastic strain was calculated by subtracting the elastic strain from the total strain ($\varepsilon_v^{in} = \varepsilon_v^{tot} - \varepsilon_v^{el}$). For some experiments, I also noted the dilation initiation point, $C^{*\prime}$ (see Figure S2).

The constitutive model for the yield function is an elliptical cap, where A and B are the ellipse minor/ major semi-axes and C is the x coordinate for the ellipse center (Wong *et al.*, 1997; Baud *et al.*, 2006). A_0, B_0, and C_0 are the parameters of the initial elliptic yield curve at C^*. For the evolution of the yield function I used Carroll's critical state model (Carroll, *1991*); the yield cap evolves under work hardening while obeying two constraints: 1- the semi-axis on the abscissa remains constant, $A=A_0$, 2- the other two parameters are related by $B=B_0+m(C-C_0)$; i.e., the ellipse tip point (C,B) moves on a "critical state line" with a constant slope m. Our reasons for selecting Carroll's model were purely empirical, as it fitted our experimental data. Tables S1 and S2 show the strength/yield points and the yield parameters for Ambrose's experiments (also see Figure 3-9).

Table S1. The strength and yield points for Vaca Muerta shale triaxial experiments conducted by Ambrose (2014). The beddings are normal to the cylinder axis (vertical sample), similar to our study. All values are in MPa.

Confining pressure	C^*	Y^p @ 0.1 me ε_v^{in}	Y^p @ 0.2 me ε_v^{in}	Y^p @ 0.5 me ε_v^{in}	$\sigma^{strength}$
0	p=24 q=72	p=30 q=89	p=31 q=94	p=32 q=95	p=32 q=95
7	p=31 q=71	p=35 q=85	p=39 q=96	p=46 q=118	p=51 q=132
34	p=62 q=83	p=67 q=97	p=71 q=109	p=79 q=133	p=94 q=178
69	p=90 q=64	-	-	-	p=184 q=345

Table S2. The constitutive parameters for the yield curve family and strength line shown in Figure 3-9.

	Y^{p}[1] @ C^*	Y^p @ 0.1 me ε_v^{in}	Y^p @ 0.2 me ε_v^{in}	Y^p @ 0.5 me ε_v^{in}	$\sigma^{strength}$[2]
m	3.5	3.5	3.5	3.5	
***A* (MPa)**	50	50	50	50	
***B* (MPa)**	86	97	111	132	
***C* (MPa)**	55	58	62	68	
m_1					45
m_2					4

---

[1] For cap models I used an elliptical function with a form adapted from Carroll's critical state model (*Carroll, 1991*):

$\frac{(p-C)^2}{A^2} + \frac{q^2}{B^2} = 0$ where $A=A_0$ and $B=B_0+m(C-C_0)$. A_0, B_0, and C_0 are the initial yield surface parameters at C^*. m is the critical state line slope.

[2] The strength line is a Coulomb-type straight line with a form of $q= m_1 + m_2.p$.

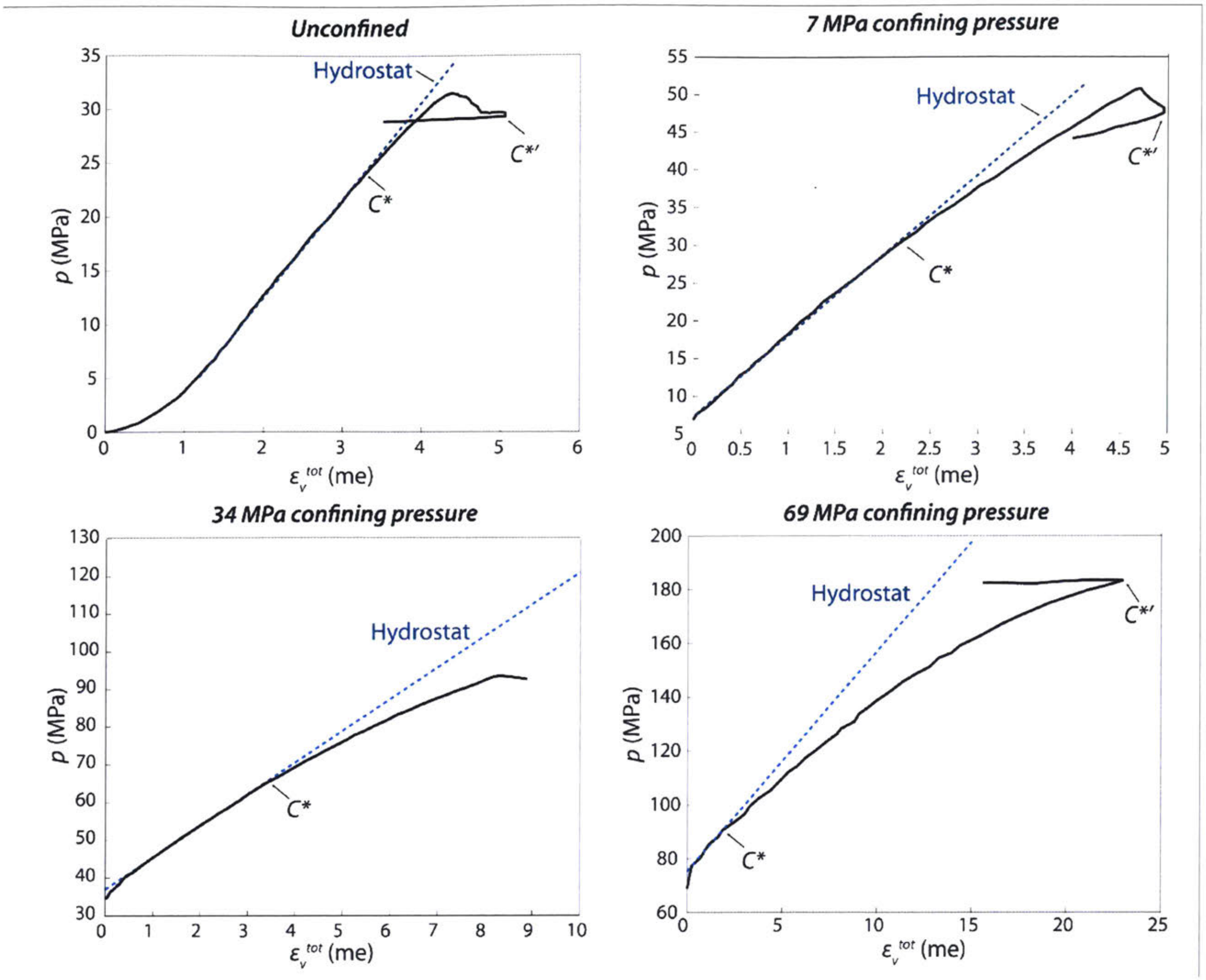

Figure S2. Triaxial experiments on Vaca Muerta shale (Ambrose, 2014). Plots show the mean stress (p) vs. total volumetric strain (ε_v^{tot}); positive volumetric strain shows volumetric compaction. Hydrostat blue lines show the linear compaction behavior based on fits on the early linear part of the curve. During isostatic conditions, up to certain mean stress (p^*), the material would compact linearly. C^* is denoted at the deviation point from linearity. $C^{*\prime}$ is denoted at the dilation initiation point.

Text S3. Elastic strain of a transversely isotropic solid subjected to a p_c step

I consider a transverse isotropic (TI) cylinder with its axis oriented normal to the isotropic plane. The stiffness tensor can be expressed in Voigt notation as (Amadei, 2012):

$$\begin{vmatrix} C_{11} & C_{12} & C_{13} & & & \\ C_{12} & C_{11} & C_{13} & & 0 & \\ C_{13} & C_{13} & C_{33} & & & \\ & & & C_{44} & 0 & 0 \\ & 0 & & 0 & C_{44} & 0 \\ & & & 0 & 0 & \dfrac{C_{11}-C_{12}}{2} \end{vmatrix}$$

where index 3 refers to the direction of the axis of symmetry. The Young's moduli normal and parallel to the isotropic plane are given by:

$$E_N = C_{33} - 2\frac{C_{13}^2}{C_{11}+C_{12}} \text{ and } E_P = \frac{(C_{11}-C_{12})[C_{33}(C_{11}+C_{12})-2C_{13}^2]}{C_{11}C_{33}-C_{13}^2}$$

Similarly, the normal and parallel Poisson's ratios are:

$$\nu_N = \frac{C_{13}}{C_{11}+C_{12}} \text{ and } \nu_P = \frac{C_{12}C_{33}-C_{13}^2}{C_{11}C_{33}-C_{13}^2}$$

The axial and radial elastic strains produced during isostatic loading steps (equal changes in confining pressure, δp_c, and axial stress, $\delta\sigma_1$) can then be expressed as:

$$\delta\varepsilon_a{}^{el} = \frac{\delta p_c}{E_N}(1 - 2\nu_N) \tag{S1}$$

and

$$\delta\varepsilon_r{}^{el} = \delta p_c\left(-\frac{\nu_N}{E_N} + \frac{1-\nu_P}{E_P}\right) \tag{S2}$$

The fifth elastic constant needed to fully define the TI stiffness tensor is not accessible in this configuration. Using $E_P/E_N \approx 1.5$ as observed in (Ambrose, 2014), I obtain the following expression for ν_P:

$$\nu_P = 1 - 1.5\left[\nu_N + \frac{\delta\varepsilon_r{}^{el}}{\delta\varepsilon_a{}^{el}}(1 - 2\nu_N)\right] \tag{S3}$$

Text S4. Averaging nanoindentation elastic properties

Following Boulenouar *et al.* (2017), I consider Vaca Muerta shale as a random ternary mixture three phases corresponding to the three groups G1, G2 and G3 described in results section. The three phases have volume fractions, p_1, p_2, and $p_3 = 1 - p_1 - p_2$, Young's moduli, $E_1 < E_2 < E_3$, and contact creep moduli, $C_1 < C_2 < C_3$ (Table S3). The effective properties were then calculated by:

1- homogenizing phases G1 and G2 into an effective phase: G*

2- homogenizing the composite G* with the hardest phase G3 to obtain G^{ups}.

Each binary homogenization is performed using the Hashin-Shtrikman (HS) elastic bounds (Herrmann and Bernabé, 2004). The HS upper bound must be used if the stiffest phase percolates (i.e., if its volume fraction is greater than the site percolation threshold $p_c \approx 0.2$); otherwise, the HS lower bound is used. The HS upper bounds are:

$$K = K_+\left(1 + \frac{p_-(K_- - K_+)}{p_+(K_- - K_+)a_+ + K_+}\right) \tag{S4}$$

and

$$G = G_+\left(1 + \frac{p_-(G_- - G_+)}{p_+(G_- - G_+)b_+ + G_+}\right) \tag{S5}$$

where K and G denote the bulk and shear moduli, respectively; $a^+ = 3K^+/(3K^+ + 4G^+)$, $b^+ = 6(K^+ + 2G^+)/5(3K^+ + G^+)$ and the subscripts + and - refer to the stiff and soft phases, respectively. The lower HS bounds are obtained by exchanging the subscripts + and – in equations (S4) and (S5). Local values of E, Young's modulus, were measured in nanoindentation tests; the bulk and shear moduli can be estimated from them by assuming plausible values of the Poisson's ratio. The same mixture model can be applied to calculate the elastic and contact creep moduli for the three groups (Figure 3-6,7). Since C characterizes the creep compliance in shear, I interpreted it as shear contact creep modulus and calculated the corresponding bulk contact creep modulus based on the Poisson's ratio previously used.

Table S3. Volume fraction (p_i), average Young's modulus, E_i, creep modulus, C_i, and Poisson's ratio, v_i for the three phase groups. These values were used in Hashin-Shtrikman calculations.

Group	P_i (%)	E_i (GPa)	C_i (GPa)	v_i
1	15	6	50	0.25

2	70	25	1000	0.25
3	15	60	20000	0.1

Chapter 4: Solid-Fluid interaction during nanoindentation

Yves Bernabé, Ulrich Mok, Matěj Peč, Alan Schwartzman, and Brian Evans contributed to this chapter.

Abstract

In this chapter, I explored the ability of nanoindentation technique to evaluate the pore scale interactions between the microporous solid and pore fluid. I measured the creep deformation on a natural carbonate and an analog synthetic micro-porous alumina ceramic using a nano-DMA transducer. The experiments were performed on dry, as well as saturated with water (1 cp and buffered with 30 ppm calcite powder) and silicone oil (100 cp) samples. Thus, the fluids presented a wide variation in viscosity and chemical reactivity. Saturation with water and oil had contrasting effects on the indentations in both carbonate and ceramic samples. The indentations in the water-saturated carbonate showed a drastically reduced Young's modulus (from 38 to 6 GPa in carbonate and from 8 to 2 GPa in alumina) and increased creep compared with the dry indentations. I attribute these large differences to the possible chemical weakening of the porous solid in the presence of water. This is further confirmed by comparing the hardness values, which showed that water softened the matrix (from 0.87 to 0.20 GPa in carbonate and from 0.19 to 0.01 GPa in alumina). The oil-saturated sample, on the other hand, showed a higher modulus (47 GPa in carbonate and 17 GPa in alumina) and greater hardness (1.39 GPa in carbonate and 0.47 GPa in alumina), while the creep magnitude was less than that observed in the dry sample. The viscous displacement of oil during the consolidation of the poroelastic matrix can explain the higher modulus and lower creep. The loading rate-dependency and size (maximum load) sensitivity of the observed creep also corroborate the poroelastic nature of deformation. I used Agbezuge and Deresiewicz (1974) solution to derive poroelastic constants based on the recorded amount of creep. The analysis yields estimates of the diffusivity constant of the rock and the equilibrium creep depth. In summary, the oil was displaced during the creep time, while water weakened the matrix in addition to its displacement during the creep time. The drastic water weakening effect has important implications for the reservoir scale time-dependent phenomena. Instrumented nanoindentations could be complementary measurements for understanding the matrix permeability of tight rocks.

In this chapter, I investigate pore-scale interactions between aqueous pore fluids and microporous solids during nanoindentation. Using a nano-DMA transducer, I measured indentation creep on samples of a natural carbonate rock and an analog synthetic micro-porous alumina ceramic. The indentation tests were performed on dry samples, as well as those saturated with water (1 cp and buffered with 30 ppm calcite powder) and silicone oil (100 cp). Thus, the fluids varied widely in both viscosity and chemical reactivity. Saturation with water and oil had contrasting effects on deformation in both carbonate and ceramic samples. Indentations in the water-saturated carbonate showed a drastically reduced Young's modulus (from 38 to 6 GPa in carbonate and from 8 to 2 GPa in alumina) and increased creep compared with the dry indentations. Hardness values were also affected, decreasing in the carbonate from 0.87 when dry to 0.20 GPa when water was present; in the alumina samples, hardness decreased from 0.19 to 0.01 GPa. Compared to dry samples, those saturated with oil showed increased modulus (47 GPa in carbonate and 17 GPa in alumina) and greater hardness (1.39 GPa in carbonate and 0.47 GPa in alumina), the creep displacement was less than that observed in the dry sample. These results are consistent with the influence of poroelastic effects and of. chemical interactions between the solids and aqueous fluids. For example, viscous displacement of oil during the consolidation of the poroelastic matrix can explain the higher modulus and lower creep. Loading rate-dependency and size (maximum load) sensitivity of the observed creep also suggests poroelastic effects. Using the analysis of Agbezuge and Deresiewicz (1974), I estimated values of the diffusivity constant of the rock and the equilibrium creep depth. The drastic effect of water chemical weakening has important implications for time-dependent phenomena at the reservoir scale. Instrumented nanoindentations could be complementary measurements for understanding the matrix permeability of tight rocks.

4.1. Introduction

Nanoindentation is a versatile technique which can be used to obtain hardness, elastic modulus (Oliver and Pharr, 1992; Oliver and Pharr, 2004), fracture toughness (Lawn and Marshall, 1979), fatigue and impact load (Beake *et al.*, 2001) and creep parameters (Bower *et al.*, 1993). The ability of the technique to obtain the static Young's modulus of rock at a local scale is well-established (Kumar *et al.*, 2012; Abedi *et al.*, 2016a). Local measurements of Young's modulus obtained by nanoindentation can then be averaged using mixing rules to obtain estimates of macroscale dynamic moduli (Kumar *et al.*, 2012; Boulenouar *et al.*, 2017). Nanoindentation creep has also be used to estimate time-dependent behavior of rocks at larger scales. For example, short-term (10 seconds) creep displacements in Wolfcamp shale were well correlated with mineral composition; creep rates increased with organic and clay content and decreased with carbonate content (Mighani *et al.*, 2015b). The clay and organic content in those samples hosted a large portion of nanometer pores. Boulenouar *et al.* (2017) showed that organic-rich samples of Vaca Muerta shale had higher creep compliance than those poor in organics. Creep compliances measured during nanoindentation [for a description, see Vandamme *et al.* (2012)] are often consistent with macroscale experiments with durations of less than one day, but the nanoindentation compliances may differ from those determined in longer-term experiments (cf. Chapter 3).

Interpretation of creep deformation during nanoindentation also presents several challenges, two of which are quite pertinent to this study. First, nanoindentation creep measurements can be plagued by thermal drift, which, with increased time, can result in substantial errors in measurement of contact area. Second, the physical processes involved during rock deformation are still not very well-constrained, which makes the specification of a comprehensive constitutive law difficult. Errors owing to the first effect, thermal drift, can be mitigated by using a reference frequency analysis called Nano-DMA (Dynamic Mechanical Analysis). This technique provides continuous determination of the elastic and loss moduli by measuring contact stiffness and viscous damping during the creep period. Provided that the elastic modulus is relatively constant over the creep period, the dynamic stiffness can be used to compute the contact area and penetration depth at any given time (see discussion below).

The purpose of this study is to investigate the importance of poroelastic effects on nanoindentation creep in materials with micro-porosity. To this end, a carbonate rock and an alumina ceramic with known pore structures were saturated with fluids with known viscosities. There were large differences between the creep response in dry and fluid-saturated samples, and there were demonstrable effects of changes in fluid chemistry and viscosity.

4.2 Microstructural analysis

I selected two samples for the nanoindentation experiments, a natural carbonate rock from Abu Dhabi and a porous alumina ceramic. The rock sample is a reef carbonate with shell fragments separated by micritic cement, containing connected micro-porosity. The total porosity is 13%, and permeability is 40-200 μD (Wang *et al.*, 2016). Observations of both samples were made in scanning electron microscopes (SEM) using secondary electrons (SE) and x-ray energy dispersive spectroscopy (EDS). The EDS observations show that the reef rock is 95% calcium carbonate with a low percentage of quartz and dolomite impurities (Table 4-1). Secondary electron (SE) microscopy shows a wide range of pore diameters (Figure 4-1). Micro-pores with radii smaller than 5 μm are dominant, but some vugs have diameters as large as 60 μm. The spatial resolution of these observations is probably about 1 μm; and a substantial number of pores with radii less than that may be unresolved (Wang *et al.*, 2016). The images show two distinct regions (Figure 4-1): Region A consists of a micritic matrix with many small pores uniformly distributed throughout. Region B contains large grains and intergranular vuggy pores with non-uniform shapes, and which are not evenly distributed. I performed indentation experiments within both regions.

Table 4-1. The chemical composition of carbonate and alumina samples in normalized mass percent (%). The elements composition (given in mass percent) was obtained using x-ray energy dispersive spectroscopy (EDS).

Sample name	Carbonate	Alumina
Al	-	100
Ca	95	-
Si	2	0
Fe	0	-
Mg	3	-
Na	0	-
Total	100	100

A second set of experiments was performed on a synthetic, porous, alumina ceramic (provided by Saint-Gobain Inc.). EDS analysis confirmed these were >99.9% Al_2O_3. Mercury intrusion measurements provided by the manufacturer (Figure 4-2) indicate that the pores in the synthetic alumina have a very narrow range of diameters, with a median pore size of 8.1 nm. SEM observations (Figure 4-3) show some of the largest porosity but, owing to limits in resolution, the nm-size pores were not visible. The uniform and homogeneous pore structure was the main motivation to test this material. The surface area and total pore volume for alumina are 184 m^2/g and 0.69 cc/g, respectively. Based on water saturation tests, we estimate the effective porosity to be quite large, 67%. Thus, although both the alumina and carbonate specimens are porous and contain a dominant population of submicron pores, the size distributions of the two vary substantially. The physical properties of both materials are summarized in Table 4-1 and Table 4-2.

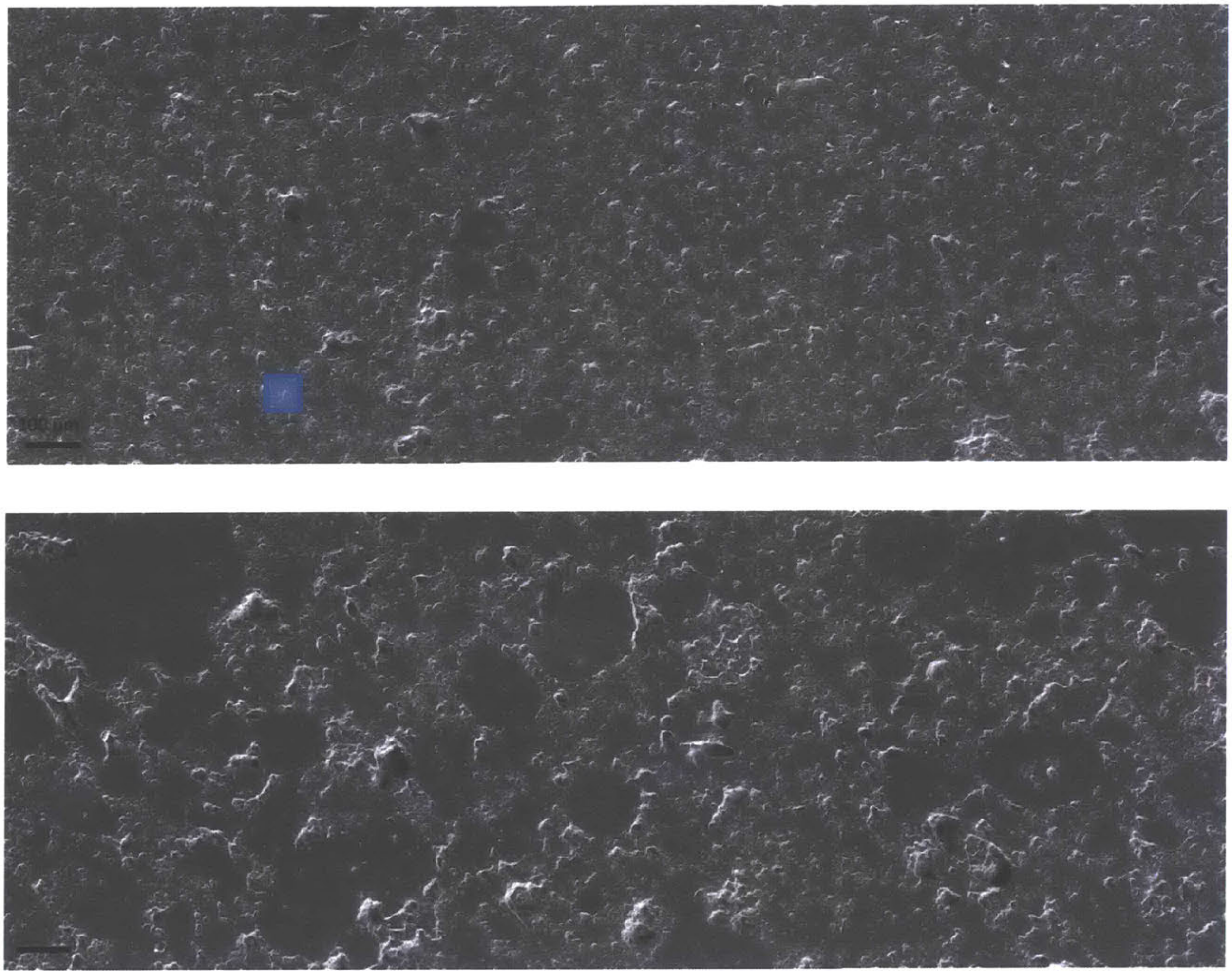

Figure 4-1. Stitched secondary electron (SE) images of the carbonate sample: (top) region A with microporous micritic cement; the matrix contains plenty of small pores which seem to be uniformly distributed throughout the matrix. (bottom) Region B with large grains containing vuggy intergranular pores. These pores are not evenly distributed and have non-uniform shapes. The black scale bar represents 100 μm. The blue cube shows the relative magnitude of the nanoindentation grid area.

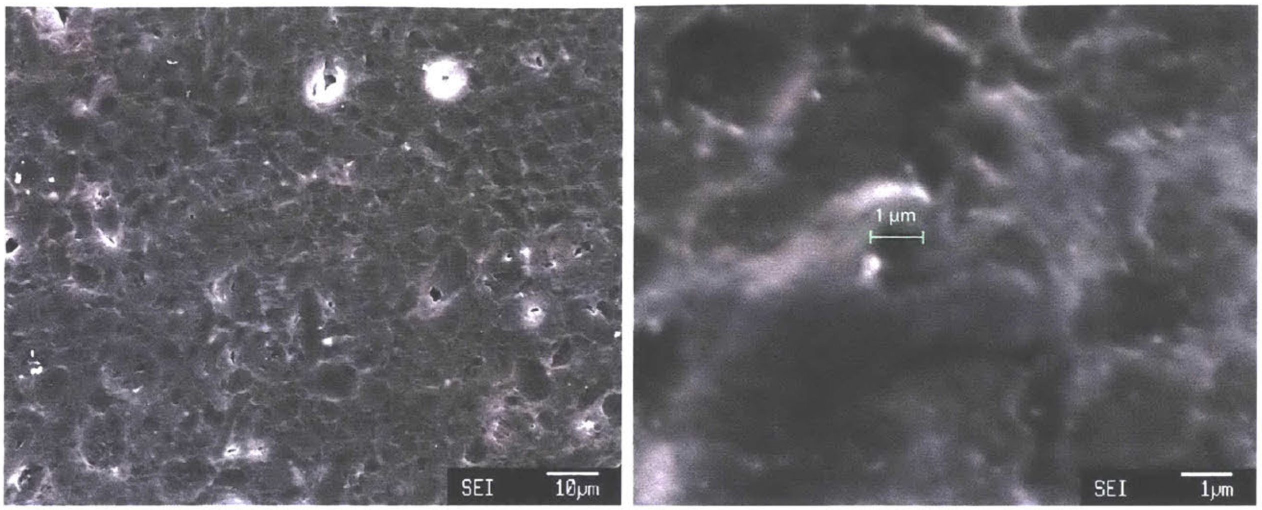

Figure 4-2. Secondary Electron (SE) images of the synthetic porous ceramic sample. Pores with diameters less than 1 μm (indicated in the right image) are not resolved. Compared to the carbonate (Figure 4-1), the ceramic has a relatively homogeneous structure.

Table 4-2. The physical properties of the specimens.

Sample name	**Carbonate**	**Alumina**
Porosity (%)	13 [a]	67
Permeability (μD)	40-200 [a]	-
Mean pore size (nm)	< 1000 [a]	8.4

[a] **Wang et al. (2016)**

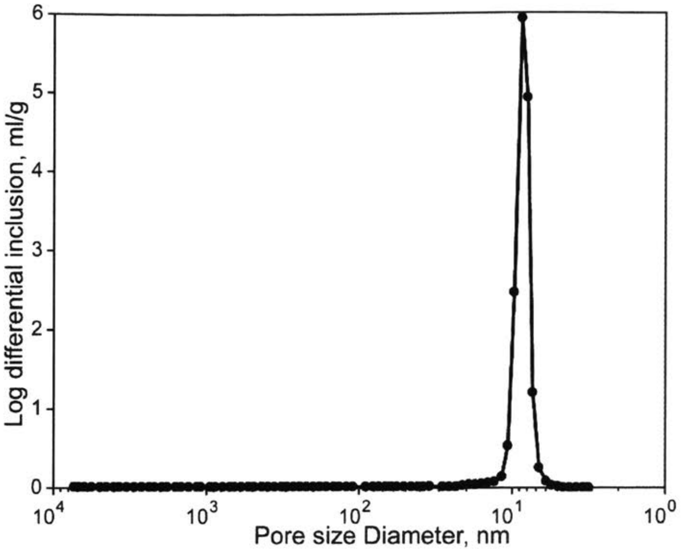

Figure 4-3. Pore size distribution (median pore size is 8.1 nm) in the synthetic porous alumina ceramic determined using Mercury Injection Capillary Intrusion (MICP). The sample and data were provided by Saint-Gobain Inc.

4.3 Experimental procedure

The specimens were finely polished using sandpaper without water. The root mean square (rms) surface roughness of the finished samples was <1 μm. The samples were then attached to the bottom of a container (Figure 4-4) and saturated with fluids using the following procedure: 1- A vacuum was pulled on the sample to evacuate the air out of the connected pores. 2- The desired fluid was poured onto the sample using another valve in the chamber until the sample was submerged. 3- We pulled the vacuum again; during this stage, fluid ingress was indicated by air bubbles that formed on the sample surface. 4- The vacuum pump was stopped; and the submerged sample was exposed to atmospheric pressure to help imbibition. After saturation, the top surfaces were 1 mm below the fluid surface; the samples remained submerged during the indentation experiments. Two fluids with different viscosities were used: deionized water with 1 cp viscosity and silicone oil with 100 cp viscosity (Table 4-3). The water used was buffered to contain 30 ppm calcium carbonate powder.

Table 4-3. Properties of the fluid used for saturating the carbonate and alumina samples.

Fluid	**Viscosity (cp)**	**Density, kg/m^3**	**Bulk modulus, GPa**

Water	1	1000	2.15
Oil (silicone oil)	100	946	1.75

I conducted nanoindentation experiments using a Hysitron TriboIndenter (Hysitron's nanoDMA III) located in MIT NanoMechanical Technology Laboratory. The indenter is instrumented with a dynamic mechanical analysis (DMA) transducer. It also has in-situ imaging capabilities, which allowed the surface topography to be scanned before and after experiments (Figure 4-5d). The indenter has a Berkovich tip, attached to a titanium shaft, 5 mm long, custom-designed by Hysitron Inc. for fluid-saturated specimens. The tip has a radius of 150 nm, subtends an angle of 142.35^0, and can be used to depths of 130μm. The tip area function was calibrated using fused quartz (fq). These calibrations consistently indicated a reduced modulus of 70 GPa and hardness value of 9.6 GPa for maximum forces between 0.4 and 10 mN. I set the minimum set-point force (the minimum force to detect the surface during the tip approach) to 20 μN to make sure the tip traversed the fluid surface. A simple numerical analysis of the capillary forces of the fluid layer between a substrate and the indenter tip (Chen and Soh, 2008) suggested that these forces do not exceed 400 nN, far less than the force set-point chosen. We made several arrays of either 2×2 or 4×4 single indentations, spaced 20 μm apart.

An example of the load and displacement history during indentation of a dry carbonate sample is shown in Figure 4-5. The loading consisted of three stages: 1- Loading up to a maximum force, i.e., between 2 and 12 mN with a constant rate (0.2-1 mN/s). 2- Applying a constant maximum force for three minutes (creep period). 3- Unloading to a certain minimum value with the same rate as for loading. I varied the maximum loads and loading rates in the saturated experiments and compared these results to those from dry experiments loaded to 2 mN at a rate of 0.4 mN/s. As can be seen from the quasi-static displacement history (Figure 4-5a), after 60 seconds, the tip showed apparent retraction, a physically implausible motion; such anomalies arise from temperature variations under the indenter, which can cause strains that override the creep displacement.

To eliminate thermal drift, the DMA technique was used to continually measure the dynamic storage modulus during creep. In this method, the constant load during the hold steps is modulated by small oscillations with an amplitude of 100-200 μN and a reference frequency of 220 Hz. The resulting response was an oscillatory displacement of 1-2 nm. The dynamic response can be expressed as a complex modulus:

$$E^* = E' + iE'' \tag{30}$$

with E' being the storage modulus and E'' the loss modulus. The storage modulus is related to the in-phase displacement of the material and can be estimated by measuring the ratio of the amplitude of the cyclic load and the observed displacement. The loss modulus, E'', measures the energy dissipation during each loading cycle. This viscous dissipation results in a phase lag between force and displacement. The phase angle, δ, that determines the lag between the stress and strain is

$$\tan(\delta) = \frac{E''}{E'} \tag{31}$$

In these experiments, the phase shift between load and displacement is very small, implying that the storage modulus is a measure of the elastic Young's modulus, E (Asif *et al.*, 1999). Since thermal drift is negligible at very early times, an accurate reference value for E can be measured during the 5-second segment at the beginning of the hold step (see Figure 3-2). The storage modulus is then assumed to be constant during creep, and can be used to obtain a time-dependent correction factor. Thus, the contact stiffness at any given time can be obtained (See appendix A for a more complete description). Uncorrected and corrected creep curves for the same indentation are shown in Figure 4-5a,b.

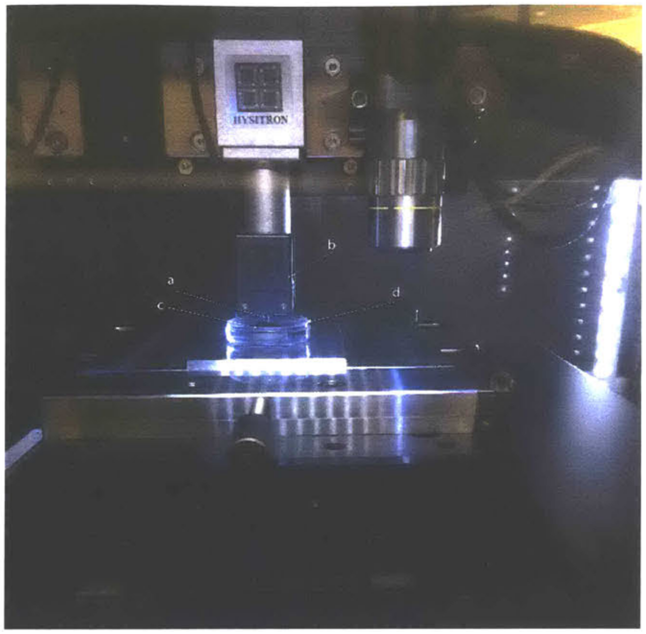

Figure 4-4. The Hysitron TriboIndenter machine during a nanoindentation experiment on a saturated specimen. The tip is visible in this picture (a) mounted on the DMA transducer (b). The sample (c) is submerged inside the container (d) with the sample surface about 1 mm below the fluid free surface.

4.4 Results

4.4.1 Dry indentations

Figure 4-5 shows the load history and corrected creep deformation accumulating during a 3-minute hold period for a dry indentation in the carbonate. The creep rates are initially high, but they steadily decrease with time. Hardness also decreases with time during the hold period. For the reference case, i.e., loading of the dry carbonate rock to 2 mN maximum force at a rate of 0.4 mN/sec, the average Young's moduli in regions A and B are 38±15 GPa, and 26±17 GPa respectively. The uncertainties represent the standard deviation of the measurements. The Young's modulus in the dry alumina is 8±2 GPa. Figure 4-5d,e show an example of indentation imprint and the corresponding depth profile in a dry carbonate sample. The depth and width of the imprint are 1.1 and 9 μm, respectively. If we assume that the material influenced by the indentation occupies an oblate spheroid with these semi-axes then the volume influenced is about 210 μm^3, and must include a large number of the sub-micron pores. Notice that the volume influenced in the alumina sample is even larger, because the indentation is deeper, owing to its lower Young's modulus.

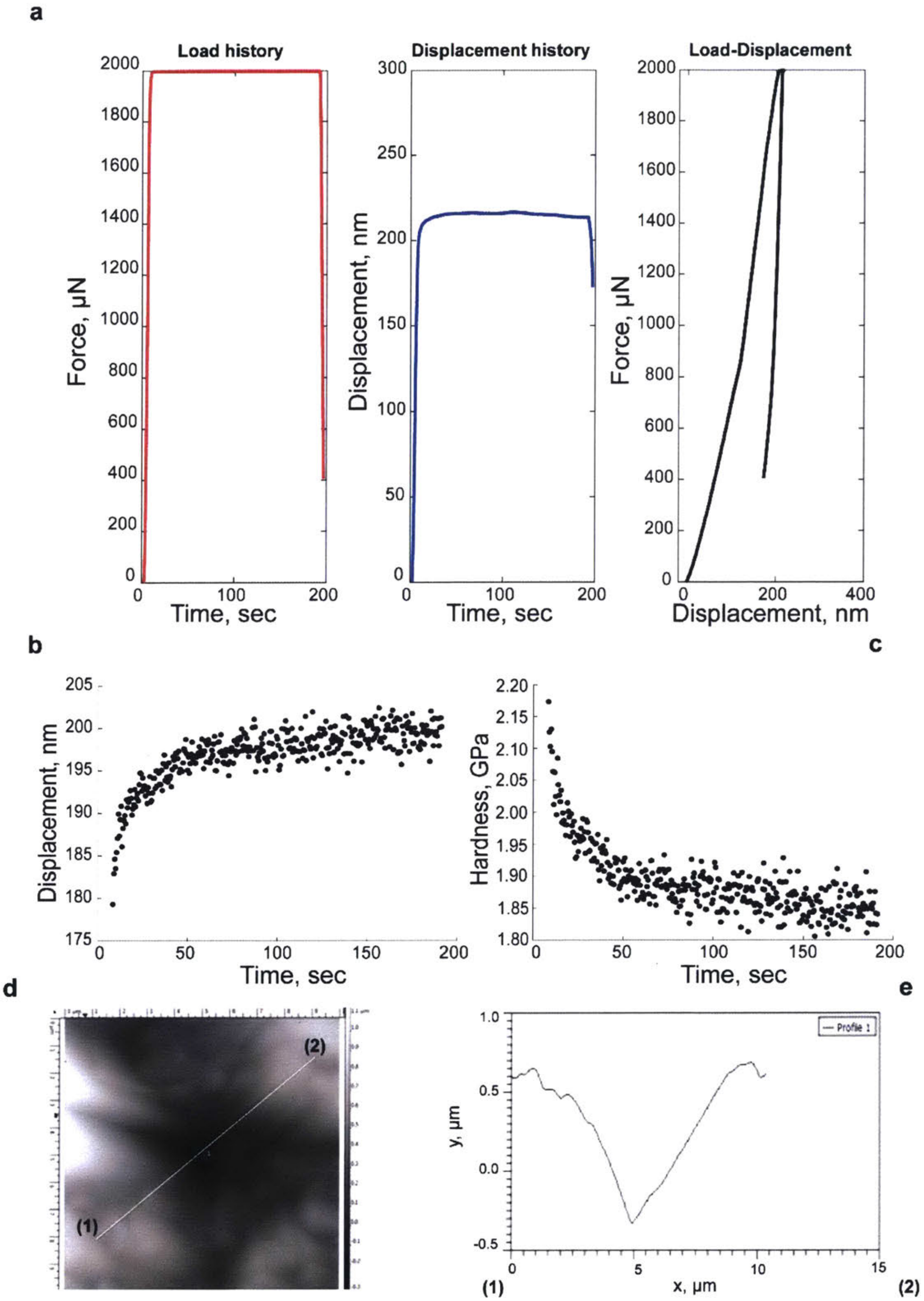

Figure 4-5. Nanoindentation of a dry carbonate sample with 2 mN maximum force. This experiment was used as a reference case. (**a**) Quasi-static measurements of force-displacement

using the quasi-static transducers. (**b**, **c**) Dynamic creep values and hardness during the 3-minute hold period determined using reference frequency (DMA) technique. (**d**, **e**) The imprint after an indentation imaged using the SPM method. (e) Surface depth profile along the white line in (d) starting from SW-NE.

4.4.2 Fluid-saturated indentations

Fluid-saturated indentations were performed on arrays of 4×4, spaced 20 μm apart. All the individual indentation tests for dry and saturated samples are compiled in Figure 4-6. There is significant scatter in the data for the carbonate, but some trends do emerge (Figure 4-6a,b). Water saturation significantly reduced the hardness and modulus in both regions A and B; the total displacements during creep were increased. Saturating the carbonate sample with oil slightly increased the modulus and hardness and decreased the total amount of creep. The effects of water and oil saturation were similar to those in the carbonate, but the influence of water was clearer in the alumina ceramic (Figure 4-6c, d). Moduli and hardness were correlated in both materials; power-law fits gave $H \sim E^{1.7}$ for the carbonate and $H \sim E^{1.9}$ for alumina. Both exponents are close to that found in nanoindentation experiments on Vaca Muerta shale (1.8) (Boulenouar *et al.*, 2017). Average values and uncertainties (standard deviation) are given in

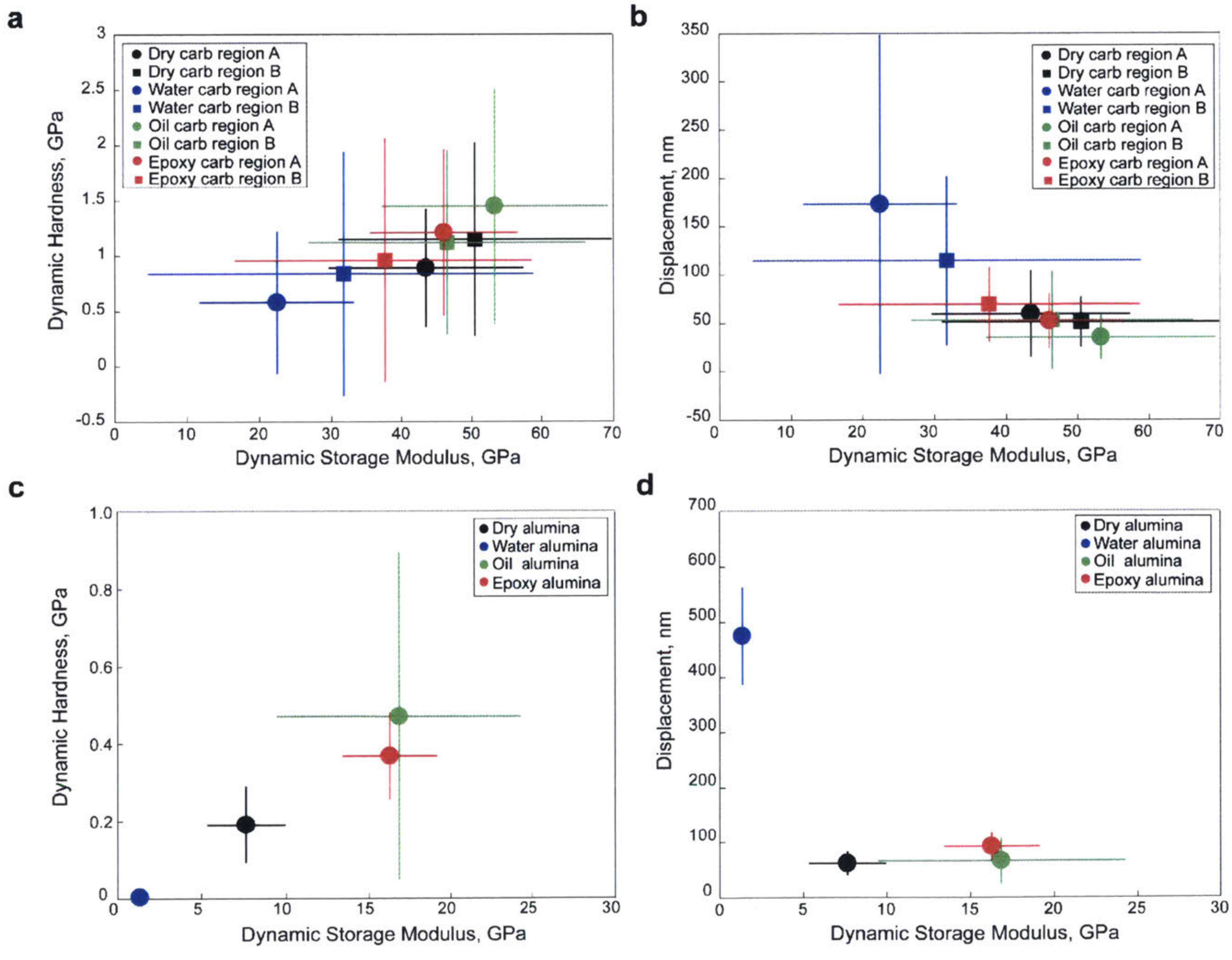

Figure 4-7 and **Error! Reference source not found.**.

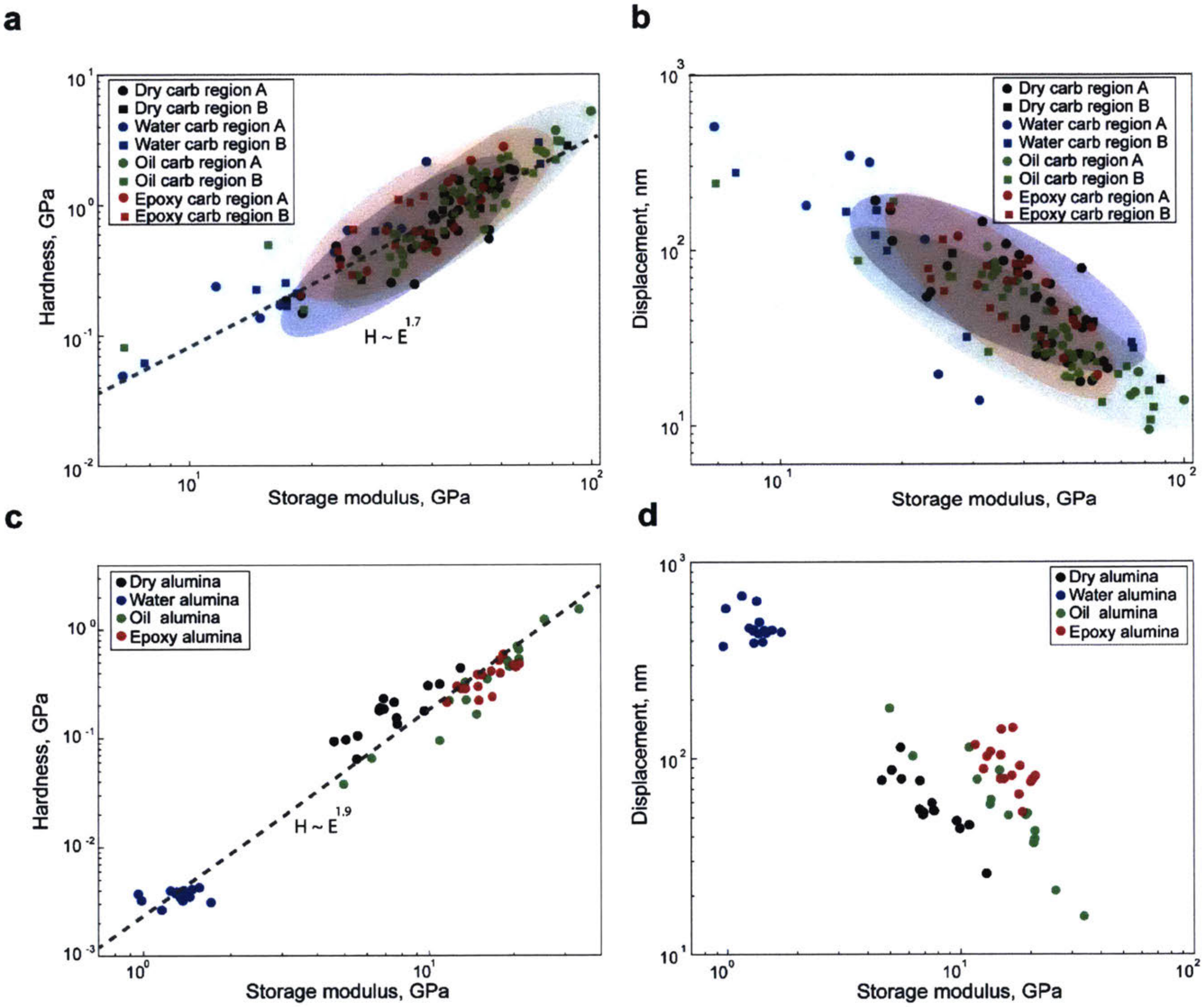

Figure 4-6. Data for all indentation tests on dry and fluid-saturated carbonate (**a**, **b**) and alumina (**c**, **d**). Log-log plots of hardness vs. storage modulus are shown on the left; total creep displacement vs. storage modulus on the right. In both carbonate and alumina, water saturation reduces the matrix modulus and hardness. Saturating with oil increased the hardness and modulus and decreased the creep displacement. The purple, light blue, light green, and light red ellipses indicate data clusters for dry, water-saturated, oil-saturated and epoxy-saturated carbonates, respectively.

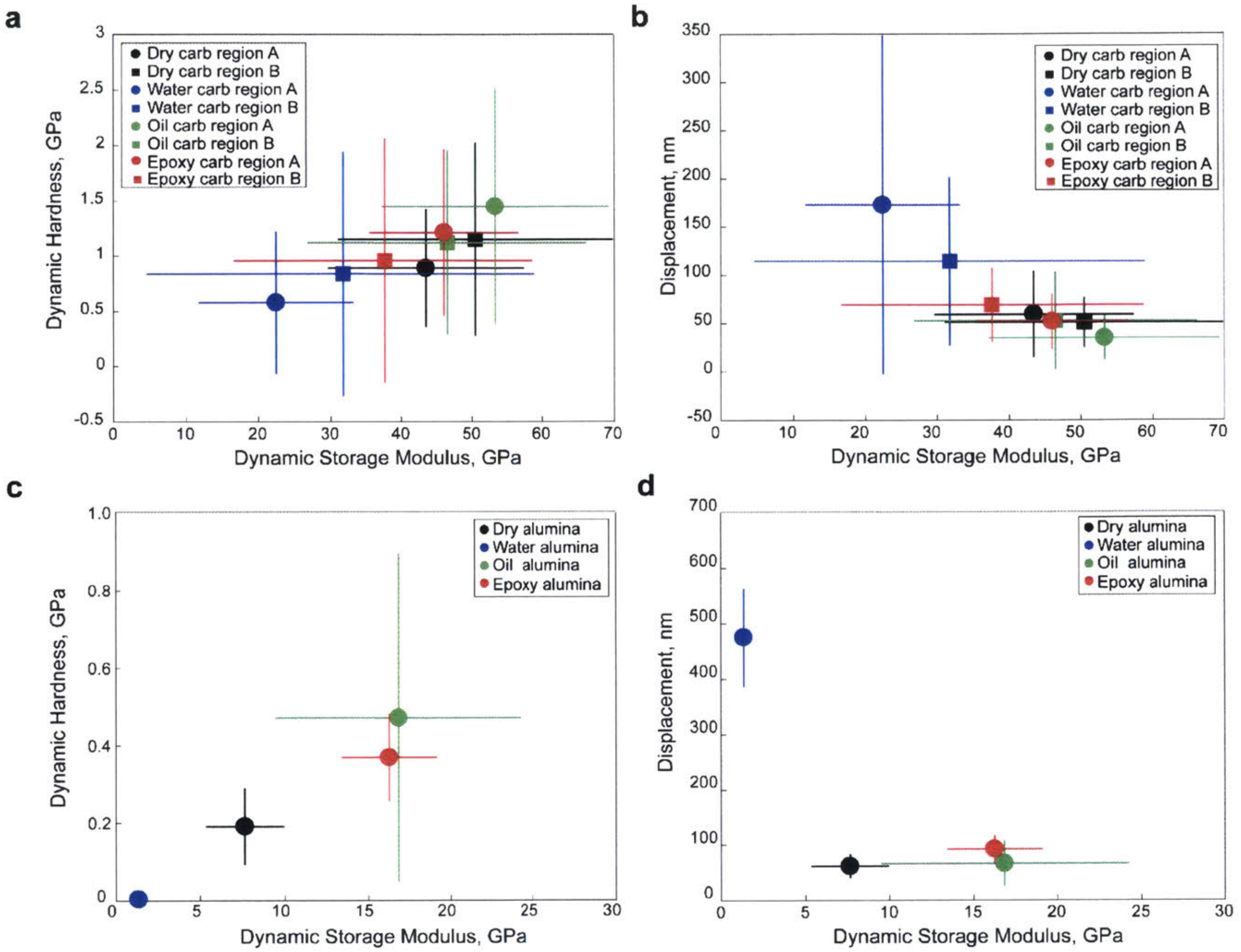

Figure 4-7. The total creep vs. Young's and storage modulus for dry, water-saturated, and oil-saturated indentations in carbonate (**a, b**) and alumina (**c, d**). The water-saturated indentations showed significant decrease in Young's modulus and hardness indicating alteration inside the matrix. The oil-saturated samples showed a decrease in creep magnitude and increase in modulus.

The mean values of indentation results are also a helpful tool for comparing the global variations inside the medium (see

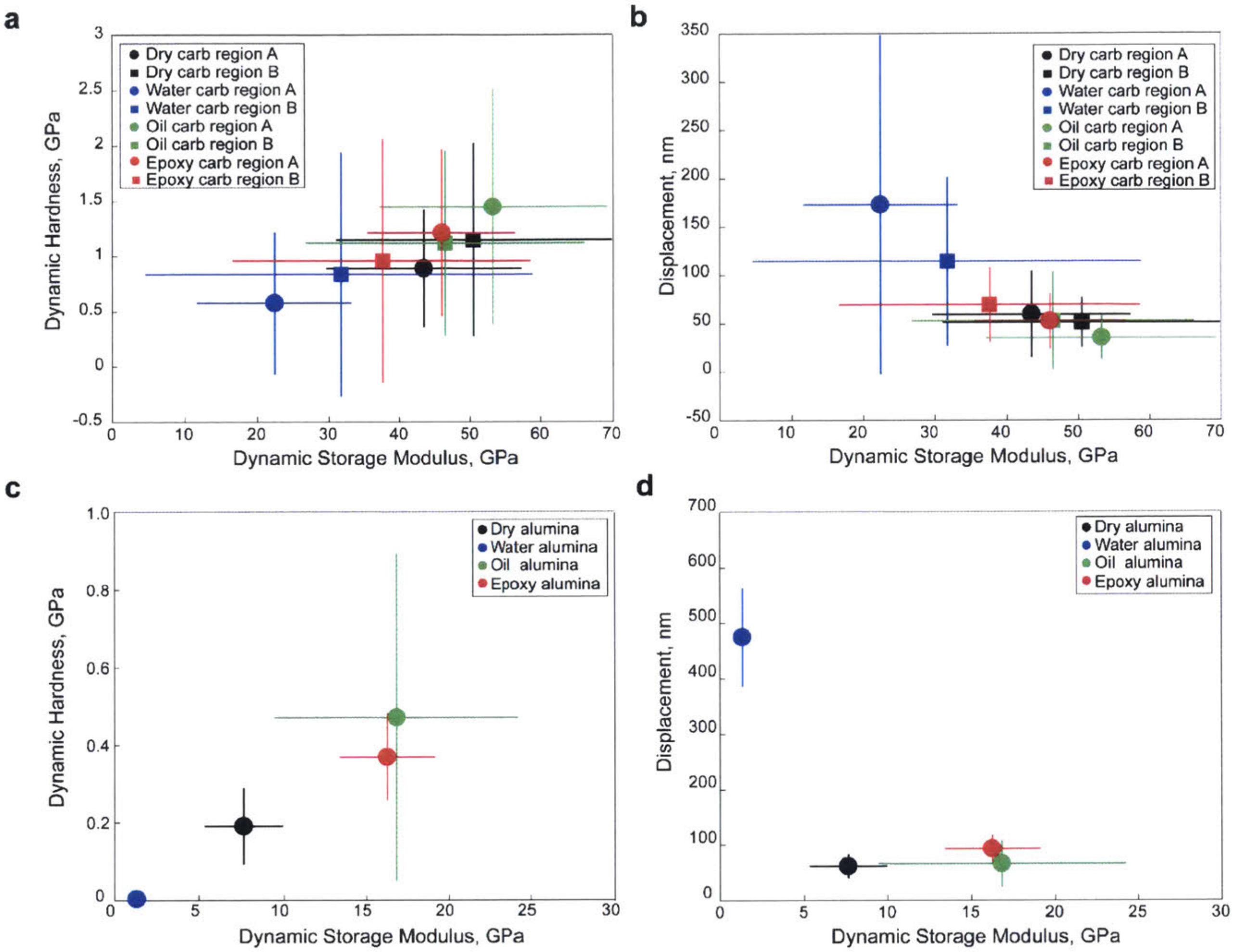

Figure 4-7 and **Error! Reference source not found.**). When the carbonate is saturated with water, the average Young's modulus in region A is reduced by a factor of 6, and hardness is reduced 4 times; creep displacements were twice as large. The Young's modulus and hardness in region B reduced by 4 and 3 times, respectively, i.e., not as high as in region A with micro-pores. In contrast, saturating the carbonate with oil, resulted in increased modulus and hardness and lower values of creep.

The average moduli for alumina were also reduced when water was added: the storage modulus by a factor of 8, and hardness by 19; creep displacements increased by 8 times. Saturating with oil increased the storage moduli by 2x, hardness increased by 2x. Surprisingly, the mean value of the creep displacements increased by 8%. However, although the mean value for the oil-saturated alumina increased, comparison with the cloud of data in Figure 4-6c suggests that this change might not be significant.

4.4.3 Rate and size dependence

The data suggest that the identity of the saturating fluid may affect the nanoindentation mechanics: Water decreases both the elastic modulus and the hardness relative to those of the dry samples, while saturating the samples with oil, increases both parameters. The exact causes of these changes are not clear. But, amongst other possibilities, increases in elastic modulus might indicate a poroelastic effect, while decreases in hardness might owe to chemo-mechanical effects, including subcritical crack growth.

One way to evaluate the poroelastic behavior is to assess the rate- and size-dependence of the creep deformation; it is thought that if poroelasticity exists, the loading rate would possibly influence the creep displacement by bringing the initial creep conditions to different drainage levels. Also, if fluid flow is involved, by increasing the probed volume, the displaced fluid volume, i.e., the creep displacement increases (Oyen, 2008; Nia *et al.*, 2011). This hypothesis test is aimed to rule out the possibility of viscoelasticity, which is thought of as an intrinsic material parameter, independent from probing scale. However, this test does not completely rule out the viscoelasticity, especially for cases where the porous rock frame may also be modified depending on the rate and size. To test for scale-dependence, I measured the influence of scale and loading rate on dry ceramic samples and those saturated with oil. The alumina ceramic was selected because of its simple microstructure, and oil was chosen to avoid any chemical weakening effects. Loading rates ranged between 0.2-1 mN/s and maximum forces between 2-12 mN were applied. At higher loading rates, the displacements accrued during creep increased (Figure 4-8a), although the effect is not large. Similarly, there may also be an increase of creep displacement when the hold period is constant, but the maximum load increased.

Table 4-4. Statistics of dry and saturated indentations. Notice the effect of water saturation on modulus, hardness and creep. The oil saturation, however, suppresses the creep and increases the modulus and hardness.

Sample	Young's modulus, GPa	Hardness, GPa	Total creep (3 min), nm
Dry carb region A	38±15	0.87±0.584	59.2±43.9
Dry carb region B	26±17	0.98±0.880	50±24.3
Water carb region A	6±4	0.20±0.22	119.4±145
Water carb region B	6±5	0.29±0.63	91.1±77.3

Oil (100 cp) carb region A	47±17	1.39±1.09	31.5±16.9
Oil (100 cp) carb region B	39±19	1.05±0.88	39.2±22.3
Dry alumina	8±2*	0.19±0.09*	61.5±21.5
Water alumina	1±0*	0.01±0.00*	475.1±88.4
Oil (100 cp) alumina	17±7*	0.47±0.42*	66.1±42.0

***Dynamic moduli**

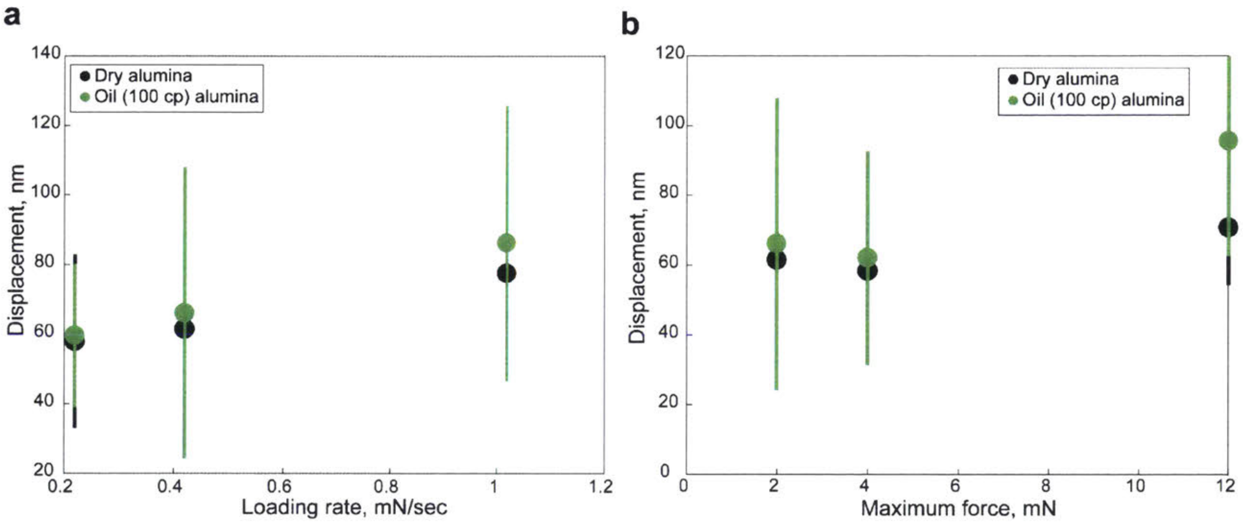

Figure 4-8. The dependence of creep magnitude on the loading rate and maximum load for oil-saturated alumina.

4.4.4 Indentations in epoxy-filled samples

To further investigate the effect of fluid viscosity, I saturated the carbonate and alumina samples with EPO-TEK 301 epoxy. Before curing, the liquid epoxy has a viscosity of about 10 cp. The curing time is 24 hours, long enough to vacuum saturate the pores. I used the same saturation protocol for the epoxy as for oil and water. After curing, to characterize the epoxy, I performed nanoindentation tests using forces of 2 μN. At higher loads, the indenter tip would reach its maximum displacement, 5 μm, forcing the experiment to be terminated. Under 2 μN, Young's modulus and hardness were 0.4 GPa and 0.6 MPa, respectively. Contrary to expectations, the behavior of epoxy-filled rocks was intermediate between that of the dry and oil- samples, rather than being stronger and stiffer than the oil-saturated samples. At this point, the exact cause of this discrepancy is not resolved. One possible scenario is the reactions occurring during the curing of the epoxy may have altered the pore structure. Also, the under-saturation of small pores, where epoxy could not fill, is another viable scenario. More work is needed to clarify these results.

4.5 Discussion

The results showed that creep deformation during nanoindentation in both carbonate and alumina samples was strongly affected by the presence of a saturating fluid. When water was present, the elastic modulus and hardness of both materials were reduced; and the creep displacements were greater than for dry samples. Relative to dry samples, when oil was present, elastic modulus and hardness were increased in both systems; creep displacement was less in the carbonate, but slightly larger in the alumina samples. The latter result is surprising for a poroelastic solid containing no pore fluid. In the carbonate, the effects of fluids were more noticeable in region A, which also contained more micropores. In all cases, the hardness is related to the elastic modulus raised to a power of between 1.7-1.9. Many of these results can be rationalized by appealing to poroelastic theory or to chemo-mechanical weakening attributable to aqueous fluids. However, some results are anomalous and questions remain.

4.5.1 Poroelasticity during creep.

The increase in elastic modulus and hardness after saturation with a chemically inactive fluid with elevated viscosity is consistent with poroelastic theory. Initially, during fast loading the medium is effectively undrained, resulting in increased elastic modulus, hardness, and elevated local pore-fluid pressure. Although the effects are very small, the rate and size dependence of the nanoindentation behavior also suggests the poroelasticity. However, the increased creep displacement of the oil-saturated alumina relative to the dry case is surprising. The exact cause is not clear but might owe to the different time scales for deformation of the solid frame and for egress of the fluid. During creep in a poroelastic solid, the unrelaxed fluid is slowly displaced, taking the sample from the undrained to drained state. In our tests, creep displacement is measured relative to a starting point defined by the depth of the indentation after the initial loading and before the hold period. This depth is less for the ceramic saturated with fluid, and the total creep displacement in the saturated case would include two components, one owing to fluid transport and the second owing to deformation of the solid framework. However, more work is necessary to verify or refute this hypothesis.

The increased rate dependence of the oil-saturated ceramic is also consistent with poroelastic behavior, but the effects are very small. It should also be mentioned that the dry alumina sample showed a significant rate-dependence, albeit smaller than those for samples saturated with oil. Finally, we note that the attempt to introduce a very high viscosity fluid, i.e., the epoxy, gave results that were inconclusive.

In the previous sections, we found that the creep deformation of the carbonate and alumina samples was governed, in large part, by the saturating fluid inside the pore system. For the carbonate samples, we could observe this fluid-dependence more in region A, which contained more micropores. In this section, we try to estimate the flow properties of the indented matrix. The consolidation of a poroelastic half-space under a spherical indenter does not have a closed-form analytical solution (Agbezuge and Deresiewicz, 1974). However, this problem is solved numerically by several authors (Agbezuge and Deresiewicz, 1974; Yue and Selvadurai, 1995). Here, I utilized Agbezuge and Deresiewicz (1974) solution. They used Hankel-Laplace transforms to treat the problem. In the Agbezuge and Deresiewicz (1974) solution (AD74), the half-space solution evolves from a Hertzian stress distribution for an incompressible bulk at time zero to the Hertzian distribution for the elastic frame after the fluid excursion. The porous frame is assumed to be isotropic and linearly elastic. The solution yields settlement (here contact depth), contact radius growth, and contact pressure distribution as time evolves under constant indentation load. The relaxation due to the fluid extraction results in 37% reduction in the maximum contact pressure after the system reaches the equilibrium condition. The contact depth effectively reaches an equilibrium condition (equilibrium depth) after 5 units of dimensionless time, γ, which is stated as:

$$\gamma = \frac{\sqrt{ct}}{a(t)} \tag{32}$$

where c is the poroelastic coefficient of consolidation, with a nature of diffusivity, and $a(t)$ is the indentation contact radius. γ grows as the creep accrues. An immediate outcome of our analysis is c, which will be used to obtain the matrix permeability through the following relation:

$$c=2Gk/\eta \tag{33}$$

with k and η being the medium permeability and fluid viscosity, respectively. G is the shear modulus. In reality, compactional deformation during indentation of porous rocks may result in changes in *c*; *G* may increase as the rock compacts, while *k* may decrease during compaction. However, for the purpose of our poroelastic analysis, we assumed *c* to be constant during the entire creep deformation. Also, the value of *G* is estimated using the measured DMA storage moduli and plausible values for the material's Poisson's ratio. The depth of the spherical indenter can be expressed as a dimensionless parameter, i.e., *H*, where:

$$H = \frac{h(t)-h(0)}{h(\infty)-h(0)} \tag{34}$$

where h (0) and h (∞) are the indenter depth after initial loading and that at poroelastic equilibrium, respectively. Oyen (2008) developed an empirical fit of the AD74 solution, between *H* and *γ*:

$$H = 0.93 - 0.93\left[1 + \left(\frac{\gamma}{0.77}\right)^{2.08}\right]^{-1} \tag{35}$$

The contact radius, *a*(*t*), evolves with time as the indenter settles into the medium and can be expressed as a function of the depth of the indenter, *h*(t), and the half-angle of the Berkovich tip, *θ*=71.1°:

$$a(t) = \frac{tan(\theta)}{\pi} h(t) \tag{36}$$

Using equations (34), (36), and (38), equation (37) can be rewritten as:

$$h(t) = h(0) + \left(0.93 - 0.93\left[1 + \left(\frac{\sqrt{ct}}{0.77a(t)}\right)^{2.08}\right]^{-1}\right)\times\left(h(\infty) - h(0)\right) \tag{37}$$

The normalized displacement, *H*, as a function of γ is shown in Figure 4-9. It is observed that *H* reaches equilibrium at 5 γ. A medium with a low *c* reaches equilibrium slowly; while one with a higher *c* requires a shorter time. Using the data for *h*(*t*), we used MATLAB's nonlinear least square function, lsqnonlin, to solve equation (39) for *h*(∞) and *c*. Figure 4-9b shows an example of the fit for a carbonate sample. The results of the estimates of the matrix permeability are given in Table 4-5. Each indentation provides a local estimate of permeability; and a permeability map for one of the indentation grids is shown in Figure 4-10. It is important to notice that these estimates are wildly inconsistent with macroscopic measurements of permeability (cf. Table 4-2) being 10 orders of magnitude lower. Similar inconsistencies were noted for estimates in biological materials (Oyen, 2008, 2015).

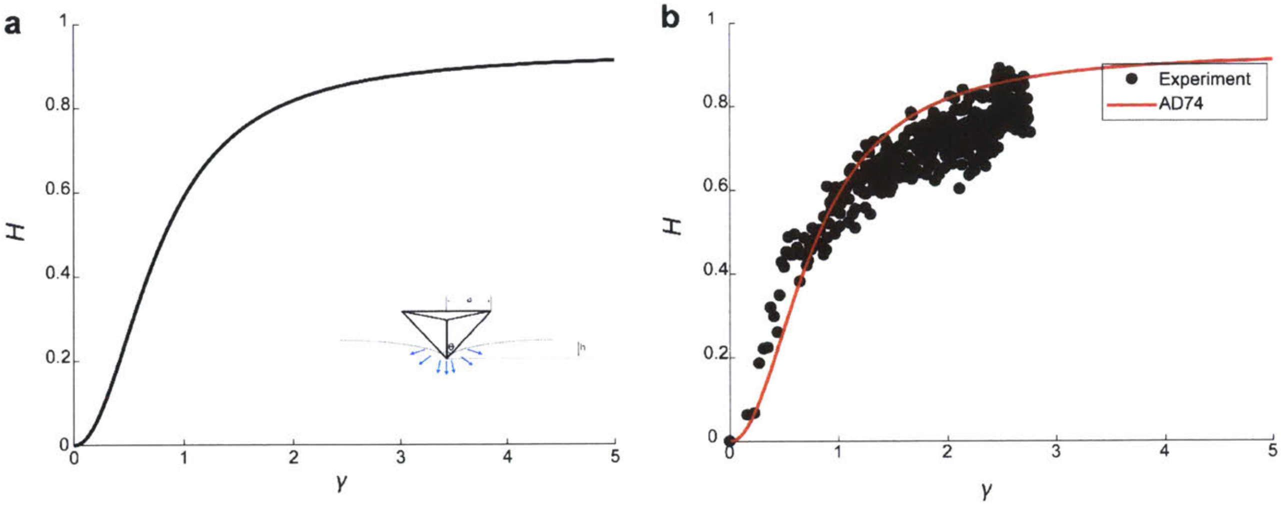

Figure 4-9. (**a**) H-γ relation for AD74 solution. A medium with high c reaches equilibrium depth more quickly than that with low c. Inset is a schematic of the infinite half-space under the indenter tip. The fluid extrusion results in relaxing the stresses inside the system and deformation under constant load. (**b**) An example of the fitting the creep data to equation (39).

I summarize the results of our analysis in Table 4-5. Here, I derive the matrix permeability only for oil-saturated samples. The water-saturated experiments showed softening of the matrix, which suggested the occurrence of chemical processes in addition to fluid flow. This makes a purely poroelastic analysis of the observed creep less appropriate for water-saturated experiments.

Table 4-5. Average matrix permeabilities during indentation creep on oil- saturated samples.

Sample	Average matrix permeability, m^2
Oil (100 cp) carb region A	$1.9\times10^{-26}\pm2.4\times10^{-26}$
Oil (100 cp) carb region B	$6.4\times10^{-26}\pm1.5\times10^{-25}$
Oil (100 cp) alumina	$1.5\times10^{-25}\pm1.3\times10^{-25}$

As an example of the permeability distribution, I show the distribution map of permeability in a 4×4 grid in carbonate, region A in Figure 4-10. Table 4-5 suggests that the derived permeability for region A has a lower average value, owing to its micro-porous nature; while the derived permeability in region B shows a higher average permeability owing to its more abundant vuggy pores, while the standard deviation is larger. The higher standard deviation suggests that the indenter tip has sampled some vuggy pores and some carbonate grains during the measurement.

The secondary electron images in Figure 4-2 reconfirm the presence of these pores. Alumina has a matrix permeability with the mean value one order of magnitude larger than carbonate region A.

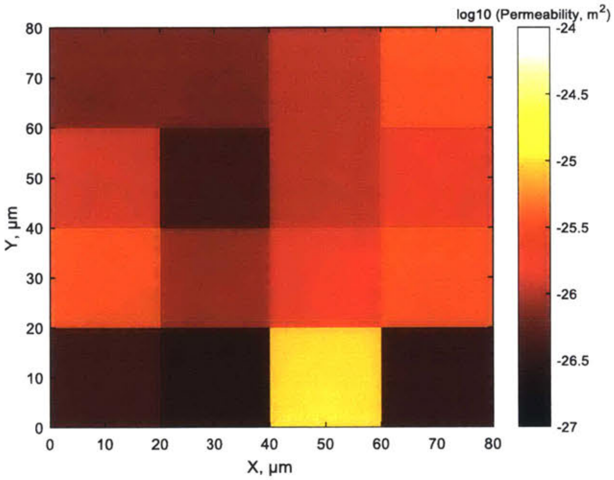

Figure 4-10. Permeability map for a 4×4 indentation grid in region A of an oil-saturated carbonate. The color represents the permeability in log-scale (scale bar on right).

4.5.2 Water-weakening effect

Saturating the solid with water reduces both elastic modulus and hardness. Decreased hardness is easily reconciled with copious observations of reduction of strength of rocks when water is introduced. At low temperatures, stress corrosion or subcritical crack growth is commonly observed in single crystal quartz, glass, granite, sandstones, and many other rocks [e.g., (Orowan, 1944; Parks, 1984; Chester and Logan, 1986; Atkinson and Meredith, 1987; Wong *et al.*, 2016)]. Observations of weakening include reductions in the short-term uniaxial compressive strength, the stress under which cracks initiate, and time to failure during long-term creep experiments. Carbonates are also affected (Rutter, 1974; Brantut *et al.*, 2012b; Brantut *et al.*, 2014b, 2014c). In addition to natural rocks, biological materials also show significant weakening in the presence of water. Nanoindentation measurements indicate that Young's modulus in wet bone is about 11.7 GP versus 19.4 GPa for dehydrated bone (Bushby *et al.*, 2004). Hydrogels show even more drastic weakening (Galli et al., 2009).

The magnitude and kinetics of this weakening depend on temperatures, confining pressure, loading rates, materials, and fluid chemistry. The mechanisms responsible may include subcritical crack growth, pressure solution, enhanced dislocation glide, or increased diffusion kinetics. In these indentation experiments, the temperature is relatively low and deformation times are short, so subcritical crack growth is a likely candidate (Brantut *et al.*, 2014a). However, a definitive identification of mechanism would require more work.

The tests also indicate a reduction in Young's modulus during indentation creep. This result is more enigmatic. With the exception of cracking, the mechanisms responsible for inelastic strain are not normally considered to be direct causes of changes in elastic modulus. Because the DMA technique involves small loading and unloading cycles after reaching the peak load, it is possible that the modulus might be affected by cracking in the vicinity of the indentation induced during loading. Once again, further work is necessary to address this issue.

4.5.3 Simple visualization of fluid-rock interactions during indentation

Chemical weakening and poroelastic effects can coexist, and, depending on the conditions, either could dominate the mechanical response. The two effects on the indentation experiments can be represented in a simple conceptual model by plotting indentation creep displacement versus storage modulus. These experiments suggest that chemical weakening, probably owing to stress corrosion, decreases hardness. Correspondingly indentation creep displacement increased by about 100% and 700% for carbonate and alumina samples, respectively. In addition, the storage modulus measured during DMA is also lowered by about 90% for both materials.

Poroelasticity results in increase in storage modulus and decreases in indentation creep depth. The magnitude of which depends on the ability of the fluid to flow and equilibrate local gradients in pore fluid pressure (Biot, 1956; Smith *et al.*, 2003). At high-frequencies or short relaxation times, the unrelaxed fluid pressures stiffen the medium (Biot, 1956). The lower-bound for the modulus when the fluid is completely drained is the dry moduli. Finally, the indentation tests indicate that hardness (inverse square of the creep displacement, i.e., imprint radius) is directly related to storage modulus to a power of about 1.8. Thus, the two effects can be represented in a plot of log(displacement) versus log(storage modulus). Chemical weakening effects will cause indentation responses to be displaced into the upper left-hand quadrant of the plot, while poroelastic effects will displace the responses to the lower right-hand quadrant, with the dry frame modulus providing an upper limit.

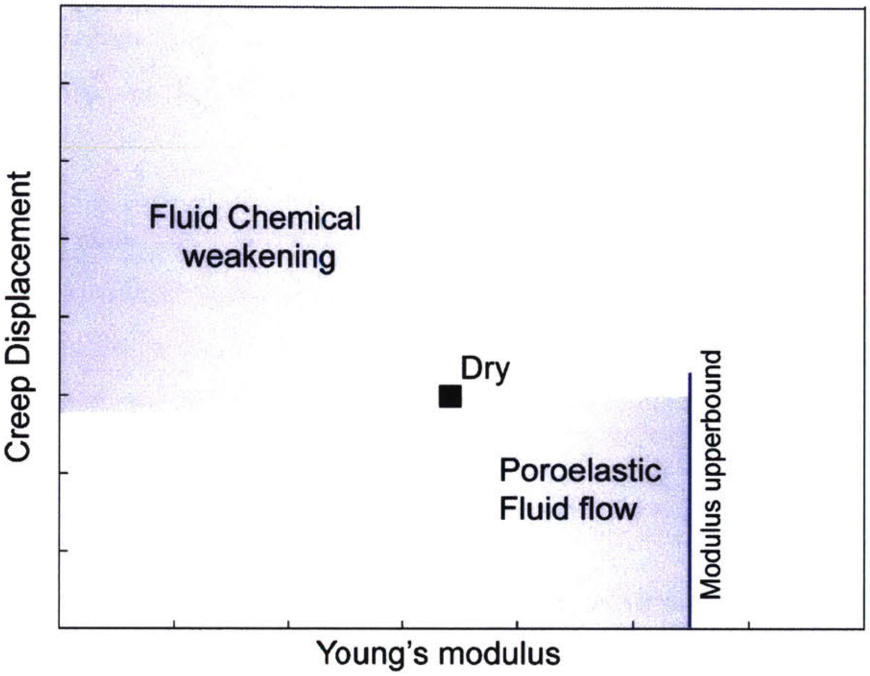

Figure 4-11. Conceptual model for the indentation creep displacement at a given hold time vs. Young's modulus for a saturated medium. Chemical-weakening increases creep displacement and decrease the storage modulus. Poroelasticity decreases creep decreases and increases the storage modulus. At high-frequency, the storage modulus is limited to that of the undrained porous solid. The two effects can coexist. If hold time is increased, creep displacements will also increase.

4.6. Conclusion

Creep deformation during nanoindentation in both carbonate and alumina samples is strongly affected by the presence of a saturating fluid. Saturating the samples with water or oil altered Young's modulus, hardness, and the indentation displacement during hold periods. In particular:

Relative to dry samples, Young's modulus and hardness of water-saturated samples were significantly smaller, while creep rates increased.

For oil-saturated samples, Young's modulus and hardness increased. In the carbonates indentation creep displacements decreased, but there may have been a slight increase in oil-saturated alumina samples.

In all cases, hardness could be empirically related to the elastic modulus raised to a power of between 1.7-1.9.

The reduced hardness in the water-saturated samples can be rationalized by the chemical interaction between the aqueous fluid and the solid. When oil is present as the pore fluid, both modulus and hardness after a 3-minute hold period were larger. An important implication of these measurements is that poroelasticity can affect indentation creep deformation. Using the treatment of Agbezuge and Deresiewicz (1974) I estimated an effective permeability for the oil-saturated alumina. The permeability values ranged between 10^{-27}-10^{-25} m^2, much lower than that measured in macroscopic samples of the same material. With our present limited observations, it is difficult to rationalize this discrepancy, but two lines of published interpretations may be important to consider. First, the compilation of permeabilities from laboratory vs. field-scale data (Brace, 1980) suggested that laboratory-measured k's are lower than the field data by at least an order of magnitude. This discrepancy could reach 10^3 in crystalline rocks, where the presence of fractures at macro-scale are expected. Therefore, one would expect that the indentation might under-sample the larger scale defects, resulting in higher k. Second, estimates of the dependence of k on length-scale in biological materials (Gibson and Ashby, 1999) suggest that $k \alpha L^2$, where L is the effective pore size, L (k), a finding consistent with the indentation data of Oyen (2008) on saturated bones. Although k is supposedly an intrinsic property of the porous medium, its measured value could easily be scale-dependent. Hence, if our indenter sensed nm-size pores as opposed to larger μm-pores in laboratory measurements, scale dependency might be introduced. Again, these are speculations and could not be directly inferred from our observations.

Supplementary information

In this section I explain the formulation to derive the complex moduli and dynamic hardness from the modulated force and displacement measurements. In addition to usual calibration parameters for quasi-static transducers such as tip geometry, ..., the NanoDMA transducer is characterized by its spring constant, mass, and damping (Hysitron Inc., 2011). Typical values for these parameters are 350 N/m, 500 mg, and 60 g/s for spring constant, mass, and damping, respectively. I show a schematic for the force and response during the dynamic measurements.

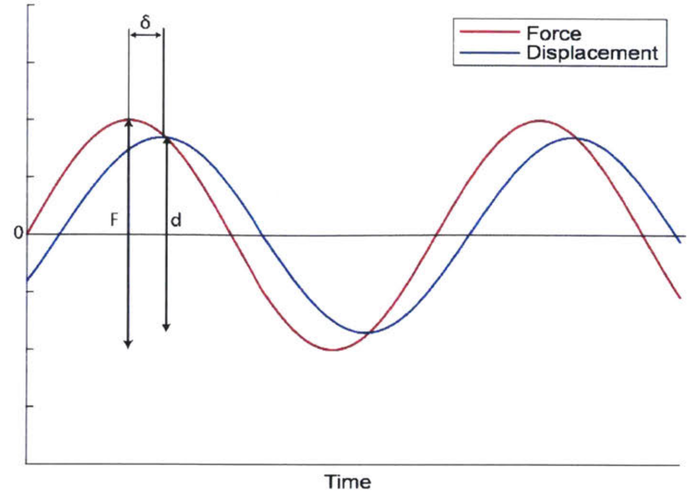

Figure S1. The principles of complex modulus calculations using DMA's reference frequency technique. A sinusoidal force (displacement) with a predefined frequency and amplitude, F (d), is applied and the displacement (force) is recorded with a delayed phase, δ. The storage and loss modulus is computed from the F/d and δ.

The storage stiffness is obtained as:

$$k_{storage} = \frac{F.cos(\delta)+m_T\overline{\omega}}{d} - k_T \tag{S1}$$

with m_T and k_T being the transducer mass and stiffness, respectively. ω^{-} is the radial frequency. The loss stiffness is obtained as:

$$k_{loss} = \frac{F.sin(\delta)}{d} - C_T\overline{\omega} \tag{S2}$$

where C_T is the transducer damping. Now, the complex stiffness is derived from the storage and loss modulus as:

$$k_{complex} = \frac{1}{\frac{1}{\sqrt{{k_{storage}}^2+{k_{loss}}^2}}-MC} \tag{S3}$$

MC is the machine compliance. The modulus is then derived from stiffness:

$$E = \frac{k\sqrt{\pi}}{2\sqrt{A_c}} \tag{S4}$$

A_c is the calibrated tip area function. The equation A4 is a general formula for obtaining the storage, loss, and complex moduli. The hardness is also estimated as:

$$H = \frac{P+F}{A_c} \tag{S5}$$

with P being the maximum quasi-static force.

Chapter 5: Summary of thesis and suggestions for future work

Throughout this thesis, I presented a few experimental methodologies to investigate hydraulic fracture and time-dependence in rocks. As the nature of controlled experimental observation implies, the results, as well as implications, would not be able to wholly capture the true subsurface conditions. Such methodologies are subject to limitations, and the future experimental efforts will build on these observations as the experimental tools, as well as data analysis techniques, improve. In the following, I summarize a few limitations and suggestions for future work based on our acquired knowledge.

Chapter 2 presented the observations of the interaction between a hydraulic fracture and pre-existing saw-cut fault. The influence of fault transmissivity was shown to govern the cross/arrest conditions. However, at this point, it is not clear whether the quasi-static or dynamic transmissivities should be considered for the cross condition assessments. In other words, does the fault locally activate before HF intersection?

The observations of this interaction could be tested against field observations, specifically in the area of microseismic events during stimulation processes. Also, future modeling attempts will provide a more solid foundation on the mechanics of this interaction.

Chapter 3 presented a relation between the elastic and creep properties at the nanoindentation vs. triaxial scale on shale. The observations of creep strains also suggested that shale rocks yield under low stresses at slower strain rates. However, our experiments have certain limitations, which could be a start point for future research:

1- I tested samples of only one bedding-plane orientation, even though the influence of anisotropy on elastic moduli, creep, and the yield surface is likely quite large. Future work on shales with different bedding orientations is critical and might involve the development of anisotropic hardening rules like the rotational hardening model developed for soils (Leoni *et al.*, 2008).

2- Both the triaxial creep experiments and the indentation experiments were short-term, making long-term predictions for the Vaca Muerta shale difficult. Creep experiments longer than several weeks would be desirable to investigate the possible transition from the log(t) to linear viscoelastic behavior. The *in-situ* stress conditions were chosen to be relevant to shale gas reservoirs, but there are special situations where locally concentrated stresses are of interest. Thus, it would be desirable to study the conditions under which the material evolves to tertiary creep and failure.

3- I did not control or change temperature, fluid pressure, and fluid chemistry; in this regard, the conditions I used likely differed from those *in-situ*. Coupling fluid pressure and volumetric deformation should presumably affect creep, but the permeability of Vaca Muerta shale was too low to allow external control of the pore pressure. Given the low matrix permeability and decimeter size of our sample, and the relatively short test duration, our triaxial creep tests were definitely run in undrained conditions (Wang, 2017). Details of poroelastic effects are considered outside the scope of this report.

4- Finally, although averaged results of elastic and contact moduli from the indentation tests were similar to those determined in triaxial experiments, the two techniques differ substantially in loading and boundary conditions. Thus, it is not clear which pressure and inelastic strain conditions are appropriate for the comparison between the two techniques.

Chapter 4 presented an experimental methodology to study the fluid-rock chemical and physical interactions. The creep experiment suites in these studies suggested a new way to analyze the deformation of porous rock. They also implied the significance of the poroelastic response of a rock relative to other processes during its creep, even at such small time and length scales. The chemical effects observed during water-saturated creep experiments might help us look more closely into chemo-poroelastic rock deformation. Future experiments could direct us towards understanding this chemical effect by changing the exposure time, saturation state of the water, and fluids with different polarities. In the following, I mention a few limitations in our analysis and also possible future directions to extend this research:

1- The state of saturation of the porous medium is difficult to evaluate; the vacuum saturation technique used here cannot be expected to fill the smallest sub-micron pores. Differences in the wetting properties in the two fluids and in the epoxy complicate this problem.

2- The solution given by Agbezuge and Deresiewicz (1974) is for a spherical indenter contacting a poroelastic solid. No consideration was given to creep deformation of the solid frame. Further, the experiments done here used a Berkovich tip, rather than a spherical indenter. Further numerical analysis is needed to provide a better estimate of the depth evolution using a Berkovich tip. It would also be desirable to include treatment of the inelastic deformation within the solid frame.

3- The permeability values estimated from the poroelastic solution are very low; for the carbonate the estimate from the indentation creep is 10 orders of magnitude lower than macroscopic measurements. The cause of this discrepancy is not clear. The volume activated during nanoindentation is small and it may be that only very small pores are present, thus lowering the local permeability that is being sampled. But other explanations are also possible.

Bibliography

Abedi, S., Slim, M., Hofmann, R., Bryndzia, T., and Ulm, F.-J. (2016a). Nanochemo-mechanical signature of organic-rich shales: a coupled indentation–EDX analysis. *Acta Geotechnica, 11*(3), 559-572.

Abedi, S., Slim, M., and Ulm, F.-J. (2016b). Nanomechanics of organic-rich shales: the role of thermal maturity and organic matter content on texture. *Acta Geotechnica, 11*(4), 775-787.

Agbezuge, L. K., and Deresiewicz, H. (1974). On the indentation of a consolidating half-space. *Isr. J. Technol, 12*(5-6), 322-338.

Aki, K., and Richards, P. G. (2002). *Quantitative seismology.*

Almasoodi, M. M., Abousleiman, Y. N., and Hoang, S. K. (2014). *Viscoelastic creep of eagle ford shale: investigating fluid-shale interaction.* Paper presented at the SPE/CSUR Unconventional Resources Conference–Canada.

Altmann, J. B., Müller, T. M., Müller, B. I., Tingay, M. R., and Heidbach, O. (2010). Poroelastic contribution to the reservoir stress path. *International Journal of Rock Mechanics and Mining Sciences, 47*(7), 1104-1113.

Amadei, B. (2012). *Rock anisotropy and the theory of stress measurements* (Vol. 2): Springer Science & Business Media.

Ambrose, J. (2014). Failure of anisotropic shales under triaxial stress conditions, (Doctoral dissertation), Imperial College London.

Asif, S. A. S., Wahl, K. J., and Colton, R. J. (1999). Nanoindentation and contact stiffness measurement using force modulation with a capacitive load-displacement transducer. *Review of scientific instruments, 70*(5), 2408-2413.

Asif, S. A. S., Wahl, K. J., Colton, R. J., and Warren, O. L. (2001). Quantitative imaging of nanoscale mechanical properties using hybrid nanoindentation and force modulation. *Journal of Applied Physics, 90*(3), 1192-1200.

Atkinson, B. K., and Meredith, P. G. (1987). The theory of subcritical crack growth with applications to minerals and rocks. *Fracture mechanics of rock, 2*, 111-166.

Augustesen, A., Liingaard, M., and Lade, P. V. (2004). Evaluation of time-dependent behavior of soils. *International Journal of Geomechanics, 4*(3), 137-156.

Baig, A., and Urbancic, T. (2010). Microseismic moment tensors: A path to understanding frac growth. *The Leading Edge, 29*(3), 320-324.

Baud, P., Vajdova, V., and Wong, T. f. (2006). Shear- enhanced compaction and strain localization: Inelastic deformation and constitutive modeling of four porous sandstones. *Journal of Geophysical Research: Solid Earth, 111*(B12).

Baud, P., Zhu, W., and Wong, T. f. (2000). Failure mode and weakening effect of water on sandstone. *Journal of Geophysical Research: Solid Earth, 105*(B7), 16371-16389.

Beake, B., Goodes, S., and Smith, J. (2001). Micro-impact testing: a new technique for investigating thin film toughness, adhesion, erosive wear resistance, and dynamic hardness. *Surface engineering, 17*(3), 187-192.

Bernabe, Y., and Brace, W. (1990). Deformation and fracture of Berea sandstone. *The Brittle-Ductile Transition in Rocks, Geophys. Monogr. Serf. Vp, 56*, 91-101.

Bernabe, Y., Fryer, D., and Shively, R. (1994). Experimental observations of the elastic and inelastic behaviour of porous sandstones. *Geophysical Journal International, 117*(2), 403-418.

Beugelsdijk, L., De Pater, C., and Sato, K. (2000). *Experimental hydraulic fracture propagation in a multi-fractured medium.* Paper presented at the SPE Asia Pacific conference on integrated modelling for asset management.

Biot, M. A. (1956). Theory of propagation of elastic waves in a fluid- saturated porous solid. II. Higher frequency range. *The Journal of the acoustical Society of america, 28*(2), 179-191.

Blanton, T. L. (1982). *An experimental study of interaction between hydraulically induced and pre-existing fractures.* Paper presented at the SPE unconventional gas recovery symposium.

Blanton, T. L. (1986). *Propagation of hydraulically and dynamically induced fractures in naturally fractured reservoirs.* Paper presented at the SPE unconventional gas technology symposium.

Boudali, M. (1995). Comportement tridimensionnel et visqueux des argiles naturelles, (Doctoral dissertation), Universite´ Laval, Que´bec.

Boulenouar, A., Mighani, S., Pourpak, H., Bernabé, Y., and Evans, B. (2017). *Mechanical Properties of Vaca Muerta Shales From Nano-Indentation Tests.* Paper presented at the 51st US Rock Mechanics/Geomechanics Symposium.

Bower, A., Fleck, N. A., Needleman, A., and Ogbonna, N. (1993). Indentation of a power law creeping solid. *Proceedings of the Royal Society of London. Series A: Mathematical and Physical Sciences, 441*(1911), 97-124.

Brace, W. (1980). *Permeability of crystalline and argillaceous rocks.* Paper presented at the International Journal of Rock Mechanics and Mining Sciences & Geomechanics Abstracts.

Brantut, N., Baud, P., Heap, M., and Meredith, P. (2012a). Micromechanics of brittle creep in rocks. *Journal of Geophysical Research: Solid Earth, 117*(B8).

Brantut, N., Baud, P., Heap, M. J., and Meredith, P. G. (2012b). Micromechanics of brittle creep in rocks. *Journal of Geophysical Research-Solid Earth, 117.* doi:10.1029/2012jb009299

Brantut, N., Heap, M., Baud, P., and Meredith, P. (2014a). Rate- and strain- dependent brittle deformation of rocks. *Journal of Geophysical Research: Solid Earth, 119*(3), 1818-1836.

Brantut, N., Heap, M., Meredith, P., and Baud, P. (2013). Time-dependent cracking and brittle creep in crustal rocks: A review. *Journal of Structural Geology, 52*, 17-43.

Brantut, N., Heap, M. J., Baud, P., and Meredith, P. G. (2014b). Mechanisms of time-dependent deformation in porous limestone. *Journal of Geophysical Research-Solid Earth, 119*(7), 5444-5463. doi:10.1002/2014jb011186

Brantut, N., Heap, M. J., Baud, P., and Meredith, P. G. (2014c). Rate- and strain-dependent brittle deformation of rocks. *Journal of Geophysical Research-Solid Earth, 119*(3), 1818-1836. doi:10.1002/2013jb010448

Broek, D. (2012). *Elementary engineering fracture mechanics*: Springer Science & Business Media.

Brown, S. R. (1987). Fluid flow through rock joints: the effect of surface roughness. *Journal of Geophysical Research: Solid Earth, 92*(B2), 1337-1347.

Brune, J. N. (1970). Tectonic stress and the spectra of seismic shear waves from earthquakes. *Journal of Geophysical Research, 75*(26), 4997-5009.

Bunger, A. P., Kear, J., Jeffrey, R. G., Prioul, R., and Chuprakov, D. (2015). *Laboratory investigation of hydraulic fracture growth through weak discontinuities with active* *ultrasound monitoring.* Paper presented at the 13th ISRM International Congress of Rock Mechanics.

Bushby, A., Ferguson, V., and Boyde, A. (2004). Nanoindentation of bone: Comparison of specimens tested in liquid and embedded in polymethylmethacrylate. *Journal of materials research, 19*(1), 249-259.

Byerlee, J., and Summers, R. (1976). *A note on the effect of fault gouge thickness on fault stability.* Paper presented at the International Journal of Rock Mechanics and Mining Sciences & Geomechanics Abstracts.

Byerlee, J. D., and Brace, W. (1968). Stick slip, stable sliding, and earthquakes—effect of rock type, pressure, strain rate, and stiffness. *Journal of Geophysical Research, 73*(18), 6031-6037.

Carroll, M. (1991). A critical state plasticity theory for porous reservoir rock. *Recent Advances in Mechanics of Structured Continua, 117*, 1-8.

Carslaw, H. S., and Jaeger, J. C. (1959). *The Conduction of Heat in Solids* (Second ed.). London: Oxford University Press.

Chang, C., Mallman, E., and Zoback, M. (2014). Time-dependent subsidence associated with drainage-induced compaction in Gulf of Mexico shales bounding a severely depleted gas reservoir. *Aapg Bulletin, 98*(6), 1145-1159.

Chang, C., and Zoback, M. (2008). *Creep in unconsolidated shale and its implication on rock physical properties.* Paper presented at the 42nd US Rock Mechanics Symposium (USRMS).

Chen, S., and Soh, A. (2008). The capillary force in micro-and nano-indentation with different indenter shapes. *International journal of solids and structures, 45*(10), 3122-3137.

Chen, X., Madden, A. S., Bickmore, B. R., and Reches, Z. e. (2013). Dynamic weakening by nanoscale smoothing during high-velocity fault slip. *Geology, 41*(7), 739-742.

Chen, Z., Jeffrey, R. G., Zhang, X., and Kear, J. (2017). Finite-element simulation of a hydraulic fracture interacting with a natural fracture. *SPE Journal, 22*(01), 219-234.

Chester, F., Chester, J., Kronenberg, A., and Hajash, A. (2007). Subcritical creep compaction of quartz sand at diagenetic conditions: Effects of water and grain size. *Journal of Geophysical Research: Solid Earth, 112*(B6).

Chester, F., and Logan, J. M. (1986). Implications for mechanical properties of brittle faults from observations of the Punchbowl fault zone, California. *Pure and Applied Geophysics, 124*(1-2), 79-106.

Choens, R., and Chester, F. (2018). Time- Dependent Consolidation in Porous Geomaterials at In Situ Conditions of Temperature and Pressure. *Journal of Geophysical Research: Solid Earth, 123*(8), 6424-6441.

Cohen, S. R., and Kalfon-Cohen, E. (2013). Dynamic nanoindentation by instrumented nanoindentation and force microscopy: A comparative review. *Beilstein journal of nanotechnology, 4*, 815.

Conder, J. A., and Arciniegas, C. A. (2017). Conjugate Faulting in the Wabash Valley Fault Zone Exhibited by the 20 November 2012 mb 3.6 Earthquake, a Mt. Carmel Late Aftershock. *Seismological Research Letters, 88*(4), 1203-1209.

Dahi-Taleghani, A., and Olson, J. E. (2011). Numerical modeling of multistranded-hydraulic-fracture propagation: accounting for the interaction between induced and natural fractures. *SPE Journal, 16*(03), 575-581.

Dahm, T. (1996). Relative moment tensor inversion based on ray theory: theory and synthetic tests. *Geophysical Journal International, 124*(1), 245-257.

Damani, A., Sondergeld, C., and Rai, C. (2018). Experimental investigation of in situ and injection fluid effect on hydraulic fracture mechanism using acoustic emission in Tennessee sandstone. *Journal of Petroleum Science and Engineering, 171*, 315-324.

Das, I., and Zoback, M. D. (2013). Long-period, long-duration seismic events during hydraulic stimulation of shale and tight-gas reservoirs—Part 1: Waveform characteristicsLPLD events: Waveform characteristics. *Geophysics, 78*(6), KS107-KS118.

Davies, R., Foulger, G., Bindley, A., and Styles, P. (2013). Induced seismicity and hydraulic fracturing for the recovery of hydrocarbons. *Marine and petroleum geology, 45*, 171-185.

Den Brok, S., and Spiers, C. (1991). Experimental evidence for water weakening of quartzite by microcracking plus solution–precipitation creep. *Journal of the Geological Society, 148*(3), 541-548.

Detournay, E., and Cheng, A. (1992). *Influence of pressurization rate on the magnitude of the breakdown pressure.* Paper presented at the The 33th US Symposium on Rock Mechanics (USRMS).

Dewhurst, D. N., Sarout, J., Delle Piane, C., Siggins, A. F., and Raven, M. D. (2015). Empirical strength prediction for preserved shales. *Marine and petroleum geology, 67*, 512-525.

Dieterich, J. H. (1978). Time-dependent friction and the mechanics of stick-slip. In *Rock Friction and Earthquake Prediction* (pp. 790-806): Springer.

Dieterich, J. H., and Kilgore, B. D. (1994). Direct observation of frictional contacts: New insights for state-dependent properties. *Pure and Applied Geophysics, 143*(1-3), 283-302.

Donath, F., Fruth, L., and Olsson, W. (1972). *Experimental study of frictional properties of faults.* Paper presented at the The 14th US Symposium on Rock Mechanics (USRMS).

Eaton, D. W., and Forouhideh, F. (2011). Solid angles and the impact of receiver-array geometry on microseismic moment-tensor inversion. *Geophysics, 76*(6), WC77-WC85.

Ellsworth, W. L. (2013). Injection-induced earthquakes. *Science, 341*(6142), 1225942.

Engelder, J., and Scholz, C. (1976). *The role of asperity indentation and ploughing in rock friction—II: Influence of relative hardness and normal load.* Paper presented at the International Journal of Rock Mechanics and Mining Sciences & Geomechanics Abstracts.

Engelder, J. T., Logan, J. M., and Handin, J. (1975). The sliding characteristics of sandstone on quartz fault-gouge. *Pure and Applied Geophysics, 113*(1), 69-86.

Enomoto, T., Koseki, J., Tatsuoka, F., and Sato, T. (2015). Creep failure of sands exhibiting various viscosity types and its simulation. *Soils and Foundations, 55*(6), 1346-1363.

Fabre, G., and Pellet, F. (2006). Creep and time-dependent damage in argillaceous rocks. *International Journal of Rock Mechanics and Mining Sciences, 43*(6), 950-960.

French, M. E., and Zhu, W. (2017). Slow fault propagation in serpentinite under conditions of high pore fluid pressure. *Earth and Planetary Science Letters, 473*, 131-140.

Fu, W., Savitski, A. A., and Bunger, A. P. (2018). Analytical criterion predicting the impact of natural fracture strength, height and cemented portion on hydraulic fracture growth. *Engineering Fracture Mechanics, 204*, 497-516.

Gale, J. F., Reed, R. M., and Holder, J. (2007). Natural fractures in the Barnett Shale and their importance for hydraulic fracture treatments. *Aapg Bulletin, 91*(4), 603-622.

Galli, M., Comley, K. S., Shean, T. A., and Oyen, M. L. (2009). Viscoelastic and poroelastic mechanical characterization of hydrated gels. *Journal of materials research, 24*(3), 973-979.

Gan, W., and Frohlich, C. (2013). Gas injection may have triggered earthquakes in the Cogdell oil field, Texas. *Proceedings of the National Academy of Sciences, 110*(47), 18786-18791.

Garcia, M. N., Sorenson, F., Bonapace, J. C., Motta, F., Bajuk, C., and Stockman, H. (2013). *Vaca Muerta Shale reservoir characterization and description: The starting point for development of a Shale play with very good possibilities for a successful project.* Paper presented at the Unconventional Resources Technology Conference.

Geng, Z., Bonnelye, A., Chen, M., Jin, Y., Dick, P., David, C., Fang, X., and Schubnel, A. (2017). Elastic anisotropy reversal during brittle creep in shale. *Geophysical Research Letters, 44*(21).

Geng, Z., Bonnelye, A., Chen, M., Jin, Y., Dick, P., David, C., Fang, X., and Schubnel, A. (2018). Time and Temperature Dependent Creep in Tournemire Shale. *Journal of Geophysical Research: Solid Earth, 123*(11), 9658-9675.

Ghassemi, A., and Suarez-Rivera, R. (2012). Sustaining fracture area and conductivity of gas shale reservoirs for enhancing long-term production and recovery. *College Station.*

Ghassemi, A., and Zhang, Q. (2004). *Poro-thermoelastic mechanisms in wellbore stability and reservoir stimulation.* Paper presented at the Proc. 29th Workshop on Geothermal Reservoir Engineering Stanford University.

Gibbs, M., Evetts, J., and Leake, J. (1983). Activation energy spectra and relaxation in amorphous materials. *Journal of Materials Science, 18*(1), 278-288.

Gibson, L. J., and Ashby, M. F. (1999). *Cellular solids: structure and properties*: Cambridge university press.

Goebel, T. H., and Brodsky, E. E. (2018). The spatial footprint of injection wells in a global compilation of induced earthquake sequences. *Science, 361*(6405), 899-904.

Goldstein, R., and Osipenko, N. (2015). Initiation of a secondary crack across a frictional interface. *Engineering Fracture Mechanics, 140*, 92-105.

Gomez, J., and Basaran, C. (2006). Nanoindentation of Pb/Sn solder alloys; experimental and finite element simulation results. *International journal of solids and structures, 43*(6), 1505-1527.

Goodall, R., and Clyne, T. (2006). A critical appraisal of the extraction of creep parameters from nanoindentation data obtained at room temperature. *Acta Materialia, 54*(20), 5489-5499.

Gu, H., Weng, X., Lund, J. B., Mack, M. G., Ganguly, U., and Suarez-Rivera, R. (2012). Hydraulic fracture crossing natural fracture at nonorthogonal angles: a criterion and its validation. *SPE Production & Operations, 27*(01), 20-26.

Guglielmi, Y., Cappa, F., Avouac, J.-P., Henry, P., and Elsworth, D. (2015). Seismicity triggered by fluid injection–induced aseismic slip. *Science, 348*(6240), 1224-1226.

Haimson, B., and Fairhurst, C. (1969). *In-situ stress determination at great depth by means of hydraulic fracturing.* Paper presented at the The 11th US symposium on rock mechanics (USRMS).

Hangen, U. D., Stauffer, D. D., and Asif, S. A. S. (2014). Resolution limits of nanoindentation testing. In *Nanomechanical Analysis of High Performance Materials* (pp. 85-102): Springer.

Hanson, M., Anderson, G., and Shaffer, R. (1980). Theoretical and experimental research on hydraulic fracturing. *Journal of Energy Resources Technology, 102*(2), 92-98.

Hartley, R., and Behringer, R. (2003). Logarithmic rate dependence of force networks in sheared granular materials. *Nature, 421*(6926), 928.

Hasbani, J., and Hryb, D. (2018). *On the Characterization of the Viscoelastic Response of the Vaca Muerta Formation.* Paper presented at the 52nd US Rock Mechanics/Geomechanics Symposium.

Healy, J., Rubey, W., Griggs, D., and Raleigh, C. (1968). The denver earthquakes. *Science, 161*(3848), 1301-1310.

Heap, M., Baud, P., and Meredith, P. (2009a). Influence of temperature on brittle creep in sandstones. *Geophysical Research Letters, 36*(19).

Heap, M., Baud, P., Meredith, P., Bell, A., and Main, I. (2009b). Time- dependent brittle creep in Darley Dale sandstone. *Journal of Geophysical Research: Solid Earth, 114*(B7).

Heap, M. J., Brantut, N., Baud, P., and Meredith, P. G. (2015). Time- dependent compaction band formation in sandstone. *Journal of Geophysical Research: Solid Earth, 120*(7), 4808-4830.

Herrmann, F. J., and Bernabé, Y. (2004). Seismic singularities at upper-mantle phase transitions: a site percolation model. *Geophysical Journal International, 159*(3), 949-960.

Herrmann, J., Rybacki, E., Sone, H., and Dresen, G. (2018). Deformation Experiments on Bowland and Posidonia Shale—Part I: Strength and Young's Modulus at Ambient and In Situ p c–T Conditions. *Rock Mechanics and Rock Engineering, 51*(12), 3645-3666.

Holland, A. A. (2013). Earthquakes triggered by hydraulic fracturing in south- central Oklahoma. *Bulletin of the Seismological Society of America, 103*(3), 1784-1792.

Hou, B., Chen, M., Jin, Y., Lin, B., Diao, C., and Zhang, X. (2015). *Optimum Condition of Hydraulic Fracture-Natural Fracture Interaction in Shale Block Experiments.* Paper presented at the 49th US Rock Mechanics/Geomechanics Symposium.

Hudson, J., Pearce, R., and Rogers, R. (1989). Source type plot for inversion of the moment tensor. *Journal of Geophysical Research: Solid Earth, 94*(B1), 765-774.

Hysitron Inc. (2011). *nanoDMA III User Manual: Revision 9.2.1211.*

Johnson, K. (1970). The correlation of indentation experiments. *Journal of the Mechanics and Physics of Solids, 18*(2), 115-126.

Johnson, K. L. (1985). *Contact mechanics*: Cambridge university press.

Kanafi, M. M. (2016). 1-dimensional surface roughness power spectrum of a profile or topography. *MATLAB Central File Exchange. Retrieved February 13 2019.* doi:https://www.mathworks.com/matlabcentral/fileexchange/54315-1-dimensional-surface-roughness-power-spectrum-of-a-profile-or-topography

Kassis, S., and Sondergeld, C. H. (2010). *Fracture permeability of gas shale: Effect of roughness, fracture offset, proppant, and effective stress.* Paper presented at the International oil and gas conference and exhibition in China.

Kattenhorn, S. A., Aydin, A., and Pollard, D. D. (2000). Joints at high angles to normal fault strike: an explanation using 3-D numerical models of fault-perturbed stress fields. *Journal of Structural Geology, 22*(1), 1-23.

Kemeny, J. (1991). A model for non-linear rock deformation under compression due to sub-critical crack growth. *International journal of rock mechanics and mining sciences & geomechanics abstracts, 28*(6), 459-467.

Keranen, K. M., Weingarten, M., Abers, G. A., Bekins, B. A., and Ge, S. (2014). Sharp increase in central Oklahoma seismicity since 2008 induced by massive wastewater injection. *Science, 345*(6195), 448-451.

Kern, H., Liu, B., and Popp, T. (1997). Relationship between anisotropy of P and S wave velocities and anisotropy of attenuation in serpentinite and amphibolite. *Journal of Geophysical Research: Solid Earth, 102*(B2), 3051-3065.

Khatibi, S., Aghajanpour, A., Ostadhassan, M., Ghanbari, E., Amirian, E., and Mohammed, R. (2018). *Evaluating the Impact of Mechanical Properties of Kerogen on Hydraulic Fracturing of Organic Rich Formations.* Paper presented at the SPE Canada Unconventional Resources Conference.

Kinnari, T., Esteban, J., Zamora, N., Fernandez, R., López- Santos, C., Yubero, F., Mariscal, D., Puertolas, J., and Gomez- Barrena, E. (2010). Effect of surface roughness and sterilization on bacterial adherence to ultra- high molecular weight polyethylene. *Clinical Microbiology and Infection, 16*(7), 1036-1041.

Kirby, S. H. (1980). Tectonic stresses in the lithosphere: Constraints provided by the experimental deformation of rocks. *Journal of Geophysical Research: Solid Earth, 85*(B11), 6353-6363.

Kranzz, R., Frankel, A., Engelder, T., and Scholz, C. (1979). *The permeability of whole and jointed Barre granite.* Paper presented at the International Journal of Rock Mechanics and Mining Sciences & Geomechanics Abstracts.

Kuhn, M. R., and Mitchell, J. K. (1993). New perspectives on soil creep. *Journal of Geotechnical Engineering, 119*(3), 507-524.

Kumar, V., Sondergeld, C. H., and Rai, C. S. (2012). *Nano to macro mechanical characterization of shale.* Paper presented at the SPE Annual Technical Conference and Exhibition.

Kwiatek, G., Charalampidou, E.-M., Dresen, G., and Stanchits, S. (2014). An improved method for seismic moment tensor inversion of acoustic emissions through assessment of sensor coupling and sensitivity to incidence angle. *Int. J. Rock Mech. Min. Sci, 65*, 153-161.

Kwiatek, G., Martínez- Garzón, P., and Bohnhoff, M. (2016). HybridMT: A MATLAB/shell environment package for seismic moment tensor inversion and refinement. *Seismological Research Letters, 87*(4), 964-976.

Kwok, C., and Bolton, M. (2010). DEM simulations of thermally activated creep in soils. *Géotechnique, 60*(6), 425-433.

Lam, K., and Cleary, M. (1984). Slippage and re- initiation of (hydraulic) fractures at frictional interfaces. *International Journal for Numerical and Analytical Methods in Geomechanics, 8*(6), 589-604.

Lambe, T. W., and Whitman, R. V. (1969). Soil mechanics. Massachusetts institute of technology. In: John Wiley and Sons, New York.

Lawn, B., and Marshall, D. (1979). Hardness, toughness, and brittleness: an indentation analysis. *Journal of the American ceramic society, 62*(7- 8), 347-350.

Lee, T. C., and Delaney, P. T. (1987). Frictional heating and pore pressure rise due to a fault slip. *Geophysical Journal of the Royal Astronomical Society, 88*(3), 569-591.

Leoni, M., Karstunen, M., and Vermeer, P. (2008). Anisotropic creep model for soft soils. *Géotechnique, 58*(3), 215-226.

Li, B. Q., da Silva, B. G., and Einstein, H. (2019). Laboratory hydraulic fracturing of granite: Acoustic emission observations and interpretation. *Engineering Fracture Mechanics, 209*, 200-220.

Li, Y., and Ghassemi, A. (2012). *Creep behavior of Barnett, Haynesville, and Marcellus shale.* Paper presented at the 46th US Rock Mechanics/Geomechanics Symposium.

Lockner, D. (1993a). *The role of acoustic emission in the study of rock fracture.* Paper presented at the International Journal of Rock Mechanics and Mining Sciences & Geomechanics Abstracts.

Lockner, D. (1993b). Room temperature creep in saturated granite. *Journal of Geophysical Research: Solid Earth, 98*(B1), 475-487.

Lockner, D., and Byerlee, J. (1977). Hydrofracture in Weber sandstone at high confining pressure and differential stress. *Journal of Geophysical Research, 82*(14), 2018-2026.

Lockner, D. A. (1995). Rock failure. *Rock physics and phase relations: A handbook of physical constants, 3*, 127-147.

Lockner, D. A., Kilgore, B. D., Beeler, N. M., and Moore, D. E. (2017). The transition from frictional sliding to shear melting in laboratory stick-slip experiments. *Fault zone dynamic processes: Evolution of fault properties during seismic rupture, 227*, 105.

Mahyari, A., and Selvadurai, A. (1998). Enhanced consolidation in brittle geomaterials susceptible to damage. *Mechanics of Cohesive- frictional Materials: An International*

Journal on Experiments, Modelling and Computation of Materials and Structures, 3(3), 291-303.

Mair, K., Frye, K. M., and Marone, C. (2002). Influence of grain characteristics on the friction of granular shear zones. *Journal of Geophysical Research: Solid Earth, 107*(B10), ECV 4-1-ECV 4-9.

Majer, E. L., Baria, R., Stark, M., Oates, S., Bommer, J., Smith, B., and Asanuma, H. (2007). Induced seismicity associated with enhanced geothermal systems. *Geothermics, 36*(3), 185-222.

Manthei, G. (2005). Characterization of acoustic emission sources in a rock salt specimen under triaxial compression. *Bulletin of the Seismological Society of America, 95*(5), 1674-1700.

Marone, C., Raleigh, C. B., and Scholz, C. (1990). Frictional behavior and constitutive modeling of simulated fault gouge. *Journal of Geophysical Research: Solid Earth, 95*(B5), 7007-7025.

Martin, R. J. (1968). *The effect of pore pressure on the strength of low porosity crystalline rocks.* Massachusetts Institute of Technology,

Mavko, G., Mukerji, T., and Dvorkin, J. (2009). *The rock physics handbook: Tools for seismic analysis of porous media*: Cambridge university press.

Maxwell, S. C., Urbancic, T., Steinsberger, N., and Zinno, R. (2002). *Microseismic imaging of hydraulic fracture complexity in the Barnett shale.* Paper presented at the SPE annual technical conference and exhibition.

McGarr, A. (2012). Relating stick- slip friction experiments to earthquake source parameters. *Geophysical Research Letters, 39*(5).

McGarr, A., Bekins, B., Burkardt, N., Dewey, J., Earle, P., Ellsworth, W., Ge, S., Hickman, S., Holland, A., and Majer, E. (2015). Coping with earthquakes induced by fluid injection. *Science, 347*(6224), 830-831.

McLaskey, G. C. (2011). *Stress Wave Source Characterization: Impact, Fracture, and Sliding Friction.* UC Berkeley,

McLaskey, G. C., Kilgore, B. D., Lockner, D. A., and Beeler, N. M. (2014). Laboratory generated M-6 earthquakes. *Pure and Applied Geophysics, 171*(10), 2601-2615.

McLaskey, G. C., and Lockner, D. A. (2014). Preslip and cascade processes initiating laboratory stick slip. *Journal of Geophysical Research: Solid Earth, 119*(8), 6323-6336.

McLaskey, G. C., and Lockner, D. A. (2018). Shear failure of a granite pin traversing a sawcut fault. *International Journal of Rock Mechanics and Mining Sciences, 110*, 97-110.

McLaskey, G. C., Lockner, D. A., Kilgore, B. D., and Beeler, N. M. (2015). A robust calibration technique for acoustic emission systems based on momentum transfer from a ball drop. *Bulletin of the Seismological Society of America, 105*(1), 257-271.

Menard, K. P. (2008). *Dynamic mechanical analysis: a practical introduction*: CRC press.

Menke, W. (2018). *Geophysical data analysis: Discrete inverse theory*: Academic press.

Mighani, S., Bernabe, Y., Mok, U., Pec, M., and Evans, B. (2018a). *Can We Use Nanoindentation to Derive the Poroelastic P Arameters of Microporous Rocks?-Experimental Evidence.* Paper presented at the 52nd US Rock Mechanics/Geomechanics Symposium.

Mighani, S., Boulenouar, A., Moradian, Z., Evans, J., and Bernabe, Y. (2015a). *Fluid Compressibility Effects during Hydraulic Fracture: an Opportunity for Gas Fracture Revival.* Paper presented at the AGU Fall Meeting Abstracts.

Mighani, S., Lockner, D., Kilgore, B., and Evans, B. (2018b). *Role of Fault Gouge during Interaction between Hydraulic Fracture and a Preexisting Fracture.* Paper presented at the 52nd US Rock Mechanics/Geomechanics Symposium.

Mighani, S., Lockner, D. A., Kilgore, B. D., Sheibani, F., and Evans, B. (2018c). *Interaction between hydraulic fracture and a preexisting fracture under triaxial stress conditions.* Paper presented at the SPE Hydraulic Fracturing Technology Conference and Exhibition.

Mighani, S., Sondergeld, C. H., and Rai, C. S. (2016). Observations of tensile fracturing of anisotropic rocks. *SPE Journal, 21*(04), 1,289-281,301.

Mighani, S., Taneja, S., Sondergeld, C., and Rai, C. (2015b). *Nanoindentation creep measurements on shale.* Paper presented at the 49th US Rock Mechanics/Geomechanics Symposium.

Morgan, J. K. (2004). Particle dynamics simulations of rate-and state-dependent frictional sliding of granular fault gouge. In *Computational Earthquake Science Part I* (pp. 1877-1891): Springer.

Morgan, J. K., and Boettcher, M. S. (1999). Numerical simulations of granular shear zones using the distinct element method: 1. Shear zone kinematics and the micromechanics of localization. *Journal of Geophysical Research: Solid Earth, 104*(B2), 2703-2719.

Morrow, C., Shi, L., and Byerlee, J. (1984). Permeability of fault gouge under confining pressure and shear stress. *Journal of Geophysical Research: Solid Earth, 89*(B5), 3193-3200.

Nia, H. T., Han, L., Li, Y., Ortiz, C., and Grodzinsky, A. (2011). Poroelasticity of cartilage at the nanoscale. *Biophysical journal, 101*(9), 2304-2313.

Nicolas, A., Fortin, J., Regnet, J., Verberne, B., Plümper, O., Dimanov, A., Spiers, C., and Guéguen, Y. (2017). Brittle and semibrittle creep of Tavel limestone deformed at room temperature. *Journal of Geophysical Research: Solid Earth, 122*(6), 4436-4459.

Nur, A., and Booker, J. R. (1972). Aftershocks caused by pore fluid flow? *Science, 175*(4024), 885-887.

Oliver, W. C., and Pharr, G. M. (1992). An improved technique for determining hardness and elastic modulus using load and displacement sensing indentation experiments. *Journal of materials research, 7*(6), 1564-1583.

Oliver, W. C., and Pharr, G. M. (2004). Measurement of hardness and elastic modulus by instrumented indentation: Advances in understanding and refinements to methodology. *Journal of materials research, 19*(1), 3-20.

Orowan, E. (1944). The fatigue of glass under stress. *Nature, 154*(3906), 341.

Oyen, M. L. (2008). Poroelastic nanoindentation responses of hydrated bone. *Journal of materials research, 23*(5), 1307-1314.

Oyen, M. L. (2015). Nanoindentation of hydrated materials and tissues. *Current Opinion in Solid State and Materials Science, 19*(6), 317-323.

Parks, G. A. (1984). Surface and interfacial free energies of quartz. *Journal of Geophysical Research: Solid Earth, 89*(B6), 3997-4008.

Parsons, R., and Hedley, D. (1966). The analysis of the viscous property of rocks for classification. *International Journal of Rock Mechanics and Mining Sciences & Geomechanics Abstracts, 3*(4), 325-335.

Paterson, M. S., and Wong, T.-f. (2005). *Experimental rock deformation-the brittle field*: Springer Science & Business Media.

Patzek, T. W., Male, F., and Marder, M. (2013). Gas production in the Barnett Shale obeys a simple scaling theory. *Proceedings of the National Academy of Sciences, 110*(49), 19731-19736.

Pestana, J. M., and Whittle, A. J. (1999). Formulation of a unified constitutive model for clays and sands. *International Journal for Numerical and Analytical Methods in Geomechanics, 23*(12), 1215-1243.

Polak, A., Elsworth, D., Yasuhara, H., Grader, A., and Halleck, P. (2003). Permeability reduction of a natural fracture under net dissolution by hydrothermal fluids. *Geophysical Research Letters, 30*(20).

Pyrak-Nolte, L., and Morris, J. (2000). Single fractures under normal stress: The relation between fracture specific stiffness and fluid flow. *International Journal of Rock Mechanics and Mining Sciences, 37*(1-2), 245-262.

Rassouli, F., and Zoback, M. (2016). *A comparison of short-term and long-term creep experiments in unconventional reservoir formations.* Paper presented at the 50th US rock mechanics/geomechanics symposium.

Rassouli, F. S., and Zoback, M. D. (2018). Comparison of short-term and long-term creep experiments in shales and carbonates from unconventional gas reservoirs. *Rock Mechanics and Rock Engineering, 51*(7), 1995-2014.

Renshaw, C., and Pollard, D. (1995). *An experimentally verified criterion for propagation across unbounded frictional interfaces in brittle, linear elastic materials.* Paper presented at the International journal of rock mechanics and mining sciences & geomechanics abstracts.

Rouet- Leduc, B., Hulbert, C., Bolton, D. C., Ren, C. X., Riviere, J., Marone, C., Guyer, R. A., and Johnson, P. A. (2018). Estimating fault friction from seismic signals in the laboratory. *Geophysical Research Letters, 45*(3), 1321-1329.

Rudnicki, J. W. (2004). Shear and compaction band formation on an elliptic yield cap. *Journal of Geophysical Research-Solid Earth, 109*(B3), 10.1029/2003jb002633. doi:10.1029/2003jb002633

Rutledge, J. T., and Phillips, W. S. (2003). Hydraulic stimulation of natural fractures as revealed by induced microearthquakes, Carthage Cotton Valley gas field, east TexasHydraulic Stimulation of Natural Fractures. *Geophysics, 68*(2), 441-452.

Rutter, E. (1983). Pressure solution in nature, theory and experiment. *Journal of the Geological Society, 140*(5), 725-740.

Rutter, E. H. (1974). The influence of temperature, strain rate and interstitial water in the experimental deformation of calcite rocks. *Tectonophysics, 22*(3-4), 311-334.

Rybacki, E., Herrmann, J., Wirth, R., and Dresen, G. (2017). Creep of Posidonia shale at elevated pressure and temperature. *Rock Mechanics and Rock Engineering, 50*(12), 3121-3140.

Rybacki, E., Reinicke, A., Meier, T., Makasi, M., and Dresen, G. (2015). What controls the mechanical properties of shale rocks?–Part I: Strength and Young's modulus. *Journal of Petroleum Science and Engineering, 135*, 702-722.

Sano, O., Terada, M., and Ehara, S. (1982). A study on the time-dependent microfracturing and strength of Oshima granite. *Tectonophysics, 84*(2-4), 343-362.

Santamarina, J. C. (2003). Soil behavior at the microscale: particle forces. In *Soil behavior and soft ground construction* (pp. 25-56).

Sarmadivaleh, M., and Rasouli, V. (2014). Modified Reinshaw and Pollard criteria for a non-orthogonal cohesive natural interface intersected by an induced fracture. *Rock Mechanics and Rock Engineering, 47*(6), 2107-2115.

Sarout, J., Esteban, L., Delle Piane, C., Maney, B., and Dewhurst, D. N. (2014). Elastic anisotropy of Opalinus Clay under variable saturation and triaxial stress. *Geophysical Journal International, 198*(3), 1662-1682.

Sarout, J., and Guéguen, Y. (2008). Anisotropy of elastic wave velocities in deformed shales: Part 2—Modeling results. *Geophysics, 73*(5), D91-D103.

Savage, J., Lockner, D., and Byerlee, J. (1996). Failure in laboratory fault models in triaxial tests. *Journal of Geophysical Research: Solid Earth, 101*(B10), 22215-22224.

Schoenball, M., Sahara, D. P., and Kohl, T. (2014). Time-dependent brittle creep as a mechanism for time-delayed wellbore failure. *International Journal of Rock Mechanics and Mining Sciences, 70*, 400-406.

Schoenball, M., Walsh, F. R., Weingarten, M., and Ellsworth, W. L. (2018). How faults wake up: the Guthrie-Langston, Oklahoma earthquakes. *The Leading Edge, 37*(2), 100-106.

Scholz, C. (1968). Mechanism of creep in brittle rock. *Journal of Geophysical Research, 73*(10), 3295-3302.

Scholz, C., and Engelder, J. (1976). The role of asperity indentation and ploughing in rock friction—I: Asperity creep and stick-slip. *International Journal of Rock Mechanics and Mining Sciences & Geomechanics Abstracts, 13*(5), 149-154.

Scholz, C., and Kranz, R. (1974). Notes on dilatancy recovery. *Journal of Geophysical Research, 79*(14), 2132-2135.

Segall, P., and Lu, S. (2015). Injection- induced seismicity: Poroelastic and earthquake nucleation effects. *Journal of Geophysical Research: Solid Earth, 120*(7), 5082-5103.

Sharma, A., Damani, A., Sondergeld, C., and Rai, C. (2013). Understanding the microscale physics of hydraulic fracturing: A laboratory approach. In *SEG Technical Program Expanded Abstracts 2013* (pp. 2916-2921): Society of Exploration Geophysicists.

Sheibani, F. (2013). Solving three-dimensional problems in natural and hydraulic fracture development: insight from displacement discontinuity modeling.

Shukla, P., Kumar, V., Curtis, M., Sondergeld, C. H., and Rai, C. S. (2013). *Nanoindentation studies on shales.* Paper presented at the 47th US Rock Mechanics/Geomechanics Symposium.

Sibson, R. (1973). Interactions between temperature and pore-fluid pressure during earthquake faulting and a mechanism for partial or total stress relief. *Nature Physical Science, 243*(126), 66-68.

Sibson, R. H. (1985). A note on fault reactivation. *Journal of Structural Geology, 7*(6), 751-754.

Slim, M. (2016). Creep Properties of Source Rocks Using Indentation: The Role of Organic-Matter on Texture and Creep Rates, (Doctoral dissertation), Massachusetts Institute of Technology.

Smith, T. M., Sondergeld, C. H., and Rai, C. S. (2003). Gassmann fluid substitutions: A tutorial. *Geophysics, 68*(2), 430-440.

Snieder, R., Sens-Schönfelder, C., and Wu, R. (2016). The time dependence of rock healing as a universal relaxation process, a tutorial. *Geophysical Journal International, 208*(1), 1-9.

Sondergeld, C., and Estey, L. (1982). Source mechanisms and microfracturing during uniaxial cycling of rock. *Pure and Applied Geophysics, 120*(1), 151-166.

Sondergeld, C. H., Ambrose, R. J., Rai, C. S., and Moncrieff, J. (2010). *Micro-structural studies of gas shales.* Paper presented at the SPE Unconventional Gas Conference.

Sone, H., and Zoback, M. (2011). *Visco-plastic properties of shale gas reservoir rocks.* Paper presented at the 45th US Rock Mechanics/Geomechanics Symposium.

Sone, H., and Zoback, M. D. (2013a). Mechanical properties of shale-gas reservoir rocks—Part 1: Static and dynamic elastic properties and anisotropy. *Geophysics, 78*(5), D381-D392.

Sone, H., and Zoback, M. D. (2013b). Mechanical properties of shale-gas reservoir rocks—Part 2: Ductile creep, brittle strength, and their relation to the elastic modulusMechanical properties of gas shale—Part 2. *Geophysics, 78*(5), D393-D402.

Sone, H., and Zoback, M. D. (2014). Time-dependent deformation of shale gas reservoir rocks and its long-term effect on the in situ state of stress. *International Journal of Rock Mechanics and Mining Sciences, 69*, 120-132.

Spiers, C., De Meer, S., Niemeijer, A., and Zhang, X. (2003). Kinetics of rock deformation by pressure solution and the role of thin aqueous films. *Frontiers Science Series*, 129-158.

Stanchits, S. A., Lockner, D. A., and Ponomarev, A. V. (2003). Anisotropic changes in P-wave velocity and attenuation during deformation and fluid infiltration of granite. *Bulletin of the Seismological Society of America, 93*(4), 1803-1822.

Su, K., Onaisi, A., and Galeazzi, S. (2014, 3-7 Nov. 2014). *Geomechanical characterization and fracability assessment of the vaca muerta shale play.* Paper presented at the CONEXPLO, Mendoza City, Argentina.

Tabor, D. (1951). The hardness of metals, Clarendon. In: Oxford.

Taheri-Shakib, J., Ghaderi, A., Hosseini, S., and Hashemi, A. (2016). Debonding and coalescence in the interaction between hydraulic and natural fracture: Accounting for the effect of leak-off. *Journal of Natural Gas Science and Engineering, 36*, 454-462.

Tembe, S., Lockner, D. A., and Wong, T. F. (2010). Effect of clay content and mineralogy on frictional sliding behavior of simulated gouges: Binary and ternary mixtures of quartz, illite, and montmorillonite. *Journal of Geophysical Research: Solid Earth, 115*(B3).

TenCate, J. A., Smith, E., and Guyer, R. A. (2000). Universal slow dynamics in granular solids. *Physical Review Letters, 85*(5), 1020.

Thiercelin, M., and Roegiers, J. (2000). Formation characterization: Rock mechanics. *Reservoir stimulation, 3*(1), 3.

Thompson, B., Young, R., and Lockner, D. A. (2009). Premonitory acoustic emissions and stick- slip in natural and smooth- faulted Westerly granite. *Journal of Geophysical Research: Solid Earth, 114*(B2).

Thorpe, R. K., Hanson, M. E., Anderson, G. D., and Shaffer, R. J. (1982). *Step cracks: Theory, experiment, and field observation.* Paper presented at the The 23rd US Symposium on Rock Mechanics (USRMS).

Timoshenko, S., Goodier, J. N., and Abramson, H. N. (1970). Theory of elasticity. *Journal of Applied Mechanics, 37*, 888.

Tinni, A., Fathi, E., Agarwal, R., Sondergeld, C. H., Akkutlu, I. Y., and Rai, C. S. (2012). *Shale permeability measurements on plugs and crushed samples.* Paper presented at the SPE Canadian Unconventional Resources Conference.

Tong, X., and Tuan, C. Y. (2007). Viscoplastic cap model for soils under high strain rate loading. *Journal of Geotechnical and Geoenvironmental Engineering, 133*(2), 206-214.

Vandamme, M. (2008). The nanogranular origin of concrete creep : a nanoindentation investigation of microstructure and fundamental properties of calcium-silicate-hydrates, (Doctoral dissertation), Massachusetts Institute of Technology.

Vandamme, M., Tweedie, C. A., Constantinides, G., Ulm, F.-J., and Van Vliet, K. J. (2012). Quantifying plasticity-independent creep compliance and relaxation of viscoelastoplastic materials under contact loading. *Journal of materials research, 27*(1), 302-312.

Vandamme, M., and Ulm, F.-J. (2009). Nanogranular origin of concrete creep. *Proceedings of the National Academy of Sciences, 106*(26), 10552-10557.

Vandamme, M., and Ulm, F.-J. (2013). Nanoindentation investigation of creep properties of calcium silicate hydrates. *Cement and Concrete Research, 52*, 38-52.

Vanorio, T., Prasad, M., and Nur, A. (2003). Elastic properties of dry clay mineral aggregates, suspensions and sandstones. *Geophysical Journal International, 155*(1), 319-326.

Vavryčuk, V. (2015). Moment tensor decompositions revisited. *Journal of Seismology, 19*(1), 231-252.

Villamor Lora, R., and Ghazanfari, E. (2015). *Creep behavior of shale formations in shale gas development.* Paper presented at the IFCEE 2015.

Vogler, D., Amann, F., Bayer, P., and Elsworth, D. (2016). Permeability evolution in natural fractures subject to cyclic loading and gouge formation. *Rock Mechanics and Rock Engineering, 49*(9), 3463-3479.

Walsh, J. (1981). *Effect of pore pressure and confining pressure on fracture permeability.* Paper presented at the International Journal of Rock Mechanics and Mining Sciences & Geomechanics Abstracts.

Wang, H., Bernabé, Y., Mok, U., and Evans, B. (2016). Localized reactive flow in carbonate rocks: Core- flood experiments and network simulations. *Journal of Geophysical Research: Solid Earth, 121*(11), 7965-7983.

Wang, H., Xia, B., Lu, Y., Gong, T., and Zhang, R. (2017). Study on the propagation laws of hydrofractures meeting a faulted structure in the coal seam. *Energies, 10*(5), 654.

Wang, H. F. (2017). *Theory of linear poroelasticity with applications to geomechanics and hydrogeology*: Princeton University Press.

Wang, W., Wu, K., and Olson, J. (2019). Characterization of hydraulic fracture geometry in shale rocks through physical modeling. *International Journal of Fracture*, 1-15.

Wang, Y., and Li, C. (2017). Investigation of the Effect of Cemented Fractures on Fracturing Network Propagation in Model Block with Discrete Orthogonal Fractures. *Rock Mechanics and Rock Engineering, 50*(7), 1851-1862.

Warpinski, N., and Teufel, L. (1987). Influence of geologic discontinuities on hydraulic fracture propagation (includes associated papers 17011 and 17074). *Journal of Petroleum Technology, 39*(02), 209-220.

Warpinski, N., Wolhart, S., and Wright, C. (2001). *Analysis and prediction of microseismicity induced by hydraulic fracturing.* Paper presented at the SPE Annual Technical Conference and Exhibition.

Warpinski, N. R., Finley, S., Vollendorf, W., Obrien, M., and Eshom, E. (1982). Interface test series: An in situ study of factors affecting the containment of hydraulic fractures. *Unknown*.

Weingarten, M., Ge, S., Godt, J. W., Bekins, B. A., and Rubinstein, J. L. (2015). High-rate injection is associated with the increase in US mid-continent seismicity. *Science, 348*(6241), 1336-1340.

Weng, X., Kresse, O., Cohen, C. E., Wu, R., and Gu, H. (2011). *Modeling of hydraulic fracture network propagation in a naturally fractured formation.* Paper presented at the SPE Hydraulic Fracturing Technology Conference.

Whittle, A. (1993). Evaluation of a constitutive model for overconsolidated clays. *Géotechnique, 43*(2), 289-313.

Wilkinson, T. M., Zargari, S., Prasad, M., and Packard, C. E. (2015). Optimizing nano-dynamic mechanical analysis for high-resolution, elastic modulus mapping in organic-rich shales. *Journal of Materials Science, 50*(3), 1041-1049.

Willacy, C., van Dedem, E., Minisini, S., Li, J., Blokland, J.-W., Das, I., and Droujinine, A. (2018). Full waveform event location and moment tensor inversion for induced seismicity. *Geophysics, 84*(2), 1-76.

Wong, L. N. Y., Maruvanchery, V., and Liu, G. (2016). Water effects on rock strength and stiffness degradation. *Acta Geotechnica, 11*(4), 713-737.

Wong, T.-f., and Baud, P. (2012). The brittle-ductile transition in porous rock: A review. *Journal of Structural Geology, 44*, 25-53.

Wong, T., and Baud, P. (1999). Mechanical compaction of porous sandstone. *Oil & Gas Science and Technology, 54*(6), 715-727.

Wong, T. f., David, C., and Zhu, W. (1997). The transition from brittle faulting to cataclastic flow in porous sandstones: Mechanical deformation. *Journal of Geophysical Research: Solid Earth, 102*(B2), 3009-3025.

Wood, D. M. (1990). *Soil behaviour and critical state soil mechanics*: Cambridge university press.

Wulff, A.-M., Hashida, T., Watanabe, K., and Takahashi, H. (1999). Attenuation behaviour of tuffaceous sandstone and granite during microfracturing. *Geophysical Journal International, 139*(2), 395-409.

Yang, Y., Sone, H., and Zoback, M. (2015). *Fracture gradient prediction using the viscous relaxation model and its relation to out-of-zone microseismicity.* Paper presented at the SPE Annual Technical Conference and Exhibition.

Yang, Y., and Zoback, M. (2016). Viscoplastic deformation of the Bakken and adjacent formations and its relation to hydraulic fracture growth. *Rock Mechanics and Rock Engineering, 49*(2), 689-698.

Yue, Z., and Selvadurai, A. (1995). Contact problem for saturated poroelastic solid. *Journal of engineering mechanics, 121*(4), 502-512.

Zaitsev, V., Gusev, V., and Castagnede, B. (2003). Thermoelastic mechanism for logarithmic slow dynamics and memory in elastic wave interactions with individual cracks. *Physical Review Letters, 90*(7), 075501.